MEASURING THE ν_μ AND $\bar{\nu_\mu}$ INDUCED CHARGED-CURRENT COHERENT PION PRODUCTION CROSS SECTION ON CARBON AT THE T2K EXPERIMENT

MITCHELL YU

A DISSERTATION SUBMITTED TO
THE FACULTY OF GRADUATE STUDIES
IN PARTIAL FULFILMENT OF THE REQUIREMENTS
FOR THE DEGREE OF

DOCTOR OF PHILOSOPHY

GRADUATE PROGRAM IN PHYSICS AND ASTRONOMY
YORK UNIVERSITY
TORONTO, ONTARIO
APRIL 2022

Abstract

The Tokai-to-Kamioka (T2K) experiment is a long-baseline neutrino oscillation experiment located in Japan. The experiment aims to measure neutrino oscillation parameters through measurements of neutrino interaction rates at various locations after production. In addition, the T2K near detector ND280 can also perform neutrino cross-section measurements.

The muon neutrino (ν_μ) induced charged-current coherent pion production (COH) process ($\nu_\mu + \mathrm{A} \to \mu^- + \pi^+ + \mathrm{A}$) and the muon antineutrino ($\bar{\nu_\mu}$) induced coherent pion production process ($\bar{\nu_\mu} + \mathrm{A} \to \mu^+ + \pi^- + \mathrm{A}$) are not well modelled, and only a handful of experimental measurements are available to set constraints in the theoretical models. This thesis describes two new measurements of ν_μ ($\bar{\nu}_\mu$) induced CC-COH using the T2K near detector ND280. Both measurements are performed with a binned likelihood fitter framework developed by the T2K collaboration. The theoretical model used in the neutrino event generator for the COH process is the Berger-Sehgal model. The first measurement uses the ND280 data taken with the ν_μ-enhanced beam, with a mean neutrino energy of 0.849 GeV, and the measured CC-COH cross section on ^{12}C is $2.98 \pm 0.37(\mathrm{stat.}) \pm 0.58(\mathrm{syst.}) \times 10^{-40}\mathrm{cm}^2$. This is an updated measurement of a previously published T2K result with doubled statistics and an improved understanding of the systematic uncertainties. The second measurement uses the ND280 data taken with the $\bar{\nu}_\mu$-enhanced beam, with a mean neutrino energy of 0.849 GeV, and the measured CC-COH cross section on ^{12}C is $3.05 \pm 0.71(\mathrm{stat.}) \pm 0.84(\mathrm{syst.}) \times 10^{-40}\mathrm{cm}^2$. This is the first measurement of $\bar{\nu}_\mu$ CC-COH at the sub-GeV neutrino energy range.

Acknowledgements

As I am writing this thesis and heading toward the finish line of my Ph.D. life, in the midst of a pandemic, there are many people that I would like to thank. It is your help that made this possible.

To my family:

I want to thank my wife Louisa, who has been so supportive throughout this Ph.D. adventure. You have been extremely understanding, patient and loving.

I want to thank my father, Prof. Xiong Yu, for enlightening me into the world of science ever since I was a kid. I still remember my first popular science book, my first look through the microscope, and my first peek at the moon through the telescope. I want to thank my mother, Lynn, for all the love and caring throughout the years. Both of you made enormous sacrifices for me to live and receive an education in Canada - I hope you are proud of what I am achieving.

I want to thank my in-laws, grandparents, and other family members for all the love and support.

To Ph.D. my supervisor:

I want to thank my supervisor, Prof. Sampa Bhadra. Before I joined your team, I remember that you told me "Mitchell, I treat all my students like family". After these many years, I know you are not just saying that to be nice. You were there during my lows; you were there cheering for my successes. You witnessed my wedding, and even gave a speech! You can always see through my weaknesses, and you were never shy to point those out. You are always there, always available, to help me with my analysis and so much more. I want to let you know that I really appreciate having you as my Ph.D. supervisor and a mentor in life. You not only taught me how to become a better scientist, but also a better person.

To my colleagues:

My thesis work stands on the shoulders of so many of my fellow T2K collaborators. I want to thank the OTR group and the entire beam group for all the help while working on the OTR monitor. I also want to thank the software and cross-section groups for all the software and analysis support. I want to thank Prof. Xianguo Lu for all the physics

discussion and advice. I want to thank Dr. Sophie King for the help with the data and Monte Carlo simulation production. I want to thank Dr. Andrew Cudd and Prof. Kendall Mahn for hosting me at MSU while I learnt how to use the cross-section fitter.

I want to thank all my colleagues in the T2K-Canada group; the group meetings and the funs at the Minouchi houses are valuable to me. I want to thank all the (current and past) members of the York neutrino group, Dr. Arturo Fiorentini, Prof. Deborah Harris, Prof. Mark Hartz, Mark McCarthy, Prof. Monireh Kabirnezhad, Dr. Elder Pinzon, Dr. Gabriel Santucci, Dr. Fady Shaker, and Rowan Zaki. Especially, I want to thank Prof. Sampa Bhadra, Dr. Arturo Fiorentini, and Prof. Deborah Harris for important guidance and insightful comments during the analysis phase of this thesis.

To everyone else throughout my journey in Physics so far:

There are so many others that have helped me and guided me. I want to thank Prof. Shou Xian Fang (Academician of Chinese Academy of Sciences), who, although no longer with us, for the many physics (and life) conversations ever since I was a second-year undergraduate. Your insights in physics and especially your advice for me to study neutrino physics will always be remembered. I want to thank my undergraduate professor at UBC, Prof. Janis McKenna, for helping me look for internships in neutrino physics and eventually introducing me to Prof. Bhadra. I want to thank my supervisor during my summer internship at the Daya Bay Neutrino Experiment, Prof. Jiang Lai Liu: the two months onsite at Daya Bay strengthened my idea of studying neutrino physics. I want to thank my undergraduate supervisors at UBC and TRIUMF during my undergraduate thesis work at the T2K experiment, Prof. Hirohisa Tanaka and Prof. Kendall Mahn, for the support and guidance.

I was fortunate to have so many that have helped me up to this point in my life. So, I sincerely thank you all.

January 20, 2022

Toronto

Contributions

The cross-section analysis work presented in this thesis relied on the works and efforts of the entire T2K experiment collaboration. I will explain my contributions to the experiment and point out the existing works used, which are appropriately cited in the main body of the thesis where applicable.

Operation and Maintenance of Beamline Equipment: The York University group is responsible for the optical transition radiation monitor (OTR), which is a proton beam profile monitor placed right in front of the T2K graphite target. The OTR measurements are used as inputs to the neutrino flux simulation to constrain the proton beam direction and width uncertainties.

I helped with the installation of the current OTR system in 2014. Throughout the years, I have also helped with the (onsite) daily operation and the maintenance of OTR.

T2K data and Monte Carlo Simulation: The T2K ND280 data and the Monte Carlo simulation used by this analysis are produced by the ND280 computing group. Likewise, the reconstruction software packages used to process the data and to produce the simulation are the works of the ND280 software group.

Before I started the cross-section analysis, the Monte Carlo simulation used an older version of the NEUT neutrino event generator (NEUT5.3). The coherent pion production model used was the original Rein-Sehgal model, which is known to have deficiencies that result in overprediction in the coherent pion production cross section. At the time, a newer version of NEUT (NEUT5.4) with an updated coherent pion production model, the Berger-Sehgal model, was already available. Therefore, I initiated the effort to produce a new Monte Carlo simulation with NEUT5.4. Specifically, I used NEUT to make the neutrino interaction vector files needed to create the Monte Carlo simulation. I have also helped validate and debug the produced Monte Carlo simulation.

With the collaborative effort of the ND280 computing and software groups, the new data and Monte Carlo simulation productions (production 6T) were made. Besides the coherent pion production model change, the new production also features many changes such as bug fixes in modelling neutrino interactions and better-understood detector effects. Production

6T is currently used by the T2K oscillation analysis and the cross-section analyses.

Analysis Sample Selection: The analysis sample selections in this thesis are based on the works of the NuMu analysis group in T2K over many years. They developed the inclusive ν_μ and $\bar{\nu}_\mu$ charged-current samples and the subsamples with one detected pion (charged-current 1π). The data and Monte Carlo simulation comparisons for these samples are shown in the thesis. The selections (and detector systematics propagations) are performed with the analytical framework, High-Level-Analysis-at-the-Near-Detector (HighLAND), developed by the ND280 software group.

I have contributed to the writing of the $\bar{\nu}_\mu$ subsample technical note (TN273), where I computed the data and Monte Carlo simulation comparisons and evaluated the detector systematics.

Systematic Uncertainties: The systematic uncertainties can be subcategorized into flux, cross-section modelling, and detector systematics. The flux simulation and uncertainties are the works of the beam Monte Carlo group in T2K. The cross-section modelling uncertainties are the work of the neutrino interaction workgroup (NIWG) in T2K.

The various sources of the detector systematics are the works of the NuMu analysis group. I have made contributions to two of the detector systematics used by this analysis. Firstly, I have improved the pion secondary interaction systematics treatment with updated pion interaction cross-section tables. This work reduced the size of the pion secondary interaction systematics (one of the leading order systematics) by a factor of two. This work is documented in TN344. Secondly, the detector systematics related to the vertex activity were previously developed. However, the vertex activity systematics were not propagated, hence correlated with the other detector systematics. Therefore, I have implemented the vertex activity systematics into the framework (HighLAND) for detector systematics propagation. This work results in more accurate modelling of the vertex activity systematics.

Likelihood Fitter Framework: The likelihood fitter framework used by this analysis is the work of the Cross-Section group in T2K. Due to the nature of the single-bin measurement of this analysis, many tests and validations are performed. These validation procedures can be adapted to future studies with more complicated result formats (e.g., multi-dimensional differential measurements).

Contents

List of Figures

List of Tables

Chapter 1

Neutrino Physics

Neutrinos are the most abundant particle with mass[1] in the Universe. Nevertheless, our understanding of them is still limited. We study the properties of a particle by investigating how it interacts with matter, and the probability for a neutrino to interact is small. About one hundred trillion neutrinos, primarily produced from the Sun, pass through a human body every second without any interactions. Most of these neutrinos even travel through the Earth without leaving any trace behind. Since the postulate and discovery of neutrinos in the last century, the so-called "ghost particle"[2] never ceases to surprise the scientific community with peculiar properties, posing challenges to the existing physics theories, and pushing forward our understanding of the fundamental laws of physics of the Universe.

This chapter lays out the fundamentals of neutrino physics. First, section 1.1 introduces the particle in the context of the Standard Model of particle physics. Then, section 1.2 goes over the history of neutrino physics. Lastly, the particle's properties, specifically neutrino oscillation and neutrino interactions, are described in section 1.3 and section 1.4.

1.1 Neutrinos in the Standard Model

The Standard Model (SM) of particle physics is a theory that describes the fundamental particles and forces (excluding gravity). Figure 1.1 shows all the elementary particles and force carriers classified by the SM.

The elementary building blocks of the Universe are called fermions, which include six quarks and six leptons. The six quarks are the up, down, charm, strange, top, and bottom quarks. The three charged leptons are the electron (e), the muon (μ), and the taon (τ).

[1] We are only considering the known particles in the Universe here. The most abundant known particle in the Universe is the photon, which is massless.

[2] The name of the project led by Reines and Cowan in the 1950s was called Project Poltergeist.

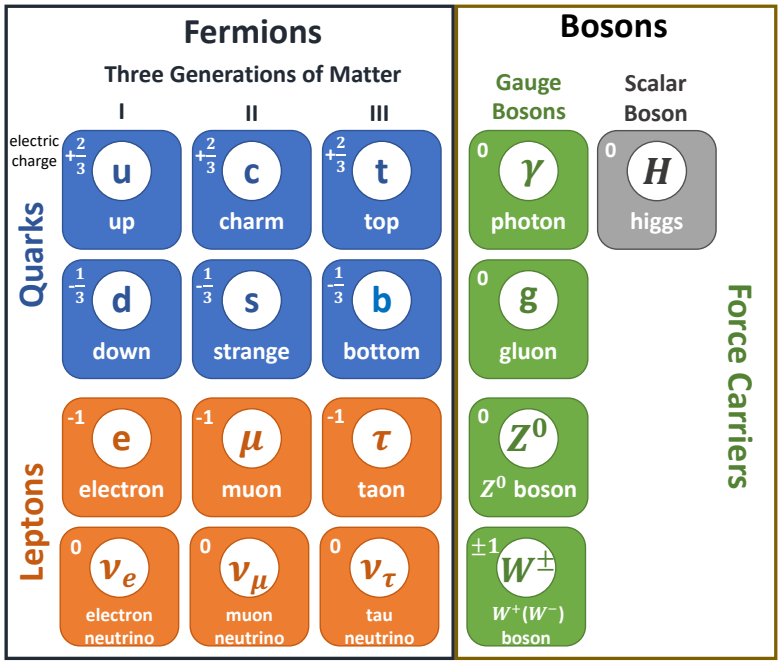

Figure 1.1. The elementary particles and force carriers classified by the Standard Model (SM) of particle physics. The elementary building blocks of the Universe are the fermions, which include six quarks and six leptons, and the force carriers of the fundamental forces, which are bosons. The Higgs boson is associated with the Higgs field that gives mass to fundamental particles (except for the neutrinos).

Neutrinos are leptons with neutral electric charge, and the three neutrinos are the electron neutrino (ν_e), the muon neutrino (ν_μ), and the tau neutrino (ν_τ). The types of neutrinos are often referred to as flavours (the physical meaning of this is described in section 1.3). Correspondingly, there exist the antimatter counterparts, which are the electron antineutrino ($\bar{\nu_e}$), the muon antineutrino ($\bar{\nu_\mu}$), and the tau antineutrino ($\bar{\nu_\tau}$). Unless stated otherwise, the word "neutrino" will refer to both neutrino and antineutrino for the rest of the thesis.

The fundamental forces covered by the SM are the electromagnetic, strong, and weak forces. The Gauge bosons (also called vector bosons) are the force carriers. The photons mediate the electromagnetic interactions. The gluons mediate the strong interactions. The weak interactions are mediated by the Z^0 or the $W^\pm$ bosons, and more details regarding these interactions are presented in section 1.4, where we describe neutrino interactions. The Higgs boson is associated with the Higgs field. The Higgs field gives mass to fundamental particles (except for the neutrinos, for which the mechanism that generates neutrino masses is still an ongoing research topic).

1.2 A Brief History of Neutrino Physics

1.2.1 The Discovery of Radioactivity

The discovery of radioactivity was one of the milestones in modern physics. It changed how we view the world from the atomic scale to the scale of the Universe. Radioactivity, and the study of the nucleus, also have significant impacts in fields such as geology, medicine, and energy.

Radioactivity was discovered by Henri Becquerel in 1896. Within a few years, it was realized that there are three types of radiation. Ernest Rutherford discovered the α and β rays in 1898. He named the two rays after the first two Greek alphabet letters, from the less-penetrating kind (α rays) to the more-powerful kind (β rays). In 1900, Paul Villard discovered the γ ray, a third kind of radiation with the most penetrating power among the three radiation types, and it was named after the third letter of the Greek alphabet. Two years later, Rutherford and Frederick Soddy proved experimentally that particle radiation could come from the spontaneous transformation of radioactive atoms into new elements. In this process of radioactive decay (also known as nuclear decay), an unstable atom with higher energy in its nucleus is transformed into an atom with lower energy, and the energy emitted by the former is in the form of radiation.

While studying radioactivity and the three types (α, β, and γ) of nuclear decay, it was first believed that the decays are all two-body kinematic processes ($A \rightarrow B + C$, where C can

be the radioactive particles). From kinematic arguments, the α, β, and γ particles produced from the decays are all expected to be monoenergetic, as is expected from a two-body decay. This was true for the α and the γ decays. However, in 1911, Lise Meitner and Otto Hahn measured the β particle spectrum and it was not a discrete spectrum. The β particle energy was usually less than that maximally allowed from kinematics. This result suggests that some energy is missing from the β decay process and taken up other undetected particle(s). This discovery challenged the validity of one of the most important laws in physics - the conservation of energy.

1.2.2 The Discovery and Detection of Neutrino

In 1930, Wolfgang Pauli hypothesized a particle that he thought "cannot be detected" as a "desperate remedy" to conserve energy in β decay. Pauli initially named this new particle "neutron", but it was later renamed "neutrino" by Enrico Fermi in 1932 to distinguish the particle from another neutrally charged and heavier particle, now known as a neutron, discovered by James Chadwick earlier in the year. Fermi formulated a theory of β decay, in which a neutron can decay into a proton, an electron (β particle), and a neutrino[3] as shown in process 1.1.

$$\mathrm{n} \rightarrow \mathrm{p} + \mathrm{e}^{-} + \nu \tag{1.1}$$

Pauli's opinion that neutrinos are undetectable did not stop experimental physicists from designing experiments to detect the particle. The scientific world waited for nearly two decades[4] until Clyde Cowan and Frederick Reines made the first neutrino detection measurement [2].

Cowan and Reines performed the first reactor neutrino experiment at the Savannah River nuclear power plant. The reaction they used for neutrino detection was

$$\bar{\nu_e} + \mathrm{p} \rightarrow \mathrm{n} \ + \mathrm{e}^{+}. \tag{1.2}$$

The reactor produced 5×10^{13} electron antineutrinos ($\bar{\nu_e}$) per square centimeter every second. They could interact with 200 litres of water that were filled inside two water tanks. The targets of the interactions were the protons (p) in the water molecules. The positron (e^{+}) from an interaction would immediately annihilate with an electron and produce two gamma rays. In order to detect the neutron (n) produced, cadmium chloride solution ($CdCl_2$) was doped into the water. The neutron would be absorbed by Cadmium as in the following

[3] We now know that the neutrino, in this case, is an electron antineutrino $\bar{\nu_e}$.

[4] Some early unsuccessful attempts can be dated back as early as 1936 [1].

reaction:

$$\mathrm{n} + {}^{108}\mathrm{Cd} \rightarrow {}^{109}\mathrm{Cd}^{*} \rightarrow {}^{109}\mathrm{Cd} + \gamma, \tag{1.3}$$

where an excited state of ^{109}Cd would be produced. The $^{109}\mathrm{Cd}^{*}$ emits an additional gamma-ray microseconds after the initial electron-positron annihilation gamma-rays. Therefore, the detection of the time-delayed gamma rays was defined as an electron antineutrino interaction signature.

The experimental result suggested roughly 3 electron antineutrino interactions per hour. The cross section[5] of the reaction (which is proportional to the interaction probability), with mean neutrino energy of 3 MeV, is $10^{-43}\,\mathrm{cm}^2$ [4]. This result proved that neutrinos are not undetectable, but the cross section is tiny. Thus, to successfully detect these particles, one needs an enormous number of neutrinos and also lots of nucleus targets for interactions to happen.

1.2.3 The "Solar Neutrino Problem" and Neutrino Oscillation

While the discovery of neutrinos was made with a human-made neutrino source from a nuclear reactor, the particles can be found everywhere in nature. Table 1.1 shows the most common natural neutrinos with the corresponding energy scale.

Name	**Neutrino Sources**	**Energy Scale (eV)**
Relic Neutrinos	Big Bang	10^{-1}
Geoneutrinos	Earth's core	10^{4}
Solar Neutrinos	Sun	10^{6}
Supernova Neutrinos	Supernova	10^{7}
Atmospheric Neutrinos	Earth's atmosphere	10^{9}
Cosmic Neutrinos	Active Galactic Nuclei Gamma Ray Burst etc.	$> 10^{14}$

TABLE 1.1. The natural neutrino sources sorted from the least to the most energetic. The energy scales are shown in the unit of electronvolt (eV). The energy scales are interpreted from this paper [5].

In 1968, Raymond Davis and John Bahcall tried to measure and count the neutrinos produced by the Sun. The experiment was located in South Dakota at the Homestake mine.

[5] According to Perkins [3], "cross-section" is "the rate of a particular reaction", and it is "numerically equal to the reaction rate per target particle per unit incident flux." Section 4.6 explains how the cross-section results for this thesis analysis are evaluated.

The mine is 1,478 meters underground, where the overburden of rock provides shielding to the cosmic rays. The detector was filled with 100,000-gallon chlorine-rich perchloroethylene[6]. The electron neutrinos with energy greater than 0.814 MeV, which is the minimum energy for the ^{37}Cl nucleus to capture the neutrino, can result in the following process:

$$\nu_e + {}^{37}\mathrm{Cl} \rightarrow {}^{37}\mathrm{Ar} + \mathrm{e}^{-}. \tag{1.4}$$

The surprising result was that the detected solar neutrino rate was only a third of the prediction of solar neutrino flux based on Bahcall's Standard Solar Model [6]. The deficiency of solar neutrinos raised doubt against Davis' experimental method and Bahcall's solar neutrino flux calculation. However, other experiments observed similar deficiencies and thus confirmed that some flaws existed in our understanding of neutrinos at the time. This deficiency was known as the "Solar Neutrino Problem". In the same year, Bruno Pontecorvo suggested a possible explanation that the solar electron neutrinos transformed into a different type of neutrino during its journey to Earth, which the Davis experiment perhaps could not detect. The recognition of the "Solar Neutrino Problem" and Pontecorvo's idea about the different neutrino types morphing into other types started the still ongoing studies on how neutrinos change characteristics during travel. This has opened the field of "neutrino oscillation".

1.2.4 Milestones in Neutrino Physics

Frederick Reines was awarded the Nobel Prize in Physics in 1995 for the co-discovery[7] of electron neutrinos in 1956. Leon Lederman, Melvin Schwartz, and Jack Steinberg discovered the muon neutrinos in 1962 and shared the Nobel Prize in Physics in 1988. The DONUT experiment discovered the third and final generation of neutrinos, the tau neutrinos, in 2000.

Masatoshi Koshiba and Raymond Davis Jr. shared the Nobel Prize in Physics in 2002 for the detection of cosmic neutrinos. In 2015, Arthur McDonald and Takaaki Kajita shared the Nobel Prize in Physics for the experimental confirmations that neutrinos change their identities as they travel ("oscillate").

[6] Perchloroethylene has a much more well-known name, which is dry-cleaning solvent.

[7] The other co-discoverer, Clyde Cowan, passed away in 1974. The Nobel Prizes are not awarded posthumously.

1.3 Neutrino Oscillation

In the theory of "neutrino oscillation", the neutrinos are created in the "flavour" eigenstates,

$$|\nu_\alpha\rangle\,, \qquad (\alpha = \mathrm{e}, \mu, \tau). \tag{1.5}$$

However, neutrinos travel as a mix of the three flavor eigenstates, and these are known as the "mass" eigenstates,

$$|\nu_k\rangle\,, \qquad (k = 1, 2, 3). \tag{1.6}$$

The flavour eigenstates are linear combinations (this will be demonstrated in section 1.3.1) of the mass eigenstates.

In this section, we will first discuss the neutrino oscillation theory with a simplified scenario where we only consider two neutrino flavours (ν_e and ν_μ) in section 1.3.1. Then, discussions of the parameters of neutrino oscillation with all three neutrino flavours (ν_e, ν_μ and ν_τ) are shown in section 1.3.2 (full derivation presented in appendix A). The current measurements of the neutrino oscillation parameters are presented in section 1.3.3.

1.3.1 Two-flavour Neutrino Mixing

Let's first study the neutrino oscillation theory with only two neutrino flavours (ν_e and ν_μ). These two flavour eigenstates are linear combinations of the two mass eigenstates (ν_1 and ν_2). A 2×2 unitary mixing matrix,

$$\mathbf{U} = \begin{pmatrix} \cos\theta & \sin\theta \\ -\sin\theta & \cos\theta \end{pmatrix}, \tag{1.7}$$

with an arbitrary mixing angle θ, describes the mixing between the eigenstates:

$$\begin{pmatrix} \nu_e \\ \nu_\mu \end{pmatrix} = \begin{pmatrix} \cos\theta & \sin\theta \\ -\sin\theta & \cos\theta \end{pmatrix} \begin{pmatrix} \nu_1 \\ \nu_2 \end{pmatrix}. \tag{1.8}$$

Using equation 1.8, we can write down the flavour eigenstates (ν_e and ν_μ) as linear combinations of the two mass eigenstates (ν_1 and ν_2) as

$$\begin{aligned} |\nu_e\rangle &= \cos\theta\,|\nu_1\rangle + \sin\theta\,|\nu_2\rangle \\ |\nu_\mu\rangle &= -\sin\theta\,|\nu_1\rangle + \cos\theta\,|\nu_2\rangle\,. \end{aligned} \tag{1.9}$$

From figure 1.2, we can see that in the case of two-flavour neutrino mixing, the so-called "mixing" is the rotation between the flavour and the mass eigenstates. The "mixing angle"

θ is the angle of rotation, which tells us the amount of mixing between the flavour and the mass eigenstates.

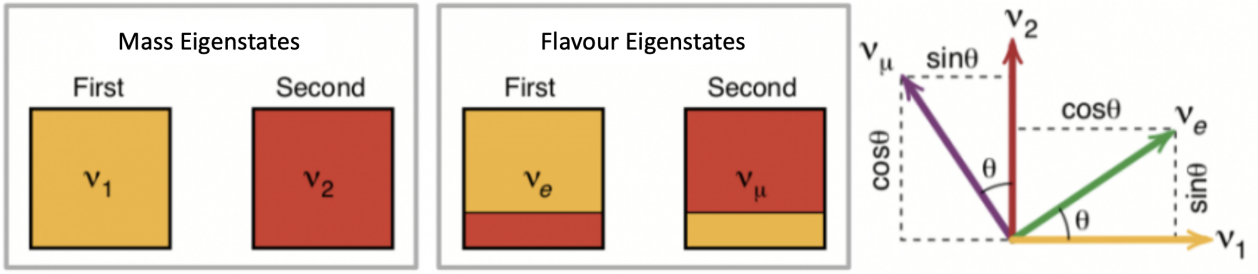

Figure 1.2. The two flavour eigenstates (ν_e and ν_μ) are linear combinations of the two mass eigenstates (ν_1 and ν_2). The mixing matrix $\mathbf{U}$ (equation 1.7) rotates ν_1 and ν_2 into ν_e and ν_μ. The angle of rotation is the mixing angle θ. The figure is taken from [7].

Starting with muon neutrinos (ν_μ) at $t = 0$, we have:

$$\left|\nu_\mu(0)\right\rangle = \left|\nu_\mu\right\rangle = -\sin\theta \left|\nu_1\right\rangle + \cos\theta \left|\nu_2\right\rangle . \tag{1.10}$$

The neutrino mass eigenstates are eigenstates of the Hamiltonian:

$$\mathcal{H} \left|\nu_k\right\rangle = E_k \left|\nu_k\right\rangle , \; k = 1, 2, \tag{1.11}$$

where the energy eigenvalues E_k are

$$E_k = \sqrt{p_k^2 + m_k^2}. \tag{1.12}$$

p_k and m_k are the momentum and mass of the neutrino.

The Schrödinger equation gives the time evolution (t) of a wavefunction. Using equation 1.10 and the plane wave solution of the Schrödinger equation, we can express the time evolution of the muon neutrinos (ν_μ) as

$$\left|\nu_\mu(t)\right\rangle = -e^{-iE_1 t}\sin\theta \left|\nu_1\right\rangle + e^{-iE_2 t}\cos\theta \left|\nu_2\right\rangle . \tag{1.13}$$

E_1 and E_2 here are the energies of the neutrino mass eigenstates. The Planck's constant $\hbar$ is in natural units ($\hbar = 1$) so that $e^{-iEt/\hbar} = e^{-iEt}$. The time evolution of pure muon neutrinos (at $t = 0$) is illustrated in figure 1.3. We can see the oscillatory behaviour of the mass eigenstates (ν_1 and ν_2) as functions of time as indicated in equation 1.13.

At time t, the flavour of the neutrino is a superposition of ν_e and ν_μ, and we can evaluate the following two probabilities.

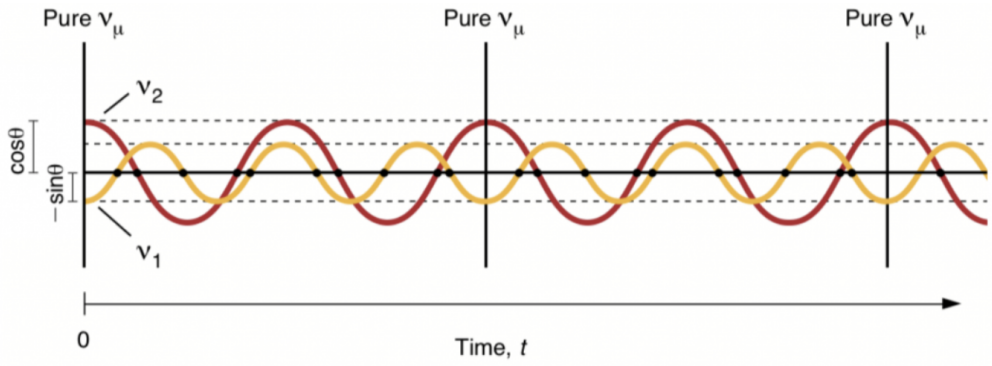

Figure 1.3. The time evolution of pure muon neutrinos (ν_μ at $t = 0$). We can see the oscillatory behaviour of the mass eigenstates (ν_1 and ν_2) as functions of time. At any time t, the flavour of the neutrino is a superposition of ν_e and ν_μ. The figure is taken from [7].

1. The muon neutrino (ν_μ) survival probability $P(\nu_\mu \to \nu_\mu)$: the probability to detect the neutrinos as muon neutrinos at time t.

2. The electron neutrino (ν_e) appearance probability $P(\nu_\mu \to \nu_e)$: the probability to detect the neutrinos as electron neutrinos at time t.

Since we are only considering two flavour eigenstates, it is trivial to see that the two probabilities should add up to 1. Therefore, we will first derive the muon neutrino (ν_μ) survival probability, and then calculate the electron neutrino (ν_e) appearance probability using the relation $P(\nu_\mu \to \nu_e) = 1$ - $P(\nu_\mu \to \nu_\mu)$.

A reminder to the reader that the mass eigenstates are orthonormal ($\langle \nu_k | \nu_j \rangle = \delta_{kj}$). Using equation 1.9 and 1.10, the amplitude of the process $\nu_\mu \to \nu_\mu$ at time t is

$$\begin{aligned} A_{\nu_\mu \to \nu_\mu}(t) &= \langle \nu_\mu | \nu_\mu(t) \rangle \\ &= (-\sin\theta \langle \nu_1| + \cos\theta \langle \nu_2|)(-e^{-iE_1 t}\sin\theta |\nu_1\rangle + e^{-iE_2 t}\cos\theta |\nu_2\rangle) \\ &= e^{-iE_1 t}\sin^2\theta + e^{-iE_2 t}\cos^2\theta. \end{aligned} \tag{1.14}$$

The muon neutrino (ν_μ) survival probability is

$$\begin{aligned} P_{\nu_\mu \to \nu_\mu}(t) &= \left| A_{\nu_\mu \to \nu_\mu}(t) \right|^2 \\ &= (A^*_{\nu_\mu \to \nu_\mu}(t))(A_{\nu_\mu \to \nu_\mu}(t)) \\ &= (e^{iE_1 t}\sin^2\theta + e^{iE_2 t}\cos^2\theta)(e^{-iE_1 t}\sin^2\theta + e^{-iE_2 t}\cos^2\theta) \\ &= 1 - \sin^2 2\theta \sin^2\left(\frac{(E_1 - E_2)t}{2}\right). \end{aligned} \tag{1.15}$$

Neutrinos are relativistic particles, therefore the energy (E) can be express in terms of

the mass (m) and the momentum (p) as

$$E = \sqrt{p^2c^2 + m^2c^4} = \sqrt{p^2 + m^2}, \tag{1.16}$$

where the speed of light (c) is in natural units (c=1). Assuming $E_1, E_2 \gg m_1, m_2$, and the two mass eigenstates have the same momentum p [3], the difference in energy $E_1 - E_2$ can be approximated (using Taylor series of $E = p\sqrt{1 + m^2/p^2}$) as

$$E_1 - E_2 = (p + \frac{m_1^2}{2p}) - (p + \frac{m_2^2}{2p}) \approx \frac{\Delta m^2}{2p}, \tag{1.17}$$

where the mass difference squared $\Delta m^2 = m_1^2 - m_2^2$.

With two more approximations:

$$\begin{aligned} &t \approx L/c = L,\ c = 1 \\ &E = \sqrt{p^2 + m^2} \approx p,\ p \gg m, \end{aligned} \tag{1.18}$$

where L is the distance travelled by the neutrinos, we can write the $(E_1 - E_2)t/2$ term in equation 1.15 as

$$\frac{(E_1 - E_2)t}{2} = (\frac{\Delta m^2}{2p})(\frac{t}{2}) = \frac{\Delta m^2 L}{4E}. \tag{1.19}$$

When we re-introduce the values of the Planck constant, $\hbar$ and the speed of light, c, and express L in km, $\Delta m^2 c^4$ in eV^2, and E in GeV [3], we have

$$\frac{\Delta m^2 L}{4E} = \frac{\Delta m^2 c^4 L}{4E\hbar c} = 1.27 \times \frac{\Delta m^2(\text{eV}^2) L(\text{km})}{E(\text{GeV})}. \tag{1.20}$$

Finally, the muon neutrino (ν_μ) survival probability can be written as

$$P_{\nu_\mu \to \nu_\mu}(t) = 1 - \sin^2 2\theta \sin^2(\frac{1.27\Delta m^2 L}{E}). \tag{1.21}$$

The electron neutrino (ν_e) appearance probability is

$$\begin{aligned} P_{\nu_\mu \to \nu_e}(t) &= 1 - P_{\nu_\mu \to \nu_\mu}(t) \\ &= \sin^2 2\theta \sin^2(\frac{1.27\Delta m^2 L}{E}). \end{aligned} \tag{1.22}$$

In both equation 1.21 and 1.22, the mixing angle θ and the mass difference squared Δm^2

are the neutrino oscillation parameters that neutrino experiments want to study. The maximum probability of the mixing (conversion from muon neutrinos to electron neutrinos in this case) is governed by $\sin^2 2\theta$ and the frequency of the mixing is related to Δm^2. The electron neutrino appearance probability (equation 1.22) is maximized when $(1.27\Delta m^2 L)/(E)$ is equal to $\pi/2$, $3\pi/2$, and so on.

In figure 1.4, the two probabilities are plotted assuming maximum mixing ($\sin^2 2\theta = 1$), neutrino energy of 0.6 GeV, and mass difference square of $2.5 \times 10^{-3}\,\mathrm{eV}^2$ (motivated by current experimentally measured value that will be discussed later in table 1.2). We can see that around $L = 300$ km, the neutrino oscillation effect is at the maximum (only electron neutrinos will be observed, as $\sin^2 2\theta$ has been set to 1, which corresponds to 100% conversion probability). The ratio between the distance (often referred to as baseline) and the neutrino energy, L/E, can be optimized by neutrino experiments to maximize the oscillation effect.

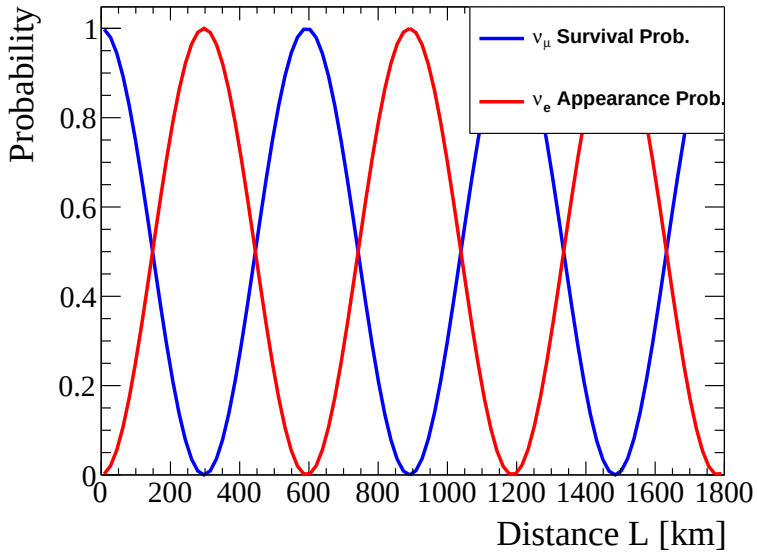

Figure 1.4. The muon neutrino (ν_μ) survival probability and the electron neutrino (ν_e) appearance probability as functions of the distance (L) travelled by the neutrino. The probabilities are computed using equation 1.21 and 1.22, and assuming $\sin^2 2\theta = 1$, neutrino energy of 0.6 GeV, and mass difference square of $2.5 \times 10^{-3}\,\mathrm{eV}^2$. The effect of neutrino oscillation is the largest around 300 km, 900 km, and so on.

1.3.2 Three-flavour Neutrino Mixing

For three-flavour neutrino mixing, with the three flavours eigenstates (ν_e, ν_μ, and ν_τ) and the three mass eigenstates (ν_1, ν_2, and ν_3), the relations between the flavour and the mass

eigenstates are described by the 3×3 Pontecorvo–Maki–Nakagawa–Sakata matrix (PMNS matrix, also referred to as the lepton mixing matrix),

$$\mathbf{U} = \begin{bmatrix} U_{e1} & U_{e2} & U_{e3} \\ U_{\mu 1} & U_{\mu 2} & U_{\mu 3} \\ U_{\tau 1} & U_{\tau 2} & U_{\tau 3} \end{bmatrix}. \tag{1.23}$$

The PMNS matrix is often written in the following form:

$$\begin{aligned} U &= \begin{bmatrix} U_{e1} & U_{e2} & U_{e3} \\ U_{\mu 1} & U_{\mu 2} & U_{\mu 3} \\ U_{\tau 1} & U_{\tau 2} & U_{\tau 3} \end{bmatrix} \\ &= \begin{bmatrix} 1 & 0 & 0 \\ 0 & \cos\theta_{23} & \sin\theta_{23} \\ 0 & -\sin\theta_{23} & \cos\theta_{23} \end{bmatrix} \begin{bmatrix} \cos\theta_{13} & 0 & \sin\theta_{13} e^{-i\delta_{\mathrm{CP}}} \\ 0 & 1 & 0 \\ -\sin\theta_{13} e^{i\delta_{\mathrm{CP}}} & 0 & \cos\theta_{13} \end{bmatrix} \begin{bmatrix} \cos\theta_{12} & \sin\theta_{12} & 0 \\ -\sin\theta_{12} & \cos\theta_{12} & 0 \\ 0 & 0 & 1 \end{bmatrix}, \end{aligned} \tag{1.24}$$

where θ_{23}, θ_{13}, and θ_{12} are the mixing angles between the three mass eigenstates (ν_1, ν_2, and ν_3). δ_{CP} is the Dirac CP-violating phase. The charge-conjugation and parity (CP) symmetry is the combination of charge (C) and parity (P) symmetry. It is a symmetry between matter and antimatter. CP-violation (CPV) in leptons could explain the reason for the matter dominant Universe [8][9].

The derivation for the three-flavour neutrino flavour oscillation probability is presented in appendix A. The transition probability ($P_{\nu_\alpha \to \nu_\beta}(t)$) from one neutrino flavour (ν_α, $\alpha = \mathrm{e}, \mu, \tau$) to another ($\nu_\beta$, $\beta = \mathrm{e}, \mu, \tau$) is:

$$\begin{aligned} P_{\nu_\alpha \to \nu_\beta}(t) = \delta_{\alpha\beta} &- 4 \sum_{k>j} \mathfrak{Re}\left[U^*_{\alpha k} U_{\beta k} U_{\alpha j} U^*_{\beta j}\right] \sin^2\left(\frac{\Delta m^2_{kj} L}{4E}\right) \\ &+ 2 \sum_{k>j} \mathfrak{Im}\left[U^*_{\alpha k} U_{\beta k} U_{\alpha j} U^*_{\beta j}\right] \sin\left(\frac{\Delta m^2_{kj} L}{2E}\right), \end{aligned} \tag{1.25}$$

where the indices k and j correspond to the three mass eigenstates and Δm^2_{kj} are the mass difference squared (Δm^2_{21}, Δm^2_{31}, and Δm^2_{32}) between the mass eigenstates.

1.3.3 Current Measurements of the Neutrino Oscillation Parameters

The oscillation parameters are the mass difference squared (Δm^2_{21}, Δm^2_{31}, and Δm^2_{32}), the mixing angles (θ_{23}, θ_{13}, and θ_{12}), and the CP-violating phase (δ_{CP}). In order to understand the mechanism of neutrino oscillation, the neutrino oscillation parameters need to be measured and studied.

The Tokai-to-Kamioka (T2K) experiment [10] is a long-baseline neutrino oscillation experiment designed to study some of the neutrino oscillation parameters (θ_{13}, θ_{23}, Δm^2_{23}, and δ_{CP}). T2K is the first experiment that indicated a non-zero θ_{13} [11]. The significance of this result is that δ_{CP} can only be measured and studied if θ_{13} is non-zero as it is a product of the two in the PMNS matrix ($\sin\theta_{13}e^{-i\delta_{\text{CP}}}$ and $-\sin\theta_{13}e^{i\delta_{\text{CP}}}$ in equation 1.24).

Current neutrino oscillation experiments do not have enough sensitivity to measure the sign of Δm^2_{31} or Δm^2_{32}. As shown in figure 1.5, there exist two possible neutrino mass orderings:

1. Normal mass hierarchy, $m_1 < m_2 < m_3$, $\Delta m^2_{31} > 0$.
2. Inverted mass hierarchy, $m_3 < m_1 < m_2$, $\Delta m^2_{32} < 0$.

Future results will help break the ambiguity of the ordering of the neutrino mass eigenstates.

While neutrino oscillation is still an ongoing topic of study, table 1.2 summarizes the current understanding of the oscillation parameters [13][14].[8] The oscillation parameters in table 1.2 are calculated assuming either normal or inverted mass hierarchy.

A neutrino oscillation experiment measures the neutrino event rate to extract the oscillation parameters. The reconstruction of the neutrino energies (for each detected neutrino) is an important factor in the neutrino oscillation analysis. The energy reconstruction depends on the detector resolution and, more importantly, a precise understanding of neutrino interactions. For experiments such as T2K, the modelling of the neutrino interactions is one of the largest sources of systematic uncertainties.

[8] The numbers quoted in the table includes the atmospheric neutrino data from the Super-Kamiokande collaboration. The results without the inclusion of this data can be found in the reference [13].

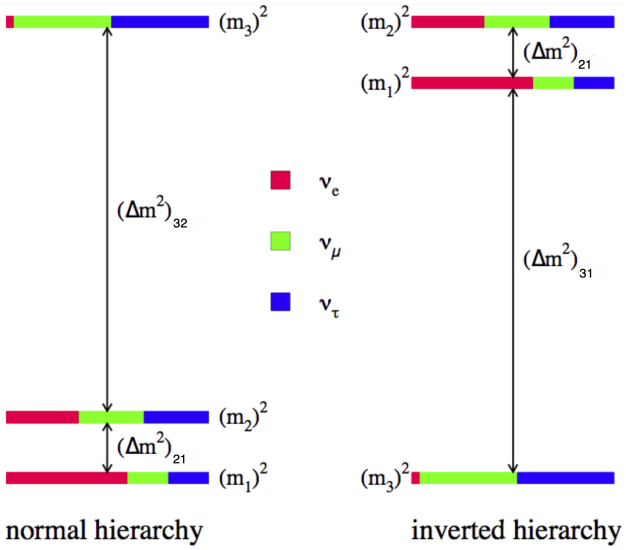

Figure 1.5. The normal (left) and inverted (right) mass hierarchy of the three neutrino mass states. The smaller mass difference can be measured with the solar neutrino experiments, and the larger mass difference can be measured with atmospheric neutrino experiments. The current measurements of the mass differences are listed in table 1.2. The figure is taken from [12].

	Normal Mass Hierarchy 3σ range	Inverted Mass Hierarchy 3σ range
$\sin^2\theta_{12}$	$0.269 \rightarrow 0.343$	$0.269 \rightarrow 0.343$
$\theta_{12}/^\circ$	$31.27 \rightarrow 35.86$	$31.27 \rightarrow 35.87$
$\sin^2\theta_{23}$	$0.415 \rightarrow 0.616$	$0.419 \rightarrow 0.617$
$\theta_{23}/^\circ$	$40.1 \rightarrow 51.7$	$40.3 \rightarrow 51.8$
$\sin^2\theta_{13}$	$0.02032 \rightarrow 0.02410$	$0.02052 \rightarrow 0.02428$
$\theta_{13}/^\circ$	$8.20 \rightarrow 8.93$	$8.24 \rightarrow 8.96$
$\delta_{\mathrm{CP}}/^\circ$	$120 \rightarrow 369$	$193 \rightarrow 352$
$\frac{\Delta m^2_{21}}{10^{-5}\mathrm{eV}^2}$	$6.82 \rightarrow 8.04$	$6.82 \rightarrow 8.04$
$\frac{\Delta m^2_{3l}}{10^{-3}\mathrm{eV}^2}$	$+2.435 \rightarrow +2.598$	$-2.581 \rightarrow -2.414$

TABLE 1.2. The values of the three-flavour neutrino oscillation parameters from fit to global data [13][14]. The 3σ range for each parameter is shown. The parameters are calculated assuming either normal ($\Delta m^2_{31} > 0$) or inverted ($\Delta m^2_{32} < 0$) mass hierarchy.

1.4 Neutrino Interactions

A neutrino interacts via the weak force. While the interactions can take place with either ν_e, ν_μ, or ν_τ, for this thesis, we will focus on the ν_μ ($\bar{\nu}_\mu$) interactions. A neutral-current (NC) neutrino interaction is mediated by a Z^0 boson, and a charged-current (CC) neutrino interaction is mediated by a $W^\pm$ boson. Figure 1.6 shows the weak interaction vertices of the NC and the CC modes.

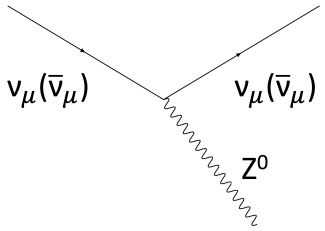

(a) neutral-current (NC) vertex

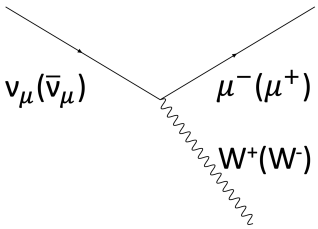

(b) charged-current (CC) vertex

Figure 1.6. The weak interaction can either be mediated by a Z^0 boson (NC channel), or a $W^\pm$ boson (CC channel).

Neutrino interactions can be subcategorized based on the particles produced. For the CC interactions, there are three common neutrino-nucleon level interactions.

The first one, illustrated in figure 1.7, is called the charged-current quasi-elastic scattering (CCQE), which results in a muon and a scattered nucleon, with $W^\pm$ as a mediator. To preserve the conservation of charge, ν_μ CCQE can only occur with a neutron, and $\bar{\nu}_\mu$ CCQE can only occur with a proton.

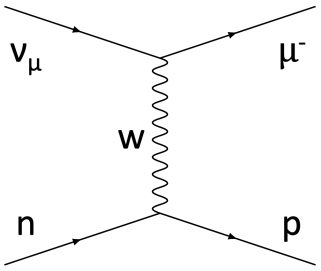

(a) ν_μ CCQE

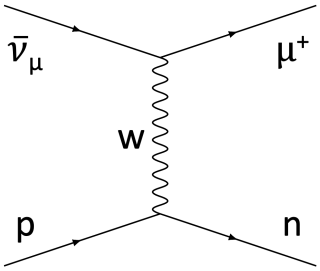

(b) $\bar{\nu}_\mu$ CCQE

Figure 1.7. Feynman diagrams of the ν_μ and $\bar{\nu}_\mu$ charged-current quasi-elastic scattering (CCQE), where a muon and a nucleon is produced.

For the second type of interaction, illustrated in figure 1.8, a charged lepton and an excited Delta resonance emerges from the neutrino interaction. The latter decays into a pion (π) and a nucleon. A pion is a meson (hadronic subatomic particle) that consists of a quark and an antiquark. This process is called the charged-current resonant pion production (CC-RES).

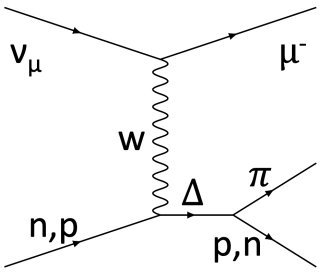

(a) ν_μ CC-RES

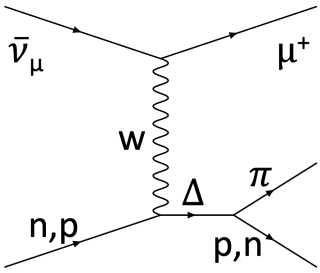

(b) $\bar{\nu}_\mu$ CC-RES

Figure 1.8. Feynman diagrams of the ν_μ and $\bar{\nu}_\mu$ charged-current resonant pion production (CC-RES). A charged lepton and an excited delta resonance is produced. The latter can decay into a pion and a nucleon.

The last common CC channel, illustrated in figure 1.9, is called deep inelastic scattering (CC-DIS). An energetic neutrino, typically with more than 1 GeV of energy, interacts with a quark inside a nucleon. The quark "hadronizes" once ejected from the nucleon, and the hadronic final state created can contain one or more pions.

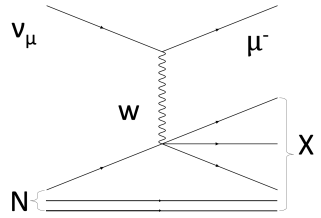

(a) ν_μ CC-DIS

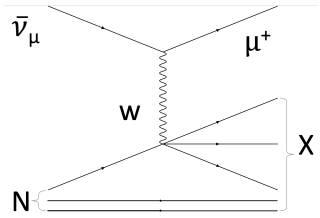

(b) $\bar{\nu}_\mu$ CC-DIS

Figure 1.9. Feynman diagrams of the ν_μ and $\bar{\nu}_\mu$ deep inelastic scattering (CC-DIS). A charged lepton and one or more pions are produced. This process happens when an energetic neutrino (with GeVs of energy) interacts with a quark inside a nucleon (N). The hadronic final state (X) created from quark hadronization can contain one or more pions.

Besides the common neutrino-nucleon level interactions described above, neutrinos can also interact with the whole target nucleus (neutrino-nucleus level interactions). In this thesis, one of the rare neutrino-nucleus interaction channels, the coherent pion production process, is studied. The details of the process, as well as the reasons why it is important to study such a process, are described in chapter 2.1.

Chapter 2

Neutrino Induced Coherent Pion Production

The focus of this thesis is on a rare interaction mode called coherent pion production (COH). This chapter starts with an introduction to this process in section 2.1. Then, the reasons and importance of studying COH are laid out in section 2.2. Next, three theoretical models of COH are derived in section 2.3. Lastly, the current status COH measurements, as well as the outline of the new measurements that are performed and described in this thesis, are shown in section 2.4 and 2.5.

2.1 Coherent Pion Production (COH)

Coherent pion production (COH) refers to the process where a muon neutrino (ν_μ) or a muon antineutrino[1] ($\bar{\nu_\mu}$) interacts with an entire nucleus (A) without knocking out any nucleons (protons and neutrons) but produces one lepton (muon neutrino or muon) and one pion. The target nucleus can only recoil but not be excited nor be fragmented. As shown in figure 2.1, this process can be mediated by either a Z^0 (NC-COH) via

$$\begin{aligned} \nu_\mu + \mathrm{A} &\rightarrow \nu_\mu + \pi^0 + \mathrm{A} \\ \bar{\nu_\mu} + \mathrm{A} &\rightarrow \bar{\nu_\mu} + \pi^0 + \mathrm{A} \end{aligned} \tag{2.1}$$

[1] The coherent pion production (COH) process can take place with any neutrino flavours. For this thesis, we focus on the muon neutrino (or muon antineutrino) induced COH.

or a $W^+(W^-)$ (CC-COH) via

$$\begin{aligned} \nu_\mu + A &\rightarrow \mu^- + \pi^+ + A \\ \bar{\nu_\mu} + A &\rightarrow \mu^+ + \pi^- + A. \end{aligned} \tag{2.2}$$

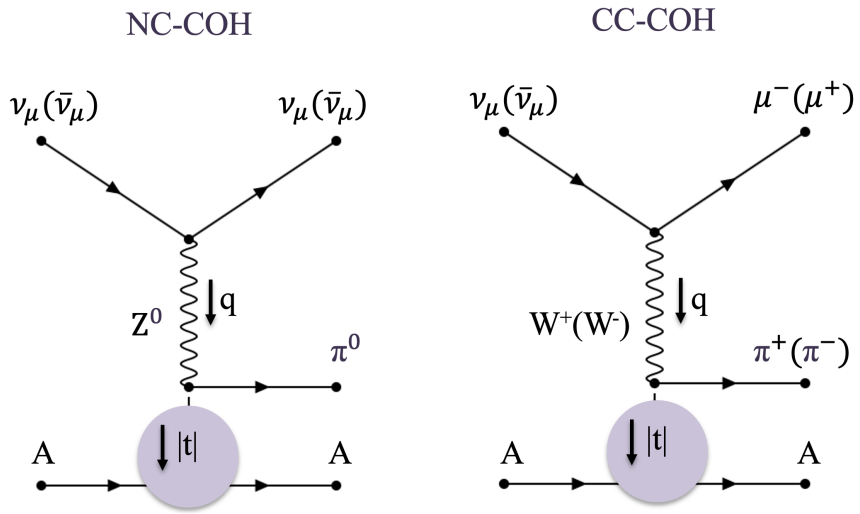

Figure 2.1. Neutrino induced coherent pion production can be mediated by either a Z^0 or a $W^+(W^-)$ boson. The neutral-current (left) case, described by the process 2.1, produces a neutrino and neutral pion; the charged-current (right) case, described by the process 2.2, results in a charged muon and a charged pion. For the muon neutrino (ν_μ) charged-current case, the variable q is the four-momentum transfer from the neutrino-muon system to the W^+ boson. The variable $|t|$ is the four-momentum transferred squared from the W^+-π^+ system to the target nucleus (A).

To help with the clarity, this section is written in the context of muon neutrino (ν_μ) CC-COH.

The variable q is the four-momentum transfer from the neutrino-muon system to the W^+ boson. It is defined as $q = P_\nu - P_\mu$, where P_ν and P_μ are the neutrino and muon four-momenta. Later in this chapter, we will work with the four-momentum transferred squared (q^2). For a virtual particle[2] (the W^+ boson in this case), the sign of the four-momentum transferred squared is negative. To work with a positive quantity, we also define Q^2 where $Q^2 = -q^2$. In addition, Q^2 can be derived to be expressed in terms of the scattering angle (θ_μ) of the muon with respect to the neutrino direction in the lab frame ($Q^2 \propto \sin(\theta_\mu)$). For example, the condition $Q^2 = 0$ implies that the outgoing muon direction is the same as the incident neutrino (the outgoing muon is "forward").

[2]According to Griffiths [15], a "virtual" particle "is represented by the internal lines of a Feynman diagram" and it is "not observed" and "cannot be observed without entirely changing the process".

The variable t is the four-momentum transferred squared from the W^+-π^+ system to the target nucleus (A). Again, t is negative in this case, and we will take the modulus ($|t|$) to obtain a positive quantity to work with. The variable $|t|$ is defined as:

$$|t| = \left|(q - P_\pi)^2\right| = \left|(P_\nu - P_\mu - P_\pi)^2\right|, \tag{2.3}$$

where P_π is the pion four-momentum. Similar to the relation between Q^2 and the scattering angle of the muon, $|t|$ is also related to the scattering angle of the pion. The condition $|t| = 0$ implies that the angle between the pion and muon is zero.

It was mentioned that the target nucleus of the COH process can only recoil but not be excited nor be fragmented. This can happen with $|t|$ close to zero. It will be demonstrated later in chapter 5 and 6 that $|t|$ for CC-COH events is small (distributed very close to zero) compared to most of the other neutrino interaction channels (such as the ones described in section 1.4). Therefore $|t|$ is an essential variable for this analysis and it is further discussed in section 4.4.2. For the rest of this thesis, we will use the name "momentum transferred squared" to refer to $|t|$.

2.2 Motivation

Theoretically, the COH process is not well modelled, and only a handful of experimental measurements are available (these measurements are described in section 2.4). As a result, for neutrino experiments such as T2K (described in chapter 3), both the NC-COH and CC-COH event rate predictions are assigned with thirty percent[3] uncertainties when neutrino oscillation measurements are performed. [17].

In the precision measurement era of neutrino oscillation experiments, uncertainties on the neutrino interaction cross sections, such as the one mentioned above, need to be better constrained to achieve the precision level required by the experiments. The T2K near detector ND280 (described in section 3.2) is used to perform neutrino interaction studies. The proposed thesis research uses the muon neutrino beam and muon antineutrino beam data collected by ND280 to study the CC-COH process. In the following section, we will see that the theoretical modelling of the NC-COH and CC-COH processes are mostly identical. Therefore, new CC-COH measurements will improve the modelling accuracy for both COH processes.

[3]Depending on the analysis, the uncertainties can be as high as one hundred percent [16].

2.3 Theoretical Models

2.3.1 Rein-Sehgal (1983) Model

The foundation of all the theoretical models described in this thesis for the COH process is Adler's partially conserved axial current (PCAC) hypothesis, which relates the neutrino-nucleus cross section ($\sigma^{\nu \mathrm{A}}$) to the pion-nucleus cross section ($\sigma^{\pi \mathrm{A}}$) [18].

The Rein and Sehgal (RS) model [19] used Adler's PCAC hypothesis formalism [18][20] to estimate the NC-COH (reaction 2.1) cross section ($\sigma^{\text{NC-COH}}$) as a function of the pion-nucleus cross section ($\sigma^{\pi^0 \mathrm{A}}$) for $Q^2 = 0$ as shown in equation 2.4. The RS formalism was first derived for the NC-COH channel and then converted to describe the CC-COH mode. The derivation in this section will follow this order.

$$\left.\frac{d\sigma^{\text{NC-COH}}}{dx dy d|t|}\right|_{Q^2=0} = \frac{G_F^2 M_N E_\nu}{\pi^2} \frac{1}{2} f_\pi^2 (1-y) \left.\frac{d\sigma(\pi^0 A \to \pi^0 A)}{d|t|}\right|_{E_\nu y = E_\pi}. \tag{2.4}$$

G_F is the Fermi coupling constant, and M_N represents the mass of the nucleon. E_ν, E_l and E_π represent the energy of the incident neutrino, the outgoing neutrino, and the outgoing pion, respectively. The neutrino energy transfer (ν) and the Bjorken scaling variables (x and y) [21] are defined as

$$\nu = E_\nu - E_l, \; x = \frac{Q^2}{2M_N \nu}, \; y = \frac{\nu}{E_\nu}. \tag{2.5}$$

The dimensionless scaling factor x equals 1 for elastic scattering and is between 0 and 1 for inelastic scattering. The scaling factor y is the fractional energy loss of the incident neutrino. The interaction kinematics of the COH process can be completely defined with x and y.

The pion decay constant f_π is related to the mass of pion m_π, where $f_\pi = 0.93 m_\pi$. The difference between the decay constants[4] for π^0 and $\pi^\pm$ is:

$$f_{\pi^0}^2 = \left(\sqrt{\frac{1}{2}} f_{\pi^\pm}\right)^2 = \frac{1}{2} f_{\pi^\pm}^2. \tag{2.6}$$

The extension from $Q^2 = 0$ region to the non-forward small Q^2 region is done with the additional propagator term $\left(1 + Q^2/m_A^2\right)^{-2}$. The axial mass[5], m_A, is set to be 1 GeV.

[4] The current PDG value for the pion decay constants are: $f_{\pi^0} = 130 \pm 5 MeV$, $f_{\pi^\pm} = 130.41 \pm 0.03 \pm 0.20 MeV$. Regardless, the derivation in this section follows equation 2.6.

[5] The axial (vector) mass m_A is a phenomenological parameter. The current experimental values of m_A are summarized in [22].

The pion-nucleus cross sections can be expressed as pion-nucleon cross sections as:

$$\frac{d\sigma(\pi^0 A \to \pi^0 A)}{d\,|t|} = A^2\,|F_A(t)|^2\,\frac{d\sigma(\pi^0 N \to \pi^0 N)}{d\,|t|}\bigg|_{|t|=0}. \tag{2.7}$$

Here A is the mass number of the target element, and $F_A(t)$ is the nuclear form factor to describe pion absorption inside the nucleus. It is related the nucleon pion absorption form factor F_{abs} (this factor is t-independent):

$$|F_A(t)|^2 = e^{-b|t|}F_{abs}, \tag{2.8}$$

where $b = \frac{1}{3}R^2$, and R is the nuclear radius calculated from the nuclear radius parameter R_0[6] ($R = R_0 A^{\frac{1}{3}}$). F_{abs} can be related to the pion inelastic cross section (σ_{inel}) by:

$$F_{abs} = \exp\left(-\frac{9A^{\frac{1}{3}}}{16\pi R_0^2}\sigma_{\text{inel}}\right) \tag{2.9}$$

As mentioned in section 2.1, when $|t| = 0$, it means the outgoing pion direction is the same as the outgoing neutrino (the pion is "forward"). The forward direction pion-nucleon differential cross section can be written as

$$\frac{d\sigma(\pi^0 N \to \pi^0 N)}{d\,|t|}\bigg|_{t=0} = \frac{1}{16\pi}\left[\sigma_{TOT}^{\pi^0 N}\right]^2(1+r^2), \tag{2.10}$$

where $r = Ref_{\pi N}(0)/Imf_{\pi N}(0)$ with the aid of the optical theorem. $\sigma_{\text{TOT}}^{\pi^0 N}$ is the average pion-nucleon cross section[7]. The ratio between the real and imaginary part of the forward direction πN scattering amplitude is r.

Combining everything together, the RS prediction of the NC-COH triple differential cross section is:

$$\begin{aligned}\frac{d\sigma^{NC-COH}}{dxdyd|t|} &= \frac{G_F^2 M_N}{2\pi^2} f_{\pi^0}^2 A^2 E_\nu (1-y) \\ &\times \frac{1}{16\pi}\left[\sigma_{TOT}^{\pi^0 N}\right]^2(1+r^2) \\ &\times \left(\frac{m_A^2}{m_A^2+Q^2}\right)^2 e^{-b|t|}F_{abs}.\end{aligned} \tag{2.11}$$

[6] The value of the constant R_0 is determined empirically to be 1.2×10^{-15} m.

[7] The average pion-nucleon cross section can be approximated with pion-deuteron cross section ($\sigma_{\text{TOT}}^{\pi^0 N} = \frac{1}{4}\left[\sigma_{\text{TOT}}^{\pi^+ D} + \sigma_{\text{TOT}}^{\pi^- D}\right]$).

Finally, to obtain the CC-COH prediction, the pion decay constant is changed from $f^2_{\pi^0}$ to $f^2_{\pi^\pm}$, where a factor of 1/2 is picked up from the relationship in equation 2.6. The pion-nucleon cross section is also changed from $\sigma^{\pi^0 N}_{TOT}$ to $\sigma^{\pi^\pm N}_{TOT}$. The RS prediction of the CC-COH triple differential cross section is shown in equation 2.12.

$$\begin{aligned}\frac{d\sigma^{CC-COH}}{dxdyd|t|} &= \frac{G_F^2 M_N}{4\pi^2} f^2_{\pi^\pm} A^2 E_\nu (1-y) \\ &\times \frac{1}{16\pi}\left[\sigma^{\pi^\pm N}_{TOT}\right]^2 (1+r^2) \\ &\times \left(\frac{m_A^2}{m_A^2+Q^2}\right)^2 e^{-b|t|} F_{abs}\end{aligned} \tag{2.12}$$

2.3.2 Rein-Sehgal (2007) Model

When the K2K neutrino experiment [23] studied the CC-COH process at the low neutrino energy range ($\langle E_\nu \rangle = 1.3\,\text{GeV}$), a significant deficit of the CC-COH rate in the $Q^2 < 0.1\,\text{GeV}^2$ region compared to the original 1983 RS prediction was observed [24]. Experimental results for COH (including the K2K result) will be further discussed in detail in 2.4. This discrepancy motivated several modifications to the RS model [25].

In the original RS derivation, the mass of the lepton, m_l, is assumed to be zero. For the NC-COH derivation, this is acceptable - the mass of the outgoing muon neutrino can indeed be ignored. However, when moving from NC to CC (see figure 2.1), the assumption of zero outgoing lepton mass no longer holds since the outgoing leptons are massive charged muons. Therefore, to include the muon mass (m_μ), a correction term,

$$C = \left(1 - \frac{1}{2}\frac{Q^2_{min}}{Q^2+m_\pi^2}\right)^2 + \frac{1}{4} y \frac{Q^2_{min}(Q^2 - Q^2_{min})}{(Q^2+m_\pi^2)^2}, \tag{2.13}$$

is added, where Q^2_{min} is defined as:

$$Q^2_{min} = m_\mu^2 \frac{y}{1-y}. \tag{2.14}$$

The valid region of variables Q^2 and y are:

$$\begin{aligned} &Q^2_{min} \leq Q^2 \leq 2M_N E_\nu y_{max}, \\ &y_{min} = \frac{m_\pi}{E_\nu},\ y_{max} = 1 - \frac{m_\mu}{E_\nu}. \end{aligned} \tag{2.15}$$

The corrected RS prediction for CC-COH is:

$$\begin{aligned}\frac{d\sigma^{CC-COH}}{dxdyd|t|} &= \frac{G_F^2 M_N}{4\pi^2} f_\pi^2 A^2 E_\nu (1-y) \\ &\times \frac{1}{16\pi}\left[\sigma_{TOT}^{\pi^\pm N}(E_\nu y)\right]^2 (1+r^2) \\ &\times \left(\frac{m_A^2}{m_A^2+Q^2}\right)^2 e^{-b|t|} F_{abs} \\ &\times C\theta(Q^2-Q^2_{min})\theta(y-y_{min})\theta(y_{max}-y),\end{aligned} \tag{2.16}$$

where $\theta(x)$ is the Heaviside step function:

$$\theta(x) := \begin{cases} 1, x > 0 \\ 0, x \leq 0 \end{cases}. \tag{2.17}$$

Figure 2.2 shows the effect of the correction, about 25% suppression, to the CC-COH prediction.

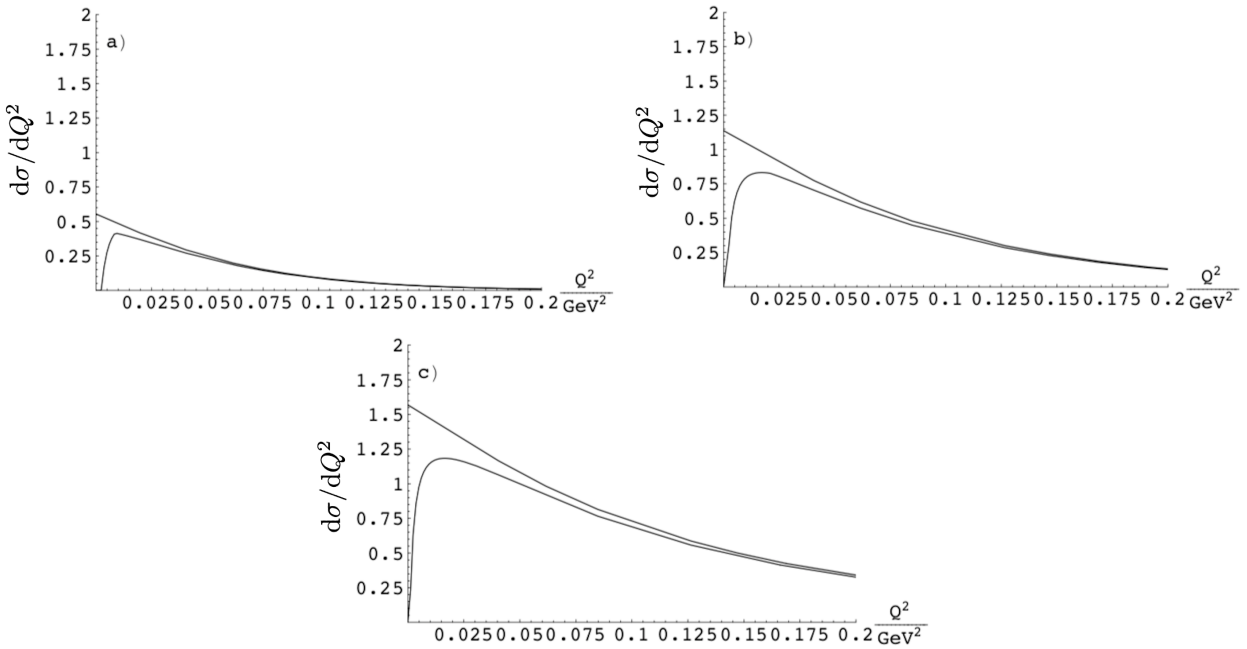

Figure 2.2. Effect of the muon mass correction to the RS prediction on the CC-COH process at neutrino energy of 0.8 GeV (a), 1.3 GeV (b), and 2.0 GeV (c). The upper (lower) curves show the RS prediction without (with) the muon mass correction term. It is clear that with the correction term, CC-COH process is suppressed at low Q^2. The figures are taken from [25].

2.3.3 Berger-Sehgal (2009) Model

Further attempts to adjust the modelling of the COH process were motivated by the disagreement between prediction and experimental data. The Berger-Sehgal formalism [26], which is also based on the PCAC hypothesis, is discussed below.

The CC inelastic neutrino scattering double differential cross section formula for zero outgoing lepton mass is:

$$\frac{d\sigma^{CC}}{dQ^2dy} = \frac{G_F^2 cos^2\theta_c}{4\pi^2}\kappa E_\nu \frac{Q^2}{|\mathbf{q}|^2}\left[u^2\sigma_L + v^2\sigma_R + 2uv\sigma_s\right]. \tag{2.18}$$

To remind the readers of the variables already defined:

- Q^2 is the negative of the four-momentum transferred squared from the neutrino-muon system to the $W^+(W^-)$. $\mathbf{q}$ is the three-momentum component of the momentum transfer.
- The Bjorken scaling variable y follows the definitions in equation 2.5.
- The term G_F and θ_C are the Fermi coupling constant and the Cabbibo angle.
- The variables u and v are kinematical factors, where $u, v = (E_\nu + E_\mu \pm |\mathbf{q}|)/2E_\nu$.
- κ is related to the invariant mass W_{inv} and the mass of the nucleon (or nucleus) M_N: $\kappa = (W_{inv}^2 - M_N^2)/2M_N$.

The left, right, and scalar cross sections (σ_L, σ_R, and σ_s) of the inelastic neutrino scattering are either measured or calculated theoretically, and in the limit of $Q^2 \to 0$, only the scalar part survives. Using the PCAC hypothesis, we can again relate the scalar cross section to the pion-nucleon scattering cross section where

$$\sigma_s = \frac{|\mathbf{q}|}{\kappa Q^2} f_\pi^2 \sigma^{\pi N}. \tag{2.19}$$

The CC neutrino inelastic cross section in the forward limit, where the lab frame outgoing muon angle $\theta_\mu \to 0$, is:

$$\left.\frac{d\sigma^{CC-COH}}{dQ^2dy}\right|_{\theta_\mu \to 0} = \frac{G_F^2 cos^2\theta_c f_\pi^2}{2\pi^2}\frac{E_\nu}{|\mathbf{q}|}uv\sigma^{\pi N}. \tag{2.20}$$

Similar to the updated 2007 RS formalism, a correction factor is needed to deal with the

non-zero outgoing muon mass:

$$C_{BS} = \left(G_A - \frac{1}{2}\frac{Q^2_{min}}{Q^2 + m^2_\pi}\right)^2 + \frac{1}{4}y\frac{Q^2_{min}(Q^2 - Q^2_{min})}{(Q^2 + m^2_\pi)^2}. \tag{2.21}$$

G_A is the axial vector form factor, where $G_A = m^2_A/(Q^2 + m^2_A)$. The difference between the RS (equation 2.13) and BS (equation 2.21) correction factors is that Q^2 is not assumed to be zero when calculating G_A, resulting in that G_A no longer equals to 1; the value for m_A is also modified from 1 GeV to 0.95 GeV[8].

Putting all the pieces together, the BS triple differential CC-COH cross section is shown in equation 2.22. The Heaviside step function $\theta(x)$ is only non-zero within the valid region, which is the same as the valid region shown in equation 2.15 for the 2007 RS formalism.

$$\begin{aligned}\frac{d\sigma^{CC-COH}}{dQ^2 dy d|t|} = &\frac{G^2_F cos^2\theta_c f^2_\pi}{4\pi^2}\frac{E_\nu}{|\mathbf{q}|}uv \\ &\times \frac{1}{16\pi}\left[\sigma^{\pi^\pm N}_{TOT}(E_\nu y)\right]^2 (1 + r^2) \\ &\times \left(\frac{m^2_A}{m^2_A + Q^2}\right)^2 e^{-b|t|} F_{abs} \\ &\times C_{BS}\theta(Q^2 - Q^2_{min})\theta(y - y_{min})\theta(y_{max} - y)\end{aligned} \tag{2.22}$$

In addition to modifying the theoretical model, the BS formalism also used available pion-carbon scattering data to compute the average pion-nucleon cross section ($\sigma^{\pi^\pm N}_{TOT}$ in equation 2.22). The effect of this change is shown in figure 2.3. The difference between the RS and BS formalism for CC-COH and NC-COH is shown in figure 2.4; both cross sections are smaller than the RS prediction as the measurements suggest.

[8]The value for the axial mass is experimentally determined. The discussion on this topic is in the reference [22].

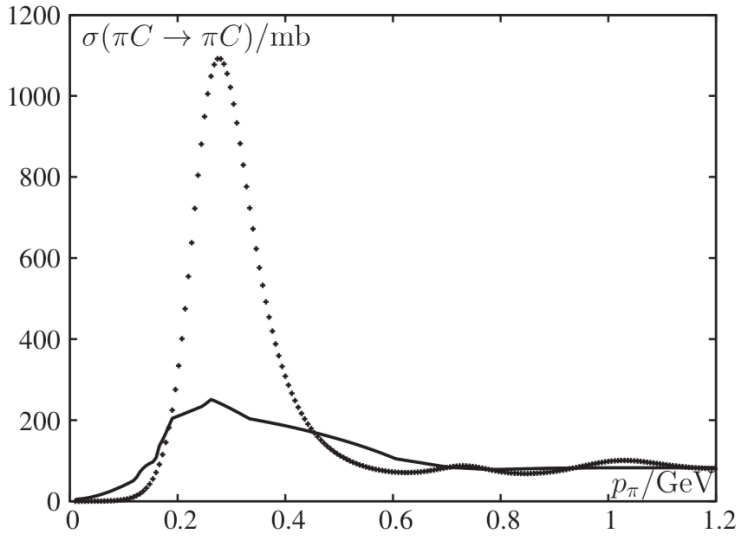

Figure 2.3. Comparison of pion-carbon scattering cross section in the Rein-Sehgal (RS) model and the Berger-Sehgal (BS) model. External pion-carbon scattering data sets are used instead of actually modeling the pion-nucleus scattering. The difference between the RS prediction (dotted line) and the BS prediction (solid line) indicates a radical difference. The figure is taken from [26].

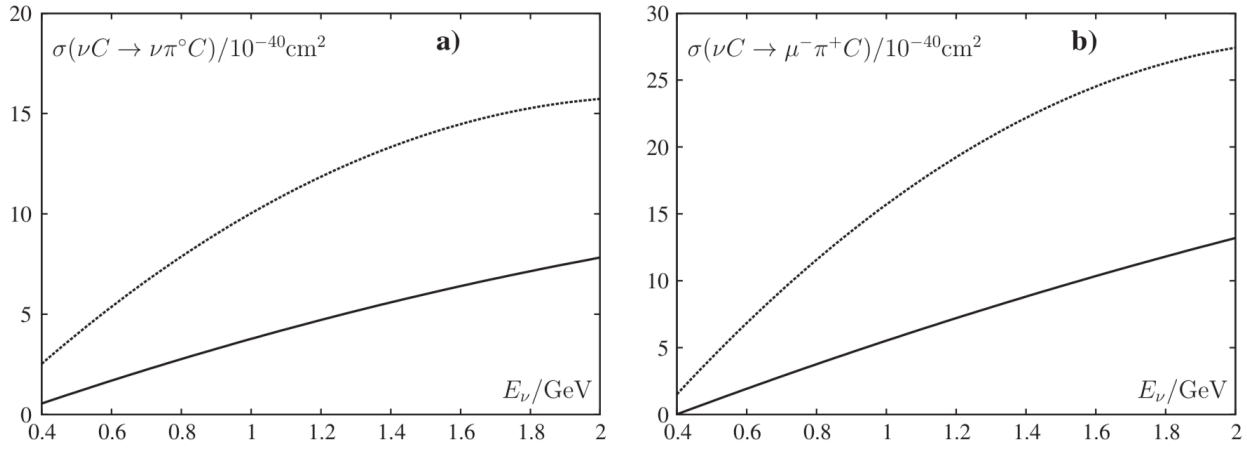

Figure 2.4. Comparison between the Rein-Sehgal (RS) (dashed line) and Berger-Sehgal (BS) (solid line) models for the NC-COH (left) and CC-COH (right) cross sections. The BS predictions are smaller than the RS predictions as expected and suggested by experimental measurements such as the result from K2K [24]. The figures are taken from [26].

2.4 Current Measurements

Most accelerator-based neutrino experiments study neutrinos with energy ranging from a few hundred Mega electron-Volts (MeV) to over a hundred Giga electron-Volts (GeV). The first experiment to measure the COH process was the Aachen-Padova experiment [27] in 1983. The experiment detected and measured NC-COH on Al^{27} target with average neutrino energy around 2 GeV. From the 1980s to the early 1990s, more experiments studied the COH process at neutrino energy from tens to over a hundred GeV [28][29][30][31]. In the recent few years, some experiments have made more precise measurements of the COH cross section at few GeV to tens of GeV neutrino energies [32][33][34].

The T2K muon neutrino beam (mean energy less than one GeV) provides an opportunity to study neutrino interactions at energies lower than most other experiments (tens of GeV). Before T2K, there were several unsuccessful attempts to measure CC-COH in the low-energy region [24][35]. These experiments set upper limits (at 90% confidence level) of the CC-COH cross section:

- K2K (2006): $\sigma^{\text{CC-COH}}_{^{12}\text{C}}(\langle \text{E}_\nu \rangle = 1.3\text{GeV}) < 7.7 \times 10^{-40}\text{cm}^2$.
- SciBooNE (2008): $\sigma^{\text{CC-COH}}_{^{12}\text{C}}(\langle \text{E}_\nu \rangle = 1.1\text{GeV}) < 8.4 \times 10^{-40}\text{cm}^2$.
- SciBooNE (2008): $\sigma^{\text{CC-COH}}_{^{12}\text{C}}(\langle \text{E}_\nu \rangle = 2.2\text{GeV}) < 28.7 \times 10^{-40}\text{cm}^2$.

Here $\langle \text{E}_\nu \rangle$ refers to mean neutrino energies. One of the reasons for the unsuccessful cross-section extractions is low data statistics which results in significant statistical uncertainties. In addition, aspects such as the hardware effects and the nuclear effects all result in large systematic uncertainties.

With the data collected by the near detector (ND280) of the T2K experiment between 2010 and 2014, T2K published a paper with the first measurement of muon neutrino CC-COH at sub-GeV neutrino energy [36]:

$$\sigma^{\text{CC-COH}}_{^{12}\text{C}}(\langle \text{E}_\nu \rangle = 0.86\text{GeV}) = 3.9 \pm 1.0(\text{stat.})^{+1.5}_{-1.4}(\text{syst.}) \times 10^{-40}\text{cm}^2. \tag{2.23}$$

The three different theoretical models described in this section and the current measurements (both upper limits from K2K (2006) and SciBooNE (2008) and the cross-section measurement from T2K (2014)) are shown in figure 2.5. A clear indication of data preference of the RS (2007) and BS(2009) over the RS (1983) can be seen.

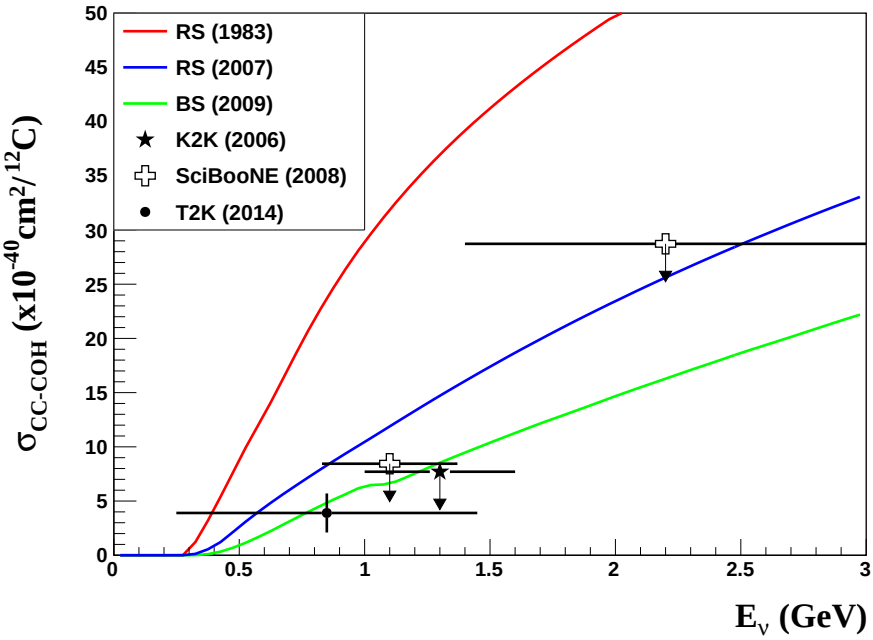

Figure 2.5. The theoretical model predictions of the CC-COH process with current measurements (upper limits and cross-section measurements) from K2K (2006), SciBooNE (2008), and T2K (2014) below 3 GeV neutrino energy.

2.5 New Measurements

Since the publication of T2K's first CC-COH paper, T2K has collected twice as much data in the neutrino beam configuration and new data in the antineutrino beam configuration. As a result of these additional data available, two measurements are performed and presented in this thesis.

The first measurement is an updated neutrino CC-COH measurement with the additional data collected; the statistical uncertainty will be significantly reduced. The second measurement will become the first antineutrino CC-COH measurement at sub-GeV neutrino energy, filling a blank spot in the global data set for CC-COH. Furthermore, since the last T2K paper on CC-COH, the detectors used for the measurements have also been better studied. Therefore, the detector systematic treatments are improved. As a result, we can make more precise CC-COH cross-section measurements.

Chapter 3

The T2K Experiment

The Tokai-to-Kamioka (T2K) experiment is a long-baseline neutrino oscillation experiment designed to study neutrino oscillation parameters. The experiment is located in Japan and has been taking data since 2010. A schematic layout of the T2K experiment is shown in figure 3.1. T2K utilizes the muon neutrino beam and the muon antineutrino beam from the Japan Proton Accelerator Research Complex (J-PARC). The beam's initial state properties are measured at the near detector complex, located 280 m downstream from the neutrino production location. At 295 km away, the far detector Super-Kamiokande (SK) can count the number of unoscillated muon neutrinos, and the number of electron neutrinos oscillated from muon neutrinos during their flight across Japan. The distance 295 km is chosen to maximize the electron neutrino appearance probability described in section 1.3 (equation 1.22) and illustrated in figure 1.4.

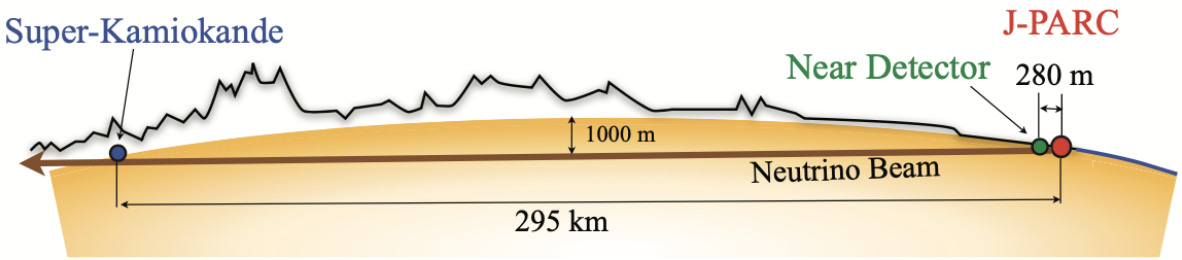

Figure 3.1. A schematic layout of the Tokai-to-Kamioka (T2K) experiment. The diagram shows a neutrino travelling from the neutrino beamline (red dot) at the Japan Proton Accelerator Research Complex (J-PARC), through the near detector complex (green dot) where the properties before neutrino oscillation are sampled, to the 1000-meters-underground far detector Super-Kamiokande (blue dot) located 295 km to the west. The figure is taken from [10].

This chapter describes the various components of T2K. Firstly, the J-PARC and neutrino beamline are described in section 3.1. Specifically, the production of the neutrinos, the simulation of the neutrino flux, and the reason why T2K adopts an off-axis beam strategy are explained. Next, the sub-detectors of the near detector complex are described in section 3.2; this section covers how the unoscillated neutrino beam is being monitored and the rich neutrino interaction program at T2K. Lastly, the far detector Super-Kamiokande, especially how it detects neutrinos, is described in section 3.3.

3.1 The Neutrino Beam

3.1.1 J-PARC

The Japan Proton Accelerator Research Complex (J-PARC) [37], located in Tokai, Japan, is a world-class proton accelerator research facility that produces the 30 GeV proton beam T2K uses for neutrino production.

The 30 GeV proton beam is achieved in three stages using three accelerators (illustrated in figure 3.2):

1. A beam of H^- ions is produced and accelerated to 400 MeV using the linear accelerator (LINAC).

2. The H^- ion beam converts into a H^+ ion (proton) beam when passing through a charge stripping foil, and then gets accelerated to 3 GeV with the rapid cycling synchrotron (RCS).

3. The proton beam energy achieves 30 GeV with the main ring (MR) synchrotron.

3.1.2 The T2K Neutrino Beamline

T2K utilizes the J-PARC 30 GeV proton beam to produce neutrinos. The proton beam is extracted from the MR to the T2K neutrino beamline. Figure 3.3 shows the overview of the neutrino beamline, divided into the primary and secondary beamlines.

The primary beamline transports the proton beam toward the near detector and the far detector with a series of focusing and bending magnets. The proton beam properties (intensity, direction, etc.) are measured with various beam monitors. These beam properties are essential for predicting the properties of the neutrino beam produced (more details described in section 3.1.4).

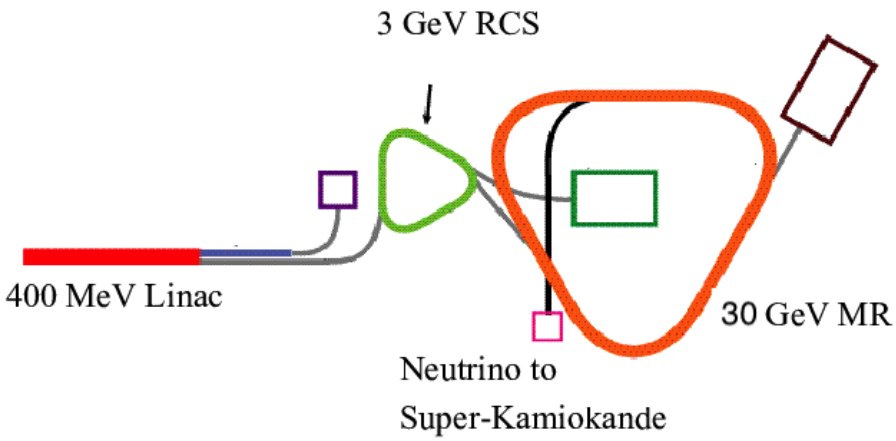

Figure 3.2. A schematic of J-PARC. The 400 MeV LINAC, 3 GeV RCS, 30 GeV MR, and the neutrino beamline are shown. The figure is taken from [37].

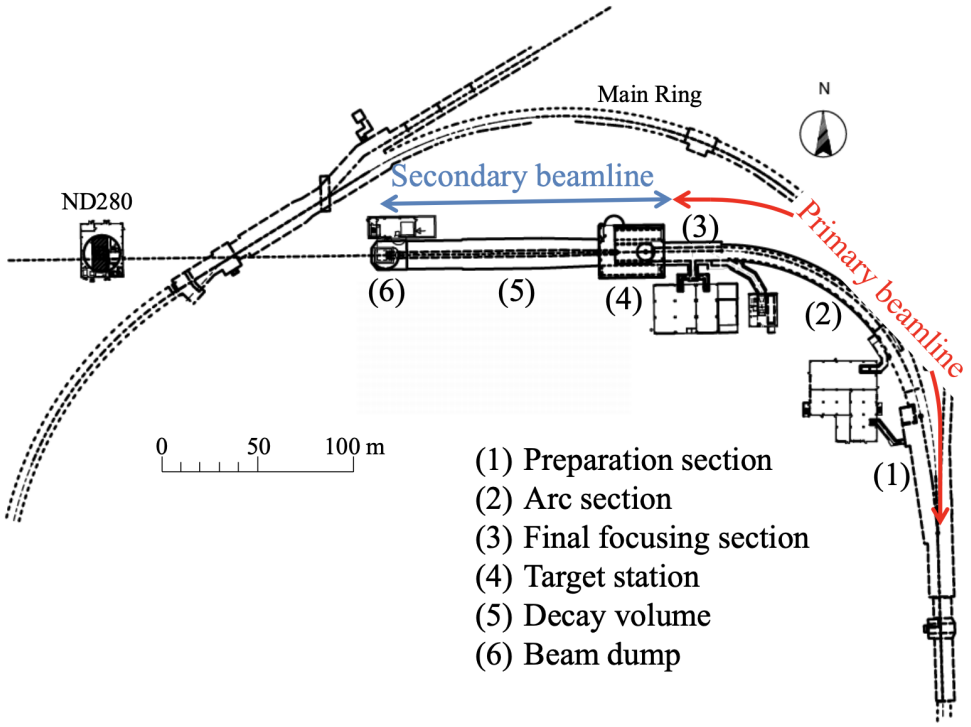

Figure 3.3. The T2K neutrino beamline. The primary beamline consists of a series of focusing and bending magnets to transport the proton beam toward the near detector and the far detector. The secondary beamline is where the neutrino beam is produced. The figure is taken from [37].

The secondary beamline, illustrated in figure 3.4, is where the neutrino beam gets produced. The secondary beamline has three sections: the target station, the decay volume, and the beam dump. Inside the target station, the beamline equipment is enclosed inside a helium vessel filled with helium gas. The purpose of the helium gas environment is to reduce hazardous gas produced by the beam (tritium and NO_X) and to reduce multiple scattering of pions (produced from the interaction between the proton beam and the target).

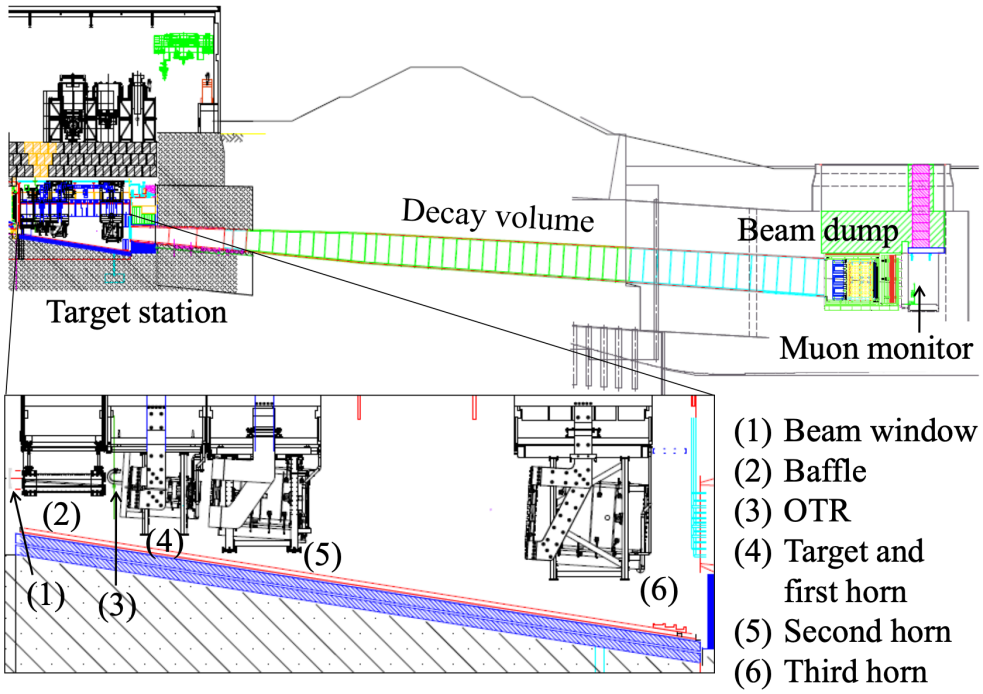

Figure 3.4. The secondary beamline, where the neutrinos are produced. The figure is taken from [37].

The proton beam enters the secondary beamline through a 0.3 mm thick titanium-alloy[1] beam window that separates the primary beamline (vacuum) and the helium-gas-filled secondary beamline. The proton beam then passes through the baffle, which is a 1.7 m long graphite block with a 30 mm hole in the middle. The baffle is a collimator for the proton beam and protects downstream equipment (such as the magnetic horns). The proton beam profile is measured one last time with an optical transition radiation monitor (OTR)[38] before it strikes a 91.4 cm long graphite rod target. The target length is 1.9 interaction lengths so that most protons will interact within the target. Mesons[2], mostly pions (π) and some kaons (K), are produced from the proton bombardment on graphite. These particles are then

[1] At the thickness of 0.3 mm, the beam loss due to the titanium-alloy can be neglected.

[2] Mesons are hadronic subatomic particles that consist of a quark and an antiquark. Pions (π) and kaons (K) are all mesons.

charge-selected and focused by a set of three magnetic horns. The polarity of the horn current can be switched to produce a predominantly neutrino or antineutrino beam. Internally for T2K, the term "forward horn current (FHC) mode" is used to refer to the neutrino beam mode, and "reverse horn current (RHC) mode" is used to refer to the antineutrino beam mode.

The focused mesons enter a 96 m decay volume (steel tunnel) and decay via the decay modes of the pions and the kaons shown in table 3.1 to produce neutrinos. At the end of the

	Decay Modes (dominant modes)	**Contamination Decay Modes** (dominant modes)
FHC	$\pi^+ \to \mu^+ + \nu_\mu$ $K^+ \to \mu^+ + \nu_\mu$	$\mu^+ \to e^+ + \nu_e + \bar{\nu}_\mu$ $K^+ \to \pi^0 + e^+ + \nu_e$
RHC	$\pi^- \to \mu^- + \bar{\nu}_\mu$ $K^- \to \mu^- + \bar{\nu}_\mu$	$\mu^- \to e^- + \bar{\nu}_e + \nu_\mu$ $K^- \to \pi^0 + e^- + \bar{\nu}_e$

TABLE 3.1. The dominant decay modes of the forward-horn-current (FHC, ν_μ) and reverse-horn-current (RHC, $\bar{\nu}_\mu$). The dominant decay modes for the contamination in the two beam modes are also listed.

decay volume, the remaining mesons and the muons (below the energy of 5 GeV) are stopped by the beam dump (75 tons of graphite). Then, a muon monitor (MUMON) studies the higher energy muons. Since most muons are produced from the two-body pion decay process (a pion decaying into a muon and a neutrino), the neutrino beam intensity and direction can be obtained by monitoring the muon profile.

3.1.3 Off-axis Neutrino Beam Strategy

T2K uses an off-axis neutrino beam strategy [39], which means the far detector Super-Kamiokande sits 2.5° off-axis from the center of the neutrino beam direction. This strategy has two advantages compared to using an on-axis (0°) neutrino beam.

First, the neutrino energy spectrum is narrower (closer to monoenergetic). The majority of the neutrinos (more than 80%) are produced by pion decays: $\pi^+ \to \mu^+ + \nu_\mu$ or $\pi^- \to \mu^- + \bar{\nu}_\mu$. The neutrino energy E_ν can be calculated for a given energy (E_π), momentum (p_π) and angle (θ_π, with respect to the neutrino direction) of the parent pion:

$$\mathrm{E}_\nu = \frac{m_\pi^2 - m_\mu^2}{2(\mathrm{E}_\nu - p_\pi cos(\theta_\pi))}, \tag{3.1}$$

where m_π and m_μ are the pion and muon masses. One property of this pion two-body decay process is that the neutrino energy becomes less dependent on the parent pion energy as the

scattering angle between the neutrino and pion increases, which is shown in figure 3.5. At 2.5° off-axis, the neutrino energy peak is around 0.6 GeV, where the baseline-to-energy (L/E in equation A.16) ratio also results in a maximum oscillation probability at the far detector Super-Kamiokande as shown in figure 3.6.

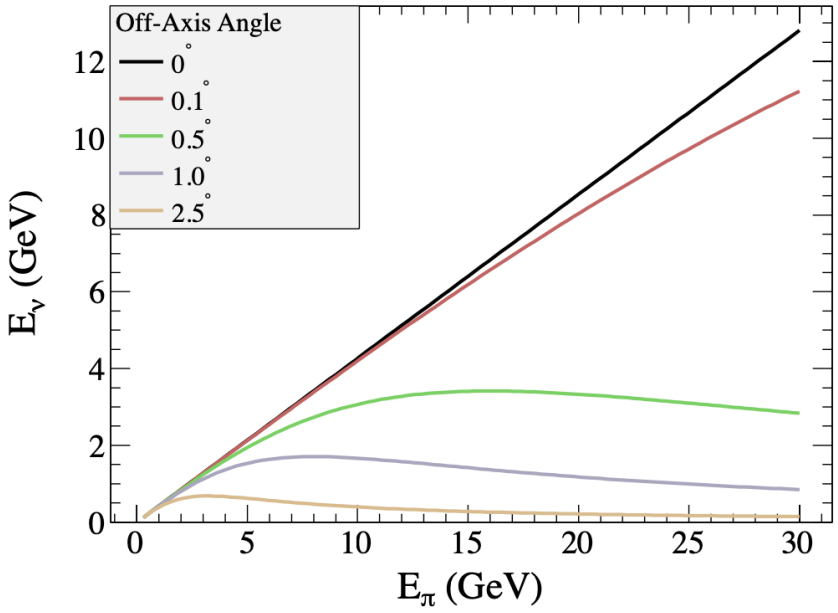

Figure 3.5. The neutrino energy as a function of the energy of the parent pion. The different curves correspond to various off-axis angles. As the off-axis angle increases, the neutrino energy becomes less dependent to the pion energy. The figure is taken from [40].

Secondly, the ν_e and $\bar{\nu}_e$ contamination[3] is reduced in the narrow energy range of the neutrino flux peak. Kaons produce these contaminations in a three-body decay process (shown in table 3.1), which are less affected by the off-axis strategy than the two-body pion decay.

3.1.4 Neutrino Flux Prediction

A neutrino experiment needs to accurately predict its neutrino beam flux to perform precise neutrino oscillation and cross-section analyses. The T2K neutrino flux prediction [41] is obtained from the Monte Carlo (MC) simulation of the neutrino production process in the neutrino (secondary) beamline (figure 3.4). The T2K beamline simulation uses FLUKA [42][43] to simulate the interaction between the 30 GeV proton beam with the T2K graphite target. The interactions outside the target region are simulated with GCALOR/GEANT3 [44].

[3] A reminder that T2K looks for oscillated ν_e and $\bar{\nu}_e$ at Super-Kamiokande. Therefore, in the ideal case, the initial neutrino at J-PARC should be purely ν_μ and $\bar{\nu}_\mu$.

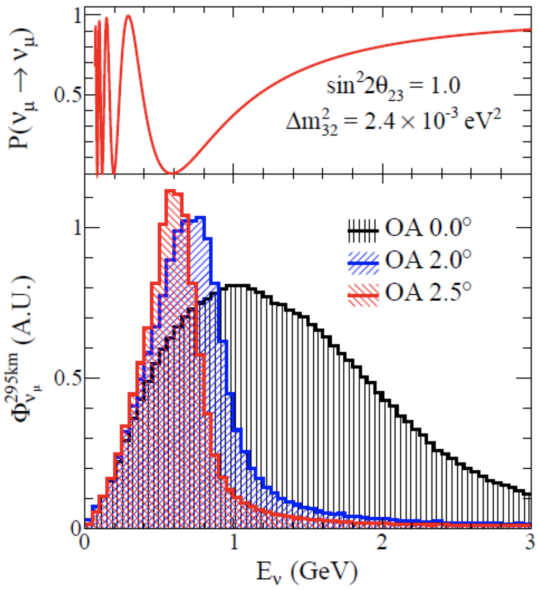

Figure 3.6. The neutrino energy spectrums for different off-axis angles. The distribution becomes narrower for larger off-axis angles. The T2K neutrino beam is 2.5° off-axis, with a peak energy of 0.6 GeV which maximizes the ν_μ disappearance oscillation probability at the far detector Super-Kamiokande. The figure is taken from [10].

External experimental data are used to improve the simulation. For example, the HARP experiment results [45] are used to constrain the pion re-interaction inside the target. The NA61/SHINE experiment [46] is a dedicated hadron production experiment that uses a 30 GeV CERN SPS proton beam and a replica T2K target[4] to study hadron productions. The NA61 results are fed into the flux prediction to reduce systematic uncertainties.

Figure 3.7 shows the flux prediction (for both the neutrino and antineutrino mode) at the near detector ND280 and the far detector Super-Kamiokande. The uncertainties of the flux prediction are described in section 7.1.

[4]Previous NA61 experiment setup also used a thin graphite target (2cm) to study hadron production. The current T2K flux prediction uses the NA61 data using a T2K replica target. The NA61 thin target data is still used for interactions not covered by the replica target data phase space and for the interactions outside of the target.

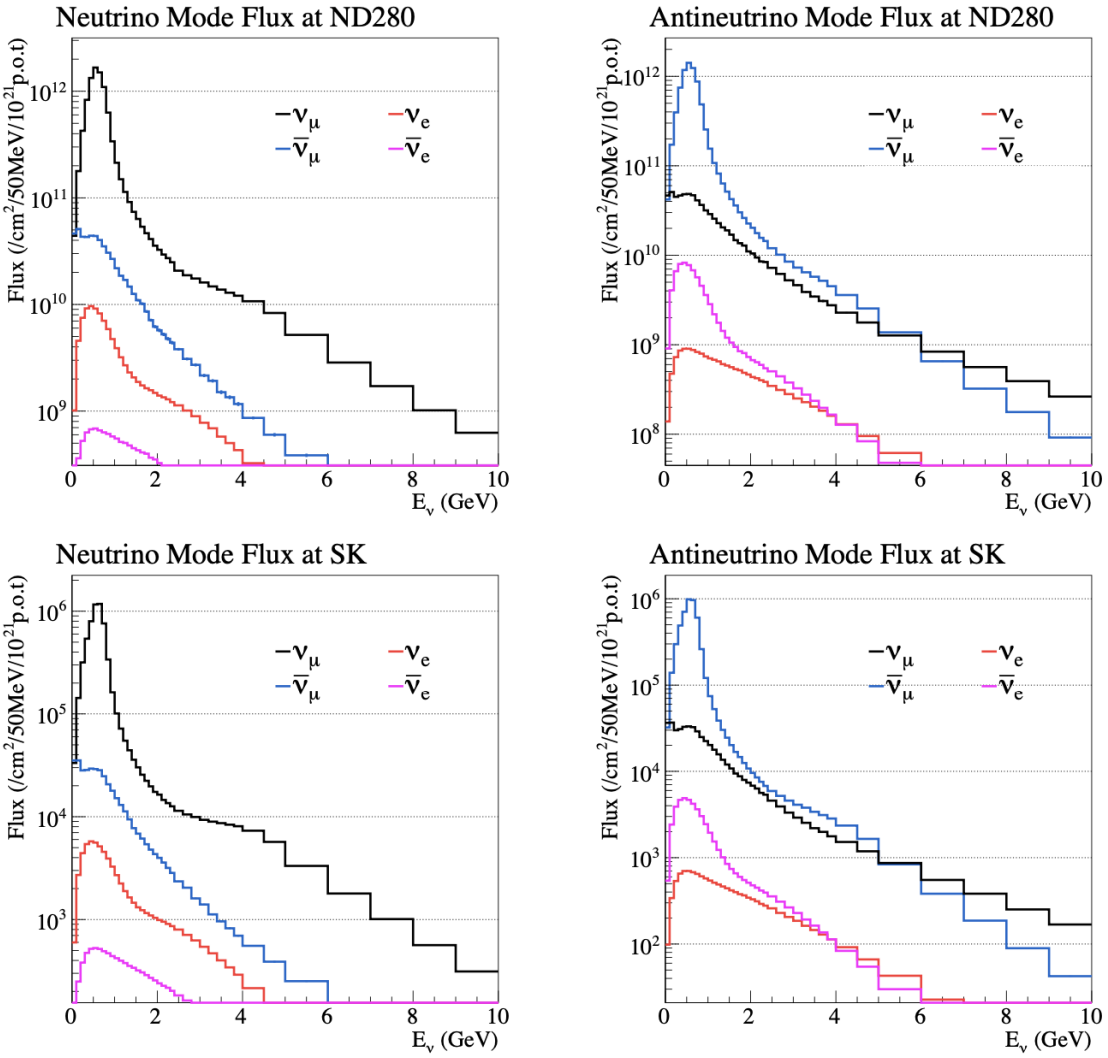

Figure 3.7. The neutrino flux (left) and antineutrino flux (right) at ND280 (top) and Super-Kamiokande (bottom) broken down into ν_μ, $\bar{\nu}_\mu$, ν_e, and $\bar{\nu}_e$ and plot as functions of neutrino energy. ν_μ dominants the neutrino mode flux and $\bar{\nu}_\mu$ dominants the antineutrino mode flux. The abbreviation P.O.T stands for "Protons-on-Target". The plots are taken from TN-217 [47].

3.2 The Near Detector Complex

The T2K near detector complex[5], shown in figure 3.8, consists of the on-axis detector - the Interactive Neutrino Grid (INGRID), and the off-axis detector - the near-detector-at-280 m (ND280). The near detector complex serves two primary purposes: to measure the unoscillated neutrino beam properties and to study neutrino interactions.

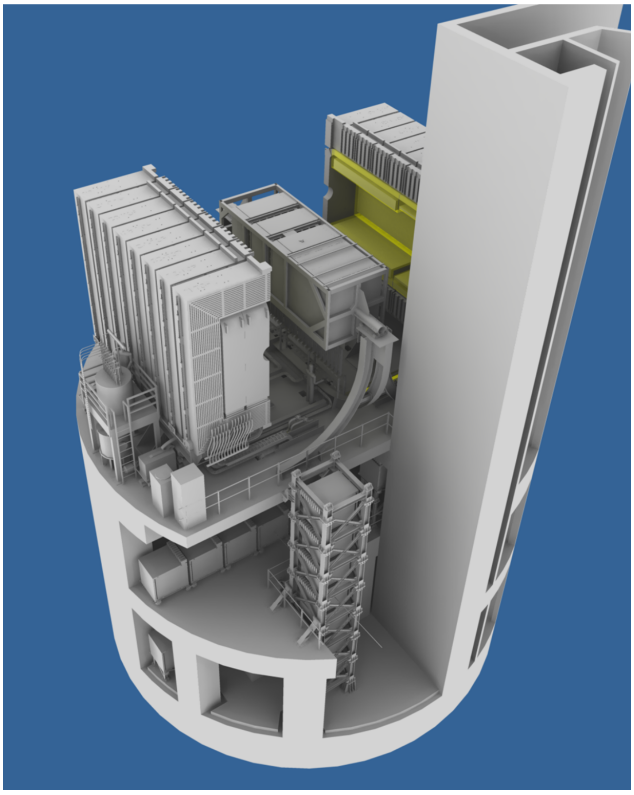

Figure 3.8. The near detector complex: the upper part is the off-axis detector (ND280), and the lower part is the on-axis detector (INGRID). The figure is taken from [10].

3.2.1 On-axis Detector (INGRID)

The Interactive Neutrino GRID (INGRID) detector [48] is the on-axis near detector for T2K. The primary purpose of the detector is to monitor the neutrino beam direction and intensity[6]. Figure 3.9 shows the layout of the sixteen (identical) modules of INGRID: seven modules arranged in the horizontal axis and seven modules arranged in the vertical axis to form a cross pattern, and two additional modules away from the cross (for beam asymmetry

[5] In some contexts, the near detector complex is also referred to as ND280. In the context of this thesis, ND280 refers to the off-axis detector alone.

[6] The INGRID detector can also be used to perform neutrino cross-section measurements.

monitoring). The modules cover an area of 10 m × 10 m since the neutrino beam spatial width (1σ) at INGRID is 5 m. Each INGRID module consists of alternating iron (the target mass for neutrino interactions) and scintillator (particle tracking) layers.

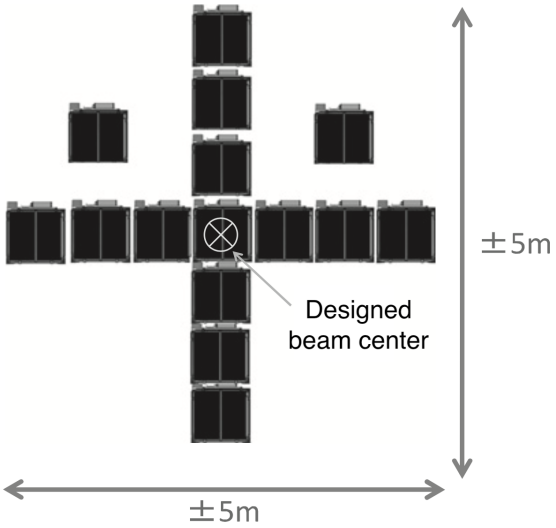

Figure 3.9. A horizontal view of the 16 modules of the on-axis Interactive Neutrino GRID (INGRID) detector at the near detector complex. The center of the horizontal and vertical rows aligns with the neutrino beam's center. Two off-axis modules are deployed to monitor the asymmetry of the neutrino beam. The figure is taken from [48].

3.2.2 Off-axis Detector (ND280)

The Near-Detector-at-280 m (ND280) is the off-axis near detector for T2K. The characteristics of the unoscillated neutrino flux are measured in the direction of the SK far detector. Another purpose of ND280 is to study neutrino interactions by performing various cross-section measurements, including the one described in this thesis. Figure 3.10 shows the sub-detector components of ND280.

Pi-Zero Detector (P0D)

The pi-zero detector (P0D) is the most upstream sub-detector of ND280. The primary goal of the detector is to study neutrino interactions that generate π^0. As explained in sec 2.2, one of the dominant sources of background for the ν_e-appearance analysis is the π^0 produced from the NC-π^0 process ($\nu_\mu + N \to \nu_\mu + N + \pi^0 + X$)[7]. The P0D can measure the process on a water target with the same neutrino beam that reaches the far detector SK. Figure 3.11

[7] If the target is not a nucleon but an entire nucleus, the process is NC-COH.

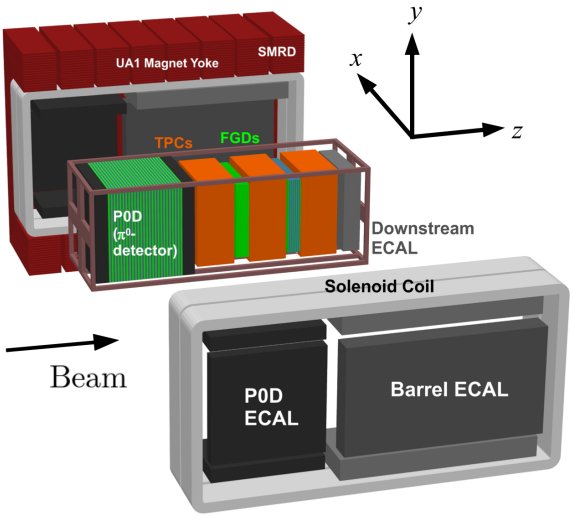

Figure 3.10. An exploded view of the off-axis near-detector-at-280 m (ND280) with all the sub-detector components. The figure is taken from [10].

shows the design of P0D. The "water target" region consists of alternating scintillator, water, and brass layers. The water layers (water bags) can be emptied and filled with air. The NC-π^0 cross section on the water target is obtained by taking the difference between the "water" and "air" P0D configuration.

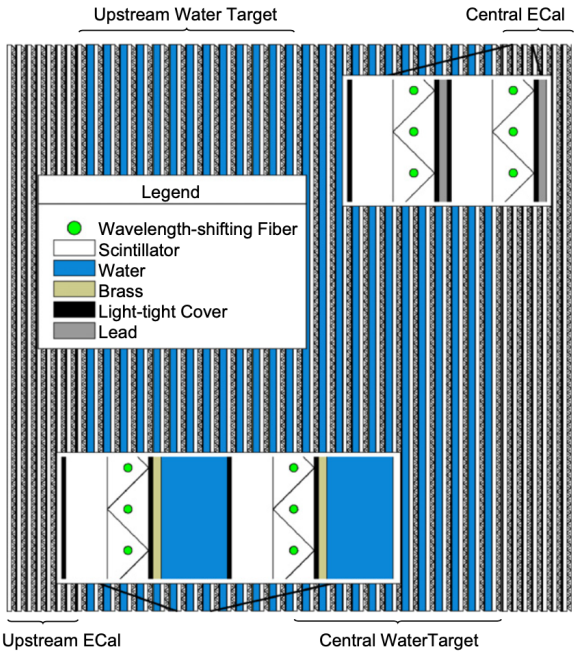

Figure 3.11. The pi-zero detector (P0D). The water layers can also be filled with air. The electromagnetic calorimeters (ECAL) are described later. The figure is taken from [49].

Fine Grained Detectors (FGD)

The two fine-grained detectors (FGDs) [50] serve as active[8] targets of ND280. The first FGD (FGD1) consists solely of scintillator bars, and the second FGD (FGD2) consists of scintillator and water layers. The geometry, mounting, and readout are the same for the two FGDs. This configuration allows separate cross-section measurements on carbon and water targets.

Both FGDs have the same outer dimensions: 2300 mm (width) × 2400 mm (height) × 365 mm (depth). Figure 3.12 shows a cross-sectional view of the FGD. The FGD scintillator modules (XY module) consist of plastic scintillator bars oriented on the x and y-axis. The scintillator bars are 9.61 mm thick, and 196 bars are glued together to form one layer. One X layer and one Y layer (based on the bars' orientations) make up one XY module. FGD1 contains fifteen XY modules. More details regarding the geometry and construct of FGD1 and the calculation for the total number of nuclei can be found in appendix D. FGD2 contains seven XY modules alternating with six water layers (each with 25 mm thickness of water).

When neutrinos interact inside the FGD, the charged particles pass through the scintillator bars, emitting scintillation light. The X-Y layout of the scintillator bars allows three-dimensional tracking of the particles. Each scintillator bar has a thin (1 mm diameter) wavelength shifting fibre (WLS) in the center. The WLS is attached to a multi-pixel photon counter (MPPC) at one end for scintillation signal readout. The other end of the scintillator bar and the bar's surface are coated (mirrored aluminum for the former and reflective TiO_2 coating for the latter) to promote light capture. The intensity of the light signal is proportional to the energy deposited by the charged particles. More details regarding the usage of energy deposition around the neutrino interaction vertex are described in section 4.4.1.

Time Projection Chambers (TPC)

Three time projection chambers (TPCs) [51] are placed downstream of the three "target mass" sub-detectors (P0D and the FGDs) to study the particles that emerged. When passing through the gas volume of a TPC, a charged particle ionizes the gas atoms along its trajectory. The TPCs have three purposes. First, since they are enclosed in a magnetic field, the charged particles' momenta can be determined from the curvature of the trajectories. Secondly, the TPCs can reconstruct the charged particle trajectories in all three dimensions. Lastly, the types of the charged particles can be distinguished using the momentum measurements and the amount of ionization left by each particle.

[8] An "active" target provides particle tracking as opposed to a "passive" target (i.e., a block of iron) that does not have any tracking ability.

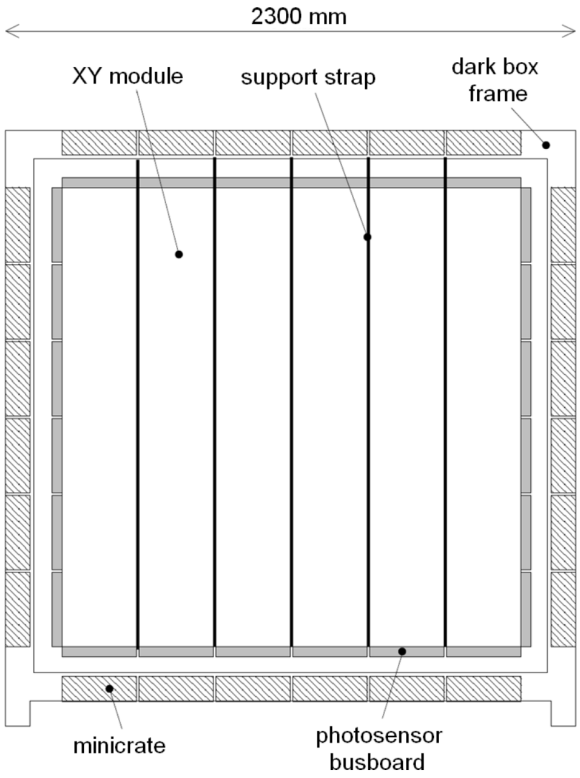

Figure 3.12. A cross-section view of a fine-grained detectors (FGD). All the detector components, the scintillator modules, electronics, and support structures, are enclosed inside a dark box. The figure is taken from [50].

The three TPCs are identical (shown in figure 3.13). Each TPC contains an inner box filled with argon-based drift gas[9] and an outer box filled with CO_2 for electrical insulation. In order to produce a uniform electric drift field for the TPC drift volume, the inner box panels are machined into 11.5 mm pitch copper strip pattern. Twelve bulk micro-mesh gas (Micromegas) detectors are placed at each side of a TPC. They amplify and sample the signals of the charged particles that pass through the TPC: the ionization electrons produced in the gas that drift away from the cathode toward the readout planes.

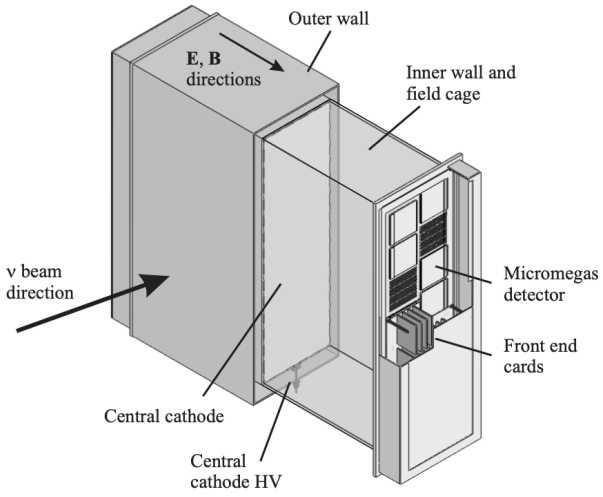

Figure 3.13. A simplified view of a time projection chamber (TPC). The figure is taken from [51].

The momentum resolution goal of the TPCs is $\delta p_\perp / p_\perp < 0.1$, where $\delta p_\perp$ is the momentum perpendicular to magnetic field. The position resolution is 0.7 mm. Figure 3.14 shows the energy loss as a function of the momentum of the particles. The resolution of the deposited energy for a minimum ionizing particle is 7.8%. For the muons and electrons with energy less than 1 GeV, the probability of misidentifying the two is only 0.2%.

Electromagnetic Calorimeters (ECAL)

The inner sub-detectors (P0D, TPCs, and FGDs) are surrounded by electromagnetic calorimeters (ECal) [52]. There are thirteen independent modules of three types (shown in figure 3.10): six P0D-ECal modules (surround the P0D), six Barrel-ECal modules (surround the TPCs and FGDs), and one downstream ECal module. The role of the P0D-ECal is to distinguish the photons and muons that originate from the P0D. The Barrel-ECal and the downstream

[9] The gas mixture used is Ar:CF_4:iC_4H_{10} (95:3:2). It is chosen for the high drift speed and low diffusion properties.

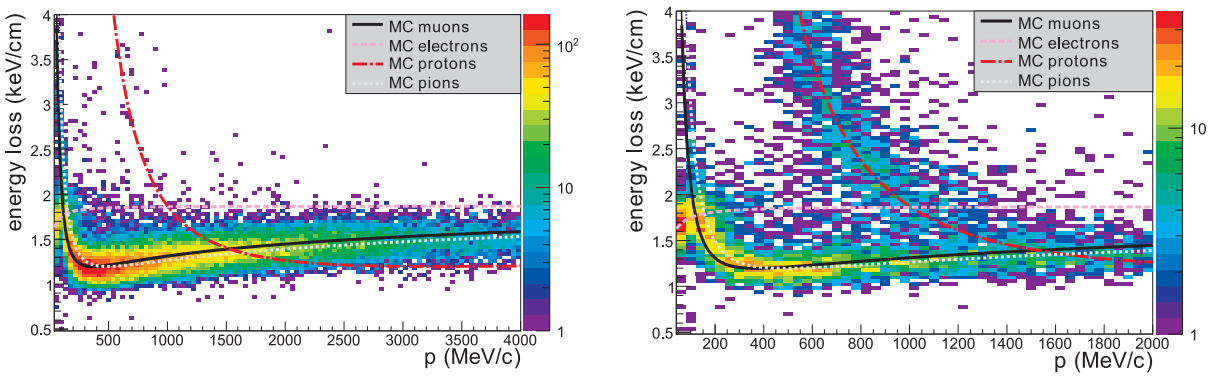

(a) Negative particles.

(b) Positive particles.

Figure 3.14. The energy loss per centimetre as a function of momentum for the negatively charged particles (left) and the positively charged particles (right). The theoretical curves generated with Monte-Carlo (MC) simulation for some particles are plotted for comparison. The figure is taken from [51].

ECal reconstruct the electromagnetic showers to complement the tracking abilities of the TPCs and FGDs. In addition, the downstream ECal also provides a veto to cosmic rays.

Magnet

All the sub-detectors described above are enclosed inside the UA1 magnet (recycled from the UA1 experiment at CERN), shown in figure 3.10. The 0.2 T magnetic field enables ND280 to determine the charge and the momentum of the particles produced from neutrino interactions

Side Muon Range Detectors (SMRD)

The Side Muon Range Detector (SMRD) [53] is the outermost component of ND280. As shown in figure 3.10, the SMRD is integrated with the UA1 magnet: plastic scintillation counter layers are placed in the air gaps in between the UA1 magnet yokes iron plates. The primary goal of the SMRD is to provide muon momenta measurements for the large angle muons that escape the inner detectors. The background interactions (outside of the ND280 detector) and the cosmic rays can also be vetoed with the help of the SMRD.

Example of Event Display at ND280

Figure 3.15 shows an example of reconstructed event display with all the ND280 subdetectors described in this section labelled. In this event, a muon entered the P0D, went through the tracker region (3 TPCs and 2 FGDs), interacted inside TPC3, and produced secondary

particles. The curvature of the trajectories of the secondary particles inside TPC3 can also be seen. The secondary particles stopped in the downstream ECAL.

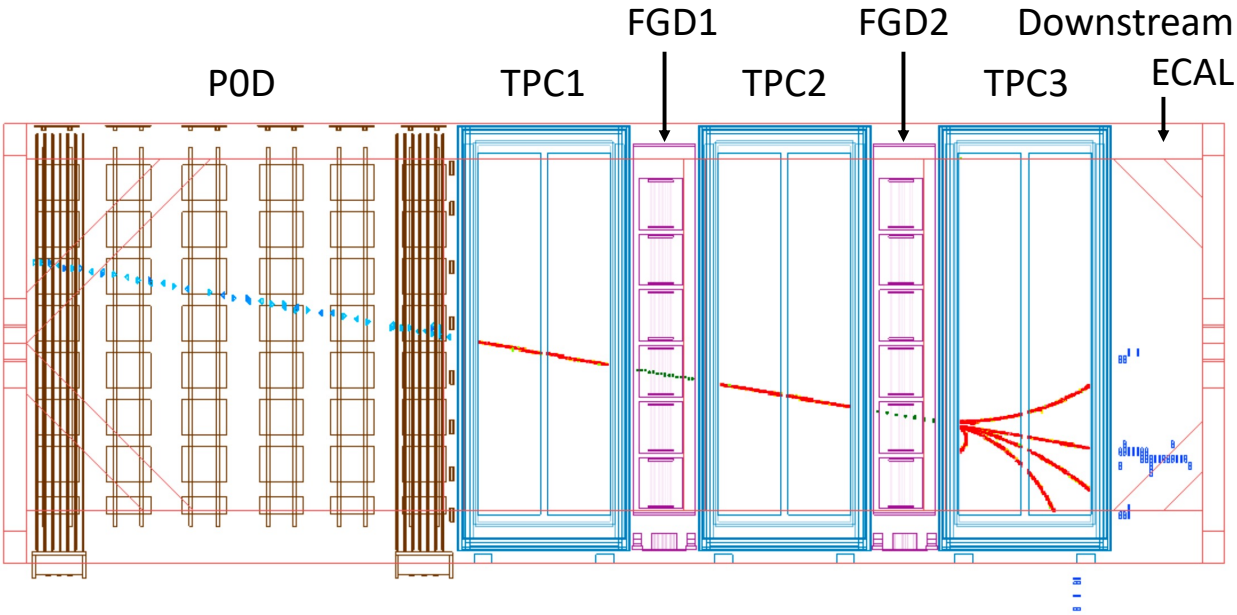

Figure 3.15. A data event display in ND280. A muon entered the P0D, went through the tracker region (3 TPCs and 2 FGDs), interacted inside TPC3, and produced secondary particles. The curvature of the trajectories of the secondary particles inside TPC3 can also be seen. The secondary particles stopped in the downstream ECAL. The figure is taken from [10].

3.3 The Far Detector

T2K uses the Super Kamiokande (SK) detector, located 295 km west of J-PARC, as the far detector to measure the flavour composition of the T2K neutrino beam after the travel. Super-Kamiokande counts the electrons and muons produced by CCQE interactions (section 1.4, figure 1.7b). The Super-Kamiokande detector has been operating since 1996. It is currently in its fourth data-taking period SK-IV (upgraded electronics compared to previous SK-I, SK-II and SK-III). The detector behaviour of Super-Kamiokande is relatively well-understood thanks to the long history of operation. The calibration of the energy scale and the software for modelling events are all known to the percent level.

Figure 3.16 shows a diagram of the detector, which sits 1000 m deep underground in the Kamioka mine. The overburdened rock provides shielding from the cosmic rays. The

Super-Kamiokande detector consists of the inner detector (ID) and the outer detector (OD). The geometry of the ID is a 33.8 m-diameter and 36.2 m-tall cylinder. A total of 11,129 (inward-facing) 50 cm photomultiplier tubes (PMTs) are installed along the inner walls of the ID. Separated with a cylindrical stainless-steel scaffold is the OD (2 m) in thickness), which completely encloses the ID. Along the inner wall of the OD, 1,885 outward-facing 20 cm PMTs are installed. The OD is sparsely instrumented compared to the ID since the purpose of the OD is to provide background veto to mostly cosmic rays. The combined Super-Kamiokande detector dimension is 39 m in diameter and 42 m in height.

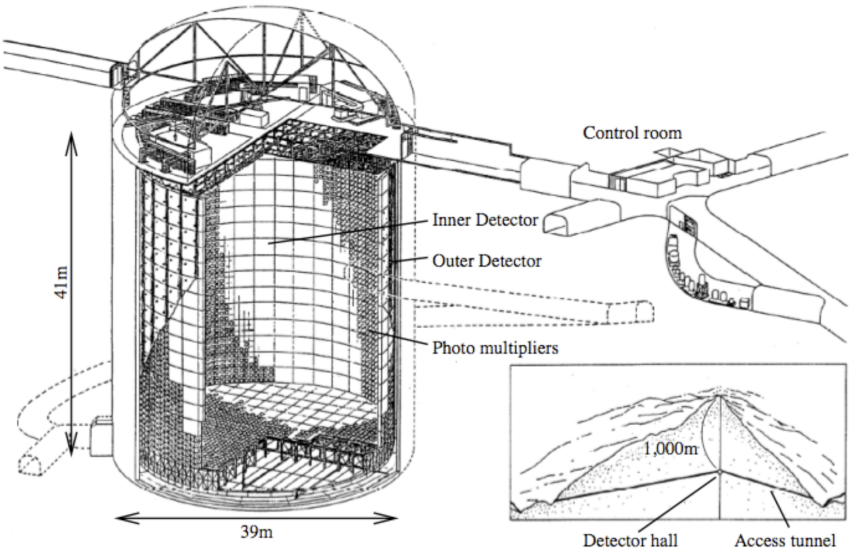

Figure 3.16. The Super Kamiokande (SK) detector. This water Cherenkov detector is placed in the Kamioka mine, 1000 m underground. The detector consists of the inner and outer detector, which are separated by a cylindrical scaffold (for photomultiplier tubes PMT mounting). The figure is taken from [10].

Cherenkov radiation is produced by a charged particle (such as an electron or a muon) that passes through a transparent medium such as water with speed greater than the speed of light for that particular medium[10]. The energy threshold to produce Cherenkov radiation is 0.8 MeV for electrons and 160 MeV for muons. Super-Kamiokande uses Cherenkov radiation for neutrino detection. When a neutrino interacts with a nucleon (or a nucleus) of the water molecule through the charged-current channels, charged leptons are produced[11].

The ID is filled with ultra-pure water for neutrinos to interact. The PMTs detect the Cherenkov radiation, which forms ring-shaped patterns. The shapes of the rings are used to extract the neutrino interaction vertex, momentum, and particle identification. Figure 3.17

[10] The speed of light in water is $2.25 \times 10^8\,\mathrm{m\,s^{-1}}$.

[11] For a neutral-current interaction, the outgoing neutrino cannot be detected.

shows examples of the reconstructed event displays: an electron-like event and a muon-like event. The rings from electrons tend to be "fuzzier" than the muon rings because the electrons scatter and produce electron showers.

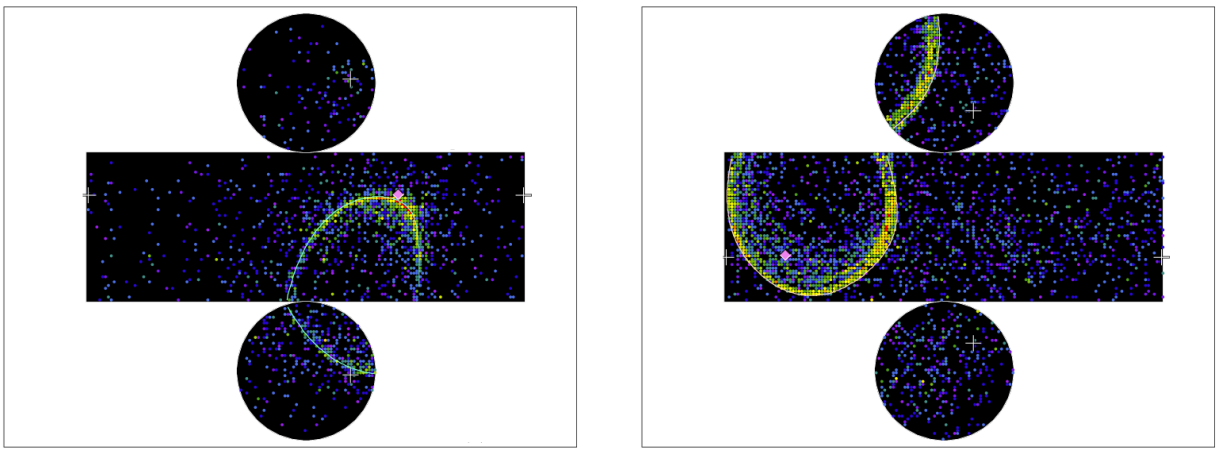

(a) an electron-like event (b) a muon-like event

Figure 3.17. Data event displays of T2K events at Super-Kamiokande. The electron-like event (left) results in a fuzzier Cherenkov ring than the muon-like event (right). The rings from electrons tend to be "fuzzier" than the muon rings because the electrons scatter and produce electron showers. Each coloured point represents a PMT signal where the colour corresponds to the charge. The figures are taken from [54].

NC-COH ($\nu_\mu + \mathrm{A} \to \nu_\mu + \pi^0 + \mathrm{A}$ or $\bar{\nu_\mu} + \mathrm{A} \to \bar{\nu_\mu} + \pi^0 + \mathrm{A}$) is a background to the Super-Kamiokande electron neutrino measurement. The π^0 produced by NC-COH decays almost instantly[12] into two photons. Sometimes, the photons can mimic the signals of electron neutrino detections at Super-Kamiokande. About three percent[13] of the neutrino interactions detected by Super-Kamiokande are NC-COH. Although NC-COH is a rare interaction mode, the thirty-percent-event-rate-uncertainty results in roughly one percent ($3\% \times 30\% \sim 1\%$) uncertainty in the number of neutrinos detected by Super-Kamiokande. This is another reason to perform CC-COH cross-section measurements, so both the CC-COH and the NC-COH modelling uncertainties can be better constrained.

[12] The mean lifetime of π^0 is 8.5×10^{-17} s.

[13] This percentage is calculated from the Super-Kamiokande NCQE cross-section result [55] and the theoretical COH cross section.

Chapter 4

Analysis Strategy

This chapter describes the strategy for the measurements of the ν_μ and $\bar{\nu}_\mu$ charged-current coherent pion production (CC-COH, as shown in process 4.1) cross-section on carbon using the T2K off-axis near detector ND280.

$$\begin{aligned} \nu_\mu + {}^{12}\mathrm{C} &\rightarrow \mu^- + \pi^+ + {}^{12}\mathrm{C} \\ \bar{\nu_\mu} + {}^{12}\mathrm{C} &\rightarrow \mu^+ + \pi^- + {}^{12}\mathrm{C} \end{aligned} \tag{4.1}$$

Some basic information regarding the measurements is discussed in section 4.1. The methodology for the analysis, including the phase space studies, variables used for the analysis, and the cross-section extraction procedures, are also presented in the later sections.

4.1 Measurements Overview

Table 4.1 shows the measurements that are performed and described in this thesis. The neutrino event generator used for the Monte Carlo simulation is NEUT5.4.0.1 [56]. The detector efficiency for the CC-COH process is model-dependent. The default model for the COH interactions is the 2009 Berger-Sehgal model (section 2.3.3).

Due to statistical limitations, the CC-COH measurements are flux-integrated in a single bin in neutrino energy. However, differential cross-section measurements could be possible in the future with more data collected by T2K-II [57].

The ν_μ and $\bar{\nu_\mu}$ induced CC-COH cross-sections are measured by two separate analyses. The target volume used for the analyses is the FGD1 detector (carbon targets). The result from each analysis is presented in two formats.

Firstly, the CC-COH cross-section on the entire FGD1 target nuclei composition (shown

Generator	Signal Model	Detector	Analysis	Signal	Target	Meas.
NEUT 5.4.0.1	Berger-Sehgal (2009)	FGD1	1	ν_μ CC-COH	FGD1	1
					^{12}C	2
			2	$\bar{\nu_\mu}$ CC-COH	FGD1	3
					^{12}C	4

TABLE 4.1. A list of the measurements that are described in this thesis. The ν_μ and $\bar{\nu_\mu}$ induced CC-COH cross sections are measured by two separate analyses. The FGD1 detector mainly consists of C, but also consists of trace amounts of O, H, Ti, Si, and N. Cross section measurements is measured with the FGD1 target composition shown in table 4.2. The cross-section measurements on ^{12}C are calculated using the FGD1 nuclei fractional composition information.

in table 4.2) is calculated. This CH target detector also contains trace amounts of O, Ti, Si, and N. It should be pointed out that CC-COH on H (also referred to as diffraction) is not within the signal definition. This process is treated separately in the Monte Carlo simulation. These events produce an extra proton (3 outgoing particles) and are not selected for the enriched CC-COH samples (2 outgoing particles, which are the muon and pion).

Secondly, using the FGD1 composition and a function that scales the cross-section to different target nuclei (A-scaling, where A is the atomic mass number), the CC-COH cross-section on ^{12}C can be obtained. Details regarding the cross-section extraction method (especially the A-scaling functions) are described in 4.6 and the calculation of FGD1 number of targets is described in appendix D.

The reason to present the results in such a way is to make the first format independent from the A-scaling (how the CC-COH cross-section scales from various target nuclei) modelling. Furthermore, having the additional cross-section on the entire FGD1 composition of nuclei would give theorists the freedom to use any A-scaling functions from different theoretical models and obtain CC-COH cross-section on^{12}C.

4.2 Analysis Strategy Overview

The analysis procedures for the two measurements are similar; they both can be summarized into the following few steps:

1. Select a sample containing a high purity of CC-COH events in the Monte Carlo simulation and the data. This sample is the signal region.

2. Identify the main background modes and select samples dominated by these background events. These samples are the background sidebands.

3. Use a likelihood fitter to determine the number of CC-COH events in data. The number of the signal and background events (for both the data and the Monte Carlo simulation) in both the signal region and the background sidebands are used.

4. Extract the CC-COH cross-section using the number of CC-COH events, the efficiency of selecting the CC-COH events, number of targets, and number of incident neutrinos.

5. Evaluate the statistical and systematic uncertainties using the data statistics and the sources of systematic uncertainties.

Some highlights are shown in the following sections.

4.3 Phase Space Study

Figure 4.1 and figure 4.2 show the ν_μ and $\bar{\nu_\mu}$ COH signal selections efficiencies ($N_{\text{signal}}^{\text{selected}}$ / $N_{\text{signal}}^{\text{simulation predicted}}$) in the Monte Carlo simulation as a function of true muon momentum (p_μ), true muon angle (θ_μ), true pion momentum (p_π) and true pion angle (θ_π) (from the Monte Carlo simulation). The momentums p_μ and p_π are in lab frame, and the angles θ_μ and θ_π are with respect to the neutrino direction. A reduced phase space is selected for the cross-section measurements to remove regions with poor detector efficiencies. In addition, to make future comparison of measurements between ν_μ and $\bar{\nu_\mu}$ measurements possible, the reduced phase space is decided based on the detector efficiencies from both selections. The reduced phase space, as shown in figure 4.1 and figure 4.2, is:

- $p_\mu > 0.2$ GeV/c and $\cos(\theta_\mu) > 0.8$.
- $p_\pi > 0.2$ GeV/c and $\cos(\theta_\pi) > 0.6$.

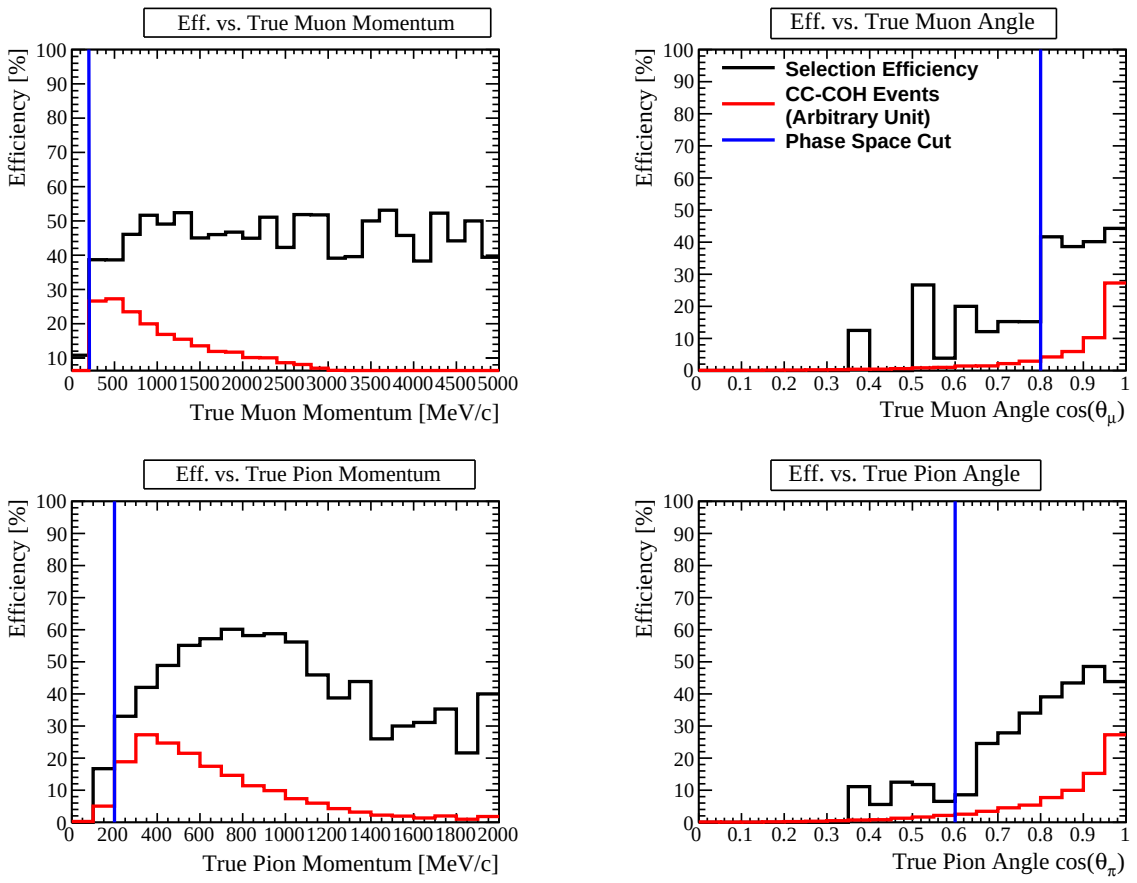

Figure 4.1. Detector efficiencies (black line) as functions of the muon (top) and pion (bottom) momentum (left) and angle (right) of the ν_μ CC-COH events before any CC-COH selection cuts. The reduced phase space is determined by removing regions with poor detector efficiency. Each plot includes the selected sample's distribution (red line) to demonstrate that the phase space cuts do not remove a significant number of selected events.

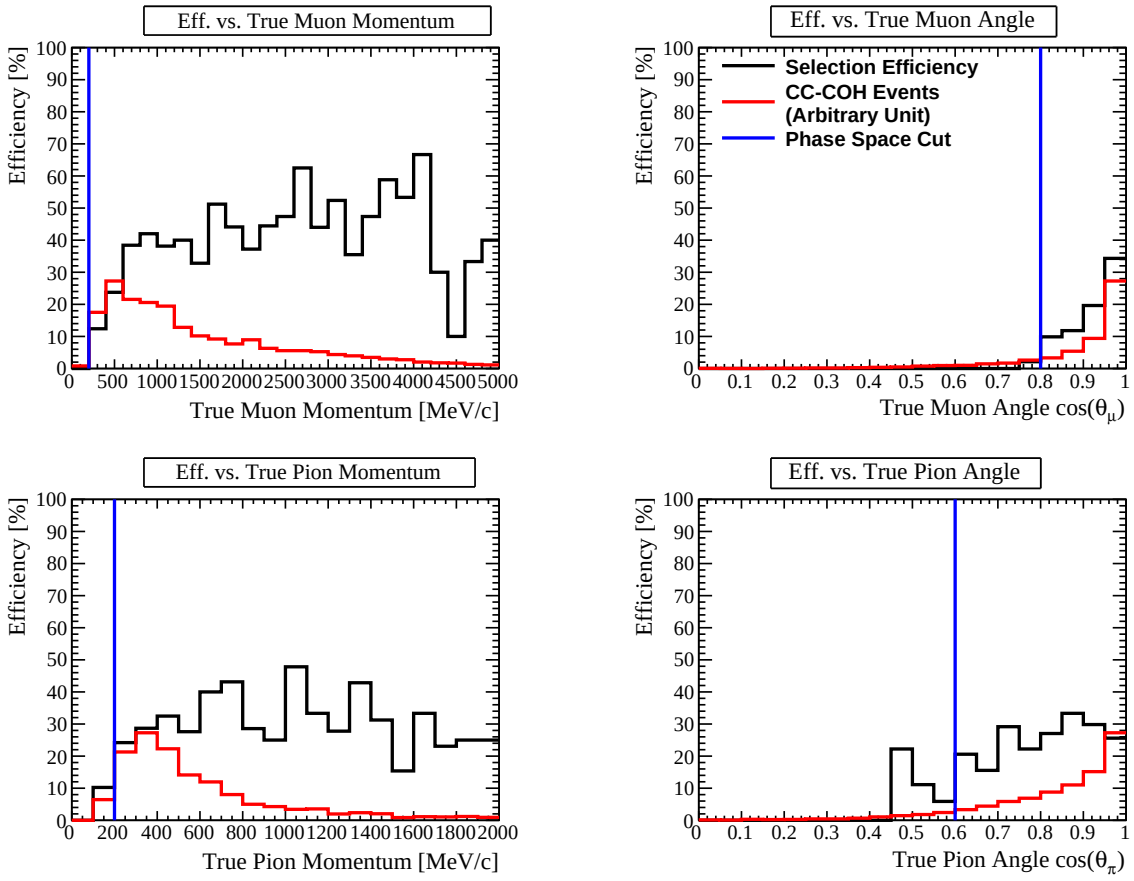

Figure 4.2. Detector efficiencies (black line) as functions of the muon (top) and pion (bottom) momentum (left) and angle (right) of the $\bar{\nu_\mu}$ CC-COH events before any CC-COH selection cuts. The reduced phase space is determined by removing regions with poor detector efficiency. Each plot includes the selected sample's distribution (red line) to demonstrate that the phase space cuts do not remove a significant number of selected events.

4.4 Analysis Variables of Importance

4.4.1 Vertex Activity

The FGD1 detector comprises plastic scintillator layers that are 1 cm in thickness [50]. The energy deposition around the neutrino interaction vertex, called vertex activity (VA), can be measured by summing up the photon signals with the Multi-Pixel Photon Counters (MPPC) attached to the two ends of each FGD1 scintillator bar. The measured energy deposition is measured in photon-equivalent units (PEU), which converts to MeV as 21.7 PEU = 1 MeV [58].

Due to the nature of the CC-COH interaction, described in chapter 2.1, the only outgoing particles from an interaction that would deposit energy are the lepton and pion. Thus, no nucleons are produced to deposit additional energy near the vertex. The VA for a CC-COH event is thus expected to be smaller than background events such as RES or DIS, in which more particles are produced and can deposit energy.

The analyses in this thesis use the vertex activity inside a 5×5 scintillator layer volume (approximately 5 cm^3), which contains five scintillator layers at each side. A 5×5 volume, compared to a 3×3 or a 7×7 volume, is an optimized size in selecting the CC-COH events and rejecting the background events. Figure 4.3 shows the FGD1 detector's layered structure and an example of a 5×5 scintillator layer volume.

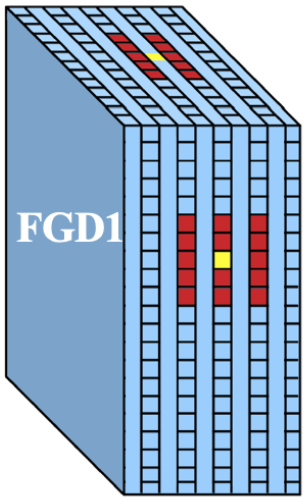

Figure 4.3. The FGD1 detector's layered plastic scintillator structure. The yellow box indicates an example of a neutrino interaction vertex. The red box indicates an example of a 5×5 scintillator layer volume for the VA calculation. The figure is taken from [59].

4.4.2 Momentum Transferred Squared

Another variable used for the analysis is the momentum transferred squared to the target nucleus ($|t|$), shown in figure 2.1. The full derivation of $|t|$ is shown in appendix E. $|t|$ can be calculated with solely detector reconstructable variables from muon and pion kinematics, as shown in equation 4.2.

$$|t| = (\sum_{i=\mu,\pi}(E_i - \left|\overrightarrow{P_i}\right| cos\theta_i))^2 + \left|\sum_{i=\mu,\pi}\left[\left|\overrightarrow{P_i}\right|(\widehat{e_i} - cos\theta_i\widehat{e_\nu})\right]\right|^2 \tag{4.2}$$

E_i is the energy, $\overrightarrow{P_i}$ is the momentum, the angle θ_i and direction $\widehat{e_i}$ are with respect to the incident neutrino direction $\widehat{e_\nu}$. Note to keep in mind that all the quantities used in the formula are in the detector coordinate system, which are with respect to the neutrino direction ($\overrightarrow{\nu} = (0, 0, z)$).

4.5 Likelihood Fitter

In this section, the method for obtaining the number of CC-COH events for the ν_μ and $\bar{\nu}_\mu$ CC-COH analysis is introduced. A flow chart for this method is shown in figure 4.4.

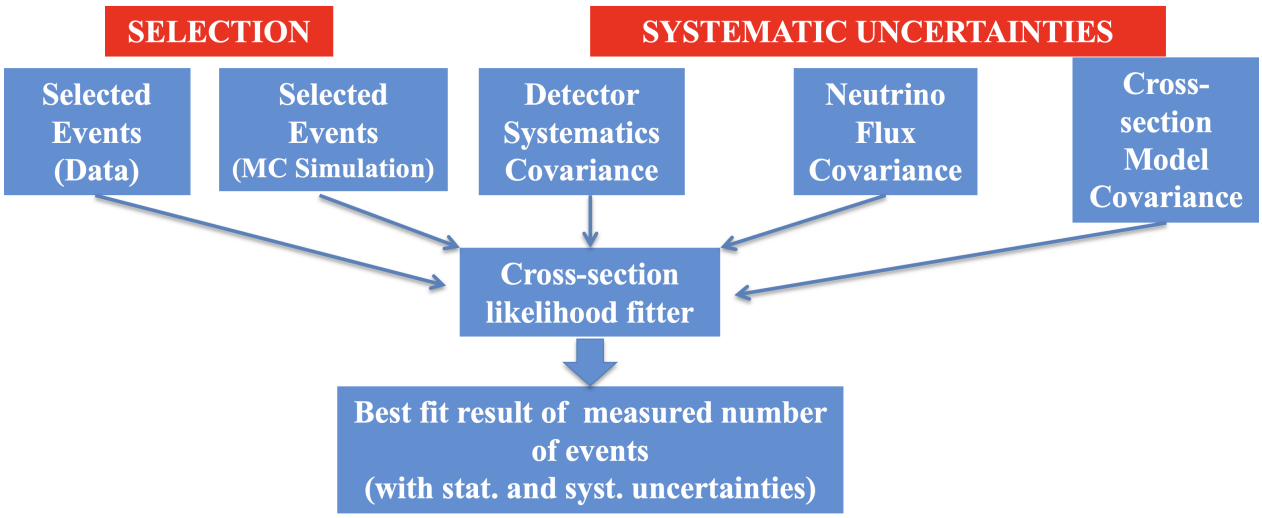

Figure 4.4. The basic logic flow of the binned likelihood fitter framework, with the inputs and output result. The fitter outputs the best fit number of events with combined statistical and systematic uncertainties.

Both analyses use a likelihood fitter to calculate the number of CC-COH events. The

fitter evaluates the χ^2 (of each fit iteration) given in equation 4.3 and tries to minimize it.

$$\chi^2 = \chi^2_{\text{stat.}} + \chi^2_{\text{syst.}} = -2\ln\mathfrak{L}_{\text{stat.}} - 2\ln\mathfrak{L}_{\text{syst.}} \tag{4.3}$$

In the limit of large statistics, a minimized χ^2 means that the likelihood ($\mathfrak{L}$), as well as the log-likelihood, are maximized (Wilk's Theorem [60]), hence the name "likelihood" fitter. Previous cross-section analyzers at T2K have developed the fitter framework, and details can be found in the T2K technical note TN-384 [61][1].

The inputs to the fitter are:

- The ν_μ and $\bar{\nu}_\mu$ CC-COH enriched sample selections are described in chapter 5 and 6.
- The sources of systematic uncertainties are described in chapter 7.

More details regarding the fitter framework, especially the validation works are described in chapter 8, 9, and 10.

The output of the fitter (presented in section 11.2) is the best fit of the number of CC-COH events, with combined statistical and systematic uncertainties[2]. The procedures to extract the cross-section measurements from the number of CC-COH events are shown in the following section.

4.6 Cross-section Extraction

Equation 4.4 describes how to extract the flux integrated single bin cross-section measurements (σ). N is the number of CC-COH events obtained by the likelihood fitter, ϵ is the detector efficiency to select the CC-COH events, T is the number of target nuclei, and Φ is the integrated flux (number of incident neutrinos).

$$\sigma^{\text{CC-COH}} = \frac{N^{\text{CC-COH}}}{\epsilon \cdot T \cdot \Phi} \tag{4.4}$$

As mentioned in section 4.1, the cross-section results are presented in two formats. For the measurements on the FGD1 target composition, equation 4.5 shows the calculation.

$$\sigma^{\text{CC-COH}}_{\text{FGD1}} = \frac{N^{\text{CC-COH}}_{\text{FGD1}}}{\epsilon \cdot T_{\text{FGD1}} \cdot \Phi} \tag{4.5}$$

[1] Additional details regarding earlier contributions to the fitter framework can also be found in the technical notes TN-214 [62], TN-287 [63], TN-337 [64], and TN-338 [65].

[2] Due to the construction of the fitter framework and the method of error propagation, the statistical and systematic components cannot be separated and are therefore reported together as one combined uncertainty.

The calculation for the number of target nuclei in FGD1, T_{FGD1}, is shown in appendix D.

The relationship between the cross-sections on FGD1 targets and ^{12}C can be written as:

$$\sigma_{\text{FGD1}}^{\text{CC-COH}} = \sum_i f_i F(A_i) \frac{\sigma_{^{12}\text{C}}^{\text{CC-COH}}}{F(A_{\text{i=C}})}, i = \text{C, O, Ti, Si, N.,} \tag{4.6}$$

where $F(A)$ is the scaling function of the cross section between different nuclei of atomic mass number A. Two scaling functions, $F(A) = A^{1/3}$ and $F(A) = A^2$ are used for the calculations and the results are discussed in section 11. The first scaling function comes from the RS (1983) paper [19]. The second scaling comes from the fact that the CC-COH cross section is coherent across all the nucleons within the target nucleus, so the cross section increases as the square of the atomic mass number [5]. f_i is the fractional composition of the nuclei in the FGD1 detector, shown in table 4.2.

Nuclei	C	O	Ti	Si	N
Atomic Mass Number (A)	12	16	48	28	14
Fractional Composition (f) (%)	95.83	3.09	0.46	0.48	0.14
Uncertainty of Fractional Composition (%)	0.5	1.3	16.6	19.7	39

TABLE 4.2. Fractional composition of the FGD1 detector excluding hydrogen. The calculations are shown in appendix D.

Chapter 5

The ν_μ CC-COH Selection

5.1 Data and Monte Carlo Simulation Samples

The T2K ND280 data and Monte Carlo (MC) simulation used for the ν_μ induced CC-COH measurements originating in FGD1 are listed in table 5.1; the total "Protons-on-Target" (POT) count for the data used is 1.15×10^{21}. The data and Monte Carlo simulation file processing software package (including detector reconstruction), ND280Software, has been developed by the T2K software group. For the Monte Carlo simulation, the total POT produced is 1.95×10^{22}, which is roughly 17 times the data POT. Unless stated otherwise, the Monte Carlo simulation is normalized to the data POT for all the plots shown in this chapter. The term "air" and "water" refer to the configuration of the P0D detector during that data-taking period; these different configurations do not directly impact this analysis. The production tag "prod6T" might be used to identify the data and the simulation to differentiate between past production versions when making comparisons.

5.2 The ν_μ CC-COH Selection within FGD1

5.2.1 Selection Overview

The High-Level-Analysis-at-the-Near-Detector (HighLAND) is the T2K near detector analysis framework developed to analyze the data and simulation files. It is being used to perform the selection of the event samples and to propagate detector systematic uncertainties. This chapter focuses on the selection part, and the details regarding the detector systematic uncertainties are discussed in 7.3.

Run	Data POT (10^{20})	MC POT (10^{21})	MC/DATA Ratio
Run 2 air	0.36	1.68	46.7
Run 2 water	0.43	1.20	27.9
Run 3	1.58	3.08	19.5
Run 4 air	1.78	3.61	20.3
Run 4 water	1.64	3.61	22.0
Run 8 air	1.58	3.61	22.8
Run 8 water	4.15	2.72	6.6
Total	11.52	19.51	16.9

TABLE 5.1. The T2K data and Monte Carlo (MC) simulation used for the ν_μ CC-COH measurements from different running periods. The "Protons-on-Target" (POT) for both data and simulation are shown with the MC/Data ratio. The total T2K ND280 neutrino (FHC) data used is 1.15×10^{21} POT. For the Monte Carlo, the total POT produced is 1.95×10^{22}, which is roughly 17 times the data POT.

The ν_μ CC-COH interaction produces a μ^- and a π^+ (as seen in figure 2.1):

$$\nu_\mu + {}^{12}\mathrm{C} \rightarrow \mu^- + \pi^+ + {}^{12}\mathrm{C}. \tag{5.1}$$

In this CC-COH process, the momentum transferred to the target nucleus is minimal, so the target nucleus does not fragment; therefore, no additional nucleons can deposit energy around the interaction vertex. The following steps summarize how to select a sample with ν_μ CC-COH events originating in the FGD1 detector:

- Select the events with a muon track[1] that starts in FGD1.
- Select the events with an additional pion track that starts in FGD1.
- Exclude events with more than two tracks.
- Select the events with low energy deposition around the interaction vertex.
- Select the events with low momentum transferred to the target nucleus.

Details regarding each step are described in the following subsection.

5.2.2 The ν_μ CC-inclusive and CC-1π Samples

The NuMu analysis group at T2K has already developed an inclusive ν_μ charged-current interaction ($\nu_\mu + \mathrm{X} \rightarrow \mu^- + X'$, where X denotes any nucleon or nucleus targets, and X'

[1] A track is a reconstructed particle trajectory inside the detector.

denotes any particles produced from the interaction) sample with events originating in the FGD1. In this sample, we select events with a muon track that starts in FGD1. The track is also required to enter the downstream TPC (TPC2) for particle identification (PID) and momentum reconstruction. Figure 5.1 shows the muon momentum and angular distributions of the CC-inclusive sample from both the T2K data and the Monte Carlo simulation. The various reaction modes plotted are:

- COH - charged-current coherent pion production, the signal events (figure 2.1).
- RES - charged-current resonant pion production (figure 1.8).
- CCQE - charged-current quasi-elastic scattering (figure 1.7).
- DIS - deep inelastic scattering (figure 1.9).
- NC - all the neutral-current modes.
- $\bar{\nu}_\mu$ - muon antineutrino interactions.
- ν_e, $\bar{\nu}_e$ - electron neutrino/antineutrino interactions.
- OOFV - the out-of-fiducial-volume events are the ones that originate outside of the FGD1 detector but with incorrectly reconstructed interaction vertex inside FGD1.
- 2p2h - two-particle-two-hole excitation (neutrino interacts with two nucleons).
- Other - any events not categorized by the reaction modes above.

The CCQE interactions dominate the sample at this stage. Based on the inclusive sample, the NuMu group developed three ν_μ charged-current samples based on the number of detected pions:

- CC-0π - zero detected pion.
- CC-1π - one detected pion.
- CC-other - any events not included in the previous two samples.

This analysis utilizes the (FGD1) ν_μ CC-1π sample, where exactly one pion is detected. Figure 5.2 shows the muon and pion kinematic distributions for the CC-1π sample from both the T2K data and the Monte Carlo simulation. Details regarding the selection up to this point are summarized in TN-212 [66].

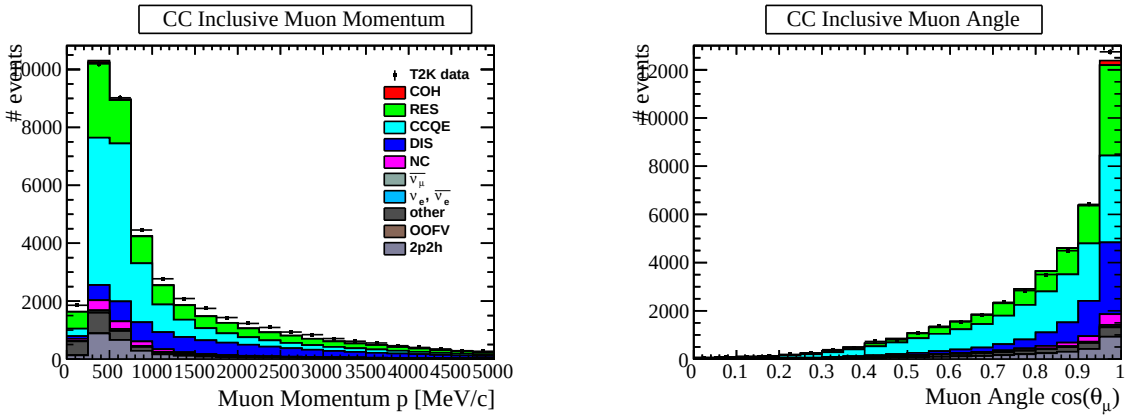

Figure 5.1. The muon kinematic distributions of the ν_μ CC-inclusive selection from both the T2K data and the Monte Carlo simulation. At this stage of the selection, the majority of the events are CCQE interactions.

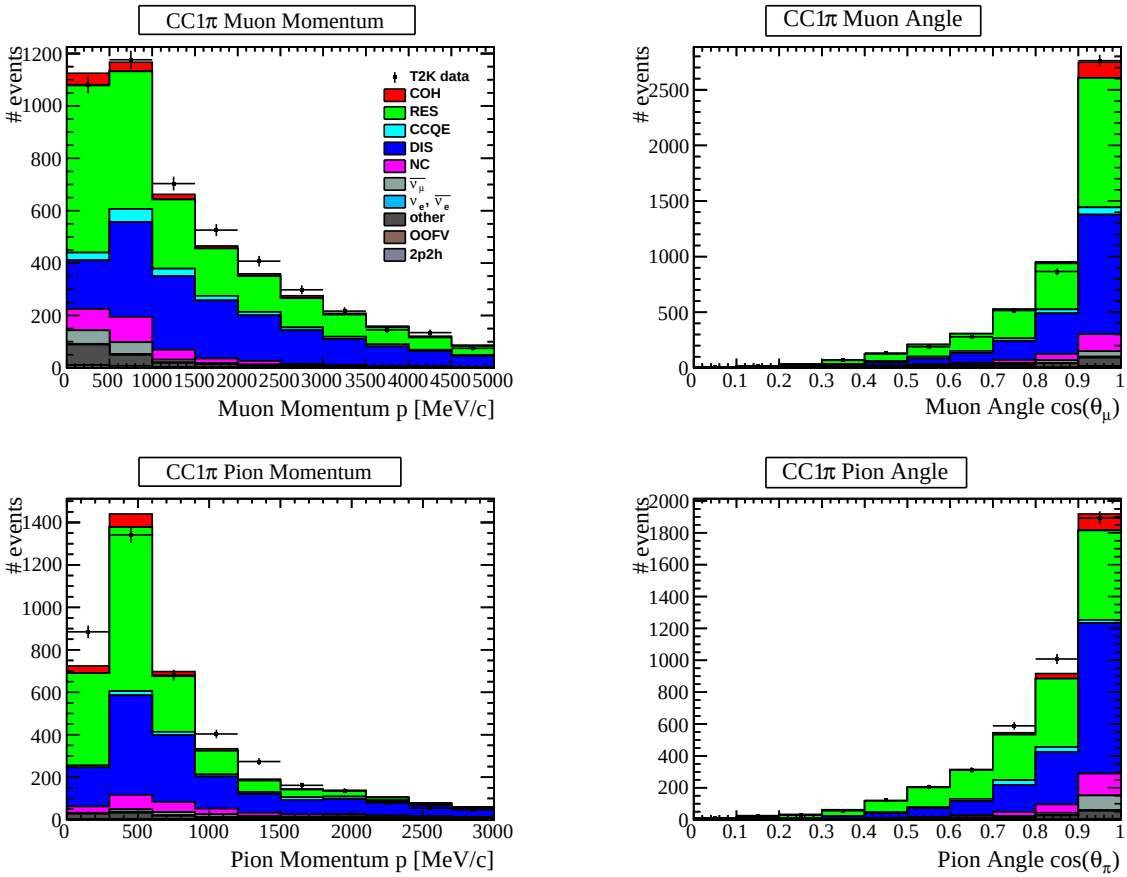

Figure 5.2. The muon and pion kinematic distributions of the ν_μ CC-1π selection from both the T2K data and the Monte Carlo simulation. By requiring a second pion track besides the leading muon track, 99% of the CCQE events are removed.

5.2.3 The ν_μ CC-COH Sample

This thesis adopts the "blind analysis" strategy[2], which means the T2K data has not been used to develop the ν_μ CC-COH selection in order to avoid any unintended biasing to the analysis results. The plots in this chapter (as well as the following chapter) include the T2K data (added to the plots after the analysis has finished) solely for the purpose of showing the comparisons between the data and the Monte Carlo simulation at each selection step. The detailed data and Monte Carlo simulation comparison studies (after unblinding the data) are shown in section 11.1.

To select an enriched ν_μ CC-COH sample, three additional cuts are performed. First, only 2 FGD1 tracks should be observed, which correspond to the μ^- and π^+ in process 5.1. As shown in figure 5.3 with a stacked histogram, 95.6% of the true CC-COH events have exactly two reconstructed FGD1 tracks.

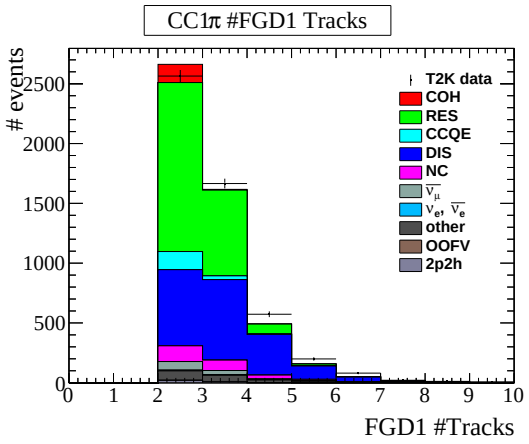

Figure 5.3. The number of reconstructed FGD1 tracks of the ν_μ CC-1π selection. Only those events with exactly 2 FGD1 tracks are selected since true CC-COH events have exactly two outgoing particles. This cut removes mostly RES and DIS events.

Secondly, since no nucleons emerge from the interaction, the outgoing muon and pion deposit a small portion of the energy they carry around the neutrino interaction vertex. Figure 5.4 shows that almost all true CC-COH events have vertex activity (VA) less than 15 MeV.

Lastly, for the CC-COH topology, the momentum transferred squared $|t|$ (equation 4.2) to the nucleus is small. The majority of the true CC-COH events has $|t|$ less than 0.15 GeV^2. Figure 5.5 shows the $|t|$ distribution of the ν_μ CC-COH sample where the signal CC-COH events are predominantly in the low $|t|$ region.

[2] According to Roodman [67]: "A blind analysis is a measurement which is performed without looking at the answer. Blind analyses are the optimal way to reduce or eliminate experimenter's bias, the unintended

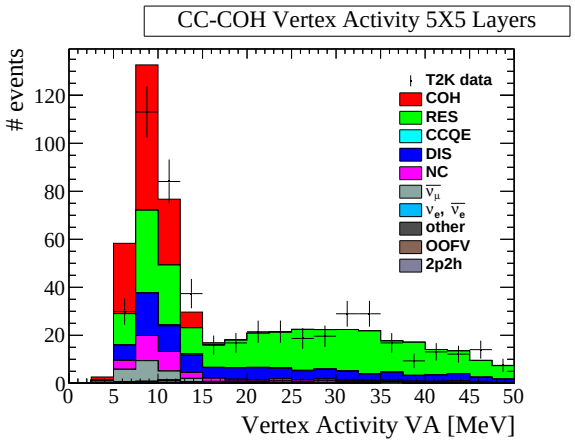

Figure 5.4. The vertex activity distribution of the ν_μ CC-COH sample (after the 2-FGD1-tracks cut). The conversion has been made from PEU to MeV. Most of the true CC-COH events have VA less than 15 MeV.

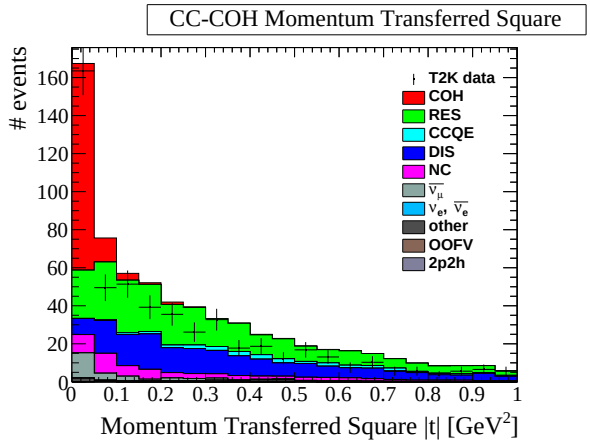

Figure 5.5. Momentum transferred squared ($|t|$) distribution of the ν_μ CC-COH sample. The majority of the CC-COH signal events are concentrated in the low $|t|$ region.

To summarize, the selection cuts to select the ν_μ CC-COH enriched sample within FGD1 are as follows:

0. Event Quality - good beam and detector event quality flag.
1. Track Multiplicity - at least one track with a TPC segment.
2. Quality & Fiducial - 18 TPC clusters for the leading candidate track; the vertex position is in the FGD1 FV.
3. External Veto (event pile-up veto) - events with additional track(s), and with start position that deviates 15 cm apart from the vertex.
4. FGD1 External Veto - rejects tracks outside of FGD1 and rejects tracks starting in last FGD1 layer.
5. Muon PID - muon particle identification (PID) cut on the highest momentum (candidate) track.
6. Pion PID - requires an additional track to exist, and the track must pass pion particle identification (PID) cut.
7. Phase Space - reduced phase space (section 4.3), in reconstructed variables, for the selection.
8. Two FGD1 Tracks - require exactly 2 FGD1 tracks (also need to enter TPC2).
9. Vertex Activity - removes events with VA more than 15 MeV.
10. Momentum Transferred Squared - selects events with $|t|$ less than 0.15 GeV^2 as signal events.

The evaluations of the VA and the $|t|$ selection cut values are presented in section 5.3.

5.3 Purity and Efficiency of the ν_μ CC-COH Selection

Table 5.2 and figure 5.6 show the number of events, the selection efficiency (equation 5.2), the relative selection efficiency (equation 5.3), and the selection purity(equation 5.4) at each selection cut level.

$$\text{Efficiency} = \frac{\#\text{ true CC-COH events selected}}{\#\text{ true CC-COH events predicted by MC}} \tag{5.2}$$

biasing of a result in a particular direction."

$$\text{Relative Efficiency} = \frac{\#\text{ true CC-COH events selected}}{\#\text{ true CC-COH events selected by the previous cut}} \tag{5.3}$$

$$\text{Purity} = \frac{\#\text{ true CC-COH events selected}}{\#\text{ events selected}} \tag{5.4}$$

$$\text{Significance} = \frac{\text{Signal}}{\sqrt{\text{Signal} + \text{Background}}} \tag{5.5}$$

The efficiency decreases after applying the pion PID cut is due to the requirement of a TPC2

Cut	**Name**	**# Event**	**Eff. (%)**	**Rel. Eff. (%)**	**Pur. (%)**
0	No Cut	66097	90.2	100.0	0.4
1	Event Quality	66097	90.2	100.0	0.4
2	Track Multiplicity	66097	90.2	100.0	0.4
3	Quality & Fiducial	66097	90.2	100.0	0.4
4	External Veto	53699	88.6	98.2	0.5
5	FGD External Veto	53693	88.6	100.0	0.5
6	Muon PID	41203	84.8	95.6	0.6
7	Pion PID	5003	54.1	63.8	3.2
8	Reduced PS	2624	57.0	85.6	5.2
9	2 FGD Seg.	1437	54.5	95.6	9.1
10	VA Cut	703	49.1	90.0	16.7
11	$\|t\|$ Cut	272	47.3	96.3	41.6

TABLE 5.2. The number of events, the selection efficiency, the relative selection efficiency, and the selection purity at each cut level for the ν_μ CC-COH selection is shown. The final selected number of events is 272 with an efficiency of 47.3% and purity of 41.6%.

pion track segment for pion momentum reconstruction. Roughly 30% of the pions produced inside FGD1 interact or stop before they reach TPC2, reducing the selection efficiency.

Figure 5.7 shows the efficiency, the purity, the product of the efficiency and the purity[3], and significance defined by equation 5.5, at various selection cut values of VA and $|t|$. Normally, the cut values are selected to optimize the efficiency, purity, or significance. However, to avoid model dependencies from the variables, the analysis uses cut values slightly above the optimal point, sometimes referred to as "*a loose cut*". The cut values for VA and $|t|$ used are 15 MeV and 0.15 GeV^2 respectively.

[3]From figure 5.7, we can see that higher efficiency usually results in lower purity, and higher purity usually results in lower efficiency. The product of efficiency and purity includes the correlation between the efficiency and the purity.

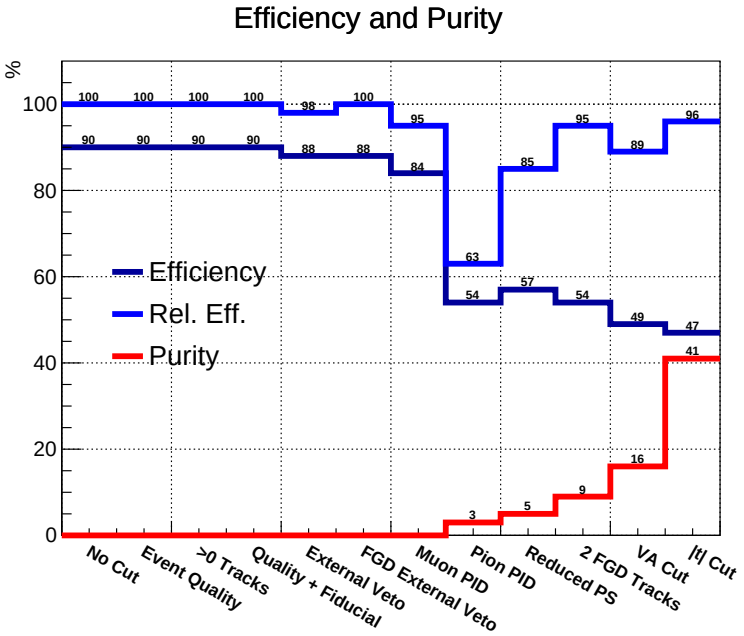

Figure 5.6. The efficiency, the relative efficiency, and the purity of the ν_μ CC-COH selection after each cut level. The most significant efficiency drop happens for the pion PID cut, which a TPC2 segment of the pion track is required for accurate momentum reconstruction. Roughly 30% of the pions produced inside FGD1 do not reach TPC2.

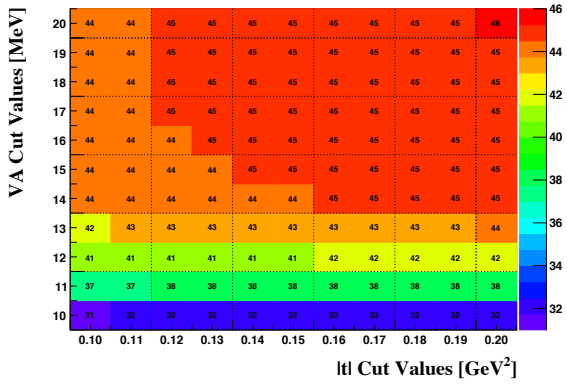

(a) Efficiency

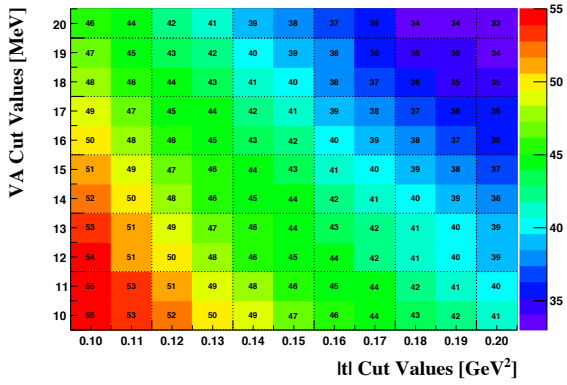

(b) Purity

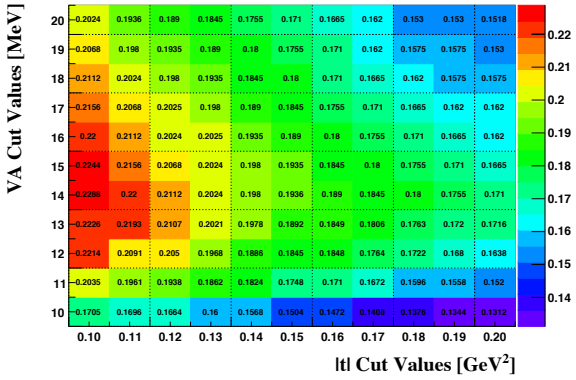

(c) Eff. * Pur.

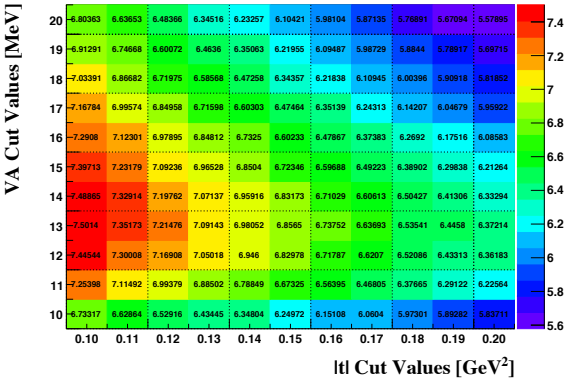

(d) Significance

Figure 5.7. The ν_μ CC-COH selection efficiency, the purity, the product of the efficiency and the purity, and the significance are computed for various VA and $|t|$ cut values. The cut values are 15 MeV for VA and 0.15 GeV^2 for $|t|$. These cut values are slightly above the optimal values to avoid model dependencies from the variables.

5.4 Signal Region (SIG) Definition for the ν_μ CC-COH Analysis

Figure 5.5 shows the $|t|$ distribution of the events that pass the vertex activity cut. The signal region (SIG) is defined to be $|t| \leq 0.15\,\mathrm{GeV}^2$. The Monte Carlo simulation predicted 272 events with an efficiency of 47.3 % and purity of 41.6 % in SIG. The muon and pion kinematic distributions of the events in SIG are shown in figure 5.8. Detailed data and Monte Carlo simulation comparison studies are described in section 11.1.1.

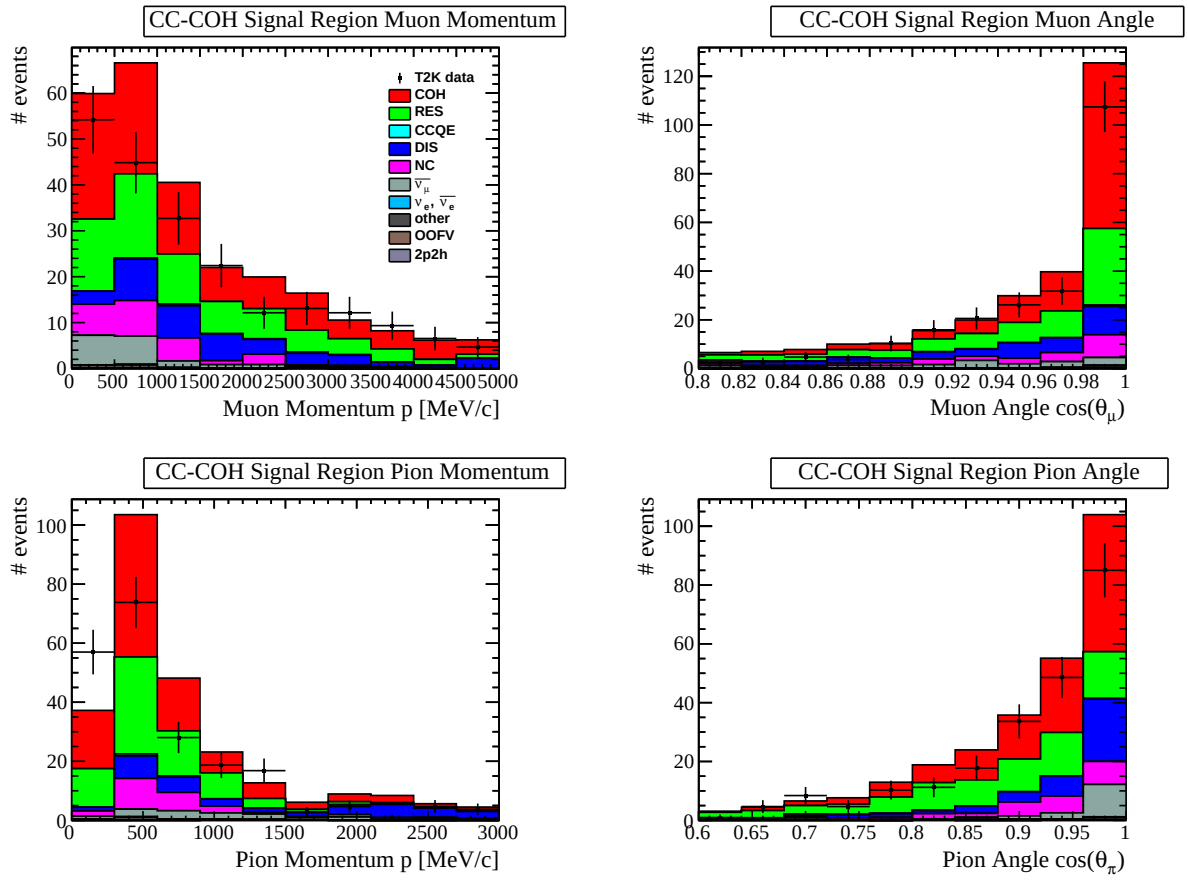

Figure 5.8. The muon and pion kinematic distributions of the ν_μ CC-COH selection signal region (SIG). Detailed data and Monte Carlo simulation comparison studies are described in section 11.1.1.

The true reaction composition in SIG is shown in table 5.3. The main background events are 28.0% RES and 14.2% DIS. The NC background events mainly consist of NC-DIS, and the $\bar{\nu}_\mu$ background events mainly consist of $\bar{\nu}_\mu$ COH and RES. Any interactions not specified are summed in the "other" category, which are mostly out-of-fiducial-volume (OOFV) events.

Reaction	# Event	Composition (%)
COH	113	41.6
RES	76	28.0
DIS	39	14.2
NC	24	8.7
$\bar{\nu}_\mu$ Background	16	5.9
Other	4	1.6

TABLE 5.3. The reaction composition of the ν_μ CC-COH selection signal region (SIG). The dominant background is RES.

5.5 Background Sideband (SB1 and SB2) Definitions for the ν_μ CC-COH Analysis

The two most significant sources of background events in the signal region (SIG) are RES and DIS, as shown in table 5.3. Two sideband regions with high purity of RES and DIS are selected to estimate the number of these two background events in the SIG region in the data. The rest of the background events are treated as irreducible backgrounds.

The definitions of the sidebands are shown in this section. The kinematics studies performed for the RES and DIS events in SIG and the sidebands are discussed in the next section.

5.5.1 Sideband to Constrain the RES and DIS Backgrounds (SB1)

The events that are excluded by the $|t|$ cut ($|t| > 0.15\,\mathrm{GeV}^2$) mostly consist of RES and DIS events. This region is defined as a background sideband region (SB1), and it is used to study RES and DIS background in further detail. The true reaction composition in the background sideband region is shown in table 5.4. The muon and pion kinematic distributions for SB1 are shown in figure 5.9. The Monte Carlo simulation overpredicts the number of events in SB1. Detailed data and Monte Carlo simulation comparison studies are described in section 11.1.1.

5.5.2 Sideband to Constrain the DIS Backgrounds (SB2)

With SB1 (5.5.1) alone, it is only possible to estimate the combined RES and DIS number of events in SIG. Most of the events with more than three [4] FGD1 tracks (shown in figure 5.3)

[4]The events with exactly three FGD1 tracks are not used by this analysis since SB2 needs to have a high DIS purity. However, the data and Monte Carlo simulation comparisons for these events are made for consistency checks. The study is described in appendix I.

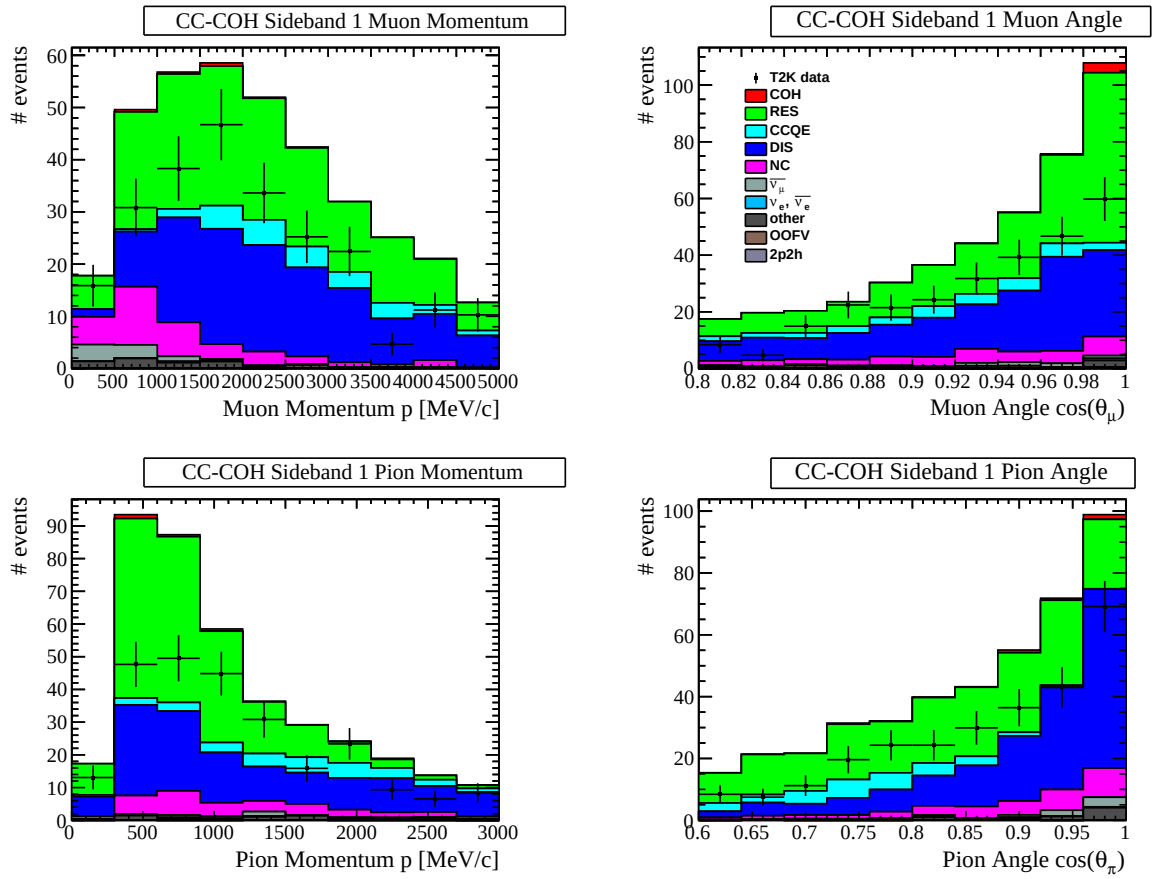

Figure 5.9. The muon and pion kinematic distributions of the ν_μ CC-COH selection sideband region SB1.

Reaction	**# Event**	**Composition (%)**
COH	4	1.1
RES	174	45.7
DIS	132	34.7
NC	34	7.8
$\bar{\nu}_\mu$ Background	8	2.2
Other	37	8.7

TABLE 5.4. The reaction composition of the ν_μ CC-COH selection SB1. The dominant background is RES and DIS. The Monte Carlo simulation overpredicts the number of events in SB1. Detailed data and Monte Carlo simulation comparison studies are described in section 11.1.1.

are DIS, and these events are selected as an additional sideband (SB2). Table 5.5 shows the reaction breakdown of SB2, where more than 70% of the events are DIS. With the help of SB2, the RES and DIS events can be estimated separately in both SIG and SB1. The muon and pion kinematic distributions for SB2 are shown in figure 5.10. The Monte Carlo simulation overpredicts the number of events in SB2. Detailed data and Monte Carlo simulation comparison studies are described in section 11.1.1.

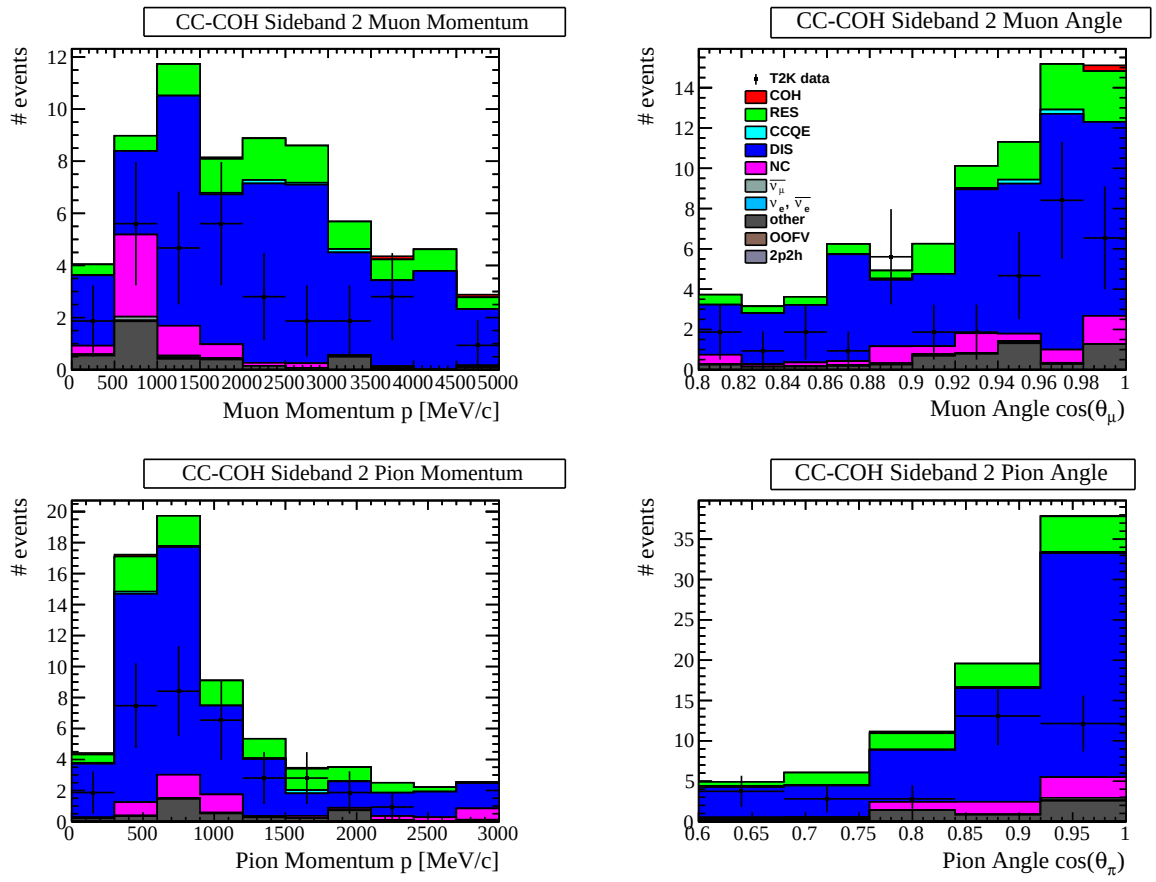

Figure 5.10. The muon and pion kinematic distributions of the ν_μ CC-COH selection sideband region SB2. This control region is dominated by DIS events.

Reaction	# Event	Composition (%)
COH	0	0.4
RES	11	14.4
DIS	56	70.9
NC	6	7.1
Other	6	7.5

TABLE 5.5. The reaction composition of the ν_μ CC-COH selection SB2. The purity of DIS in SB2 is more than 70%. The Monte Carlo simulation overpredicts the number of events in SB2. Detailed data and Monte Carlo simulation comparison studies are described in section 11.1.1.

5.6 The ν_μ CC-COH Selection Background Events

The background sidebands (SB1 and SB2) help estimate the number of resonant pion production (RES) and deep inelastic scattering (DIS) background events in the signal region (SIG). The underlying assumption is that the kinematic distributions of the background events in both regions are similar. This assumption is examined in this section using the information from the Monte Carlo simulation.

5.6.1 RES events

Figure 5.11 shows the pion kinematics comparisons of the RES events in SIG and SB1. Shape differences in the pion kinematic distributions are observed when the distributions are area normalized.

To investigate the $|t|$ dependence on the differences observed, SIG and SB1 are divided into five regions in $|t|$:

1. $0\,\mathrm{GeV}^2 < |t| \leq 0.05\,\mathrm{GeV}^2$.
2. $0.05\,\mathrm{GeV}^2 < |t| \leq 0.1\,\mathrm{GeV}^2$.
3. $0.1\,\mathrm{GeV}^2 < |t| \leq 0.15\,\mathrm{GeV}^2$.
4. $0.15\,\mathrm{GeV}^2 < |t| \leq 0.3\,\mathrm{GeV}^2$.
5. $|t| > 0.3\,\mathrm{GeV}^2$.

The first three regions come from SIG, and the last two regions come from SB1. Figure 5.12 shows the pion kinematic distributions comparisons of the five regions. The events with $|t| \leq 0.1\,\mathrm{GeV}^2$ (the first two regions in $|t|$) has different shape in pion momentum and angle compared to the events with $0.1\,\mathrm{GeV}^2 < |t| \leq 0.15\,\mathrm{GeV}^2$. When looking at the events with

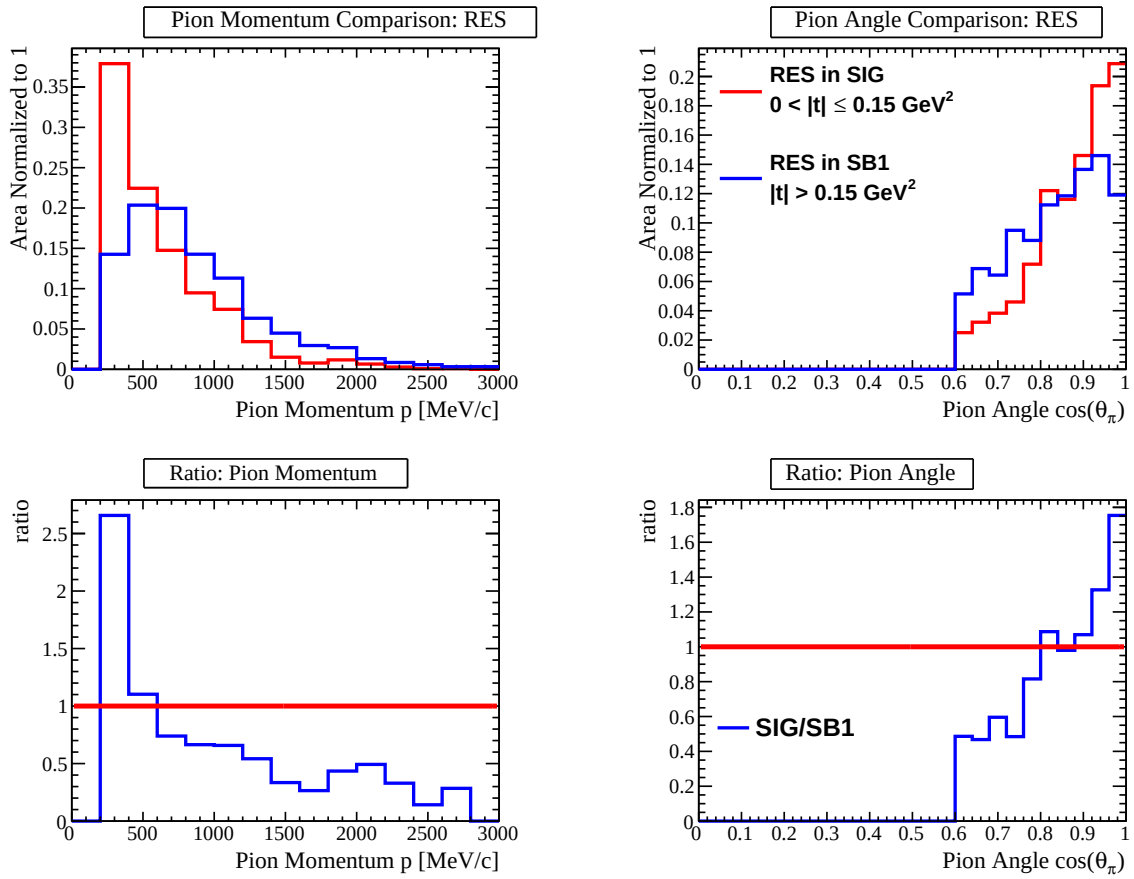

Figure 5.11. Pion kinematics comparisons of the RES events in the ν_μ CC-COH selection SIG and the SB1 (top) and the corresponding ratios (bottom).

$|t| > 0.15\,\text{GeV}^2$, the pion momentum and angle have similar shape compared to the events in SIG with $0.1\,\text{GeV}^2 < |t| \leq 0.15\,\text{GeV}^2$. This observation indicates some difference in the kinematic distributions of the RES background events in the different $|t|$ regions.

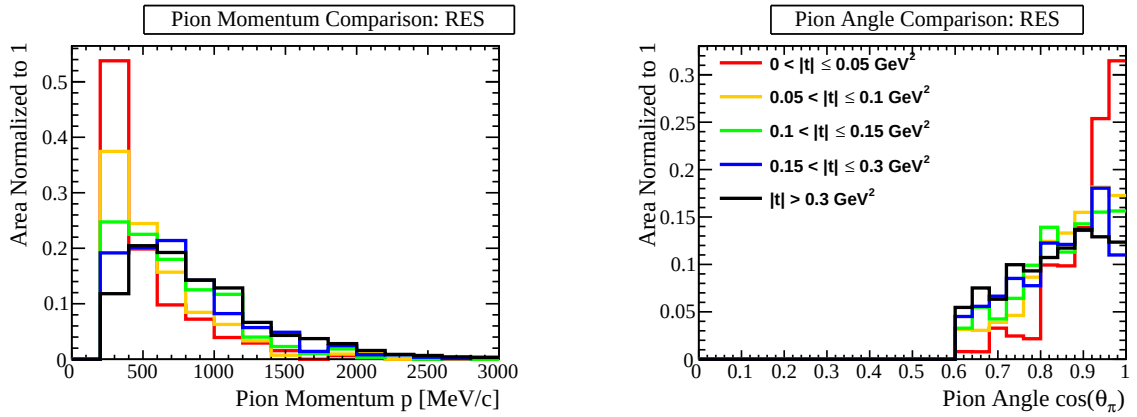

Figure 5.12. Pion kinematics comparisons of the RES events between different regions in $|t|$ of the ν_μ CC-COH selection SIG and SB1. Difference in pion momentum and angle is seen between the first two $|t|$ regions ($|t| \leq 0.1\,\text{GeV}^2$) with the rest of the events.

Table 5.6 shows the number of events in each $|t|$ region (normalized to data POT). From figure 5.12, we can see that the pion momentum and angle distributions are similar between regions 3-5, which means the RES events in SB1 share similar pion kinematics with roughly one-third of the RES events in SIG (region 3 listed in table 5.6). For the other RES events in regions 1-2, where the pion kinematics are different from the SB1 RES events, additional studies are performed to evaluate the effect of pion kinematics on the cross-section results. These studies are described in appendix H

Region	$\boldsymbol{\lvert t\rvert}$	**# Event**
1	$0\,\text{GeV}^2 < \lvert t\rvert \leq 0.05\,\text{GeV}^2$	23
2	$0.05\,\text{GeV}^2 < \lvert t\rvert \leq 0.1\,\text{GeV}^2$	29
3	$0.1\,\text{GeV}^2 < \lvert t\rvert \leq 0.15\,\text{GeV}^2$	27
4	$0.15\,\text{GeV}^2 < \lvert t\rvert \leq 0.3\,\text{GeV}^2$	64
5	$\lvert t\rvert > 0.3\,\text{GeV}^2$	129
Total	/	272

TABLE 5.6. Number of RES events (from the Monte Carlo simulation) in each $|t|$ region.

5.6.2 DIS events

Similar to the studies done for the RES events, pion kinematics are compared for DIS events in SIG, SB1, and SB2, as shown in figure 5.13. A reminder that the SB2 is the sideband for

DIS events, with 70% purity.

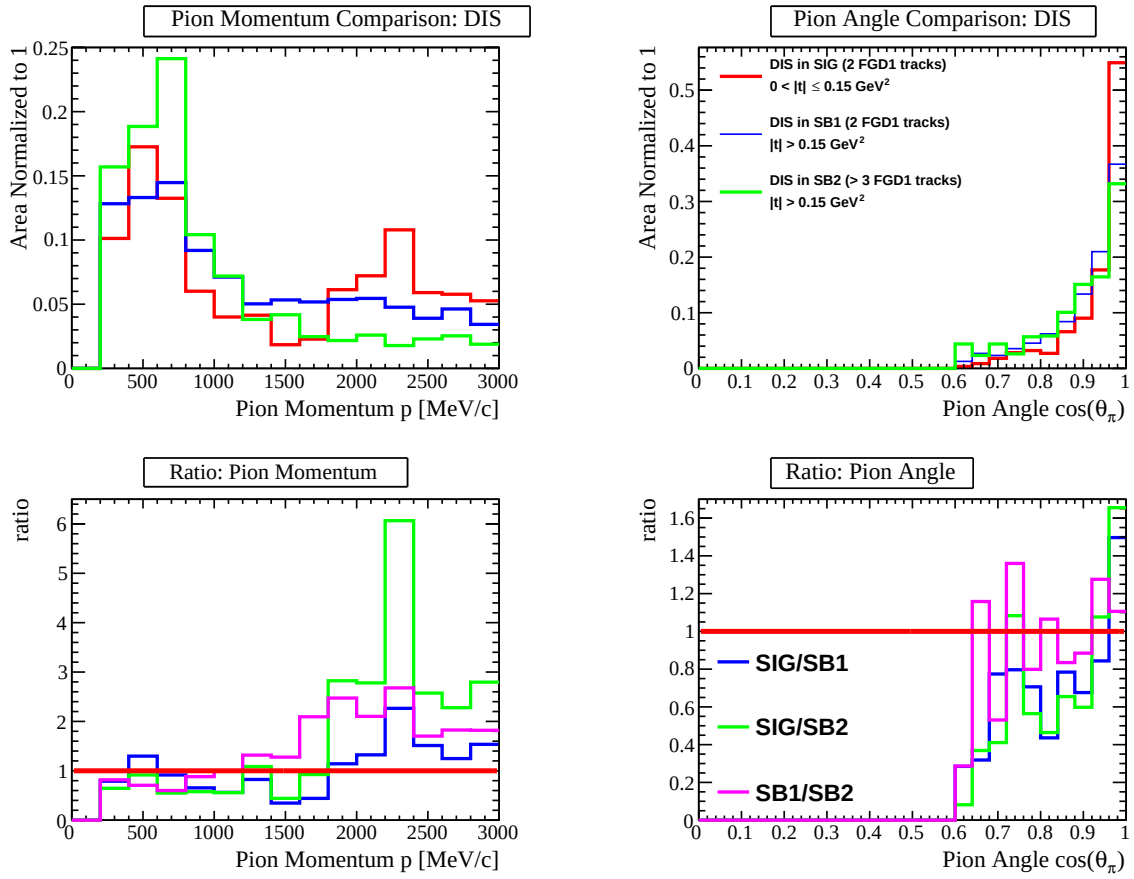

Figure 5.13. Pion kinematics comparisons of the DIS events in the ν_μ CC-COH selection SIG, SB1, and SB2 (top). The ratios (bottom) between different samples are also computed.

The pion momentum distribution of DIS in SIG (figure 5.13) has two peaks, which are not observed for the DIS events in SB1 and SB2. Figure 5.14 shows the topology and NEUT reaction breakdown of the DIS events in SIG, SB1 and SB2.

The topologies are classified by the number of pions produced from the interaction. The reason to look at the reaction code in NEUT is that the DIS reaction definition in ND280 (used for this analysis) consists of two NEUT reaction types:

- NEUT reaction code 21:
  - Multi-π Production (NEUT Multi-π Prod.)
  - $1.3\,\text{GeV} < \text{W}_{inv} \leq 2\,\text{GeV}$
  - More than one pion is produced
- NEUT reaction code 26:

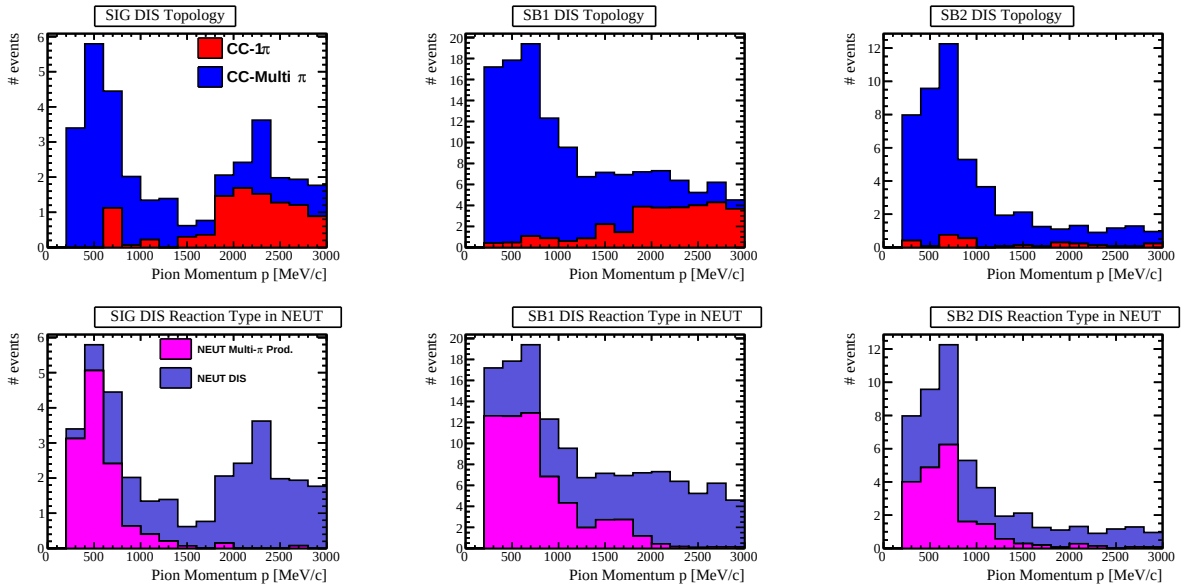

Figure 5.14. The topology and NEUT reaction breakdown of the DIS events in SIG, SB1, and SB2. The double-peaked structure of pion momentum in SIG is caused by different topology and NEUT reaction contributions.

- Deep elastic scattering (NEUT DIS)
- $W_{inv} > 2\,\text{GeV}$
- Any number of pions produced, including zero,

where the two reactions cover different regions in the invariant mass W. The second peak in pion momentum for SIG in figure 5.14 is caused by the CC-1π topology events where all events are NEUT DIS events. For these events, the invariant mass W_{inv} is more than 2 GeV, and only one pion is produced. As a result, the pion momentum is higher than the events where multiple pions are produced.

While the pion momentum and angle distributions in SIG have some shape differences between SB1 and SB2, studies performed in H.1.5 indicate that SB2 still provides a valuable constraint in the prediction of DIS events in SIG.

5.7 Likelihood Fitter Input Binning for the ν_μ CC-COH Selection

Table 5.7 summarizes the inputs (three samples) to the likelihood fitter for both the Monte Carlo (MC) simulation and the data. Due to the statistical limitation of this analysis, each sample only contains one bin in the $|t|$ space. The number of events (for the Monte Carlo

simulation) in each sample is normalized to data POT. The sources of uncertainties are discussed in chapter 7.

Sample	**# bins**	**# events (MC)**	**# events (data)**
SIG	1	272	241
SB1	1	429	290
SB2	1	79	37

TABLE 5.7. The ν_μ CC-COH selection input to the likelihood fitter contains three samples: SIG, SB1, and SB2. Each sample contains one bin in the $|t|$ space. The number of events (for the Monte Carlo simulation) in each sample is normalized to data POT.

Chapter 6

The $\bar{\nu}_\mu$ CC-COH Selection

6.1 Data and Monte Carlo Simulation Sample

The T2K ND280 data and Monte Carlo (MC) simulation used for the $\bar{\nu}_\mu$ induced CC-COH measurements originating in FGD1 are listed in table 6.1; the total "Protons-on-Target" (POT) count for the data used is 8.15×10^{20}. For the Monte Carlo simulation, the total POT produced is 1.13×10^{22}, which is roughly 14 times the data POT. Unless stated otherwise, the Monte Carlo simulation is normalized to the data POT for all the plots shown in this chapter. The term "air" and "water" refer to the configuration of the P0D detector during that data-taking period; these different configurations do not directly impact this analysis.

Run	**Data POT (10^{20})**	**MC POT (10^{21})**	**MC/DATA Ratio**
Run 5 water	0.44	2.21	50.2
Run 6 air	2.99	3.47	11.6
Run 7 water	2.41	3.33	13.8
Run 9 air	2.30	2.24	9.7
Total	8.15	11.25	13.8

TABLE 6.1. The T2K data and Monte Carlo (MC) simulation used for the $\bar{\nu}_\mu$ CC-COH measurements from different running periods. The "Protons-on-Target" (POT) for both data and simulation are shown with the MC/Data ratio. The total T2K ND280 neutrino (FHC) data used is 8.15×10^{20} POT. For the Monte Carlo, the total POT produced is 1.13×10^{22}, which is roughly 14 times the data POT.

6.2 The $\bar{\nu}_\mu$ CC-COH Selection within FGD1

6.2.1 Selection Overview

The $\bar{\nu}_\mu$ CC-COH selection shares many similarities with the ν_μ CC-COH selection. Some key points are repeated in this subsection for the reader's convenience.

The $\bar{\nu}_\mu$ CC-COH interaction produces a μ^+ and a π^- (as seen in figure 2.1):

$$\bar{\nu_\mu} + {}^{12}\mathrm{C} \rightarrow \mu^+ + \pi^- + {}^{12}\mathrm{C}. \tag{6.1}$$

In this CC-COH process, the momentum transferred to the target nucleus is minimal, so the target nucleus does not fragment; therefore, no additional nucleons can deposit energy around the interaction vertex. The following steps summarize how to select a sample with $\bar{\nu}_\mu$ CC-COH events originating in the FGD1 detector:

- Select the events with a positively charged muon track that starts in FGD1
- Select the events with an additional pion track that starts in FGD1
- Exclude events with more than two tracks
- Select the events with low energy deposition around the interaction vertex
- Select the events with low momentum transferred to the target nucleus.

Details regarding each step are described in the following subsection.

6.2.2 The $\bar{\nu}_\mu$ CC-inclusive and CC-1π Samples

The $\bar{\nu}_\mu$ selection is almost identical to the ν_μ selection described in chapter 5. The only difference between the two selections is an additional requirement for the highest momentum track to be positively charged, which serves the purpose of removing ν_μ background events in the $\bar{\nu}_\mu$ selection. This additional cut is not necessary for the ν_μ selection since the highest momentum track is most likely to be a negatively charged muon - the $\bar{\nu}_\mu$ background (wrong sign background) only consists of less than 1% of the sample. For the $\bar{\nu}_\mu$ selection however, ν_μ background contributes to 15% of the selected events. Figure 6.1 shows the events removed by the positive charge cut. According to the Monte Carlo simulation, 62% of the events removed are ν_μ background events, and the cut removes 49% of these wrong sign contaminations in the sample at this stage.

Figure. 6.2 shows the muon momentum and angular distributions of the CC-inclusive sample. The CCQE interactions dominate the sample at this stage.

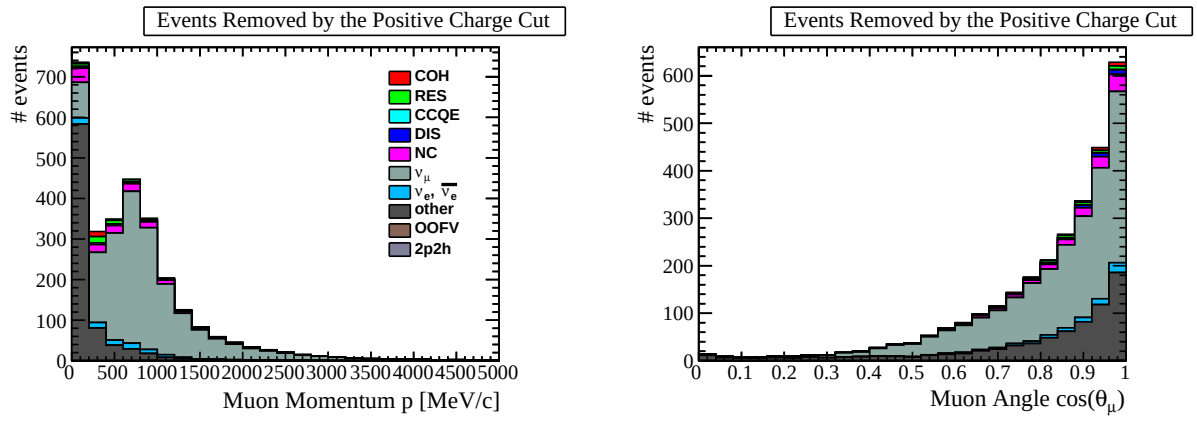

Figure 6.1. Effect of requiring the highest momentum track be positively charged in the $\bar{\nu}_\mu$ selection. According to the Monte Carlo simulation, the wrong sign background consists of 15% of the selection at this stage and the cut removes 49% of these background events. 62% of the events removed are ν_μ background events.

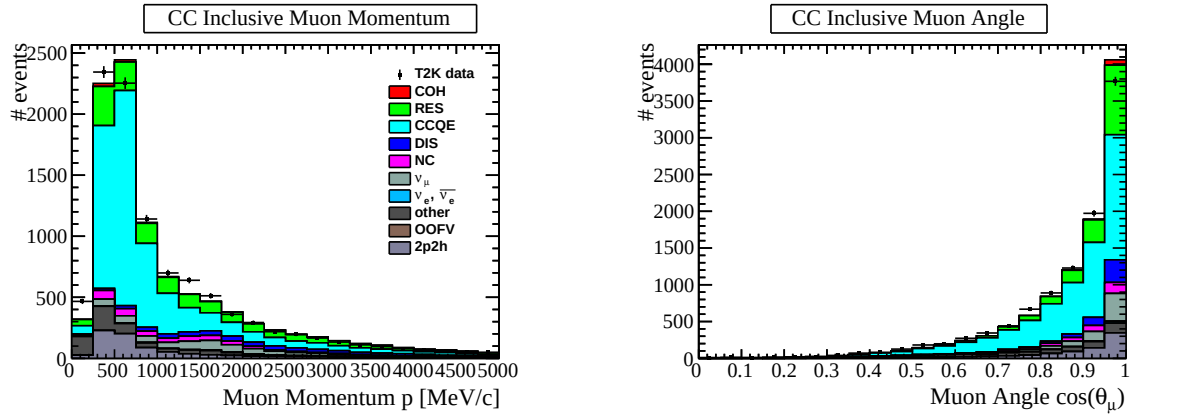

Figure 6.2. The muon kinematic distributions of the $\bar{\nu}_\mu$ CC-inclusive selection from both the T2K data and the Monte Carlo simulation. At this stage of the selection, the majority of the events are CCQE interactions.

The (FGD1) $\bar{\nu}_\mu$ CC-1π sample is obtained by requiring an additional reconstructed pion track. Figure 6.3 shows the muon and pion kinematic distributions for the $\bar{\nu}_\mu$ CC-1π sample. Details regarding the selection up to this point are summarized in TN-273 [68].

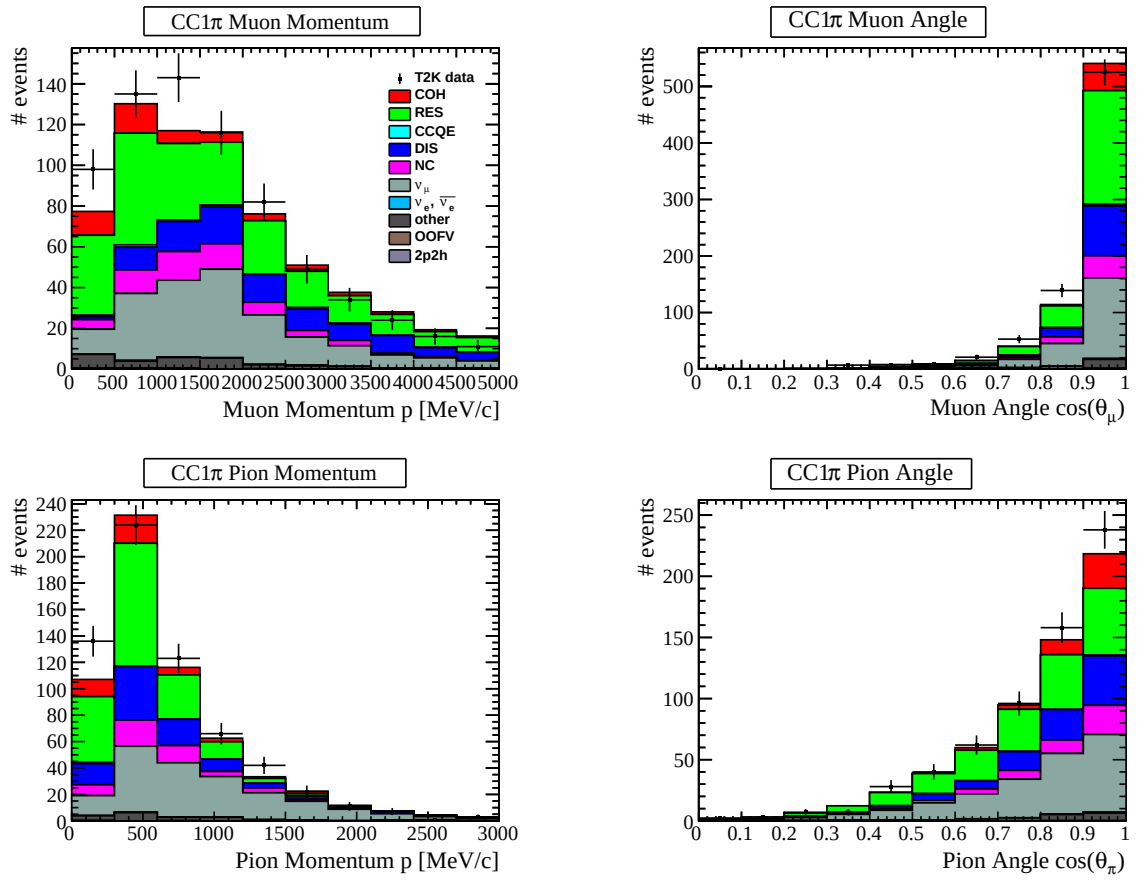

Figure 6.3. The muon and pion kinematic distributions of the $\bar{\nu}_\mu$ CC-1π selection from both the T2K data and the Monte Carlo simulation. By requiring a second (pion) track beside the leading muon track, 99.9% of the CCQE events are removed.

6.2.3 The $\bar{\nu}_\mu$ CC-COH Sample

A reminder that the T2K data is not used to develop the $\bar{\nu}_\mu$ CC-COH selection, and the detailed data and Monte Carlo simulation comparisons (after unblinding the data) are shown in section 11.1. The $\bar{\nu}_\mu$ CC-COH sample shares the same selection cuts as the ν_μ selection described in 5.2.3. Figure 6.4 shows the number of the reconstructed FGD1 tracks, where 95.5% of the true CC-COH events have exactly two reconstructed FGD1 tracks.

Figure 6.5 shows that almost all true CC-COH events have vertex activity (VA) less than 15 MeV.

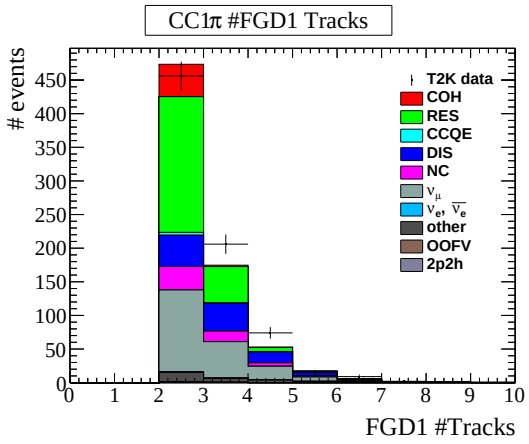

Figure 6.4. The number of reconstructed FGD1 tracks of the $\bar{\nu}_\mu$ CC-1π selection. Only those events with exactly 2 FGD1 tracks are selected since true CC-COH events have exactly 2 outgoing particles. This cut removes mostly DIS events.

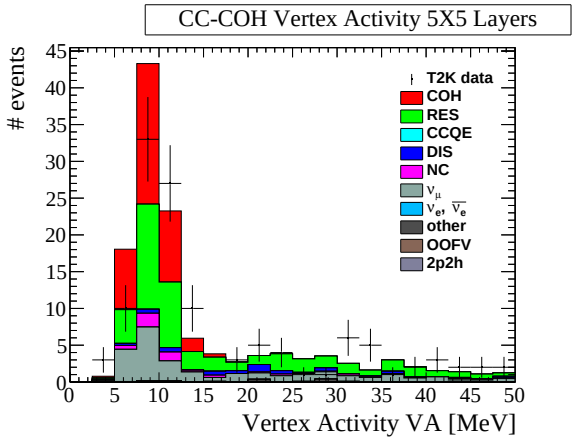

Figure 6.5. The vertex activity distribution of the $\bar{\nu}_\mu$ CC-COH sample (after the 2-FGD1-tracks cut). The conversion has been made from PEU to MeV. Most of the true CC-COH events have VA less than 15 MeV.

For the $\bar{\nu}_\mu$ CC-COH topology (as in the ν_μ CC-COH topology), the momentum transferred squared $|t|$ (equation 4.2) to the nucleus is small. The majority of the true CC-COH events has $|t|$ less than $0.15\,\mathrm{GeV}^2$. Figure 6.6 shows the $|t|$ distribution of the $\bar{\nu}_\mu$ CC-COH sample where the signal CC-COH events are predominantly in the low $|t|$ region.

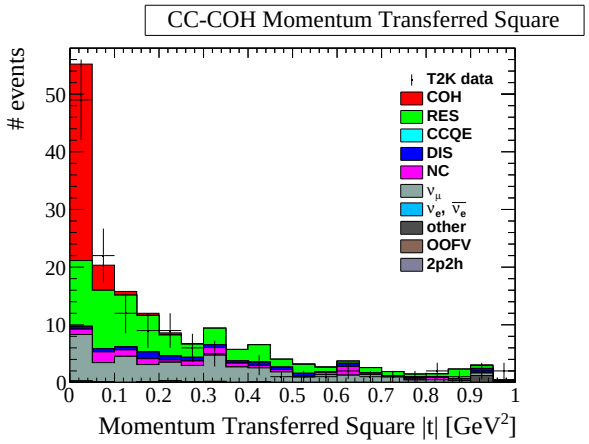

Figure 6.6. The momentum transferred squared ($|t|$) distribution of the $\bar{\nu}_\mu$ CC-COH sample. The majority of the CC-COH signal events are concentrated in the low $|t|$ region.

To summarize, the selection cuts to select the $\bar{\nu}_\mu$ CC-COH enriched sample within FGD1 are as follows:

0. Event Quality - good beam and detector event quality flag.
1. Track Multiplicity - at least one track with a TPC segment.
2. Quality & Fiducial - 18 TPC clusters for the leading candidate track; the vertex position is in the FGD1 FV.
3. Positive Charge Cut[1] - Requiring the highest momentum track to be positively charged. This is the muon candidate track.
4. External Veto (event pile-up veto) - events with additional track(s), and with start position that deviates 15 cm apart from the vertex.
5. FGD1 External Veto - rejects tracks outside of FGD1 and rejects the last FGD1 layer.
6. Muon PID - muon particle identification (PID) cut on the highest momentum (candidate) track.

[1] This cut is also referred to as the "positive multiplicity cut" in T2K documentations.

7. Pion PID - requires an additional track to exist, and the track must pass pion particle identification (PID) cut.

8. Phase Space - reduced phase space (section 4.3), in reconstructed variables, for the selection.

9. Two FGD1 Tracks - require exactly 2 FGD1 tracks (also need to enter TPC2).

10. Vertex Activity - removes events with VA more than 15 MeV.

11. Momentum Transferred Squared - selects events with $|t|$ less than 0.15 GeV^2 as signal events.

The evaluations of the VA and the $|t|$ selection cut values are presented in section 6.3.

6.3 Purity and Efficiency of the $\bar{\nu}_\mu$ CC-COH Selection

Table 6.2 and figure 6.7 show the number of events, the selection efficiency (equation 5.2), the relative selection efficiency (equation 5.3), and the selection purity (equation 5.4) at each selection cut level.

Cut	Name	# Event	Eff. (%)	Rel. Eff. (%)	Pur. (%)
0	No Cut	23078	86.0	100.0	0.5
1	Event Quality	23078	86.0	100.0	0.5
2	Track Multiplicity	23078	86.0	100.0	0.5
3	Quality & Fiducial	23078	86.0	100.0	0.5
4	Positive Charge	20202	68.0	79.1	0.5
5	External Veto	15464	67.0	98.5	0.6
6	FGD External Veto	15463	67.0	100.0	0.6
7	Muon PID	9653	63.2	94.4	0.9
8	Pion PID	687	34.4	54.4	7.0
9	Reduced PS	428	37.2	84.3	9.5
10	2 FGD Seg.	271	35.5	95.5	14.3
11	VA Cut	160	31.7	89.3	21.7
12	$\|t\|$ Cut	80	30.8	97.1	42.2

TABLE 6.2. The number of events, the selection efficiency, the relative selection efficiency, and the selection purity at each cut level for the $\bar{\nu}_\mu$ CC-COH selection is shown. The final selected number of events is 80 with an efficiency of 30.8% and purity of 42.2%.

The efficiency decreases after applying the pion PID cut is due to the requirement of a TPC2 pion track segment for pion momentum reconstruction. Roughly 30% of the pi-

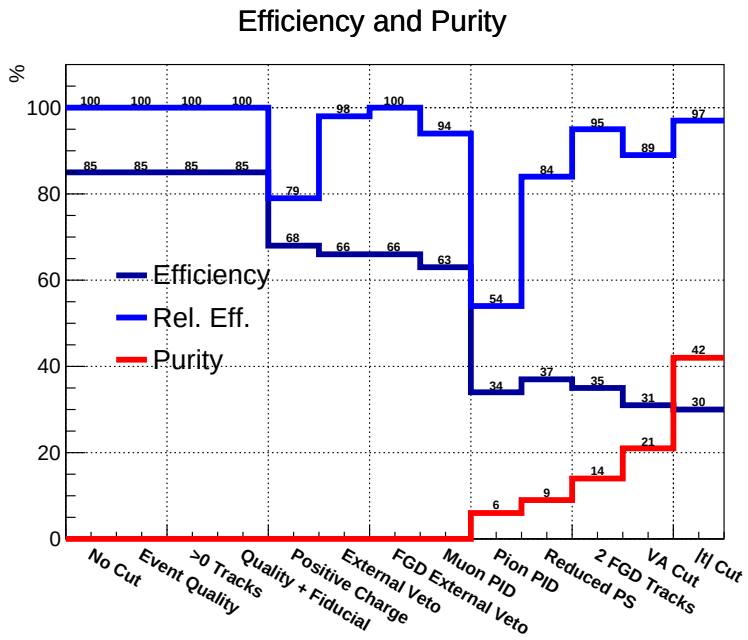

Figure 6.7. The efficiency, the relative efficiency, and the purity of the $\bar{\nu}_\mu$ CC-COH selection after each cut level. The most significant efficiency drop happens for the pion PID cut, in which a TPC2 segment of the pion track is required for accurate momentum reconstruction. Roughly 30% of the pions produced inside FGD1 do not reach TPC2. There is also a significant efficiency reduction caused by the positive charge cut, which removes half of the wrong-sign contamination.

ons produced inside FGD1 interact or stop before they reach TPC2, reducing the selection efficiency.

Figure 6.8 shows the efficiency, the purity, the product of the efficiency and the purity, and the significance defined by equation 5.5, at various selection cut values of VA and $|t|$. Normally, the cut values are selected to optimize the efficiency, purity, or significance. However, to avoid model dependencies from the variables, the analysis uses cut values slightly above the optimal point, sometimes referred to as "*a loose cut*". The cut values for VA and $|t|$ used are 15 MeV and 0.15 GeV^2 respectively.

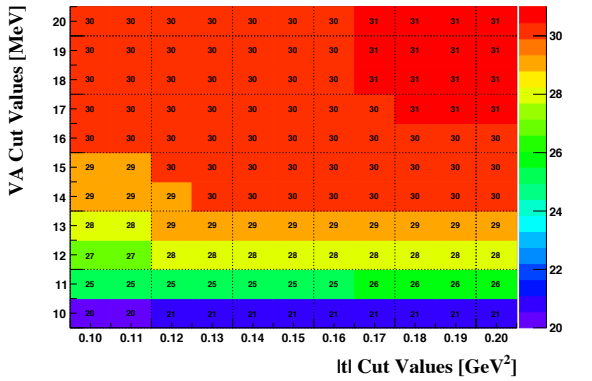

(a) Efficiency

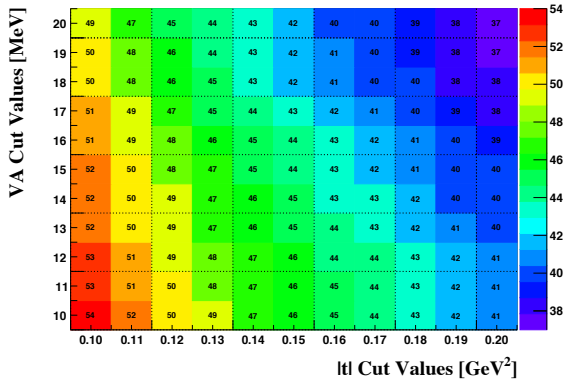

(b) Purity

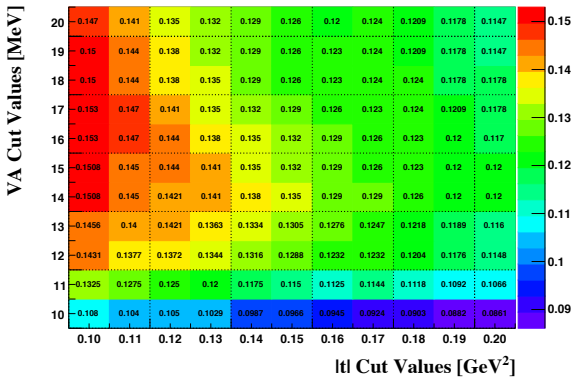

(c) Eff. * Pur.

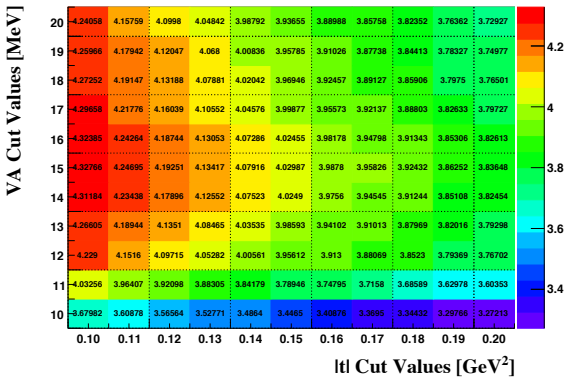

(d) Significance

Figure 6.8. The $\bar{\nu}_\mu$ CC-COH selection efficiency, the purity, the product of the efficiency and the purity, and the significance are computed for various VA and $|t|$ cut values. The cut values are 15 MeV for VA and 0.15 GeV^2 for $|t|$. These cut values are slightly above the optimal values to avoid model dependencies from the variables.

6.4 Signal Region (SIG) Definition for the $\bar{\nu}_\mu$ CC-COH Analysis

Figure 6.6 shows the $|t|$ distribution of the events that pass the vertex activity cut. The signal region (SIG) is defined to be $|t| \leq 0.15\,\mathrm{GeV}^2$. The Monte Carlo simulation predicted 80 events with an efficiency of 30.8 % and purity of 42.2 % in SIG. The muon and pion kinematic distributions of the events in the signal region are shown in figure 6.9. Detailed data and Monte Carlo simulation comparison studies are described in section 11.1.2.

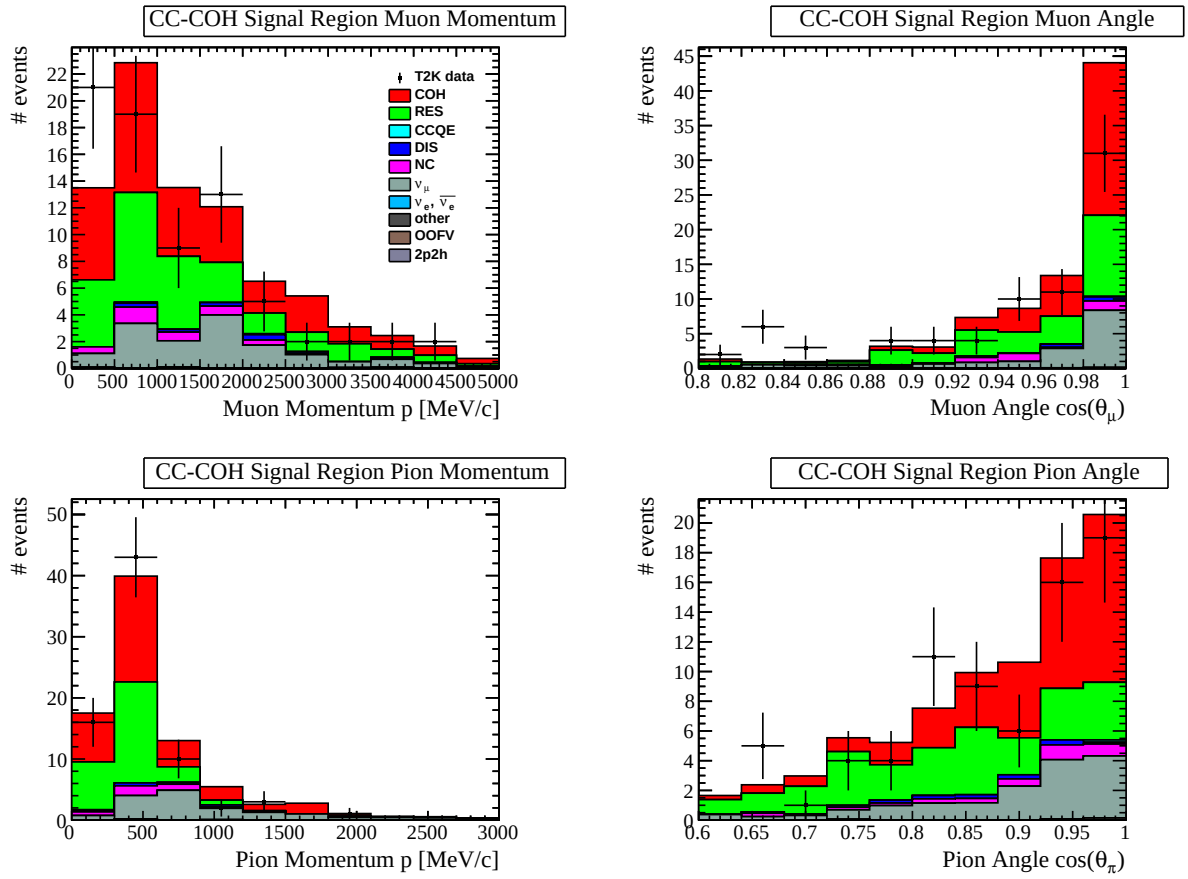

Figure 6.9. The muon and pion kinematic distributions of the $\bar{\nu_\mu}$ CC-COH selection SIG.

The true reaction composition in the signal region is shown in table 6.3. The main background events are 33.0% RES and 18.2% wrong-sign contamination (ν_μ interactions). For this analysis, no background sideband is selected to constrain the ν_μ interactions; however as shown in figure 6.1, roughly half of these backgrounds have been cut away. A detailed breakdown of reaction types for these events is shown in section 6.6.

Reaction	# Event	Composition (%)
COH	34	42.2
RES	26	33.0
DIS	2	1.9
ν_μ Background	14	18.2
Other	4	4.7

TABLE 6.3. The reaction composition of the $\bar{\nu}_\mu$ CC-COH selection SIG. The dominant background is RES.

6.5 Background Sideband (SB1) Definition for the $\bar{\nu}_\mu$ CC-COH Analysis

The main background events in the signal region are RES and ν_μ interactions, as shown in table 6.3. Unlike the ν_μ selection, DIS is not a major source of background in the $\bar{\nu}_\mu$ selection, so no sideband sample is selected for DIS.

6.5.1 Sideband to Constrain the RES Backgrounds (SB1)

The events that are excluded by the $|t|$ cut ($|t| > 0.15\,\mathrm{GeV}^2$) consists of 38.1% of RES and 35.8% ν_μ backgrounds as shown in table 6.4. This region is defined as a background sideband region (SB1), and it is used to study the RES background in further detail. The muon and pion kinematic distributions for SB1 are shown in figure 6.10. The Monte Carlo simulation overpredicts the number of events in SB1. Detailed data and Monte Carlo simulation comparison studies are described in section 11.1.2.

Reaction	# Event	Composition (%)
COH	1	1.3
RES	30	38.1
DIS	9	10.8
ν_μ Background	28	35.8
Other	11	14.0

TABLE 6.4. The reaction composition of the $\bar{\nu}_\mu$ CC-COH selection SB1. The dominant background is RES.

It is not ideal that SB1 contains both RES and ν_μ events, which limits its ability to help estimate the number of RES background events in the signal region. However, given the low statistics of events in the $\bar{\nu}_\mu$ CC-COH analysis, this sideband sample is the best (in terms of purity for RES and statistics) that can be selected.

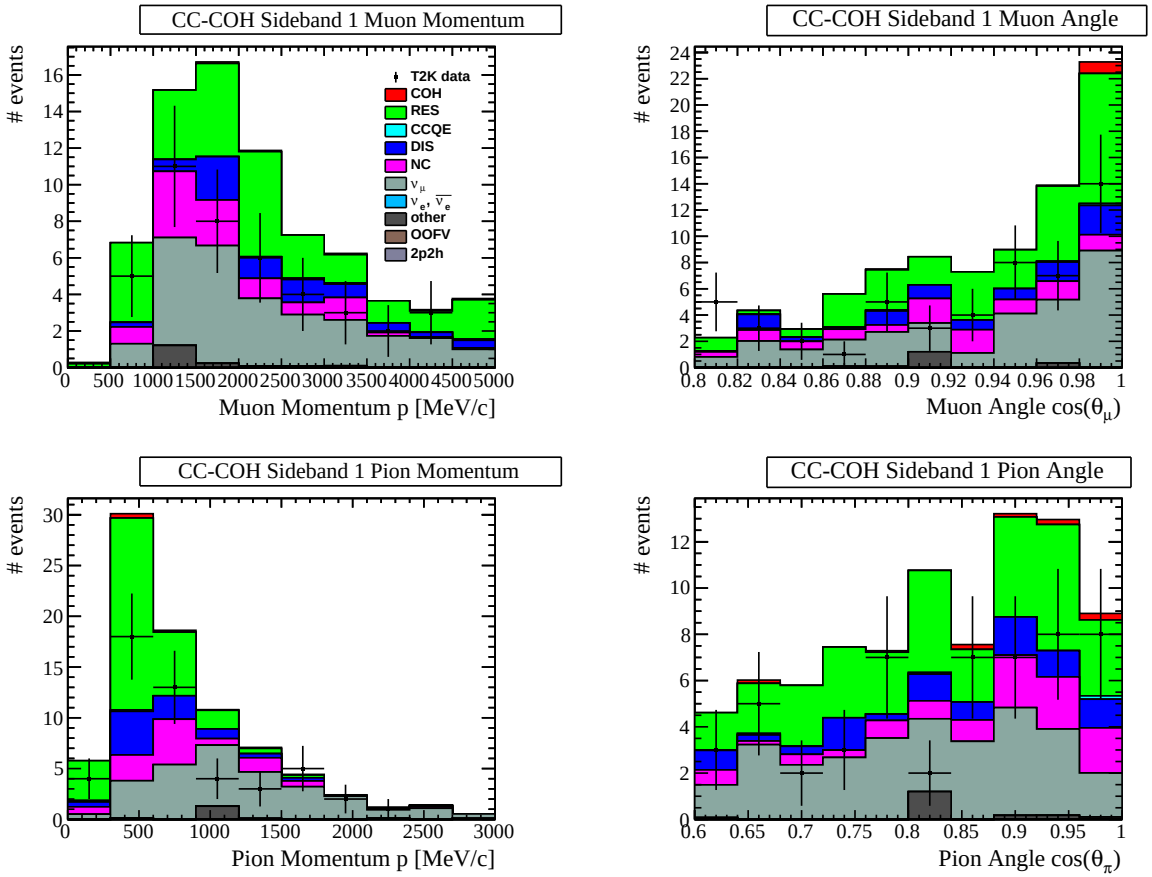

Figure 6.10. The muon and pion kinematic distributions of the $\bar{\nu_\mu}$ CC-COH selection SB1.

6.6 The $\bar{\nu}_\mu$ CC-COH Selection ν_μ Background Events

The ν_μ background events in the $\bar{\nu}_\mu$ CC-COH selection is significant in both SIG (table 6.3) and SB1 (table 6.4). In this section, using the information from the Monte Carlo simulation, the ν_μ background events are being broken down into reaction types. The muon and pion kinematic distributions are plotted with the ν_μ background events reactions illustrated. Figure 6.11 and 6.12 show the distributions for the signal and sideband regions respectively. Table 6.5 and 6.6 show the breakdown of the ν_μ background events reactions for SIG and SB1 respectively.

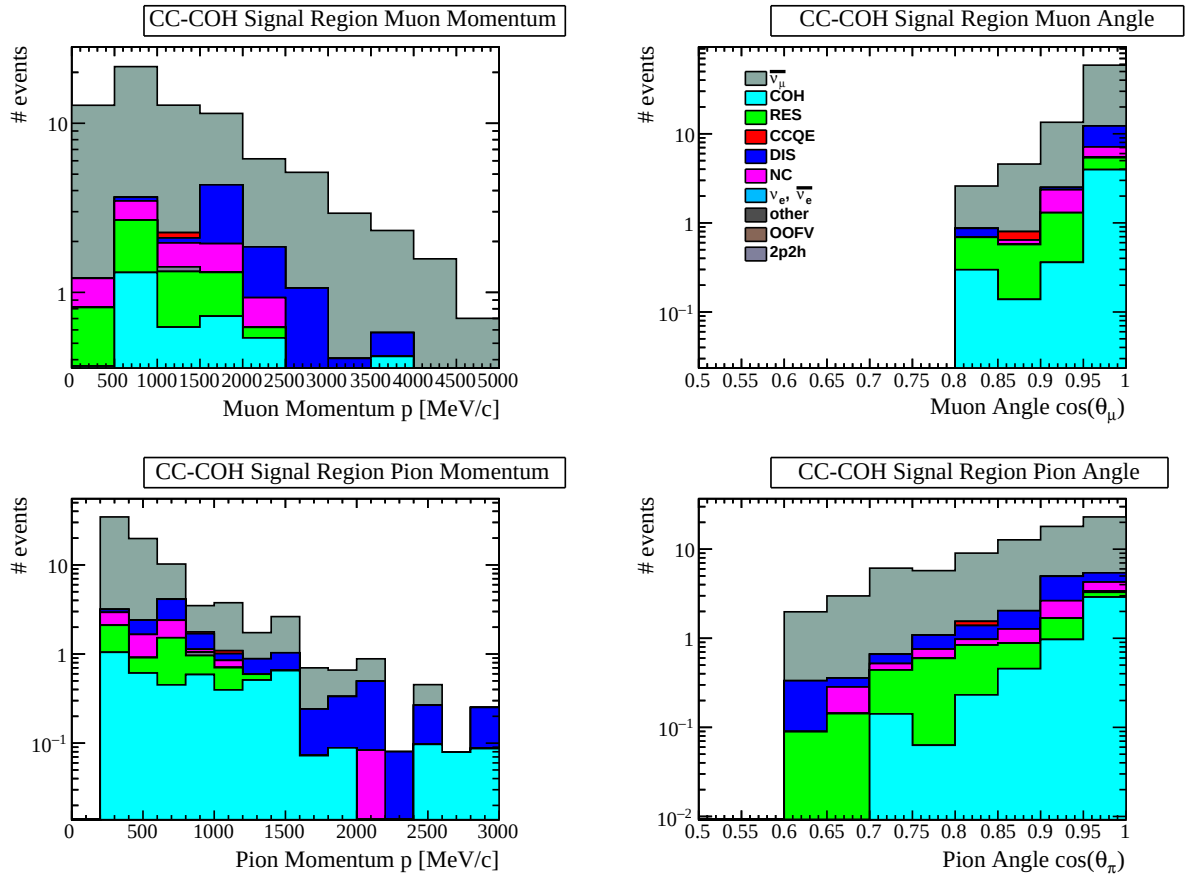

Figure 6.11. The muon and pion kinematic distributions of the $\bar{\nu}_\mu$ CC-COH selection SIG. The reactions of the ν_μ background events are being illustrated. ν_μ COH, RES, and DIS are the main contributors.

The ν_μ backgrounds mainly consist of RES and DIS events; in SIG, some ν_μ COH events are present. For future iterations of the analysis, a joint ν_μ and $\bar{\nu}_\mu$ analysis can help estimate the number of ν_μ interactions in the $\bar{\nu}_\mu$ selection.

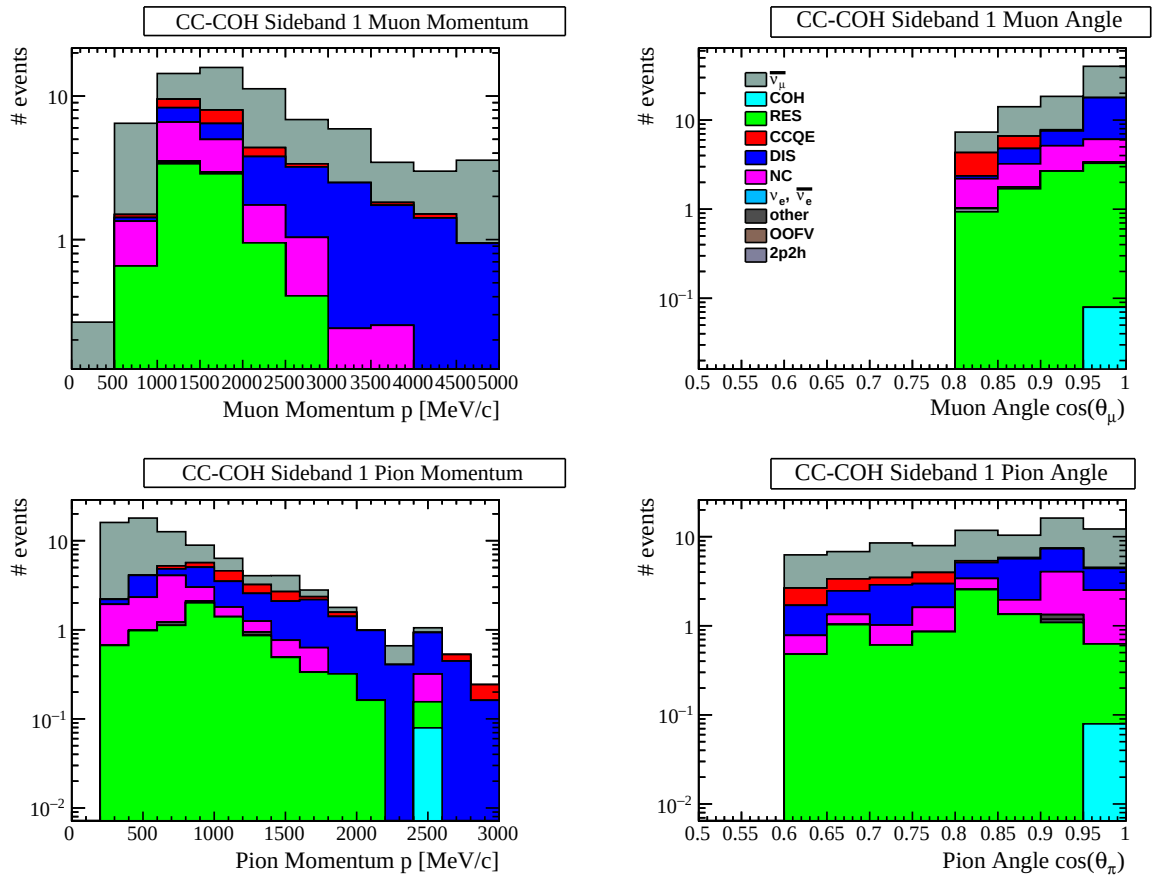

Figure 6.12. The muon and pion kinematic distributions of the $\bar{\nu_\mu}$ CC-COH selection SB1. The reactions of the ν_μ background events are being illustrated. ν_μ RES and DIS are the main contributors.

Reaction	**# Event**	**Composition (%)**
$\bar{\nu_\mu}$	63	79.4
ν_μ COH	5	6.0
ν_μ RES	3	4.0
ν_μ DIS	5	6.8
Other	3	3.8

TABLE 6.5. The reaction composition of the ν_μ background events in the $\bar{\nu_\mu}$ CC-COH selection SIG. The "Other" category mainly consists of NC events.

Reaction	# Event	Composition (%)
$\bar{\nu_\mu}$ Background	44	54.4
ν_μ COH	0	0.1
ν_μ RES	8	10.6
ν_μ DIS	16	19.8
Other	12	15.1

TABLE 6.6. The reaction composition of the ν_μ background events in the $\bar{\nu}_\mu$ CC-COH selection SB1. The "Other" category mainly consists of NC events and ν_μ CCQE events.

6.7 Likelihood Fitter Input Binning for the $\bar{\nu}_\mu$ CC-COH Selection

Table 6.7 summarizes the inputs (two samples) to the likelihood fitter for both the Monte Carlo (MC) simulation and the data. Due to the statistical limitation of this analysis, each sample only contains one bin in the $|t|$ space. The number of events (for the Monte Carlo simulation) in each sample is normalized to data POT. The sources of uncertainties are discussed in chapter 7.

Sample	# bins	# events (MC)	# events (data)
SIG	1	80	74
SB1	1	79	53

TABLE 6.7. The $\bar{\nu}_\mu$ CC-COH selection input to the likelihood fitter contains two samples: SIG and SB1. Each sample contains one bin in the $|t|$ space. The number of events (for the Monte Carlo simulation) in each sample is normalized to data POT.

Chapter 7

Systematic Uncertainties

The sources of systematic uncertainties considered for the analysis are described in this chapter. The systematic uncertainties are categorized into three groups. The systematic uncertainties related to the neutrino flux are covered in section 7.1. The sources of uncertainties related to the modelling of the neutrino interactions and the final state interactions (FSI) are shown in section 7.2. The ND280 detector related systematic uncertainties are discussed in section 7.3.

7.1 Flux Systematics

The T2K beam group provides the neutrino flux predictions[1] (section 3.1) used by this analysis. A reminder that the term FHC (forward horn current) refers to the neutrino mode for the beam, and RHC (reverse horn current) refers to the antineutrino mode. Figure 7.1 shows the neutrino (antineutrino) flux of the two modes, and it can clearly be seen that ν_μ is dominant in the neutrino mode flux, and $\bar{\nu}_\mu$ is dominant in the antineutrino mode flux.

The flux systematic uncertainties as function of neutrino energy for the neutrino mode ν_μ flux and antineutrino mode $\bar{\nu}_\mu$ flux at ND280 are shown in figure 7.2. The dominant contributions to the flux uncertainties are the modelling of hadron interactions inside the target and measurements of the proton beam profile at the production target and the neutrino beam off-axis angle (described in section 3.1.3).

T2K uses data from a dedicated hadron production experiment (NA61/SHINE) to constrain the hadron interactions. In this version of the flux prediction, the NA61 data used was collected using a replica T2K target. The advantage of doing so is to constrain the interactions of the hadrons (produced from the proton beam) with the target material before

[1] The flux prediction version 13a is described in TN217 [47]. The specific version used for the analyses in this thesis is 13av6.

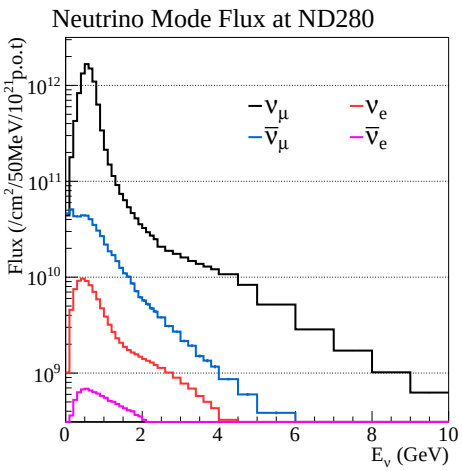

(a) Neutrino Flux at ND280

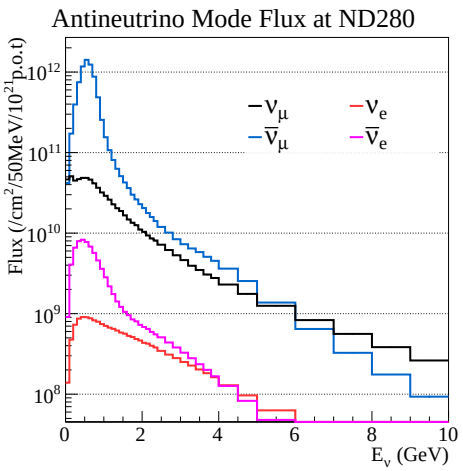

(b) Antineutrino Flux at ND280

Figure 7.1. The neutrino flux (left) and antineutrino flux (right) at ND280 broken down into ν_μ, $\bar{\nu}_\mu$, ν_e, and $\bar{\nu}_e$ and plotted as functions of neutrino energy. ν_μ is dominant in the neutrino mode flux, and $\bar{\nu}_\mu$ is dominant in the antineutrino mode flux. The figures are taken from [47].

they exit the target (this is sometimes referred to as reinteraction, or secondary interactions). In previous flux predictions, NA61 data using a thin graphite target (2 cm) configuration is used. Therefore the "reinteractions" of the hadrons are not well constrained.

As mentioned in section 3.1.2, the optical transition radiation monitor (OTR) measures the proton beam profile just before the target. The OTR measurements (along with the measurements from other upstream beam profile monitors) are used to constrain the proton beam profile measurement uncertainty.

7.1.1 Flux Systematics Covariance Matrix

The flux uncertainty input to this analysis is in the format of the flux covariance matrix. The covariance matrices for the ν_μ CC-COH analysis and the the ν_μ CC-COH analysis are shown in figure 7.3a. Both matrices are 20×20 in dimension, and they are binned in the energy of the ν_μ as shown in table 7.1. Most of the neutrino have energy less than 1 GeV (shown in fig 7.1); hence the matrices are more finely binned in the low energy region.

The flux covariance matrix[2],

$$V_{ij} = \frac{\sigma_i \sigma_j \rho_{ij}}{\Phi_i \Phi_j}, \tag{7.1}$$

is calculated from both the flux uncertainties (σ_i), the correlations between the bins (ρ_{ij}), and then normalized by the content of the bins (Φ_i). The indices i and j corresponds to the

[2]The covariance matrix used by the analysis is the fractional covariance matrix.

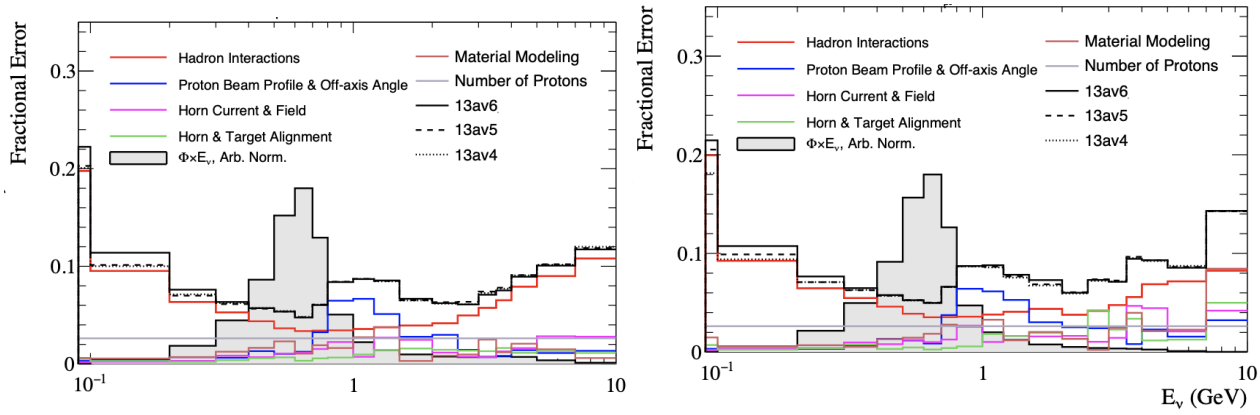

(a) Neutrino mode ν_μ flux

(b) Antineutrino mode $\bar{\nu}_\mu$ flux

Figure 7.2. The neutrino mode ν_μ flux (left) and antineutrino mode $\bar{\nu}_\mu$ flux (right) systematic uncertainties at ND280 as function of neutrino energy. The dominant contributions to the flux uncertainties are the modelling of hadron interactions and the proton beam profile (such as beam direction, width and intensity). The version of the flux prediction used is 13av6. The figures are taken from [47].

Bin #	**Bin Edge E_ν (GeV)**	**Bin #**	**Bin Edge E_ν (GeV)**
1	0.1	11	1.5
2	0.2	12	2.0
3	0.3	13	2.5
4	0.4	14	3.0
5	0.5	15	3.5
6	0.6	16	4.0
7	0.7	17	5.0
8	0.8	18	7.0
9	1.0	19	10.0
10	1.2	20	30.0

TABLE 7.1. The 20×20 flux covariance matrix is binned in neutrino energy. The T2K neutrino energy can be as high as 30 GeV. The matrix is more finely binned at lower energy (below 1 GeV) where the majority of the neutrino flux resides.

rows and columns of the matrix elements.

The matrix element values (figure 7.3) are larger for the lower energy bins (bin 1-3) and the higher energy bins (bin 17-20). This feature of the matrix agrees with the 1-dimensional plot shown in figure 7.2.

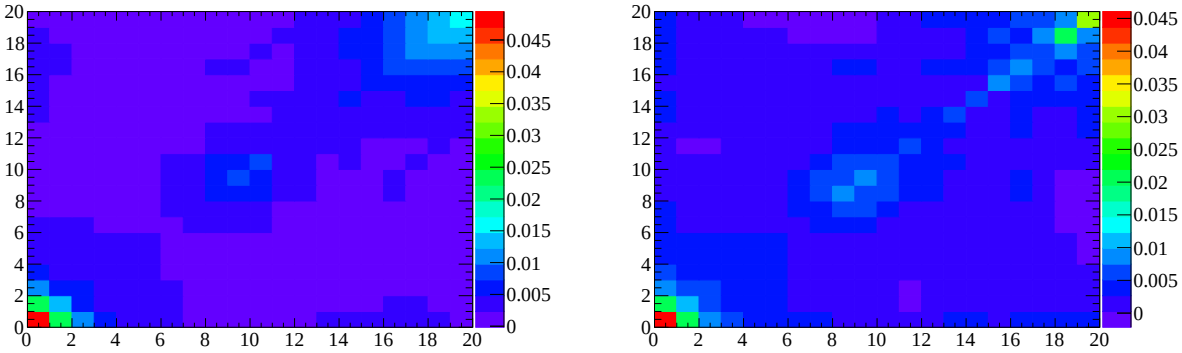

(a) ν_μ (b) $\bar{\nu}_\mu$

Figure 7.3. Covariance matrix (20×20) for the FHC ν_μ flux (left) and the RHC $\bar{\nu}_\mu$ flux (right). The binning, shown in table 7.1, is in neutrino energy and there are 20 bins in total. The diagonal bins are related to the fractional flux uncertainties. The off-diagonal bins are related to the correlation between the bins.

7.2 Cross-section modelling and FSI Systematics

Our understanding and modelling of the various neutrino interactions and final-state interactions (FSI) are imperfect. In the neutrino interaction generators used (NEUT for T2K) to generate the MC, physics parameters (such as axial mass) are implemented within the various physics models. The values reflect the current best understanding of the models. The uncertainties of these values indicate the limitation of our understanding of these neutrino interactions and FSI processes. These physics parameters ultimately affect the cross sections of the signal and background events for this analysis.

To propagate the physics parameter uncertainties, instead of generating many new MC samples with the parameter values set to different values, the uncertainties are parameterized into systematic parameters (referred to as "dials" in T2K). Table 7.2 shows the relevant cross-section and final state interaction systematic uncertainties (dials) for this analysis. The T2K Neutrino Interaction Working Group (NIWG) has developed the dials, and the prior (values of the systematic parameters set in the Monte Carlo simulation) and error values are taken from the recent T2K neutrino oscillation analysis (OA) [69]. From the list of dials

recommended by NIWG, the relevant ones to this analysis are selected. The chosen dials are described in this section, and they are grouped into resonant pion production (RES) background dials(section 7.2.1), deep-inelastic-scattering (DIS) background dials (section 7.2.2), and the final state interaction (FSI) dials (section 7.2.3).

Index	Parameter	Type	Prior	Error (%)
1	M_A^{RES}	RES Background	1.07	15
2	C_A^5	RES Background	0.96	15
3	I = 1/2 Bkg RES	RES Background	0.96	40
4	CC DIS BY	DIS Background	1.0	100
5	CC Multi-π BY	DIS Background	1.0	100
6	AGKY Multi-π	DIS Background	1.0	100
7	FSI Inelastic, LE	FSI Background	1.0	41
8	FSI π Absorption	FSI Background	1.1	41
9	FSI Charge Exchange, LE	FSI Background	1.0	57
10	FSI Inelastic, HE	FSI Background	1.8	34
11	FSI π Production	FSI Background	1.0	50
12	FSI Charge Exchange, HE	FSI Background	1.8	28

TABLE 7.2. The cross-section modelling and FSI dials that are available for systematics evaluation. The values of the systematic parameters set in the Monte Carlo simulation are call the "prior". The errors of the prior are also shown. The dials are grouped into resonant pion production (RES) background dials(section 7.2.1), deep-inelastic-scattering (DIS) background dials (section 7.2.2), and the final state interaction (FSI) dials (section 7.2.3).

This error propagation method is used because it typically takes on the scale of months to produce one ND280 MC. Therefore, it becomes impractical to generate many different MC to evaluate the uncertainties for this analysis. So instead, splines (also called response functions) are generated to characterize the changes to the signal and background event cross sections due to the adjusted dial values.

The splines are generated per topology, per reaction, and per reconstructed bin for the selections. Seven dial steps are assigned for each dial - the nominal value, three above the nominal value (prior value in table 7.2) and three below the nominal value, according to the dial's error. All the splines have been validated, and the details are documented in appendix G.

7.2.1 Resonant Pion Production Background Dials

The modelling of the resonant pion production (RES) background events can be adjusted by varying three dials. M_A^{RES} is the axial mass, which is a phenomenological parameter. We have encountered the axial mass for COH earlier in section 2.3.1. C_A^5 is an axial form factor

in the Graczyk-Sobczyk parameterization [70]. The non-resonant backgrounds[3] where the isospin I = 1/2 can also be scaled with a dedicated dial.

7.2.2 Deep Inelastic Scattering Background Dials

The modelling of the deep inelastic scattering (DIS) background events can be adjusted by varying three dials. As explained in section 5.6.2, the DIS classification corresponds to two reaction modes in NEUT: the deep-inelastic-scattering process and the multi-pion production process. The three dials are on-off "switch" dials, two of which turn the Bodek-Yang (BY) correction [71] on or off for the two DIS modes. An additional dial can enable or disable the Andreopoulous-Gallagher-Kehayias-Yang (AGKY) model [72] for the multi-pion production process.

7.2.3 Pion Final State Interaction Dials

The pion final-state interactions (FSI) refer to the interactions of the neutrino-interaction-produced pions while they propagate through the same nucleus where the neutrino interactions occur. As shown in figure 7.4, a pion, after its creation, can be scattered inelastically (INE), be absorbed by the nucleus (ABS), charge exchange to a neutrally charged pion (CEX), or interact with the nucleons to produce additional pions. These four processes can be adjusted in NEUT with six dials; the low energy (LE) events and the high energy (HE) events are adjusted by separate dials for the charge exchange and the inelastic scattering processes.

[3] RES is the dominant single pion production process (figure 1.8 in section 1.4). The pion is a decay product of an excited nucleon that interacts with a neutrino. However, it is also possible to produce a pion at the interaction vertex, which is called the "non-resonant" interaction.

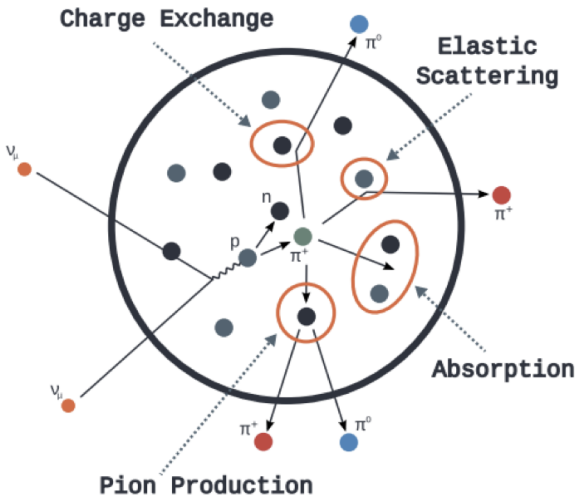

Figure 7.4. The pion final-state interactions (FSI) considered for this analysis. A pion, created from a neutrino-nucleus interaction, can be scattered inelastically (INE), be absorbed by the nucleus (ABS), charge exchange to a neutrally charged pion (CEX), or interact with the nucleons to produce additional pions. The figure is taken from [73].

7.3 ND280 Detector Systematics

In this section, it is described how the ND280 detector-related systematic uncertainties are evaluated and propagated. The detector systematics treatment used by this analysis involves two assumptions. First, the probability density functions (PDF) for all the detector systematics are assumed to be Gaussian except for the TPC magnetic field distortion uncertainty, which follows a uniformly distributed PDF. Secondly, the detector systematics are all assumed to be uncorrelated with each other. For example, the uncertainty on the magnetic field affects both the TPC momentum reconstruction and particle identification, but the uncertainties of the two variables are assumed to be not correlated. Therefore, this approximation is not entirely accurate and should be one of the main focuses for improving future analyses.

7.3.1 Systematics Propagation Models

The detector systematic uncertainties can be categorized into three groups (from the variation of the observables, the effect of efficiency differences in the Monte Carlo simulation and data, and effects of normalization) based on how they are propagated. The methods of propagation are summarized in the following paragraphs, which follow the detailed descriptions from TN-212 [66].

Observable-variation Systematics: These systematics are propagated by varying the values of the observable variables, such as the magnetic field. For an observable x, the altered value, x', after the systematic variation is:

$$x' = x + \Delta x + \alpha \cdot \delta\Delta x. \tag{7.2}$$

α is a random variable (from 0 to 1) following the PDF distribution, Δx is the difference between the mean values between the data and the Monte Carlo simulation, and $\delta\Delta x$ is the statistical uncertainty of the systematic variation. When there is a difference in mean values between the data and the Monte Carlo simulation, the observables are smeared according to the differences before rerunning the event selection on the new observables within the bounds.

Efficiency Systematics: These systematics are evaluated with efficiencies computed using the data and the Monte Carlo (MC) simulation difference for well-known control samples (CS). For example, the efficiency for the TPCs to reconstruct tracks can be studied with a cosmic muon control sample as these muons usually travel straight through the TPCs and are unrelated to any particle tracks from neutrino beam interactions.

Data and Monte Carlo simulation efficiency ratios are assumed to be the same for the control samples and the samples selected by the analysis. Therefore, the predicted efficiency in data is:

$$\epsilon_{\text{data}} = \frac{\epsilon^{\text{CS}}_{\text{data}}}{\epsilon^{\text{CS}}_{\text{MC}}} \cdot \epsilon_{\text{MC}}, \tag{7.3}$$

where $\epsilon^{\text{CS}}_{\text{data}}$ and $\epsilon^{\text{CS}}_{\text{MC}}$ are the efficiencies obtained from the studies with the control samples. ϵ_{MC} is the Monte Carlo simulation sample's efficiency, calculated using the true information from the Monte Carlo simulation. To include the statistical limitation of the control sample used, the predicted efficiency in data becomes:

$$\epsilon'_{\text{data}} = (r^{\text{CS}} + \alpha \cdot \delta r^{\text{CS}})\epsilon_{\text{MC}}, \tag{7.4}$$

where α is a random variable following the PDF distribution, $r^{\text{CS}} = \epsilon^{\text{CS}}_{\text{data}}$ / $\epsilon^{\text{CS}}_{\text{MC}}$ and δr^{CS} is the statistical uncertainty of r^{CS} from the control sample.

The events in the selected samples are weighted according to the efficiencies. The weight applied to an event is dependent on whether the reconstruction is successful or not. For successful event reconstruction, the weight applied to an event is

$$w_{eff} = \frac{\epsilon'_{\text{data}}}{\epsilon_{\text{MC}}}. \tag{7.5}$$

Normalization Systematics: These are the systematic errors associated with the normalization of the observed total event rate. An example would be the uncertainty associated with the mass of the FGD, as any variation in the number of target nuclei affects the number of neutrino interactions. The normalization weight is

$$w_{\text{norm}} = 1 + \alpha \cdot \delta w, \tag{7.6}$$

where α is a random variable following the PDF distribution, and δw is the one-sigma systematic variation for the normalization.

7.3.2 ND280 Detector Systematics

TPC Field Distortion: A magnet surrounds the ND280 detector components. The B Field distortion systematic uncertainty need to be considered since the curvature of the particle trajectories is used to reconstruct momentum in the TPCs. A laser system is used to shine on the TPC cathode, and by comparing the expected and measured drift of the photoelectrons, the difference is used to compute the systematic uncertainty [74].

TPC Momentum Scale: As mentioned in the previous paragraph, the reconstructed momentums of particles depend on the B Field. The difference between the B Field used in the Monte Carlo simulation and the calibration measurement is used to scale the calculated momentum and set the systematic error on the scale [75].

TPC Momentum Resolution: The TPC momentum resolution systematic uncertainty is computed using tracks that cross at least two TPCs to compare the momentums. A 10% fractional difference in the momentum resolution is used for the systematic propagation [76].

TPC Particle Identification: It is crucial to identify particles for all the analyses and one of the main tasks of the TPCs is to perform charged particle identification (PID). Charged particles lose energy in gas-filled TPCs through ionization, and the TPCs measure this to identify the particles. Dedicated control samples are used to evaluate the TPC-PID systematic uncertainty [77].

TPC Cluster Efficiency: When a charged particle passes through the gas in a TPC, the ionized gas creates a group of signals (cluster) along the particle path. The probability of finding such a group of adjacent signals is used to compute the TPC cluster efficiency.

The difference between the data and the Monte Carlo simulation efficiency is evaluated and propagated in the systematic uncertainty computation [78].

TPC Tracking Efficiency: The TPC tracking efficiency is related to the probability of how often the TPCs successfully reconstruct the tracks of the particles that cross the TPC detectors. Control samples of muons from the neutrino beam and cosmic events are used to evaluate the track reconstruction efficiencies of the TPCs. These efficiencies are used to evaluate the tracking efficiency systematics [79].

TPC Charge Identification Efficiency: The charge of a particle is computed using combined information from ND280 subdetectors (global charge identification). However, for each TPC, it is possible that the charge determined is different from the global charge. The difference between the data and the Monte Carlo simulation is flat across all the momentum phase space and this systematic uncertainty is propagated as an efficiency systematic uncertainty [80].

FGD Particle Identification: When a particle loses all its energy through ionization inside an FGD, it will stop in the FGD. It is possible to measure the energy deposition and compute the particle mass as different massive particles will deposit different energies. Only two types of scenarios are considered: muons and protons. Proton and muon control samples are used to evaluate the systematics associated with FGD PID [81].

FGD Hybrid Tracking Efficiency: When a particle is created in an FGD and stops in the same FGD, it is called an FGD contained track. This situation often happens with the pions and protons produced from the neutrino interactions and it is essential to reconstruct these tracks to avoid misidentifying neutrino interaction topologies. The FGD hybrid tracking efficiency describes how often FGD contained tracks are successfully reconstructed. The method developed to evaluate the systematic uncertainty is first to store the neutrino interaction vertex locations in the FGDs. Subsequently, pion and proton particle gun Monte Carlo simulations are generated at those vertices. The word "hybrid" implies the combination of the original neutrino interaction vertex and the addition of a pion or proton through a particle gun Monte Carlo simulation at the event reconstruction level. The systematics is calculated using the ratio of the particle gun events generated to the events successfully reconstructed [81].

Michel Electron Efficiency: The charged-current resonant pion production (e.g., $\nu_\mu + \mathrm{p} \rightarrow \mu^- + \pi^+ + \mathrm{p}$) produces a pion that might stop and decay inside the FGDs. When

a pion decays, a secondary muon is produced, and it will also stop and decay quickly into an electron called a Michel electron. Tagging the Michel electrons gives an extra handle at selecting the charged-current resonant pion production and distinguishing it from charged-current quasi-elastic interactions ($\nu_\mu + \mathrm{n} \rightarrow \mu^- + \mathrm{p}$). The systematic uncertainty is related to the efficiency and purity of the Michel electron selection. Cosmic muons that stop inside the FGD detectors are selected as control samples to determine the selection efficiency. The Monte Carlo simulation of neutrino interactions outside the FGDs is used to estimate the purity of the selection [82].

Out-Of-Fiducial-Volume Background: The Out-Of-Fiducial-Volume interactions happen outside the FGD fiducial volume but are reconstructed to have interaction vertices inside the FGD volume. The difference in the rate of OOFV between different event generators is used to set the rate uncertainty [83].

Pile-up: When neutrinos interact with earth materials before reaching the ND280, the muons (sand muons) produced can still enter ND280 and cause event pile-up when neutrinos from the same beam spill[4] also interact within ND280. A dedicated sand muon Monte Carlo simulation is produced to estimate the sand muons' rate and predict the event pile-up rate [84].

Pion Secondary Interactions: When pions are produced in neutrino interactions, they can interact again with the detector materials, called the secondary pion interactions (pionSI). Currently, the pionSI systematic uncertainty is the largest in many T2K analyses [85]. The event generator for pion interactions has been changed (from GEANT4 to NEUT)[5]. A fit with all the available external pion scattering data was performed to reduce the pion interaction cross-section uncertainties used in computing the pionSI systematic uncertainty [86]. Details regarding the improvements in the pionSI are described in appendix F.

FGD Mass: The areal density of the FGDs used in the Monte Carlo simulation is 0.41% higher than the actual value. Also, the measurements of the various FGD modules show a 0.38% spread in the masses. A combined 0.6% uncertainty is assigned [87].

[4]The T2K neutrino beam is a pulse beam. Each beam spill is separated by 2.47 seconds.

[5]NEUT is developed and maintained by T2K collaborators and therefore give more freedom to adjust the modelling of pion interactions.

7.3.3 Vertex Activity Systematics

Vertex activity (VA), described in 4.4.1, is the sum of energy deposition around the neutrino interaction vertex in a 5x5 FGD1 volume[6]. To evaluate the uncertainties associated with VA, stopping proton and muon control samples are used. In a 5x5 FGD1 volume, the energy deposit by a stopping particle (end activity) should be similar to the energy deposit by a particle produced from the vertex (vertex activity).

Figure 7.5 shows the data and Monte Carlo simulation end activity distributions of the two control samples in a 5x5 FGD1 volume. Both the data and the Monte Carlo simulation distributions are fit to a Gaussian function. The fit results are summarized in table 7.3. From the fit results, two VA-related uncertainties are developed. The Gaussian mean, μ, and the associated uncertainty, $\delta\mu$, are used to compute the VA scale uncertainty. The Gaussian width, σ, and the associated uncertainty, $\delta\sigma$, are used to compute the VA resolution uncertainty. Both uncertainties are propagated as observable-variation systematics.

In addition, from table 7.3, we can see that Gaussian width and the uncertainties are all larger for the stopping proton sample. The resulting VA-related uncertainties are also larger. Therefore, to be conservative, the stopping proton sample is used.

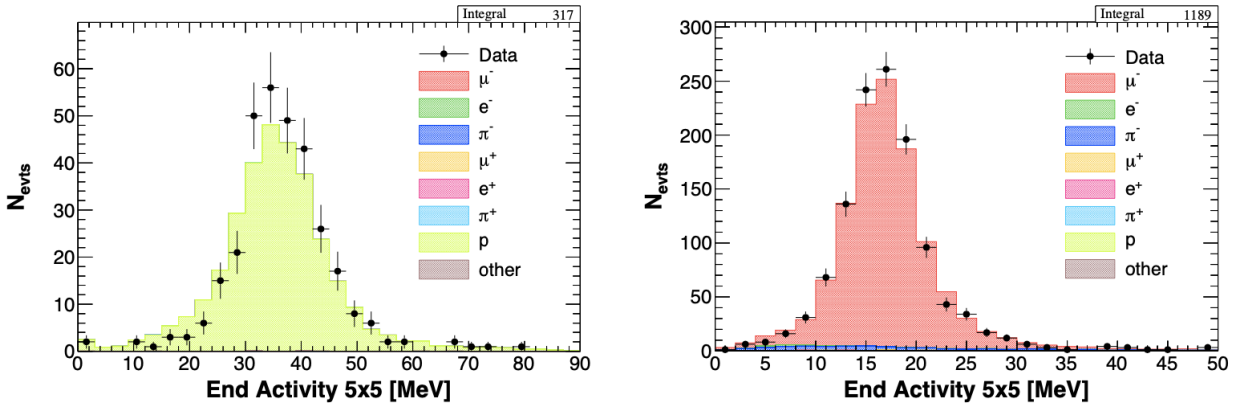

Figure 7.5. "End activity" (energy deposit by a stopping particle) distributions of the stopping proton (left) and muon (right) control samples in a 5x5 FGD1 volume. The purity of each sample can also be seen from the stacked histograms. Both the data and the Monte Carlo simulation distributions are fit to a Gaussian function to evaluate the VA-related systematics. μ is the Gaussian mean, and σ is the Gaussian width. The figures are taken from [88].

[6] As described in section 4.4.1 and shown in figure 4.3, a 5x5 FGD1 volume contains 5 scintillator layers for each side. The volume is approximately $5\,\mathrm{cm}^3$.

Stopping proton	5x5 (MeV)
$\mu_{\mathrm{MC}} \pm \delta\mu\mathrm{MC}$	35.3 ± 0.11
$\mu_{\mathrm{data}} \pm \delta\mu\mathrm{data}$	36.4 ± 0.41
$\sigma_{\mathrm{MC}} \pm \delta\sigma\mathrm{MC}$	8.57 ± 0.12
$\sigma_{\mathrm{data}} \pm \delta\sigma\mathrm{data}$	7.02 ± 0.38

Stopping muon	5x5 (MeV)
$\mu_{\mathrm{MC}} \pm \delta\mu\mathrm{MC}$	16.7 ± 0.04
$\mu_{\mathrm{data}} \pm \delta\mu\mathrm{data}$	16.5 ± 0.11
$\sigma_{\mathrm{MC}} \pm \delta\sigma\mathrm{MC}$	4.00 ± 0.04
$\sigma_{\mathrm{data}} \pm \delta\sigma\mathrm{data}$	3.80 ± 0.12

TABLE 7.3. The Gaussian parameters from the fits of the 5x5 end activity distributions for the stopping proton (left) and muon (right) samples.

7.3.4 Detector Systematics for the ν_μ and the $\bar{\nu}_\mu$ CC-COH Selections

Table 7.4 summarizes the sources of the detector systematics considered for the analyses and the corresponding error propagation models. Table 7.5 and 7.6 show the values of the detector-related systematics for the ν_μ and the $\bar{\nu}_\mu$ CC-COH selection. The dominant sources of uncertainties are TPC PID, pionSI, and the vertex activity related uncertainties.

The ν_μ and the $\bar{\nu}_\mu$ CC-COH selections share many similarities. Some of the detector systematics, especially the leading order systematics(i.e., TPC particle identification, pion secondary interaction and vertex-activity-related), are similar in size for both selections. For example, systematics such as TPC tracking and FGD mass are consistent in all samples of the two selections. However, some second-order uncertainties can be quite different between the two selections. One possible explanation is that the number of events affected by a source of uncertainty can be much smaller in one selection than the other. Therefore, the size of the uncertainty is affected largely by the statistical fluctuation.

Systematics Sources	Propagation Model
TPC Related	
Field Distortions	Observable Variation
TPC Momentum Scale	Observable Variation
TPC Momentum Resolution	Observable Variation
TPC PID	Observable Variation
TPC Cluster	Efficiency
TPC Tracking	Efficiency
TPC Charge ID	Efficiency
FGD-TPC Related	
TPC-FGD Matching	Efficiency
FGD Related	
FGD PID	Observable Variation
FGD Hybrid Tracking	Efficiency
Michel Electron	Efficiency
Background Related	
OOFV	Normalization
Pile-up	Normalization
MC Modelling Related	
Pion SI	Normalization
Proton SI	Normalization
FGD Mass	Normalization
Vertex Activity Related	
VA Scale	Observable Variation
VA Resolution	Observable Variation

TABLE 7.4. The sources of detector systematics uncertainties and the corresponding propagation models (described in section 7.3.1).

Systematics Sources	Signal Region [%]	Sideband 1 [%]	Sideband 2 [%]
TPC Related			
Field Distortions	0.24	0.17	< 0.01
TPC Momentum Scale	0.95	0.72	< 0.01
TPC Momentum Resolution	0.62	0.40	0.36
TPC PID	1.34	1.36	2.78
TPC Cluster	< 0.01	< 0.01	< 0.01
TPC Tracking	0.81	0.81	0.78
TPC Charge ID	0.08	0.07	0.08
FGD-TPC Related			
TPC-FGD Matching	< 0.01	< 0.01	< 0.01
FGD Related			
FGD PID	< 0.01	< 0.01	< 0.01
FGD Hybrid Tracking	0.08	0.23	0.53
Michel Electron	0.37	0.25	0.22
Background Related			
OOFV	< 0.01	0.04	0.93
Pile-up	0.27	0.23	0.28
MC Modelling Related			
Pion SI	2.43	3.02	8.26
Proton SI	0.01	< 0.01	< 0.01
FGD Mass	0.45	0.45	0.42
Vertex Activity Related			
VA Scale	5.55	7.05	28.17
VA Resolution	2.44	3.65	9.10
Total Detector Systematics			
Total	3.82	4.51	15.73

TABLE 7.5. The sources of detector systematics uncertainties and their values for the ν_μ CC-COH selection.

Systematics Sources	Signal Region [%]	Sideband 1 [%]
TPC Related		
Field Distortions	0.93	< 0.01
TPC Momentum Scale	< 0.01	< 0.01
TPC Momentum Resolution	1.15	1.04
TPC PID	1.02	1.15
TPC Cluster	0.02	< 0.01
TPC Tracking	0.88	1.04
TPC Charge ID	0.08	0.09
FGD-TPC Related		
TPC-FGD Matching	< 0.01	< 0.01
FGD Related		
FGD PID	< 0.01	< 0.01
FGD Hybrid Tracking	0.17	0.17
Michel Electron	0.08	0.13
Background Related		
OOFV	< 0.01	< 0.01
Pile-up	0.09	0.08
MC Modelling Related		
Pion SI	3.54	6.12
Proton SI	< 0.01	1.27
FGD Mass	0.45	0.45
Vertex Activity Related		
VA Scale	5.54	7.77
VA Resolution	1.64	2.37
Total Detector Systematics		
Total	4.33	5.14

TABLE 7.6. The sources of detector systematics uncertainties and their values for the $\bar{\nu}_\mu$ CC-COH selection.

Chapter 8

The Likelihood Fitter Framework Validations

The robustness of the likelihood fitter framework (introduced in sec 4.5) and potential biases to the analysis must be tested before using data to extract cross-section measurements. The statistical tests performed on the fitter are reviewed in this chapter. The following two chapters contain various fitter studies for the ν_μ CC-COH analysis (chapter 9) and the $\bar{\nu_\mu}$ CC-COH analysis (chapter 10).

8.1 Goodness of Fit

Before going into the details of the various tests done to validate the fitter, the "goodness-of-fit" metrics as defined by the χ^2 are shown. Two χ^2 metrics are defined to check the performance of a fit.

1. The χ^2 for the reconstructed (reco) event distribution is:

$$\chi^2_{\text{reco}} = \sum_i 2(N_i^{\text{fit}} - N_i^{\text{data}} + N_i^{\text{data}} \ln \frac{N_i^{\text{data}}}{N_i^{\text{fit}}}), \tag{8.1}$$

   where the range of the summation is the number of reconstructed bins. The range is 3 for the ν_μ CC-COH selection (section 5.7) and 2 for the $\bar{\nu_\mu}$ CC-COH selection (section 6.7). N^{fit} is the extracted number of events from the fit result, and N^{data} is the number of events in the data. A reminder that this χ^2_{reco} is purely statistical and only provides an idea of the goodness of fit for the reconstructed bins.

2. The χ^2 for the cross-section distribution is:

$$\chi^2_\sigma = (\sigma^{\text{fit}} - \sigma^{\text{true}}) V^{-1}_{\text{fit}} (\sigma^{\text{fit}} - \sigma^{\text{true}}), \tag{8.2}$$

where σ^{fit} is the cross section calculated from the fit result, σ^{true} is the cross section calculated from the Monte Carlo (MC) simulation true information, and V^{-1}_{fit} is the covariance matrix calculated from the fit result. This χ^2_σ provides insight to the compatibility of the fit result to the nominal Monte Carlo simulation.

8.2 χ^2 Distributions

Given the statistical uncertainty of the nominal Monte Carlo simulation and the sources of the systematic uncertainties (described in chapter 7), five hundred statistically and systematically fluctuated Monte Carlo simulation inputs (toy throws) around the nominal Monte Carlo simulation are generated for both the ν_μ and $\bar{\nu_\mu}$ analysis. The χ^2 for the reconstructed bins and the extracted cross-sections are computed for each toy throw. Table 8.1 shows the χ^2 to be computed and their corresponding degree of freedom (d.o.f.).

Analysis	χ^2	Degrees of Freedom
ν_μ CC-COH	χ^2_{reco}	2
ν_μ CC-COH	χ^2_σ	1
$\bar{\nu_\mu}$ CC-COH	χ^2_{reco}	1
$\bar{\nu_\mu}$ CC-COH.	χ^2_σ	1

TABLE 8.1. A list of the χ^2 computed and the corresponding degrees of freedom.

For the χ^2_{reco}, the degrees of freedom are obtained by:

$$\text{d.o.f.(reco)} = \#\text{ reco bin} - \#\text{ signal parameter.} \tag{8.3}$$

Each reconstructed bin results in 1 degree of freedom in the fitter: there are three reconstructed bins for the ν_μ CC-COH analysis (shown in section 5.7) and two reconstructed bins for the $\bar{\nu_\mu}$ CC-COH analysis (shown in section 6.7). The signal is allowed to vary freely in the fit. Therefore, the signal parameter (referred to as the "template parameter" in this thesis) does not have any prior value set, and 1 degree of freedom must be subtracted. As a result, the effective degrees of freedom are 2 for the ν_μ CC-COH analysis and 1 for the $\bar{\nu_\mu}$ CC-COH analysis.

The χ^2 distributions are compared to the theoretical probability density function (p.d.f.)

of the χ^2 distribution with k degrees of freedom given by equation 8.4.

$$f_k(x) = \frac{1}{2^{k/2}\Gamma(k/2)} x^{k/2-1} e^{-x/2} \tag{8.4}$$

The agreement between the χ^2_{reco} distributions from the toy throws and the probability density function of the χ^2 distributions with corresponding degrees of freedom (1, 2, and 3) for the ν_μ and $\bar{\nu}_\mu$ CC-COH fits is shown in figure 8.1.

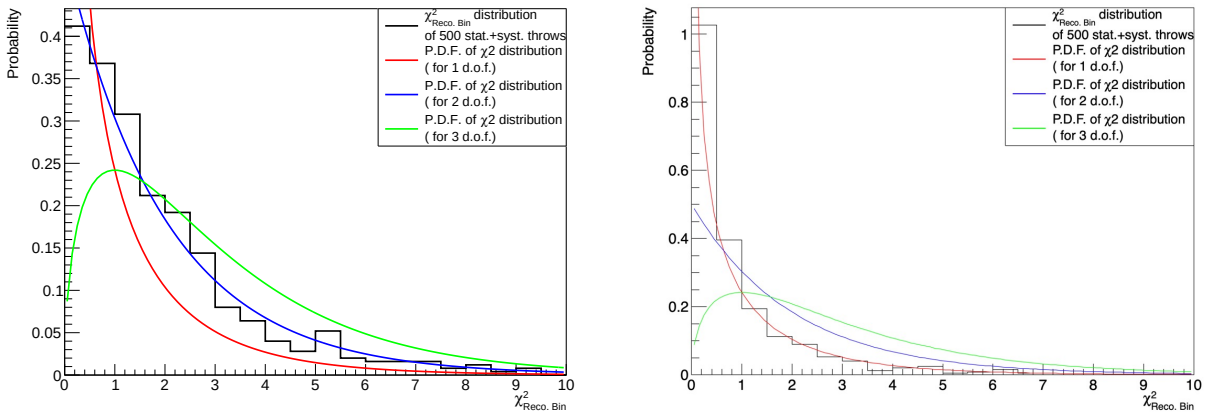

(a) ν_μ (b) $\bar{\nu}_\mu$

Figure 8.1. The ν_μ (left) and $\bar{\nu}_\mu$ (right) CC-COH χ^2_{reco} distribution (black histogram) from five hundred statistically and systematically fluctuated toy throws. The distribution agrees with the probability density function of the χ^2 distribution for 2 degrees of freedom (blue).

For the χ^2_σ, the single-bin cross-section measurements result in 1 degree of freedom for each analysis. The agreement between the χ^2_σ distributions from the toy throws and the probability density function of the χ^2 distributions with corresponding degrees of freedom (1, 2, and 3) for the ν_μ and $\bar{\nu}_\mu$ CC-COH fits is shown in figure 8.2. From figure 8.1 and 8.2, we can conclude that the degrees of freedom listed in table 8.1 for the χ^2_{reco} and the χ^2_σ are correct.

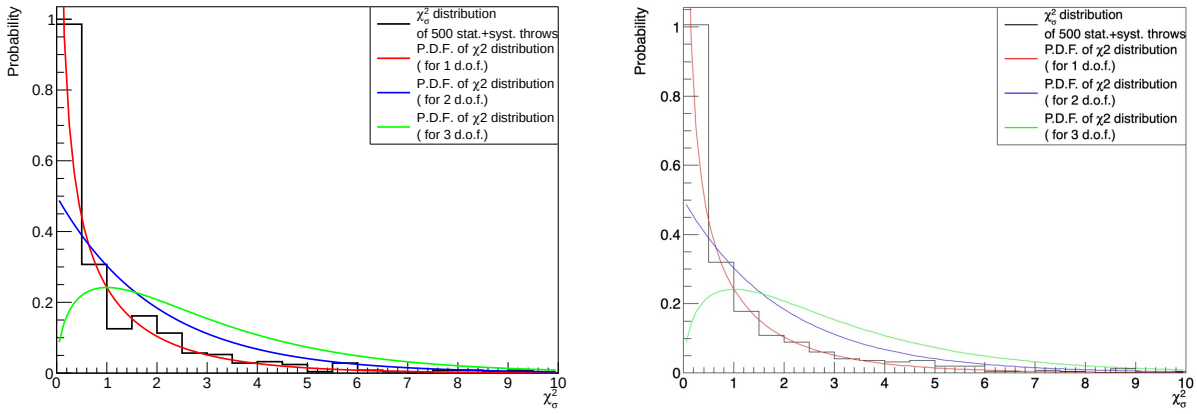

(a) ν_μ (b) $\bar{\nu}_\mu$

Figure 8.2. The ν_μ (left) and $\bar{\nu}_\mu$ (right) CC-COH χ^2_σ distribution (black histogram) from five hundred statistically and systematically fluctuated toy throws. The distribution agrees with the probability density function of the χ^2 distribution for 1 degree of freedom (red).

8.3 The p-value Studies

To further understand the significance of the fit results, p-values are computed. The p-value is the probability of finding a more extreme result than the one observed when the null hypothesis is true. The null hypothesis is that the nominal Monte Carlo simulation is true. For this thesis, the p-value is defined as:

$$\mathrm{p}(\chi^2_i) = \frac{N_i}{N}, \tag{8.5}$$

where N is the total number of toy throws (five hundred statistically and systematically fluctuated Monte Carlo simulations), i is the index for the throws (from 1 to 500), χ^2_i is calculated from the fit result, and N_i is the number of toy throws with χ^2 greater than χ^2_i. A p-value closer to 1 would mean that the fit result is more compatible with the nominal Monte Carlo simulation given the statistical and systematical fluctuation. A p-value smaller than 1 but larger than 0.32 (0.05) means that the null hypothesis (the Monte Carlo simulation is true) is not yet ruled out at the 1 (2)σ level.

8.4 Cross-section Coverage Studies

One assumption used for error propagation when extracting the cross-section measurements is that all the sources of systematic uncertainties are Gaussian distributed. To test the

validity of this assumption, the pull distribution is computed:

$$\text{pull} = (\sigma^{\text{fit}} - \sigma^{\text{true}})/\Delta\sigma^{\text{fit}}. \tag{8.6}$$

In figure 8.3, it is shown that the pull distributions for both ν_μ CC-COH and $\bar{\nu_\mu}$ CC-COH analyses can be fit to a Gaussian distribution with unit width. This means the assumption about the Gaussian distributed systematic uncertainties is valid.

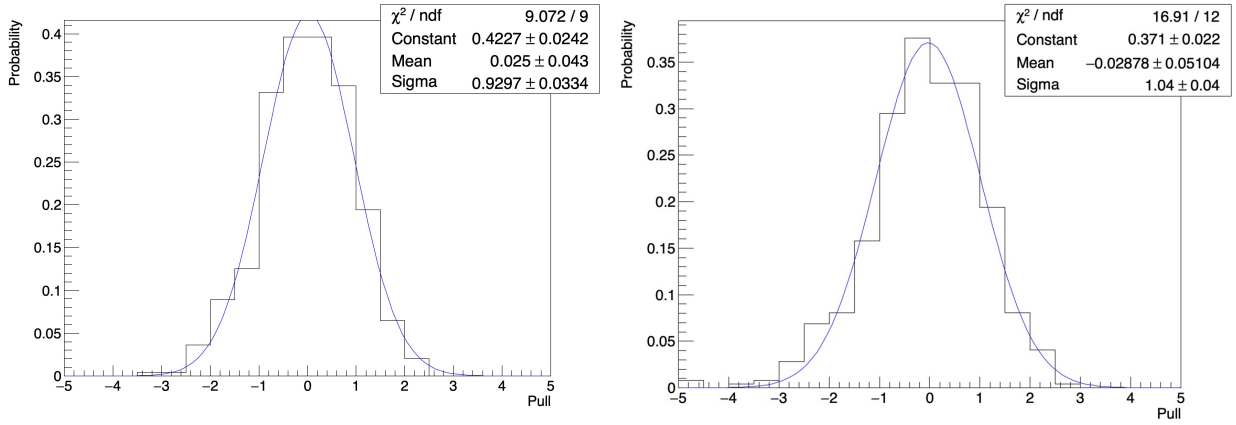

(a) ν_μ

(b) $\bar{\nu}_\mu$

Figure 8.3. The ν_μ (left) and $\bar{\nu}_\mu$ (right) CC-COH pull distribution of the five hundred statistically and systematically fluctuated toy throws. The histogram can be fitted to a Gaussian distribution with unit width, suggesting that the cross-section uncertainties remain Gaussian distributed after the error propagation. This means the assumption about the Gaussian distributed systematic uncertainties is valid.

Chapter 9

The ν_μ CC-COH Analysis Fitter Studies

9.1 Overview of the Fitter Studies

This chapter contains the various fitter studies performed for the ν_μ CC-COH analysis. A series of mock/pseudo data (referred to as "fake data" in T2K terminology) inputs obtained by changes to the nominal Monte Carlo (MC) simulation are produced (and explicitly designed) to test various framework aspects such as neutrino energy dependencies and background event modelling. The inputs are all normalized to data POT for all the fitter studies in this chapter unless specified otherwise. Table 9.4 shows the location of the studies in this chapter, along with the purpose of the studies. In section 9.2, one of the fake data studies is presented to help illustrate how the fitter works, as well as the aspects to be tested and checked for the fitter studies. The results of all the fitter studies are summarized in section 9.5.

Section	Purpose of the Study
9.2	Signal definition tests with modified CC-COH normalization
9.3	Fitter framework machinery tests (using the "Asimov fit")
9.4.1	Fitter tests with alternative MC as "data" inputs
9.4.2	Test of the fitter responses with modifications to the VA variable
9.4.3	Test of the fitter responses with CC-RES background events varied in Q^2
H.1.3	Tests of the fitter responses with modifications to the neutrino flux
H.1.4	Tests with modified normalization of the main background events (CC-RES)
H.1.5	Tests with modified normalization of the main background events (CC-DIS)

TABLE 9.1. A list of the fitter studies performed for the ν_μ CC-COH analysis. The section number of each study and the purpose of the studies are listed.

9.2 Signal Definition Tests

In this section, one of the fake data studies is used as an example to demonstrate how the likelihood fitter works and the aspects that are checked for all the fitter studies. The basic philosophy behind all the fitter studies is to see if the fitter framework can successfully recover the changes made in each fake data set, thus recovering the Monte Carlo simulation truth cross section in each study. The fitter can achieve this by varying the "fit parameters" described in table 9.2. The signal parameter (also called the template parameter for this thesis) describes the normalization of the CC-COH signal events. The 20 flux parameters are described in section 7.1. The 12 cross-section and final state interaction parameters are described in section 7.2. The detector systematics of the three samples (SIG, SB1, and SB2) are represented by three detector parameters, and they are described in section 7.3.

The studies in this section test the signal definition and the template parameter response in the fitter. Fake data sets are generated with the true signal events (ν_μ CC-COH) in the nominal Monte Carlo simulation are enhanced by 20% (equation 9.1) (test 1) and decreased by 20% (equation 9.2) (test 2).

$$\text{weight(reaction)} = \begin{cases} 1.2, & \text{reaction} = \nu_\mu \text{ CC-COH} \\ 1, & \text{Everything Else} \end{cases} \tag{9.1}$$

$$\text{weight(reaction)} = \begin{cases} 0.8, & \text{reaction} = \nu_\mu \text{ CC-COH} \\ 1, & \text{Everything Else} \end{cases} \tag{9.2}$$

The following three aspects are checked and discussed for each of the studies described in this chapter (and chapter 10 for the studies for the $\bar{\nu_\mu}$ CC-COH analysis).

The parameter values after the fit: The "pre-fit" parameter values refer to the fit parameter values obtained from the nominal Monte Carlo simulation. The fitter adjusts the fit parameter values to match the Monte Carlo simulation to the data. The adjusted parameter values after the fit are called the "post-fit" parameter values. The difference between the pre-fit and post-fit parameter values should reflect the modifications made to the nominal Monte Carlo simulation when the fake data is constructed.

For both test 1 and test 2, since only the signal events are reweighted, it is expected that the fitter would adjust only the template parameter (bin 0). Figure 9.1 shows the pre-fit and post-fit parameter values. The post-fit template parameter (bin 0) matches exactly with the weights applied to the signal events, which is 1.2 for test 1 and 0.8 for test 2. All the other parameter values remain unchanged as expected. The pre-fit and post-fit uncertainties for the parameters are also included in the figure. The template (signal) parameter (bin 0)

Bin	Type	Parameter	Details
0	Template Parameter	Parameter for the Signal Events	CC-COH Normalization
1	Flux Parameters	Flux Cov. Matrix Bin 1	$0.0 < E_\nu \leq 0.1$ GeV
2		Flux Cov. Matrix Bin 2	$0.1 < E_\nu \leq 0.2$ GeV
3		Flux Cov. Matrix Bin 3	$0.2 < E_\nu \leq 0.3$ GeV
4		Flux Cov. Matrix Bin 4	$0.3 < E_\nu \leq 0.4$ GeV
5		Flux Cov. Matrix Bin 5	$0.4 < E_\nu \leq 0.5$ GeV
6		Flux Cov. Matrix Bin 6	$0.5 < E_\nu \leq 0.6$ GeV
7		Flux Cov. Matrix Bin 7	$0.6 < E_\nu \leq 0.7$ GeV
8		Flux Cov. Matrix Bin 8	$0.7 < E_\nu \leq 0.8$ GeV
9		Flux Cov. Matrix Bin 9	$0.8 < E_\nu \leq 1.0$ GeV
10		Flux Cov. Matrix Bin 10	$1.0 < E_\nu \leq 1.2$ GeV
11		Flux Cov. Matrix Bin 11	$1.2 < E_\nu \leq 1.5$ GeV
12		Flux Cov. Matrix Bin 12	$1.5 < E_\nu \leq 2.0$ GeV
13		Flux Cov. Matrix Bin 13	$2.0 < E_\nu \leq 2.5$ GeV
14		Flux Cov. Matrix Bin 14	$2.5 < E_\nu \leq 3.0$ GeV
15		Flux Cov. Matrix Bin 15	$3.0 < E_\nu \leq 3.5$ GeV
16		Flux Cov. Matrix Bin 16	$3.5 < E_\nu \leq 4.0$ GeV
17		Flux Cov. Matrix Bin 17	$4.0 < E_\nu \leq 5.0$ GeV
18		Flux Cov. Matrix Bin 18	$5.0 < E_\nu \leq 7.0$ GeV
19		Flux Cov. Matrix Bin 19	$7.0 < E_\nu \leq 10.0$ GeV
20		Flux Cov. Matrix Bin 20	$10.0 < E_\nu \leq 30.0$ GeV
21	XSEC/FSI Parameters	M_A^{RES}	CC-RES Background Shape
22		C_A^5	CC-RES Background Shape
23		I = 1/2 Bkg RES	CC-RES Background Normalization
24		CC DIS BY	CC-DIS Background Shape
25		CC Multi-π BY	CC-DIS Background Shape
26		AGKY Multi-π	CC-DIS Background Shape
27		FSI Inelastic, LE	Background Shape
28		FSI π Absorption	Background Shape
29		FSI Charge Exchange, LE	Background Shape
30		FSI Inelastic, HE	Background Shape
31		FSI π Production	Background Shape
32		FSI Charge Exchange, HE	Background Shape
33	Detector Parameters	SIG	SIG Det. Syst. Parameter
34		SB1	SB1 Det. Syst. Parameter
35		SB2	SB2 Det. Syst. Parameter

TABLE 9.2. A list of all the fit parameters used by the likelihood fitter. Bin 0 is the template (signal) parameter. Bin 1-20 are the flux parameters (section 7.1). Bin 21-32 are the XSEC/FSI parameters (section 7.2). Bin 33-35 are the detector parameters (section 7.3).

does not have any prior uncertainty since the number of CC-COH events is what we are trying to measure (thus, no constraint is set on the uncertainty for the parameter). The post-fit uncertainties for some of the parameters (especially bin 24-26, the DIS parameters) are reduced compared to the pre-fit uncertainties. This happens when the samples constrain the parameters - the statistics is low for this analysis; therefore, no significant[1] uncertainty reductions are observed.

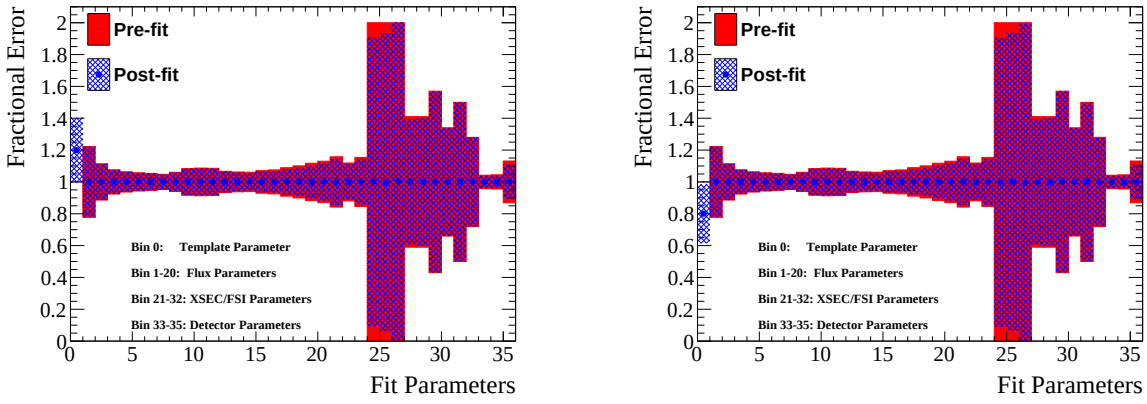

Figure 9.1. Overlayed pre-fit and post-fit parameters with their fractional error for the ν_μ fake data fits with events reweighted according to equation 9.1 (left) or equation 9.2 (right), where the true signal events (ν_μ CC-COH) are given a weight of 1.2 (left) or 0.8 (right). The post-fit template (signal) parameter (bin 0) returns exactly 1.2 (left) or 0.8 (right). The post-fit uncertainties are mostly the same as the pre-fit uncertainties other than bins 24-26, which are the three DIS dials with 100% prior uncertainties (see section 7.2). This behaviour means that the samples have slight constraining power over the DIS background events.

χ^2_{reco}: Figure 9.2 shows the pre-fit (nominal Monte Carlo simulation), fake data, and post-fit reconstructed event distributions. The uncertainties shown here are the statistical uncertainties. For SIG, the number of events is different in the fake data compared to the nominal Monte Carlo simulation due to the weights applied to the CC-COH signal events. The numbers of events in SB1 and SB2 are the same between the fake data compared to the nominal Monte Carlo simulation since the background events are not normalized.

The χ^2_{reco}, calculated by equation 8.1, can be evaluated prior to the fit with the nominal Monte Carlo simulation (χ^2_{prefit}) and after the fit (χ^2_{postfit}) using the

The χ^2_{prefit} can be large for some of the studies with large variations compared to the

[1]The largest uncertainty reduction (10%) occurs at bin 24 (a CC-DIS dial) where the pre-fit uncertainty is 100%. All three of the DIS parameters have conservative pre-fit uncertainties of 100%.

nominal Monte Carlo simulation. For test 1,

$$\begin{aligned}\chi^2_{\text{prefit}} &= \sum_{i=1}^{3} 2(N_i^{\text{fit}} - N_i^{\text{data}} + N_i^{\text{data}} \ln \frac{N_i^{\text{data}}}{N_i^{\text{fit}}}) \\ &= 2(295 - 272 + 272 \ln \frac{272}{295}) \\ &= 1.84.\end{aligned} \tag{9.3}$$

The χ^2_{postfit} describes the agreement between the nominal Monte Carlo simulation and the post-fit results, which also reflects the goodness of the fit. In general, it is expected to have a smaller χ^2_{postfit} compared to the χ^2_{prefit}. If the χ^2_{postfit} does not improve after the fit, then it suggests the fitter framework does not have enough degrees of freedom to deal with the changes applied to the fake data set. In addition, p-value studies, described in section 8.3, are also performed to evaluate the goodness of the fits.

The χ^2_{postfit} for test 1 and test 2 are both 0 since the post-fit results match exactly with the fake data. The corresponding p-values are 1. These results suggest that the fitter can recover the normalization changes applied to the signal events. However, as we will see in some of the studies later, a good fit with a small χ^2_{postfit} does not necessarily mean an unbiased fit result. Therefore, we need to perform checks (described in the next paragraph) to the extracted cross-section results as well.

χ^2_σ: For each fitter study, the cross-section χ^2_σ is evaluated. The difference between the extracted cross section and the fake data "true" cross section is used to calculate the χ^2_σ as shown in equation 8.2. A reminder that the cross-section results in this thesis are flux-integrated single bin measurements. Again, p-value studies are performed to understand the significance of the fit results and any potential bias to the cross-section result. For this thesis, p-values above 0.05 (2σ) are considered acceptable. Any studies with a p-value lower than this threshold will be flagged and discussed. In addition, a p-value larger than 0.32 (1σ) means the fake data truth cross section is within the uncertainties of the extracted cross section. In this case, we can conclude that the uncertainties of this analysis can cover any bias caused by the changes applied in the fake data study.

Figure 9.3 shows the nominal Monte Carlo simulation (pre-fit), fake data, and extracted cross sections. Both of the χ^2_σ are 0, with p-values of 1.00. The results from this study suggest that the signal definition in the fitter framework works as designed.

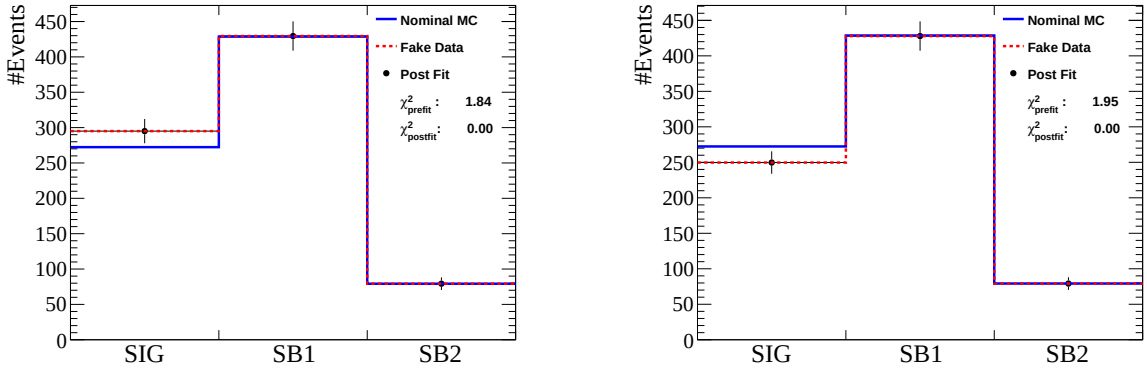

Figure 9.2. Nominal Monte Carlo simulation, fake data, and post-fit (with stat. uncertainty) reconstructed event distributions of the three samples for the ν_μ fake data fits with events reweighted according to equation 9.1 (left) or equation 9.2 (right), where the true signal events (ν_μ CC-COH) are given a weight of 1.2 (left) or 0.8 (right). The post-fit distributions match exactly with the fake data distributions, with $\chi^2_{\text{post-fit}}$ equal to zero for both studies.

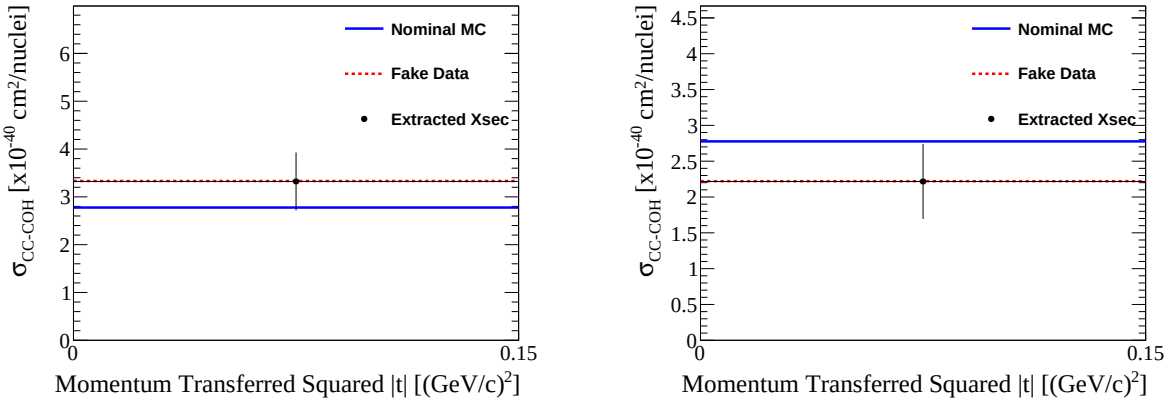

Figure 9.3. Nominal Monte Carlo simulation, fake data, and extracted cross sections for the ν_μ fake data fits with events reweighted according to equation 9.1 (left) or equation 9.2 (right), where the true signal events (ν_μ CC-COH) are given a weight of 1.2 (left) or 0.8 (right). The error bars represent the combined (stat. + syst.) uncertainties for the extracted cross sections. The extracted cross sections (black dot) are exactly the same as the fake data set cross section (dashed red).

9.3 Asimov Fits: ν_μ CC-COH

The term "Asimov fit" refers to the study where the "data" input to the fitter is the same as the Monte Carlo simulation input. The purpose of such a fit is to test the machinery of the fitter framework. Since there is no difference between the "data" and the Monte Carlo simulation inputs, all the post-fit parameter values are expected to stay the same, which figure 9.4 confirms.

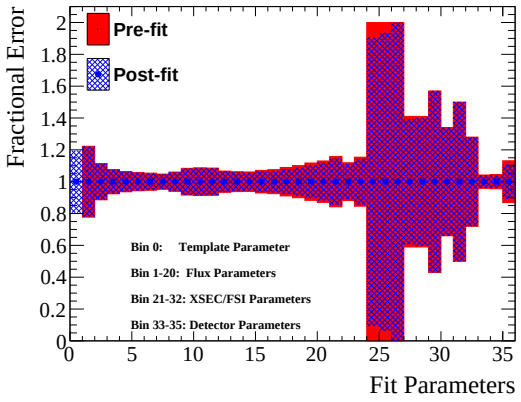

Figure 9.4. Overlayed pre-fit and post-fit parameters with their fractional error for the ν_μ Asimov fit with the nominal Monte Carlo simulation used as the data input for the fitter. All the post-fit parameters remained the same as the pre-fit values as expected for an Asimov fit.

Figure 9.5 shows the reconstructed event distributions for the three samples (SIG, SB1, and SB2). The pre-fit and post-fit values are the same by the construct of the Asimov fit; the χ^2_{postfit} is also 0 as expected.

Figure 9.6 shows the nominal Monte Carlo simulation (pre-fit), Asimov data, and extracted cross sections for the Asimov fit - all three cross sections are expected to be the same. The extracted cross-section uncertainty is the combination of the statistical and systematic uncertainties.

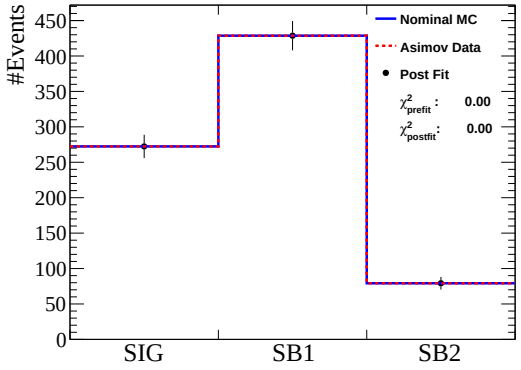

Figure 9.5. Nominal Monte Carlo simulation, Asimov data, and post-fit (with stat. uncertainty) reconstructed event distributions of the three samples for the ν_μ Asimov fit with the nominal Monte Carlo simulation used as the data input for the fitter. No difference is observed between the three distributions as expected for an Asimov fit.

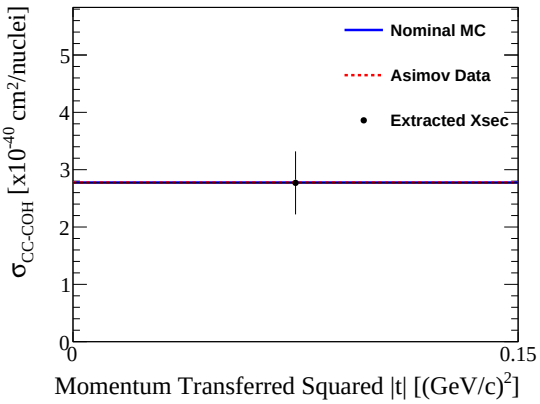

Figure 9.6. Nominal Monte Carlo simulation, Asimov data, and extracted cross sections for the ν_μ Asimov fit with the nominal Monte Carlo simulation used as the data input for the fitter. The error bar represents the combined (stat. + syst.) uncertainty for the extracted cross section. All three cross sections are exactly the same as expected for an Asimov fit.

9.4 Fake Data Studies: ν_μ CC-COH

9.4.1 Alternative Monte Carlo Simulation Input (prod6B NEUT)

This study uses an alternative[2] ND280 Monte Carlo simulation production (prod6B NEUT) as the fake data. Details regarding the differences between this Monte Carlo simulation and the nominal Monte Carlo simulation (prod6T) are shown in appendix C. The most significant difference is the COH modelling. The fake data set used in this section is the original Rein-Sehgal model (section 2.3.1), and the nominal Monte Carlo simulation uses the Berger-Sehgal model (section 2.3.3). The resulting difference in the signal event prediction is more than a factor of two. The purpose of this study is to test the fitter responses with multiple changes in the fake data set (a different Monte Carlo simulation from the nominal one) and to check if the fitter can recover the alternative Monte Carlo simulation CC-COH cross-section.

Figure 9.7 shows the pre-fit and post-fit parameters. Table 9.3 shows that the post-fit template parameter is consistent with the ratio between the prod6B and prod6T Monte Carlo simulation predicted CC-COH number of events. The rest of the post-fit parameters are changed (e.g., the DIS dials all moved down after the fit) due to the differences and changes between the two Monte Carlo simulations (various bug fixes in pion kinematics and FSI result in differences in the Monte Carlo simulation prediction of the RES and DIS background events).

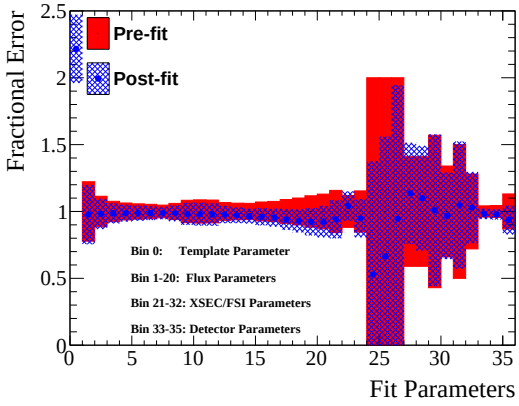

Figure 9.7. Overlayed pre-fit and post-fit parameters with their fractional error for the ν_μ fake data fit with production 6B NEUT Monte Carlo simulation as fake data. The post-fit template parameter (signal) reflects the difference between the fake data set and nominal Monte Carlo simulation predictions of CC-COH event rate.

[2]Prod6B was the previous version of ND280 Monte Carlo simulation used for past analyses. It was replaced by the latest ND280 Monte Carlo simulation (prod6T). Two neutrino event generators, NEUT[56] and GENIE[89], are used. The fake data study using the prod6B GENIE is described in appendix H.1.1.

prod6B CC-COH	247 events
prod6T CC-COH	117 events
prod6B/prod6T ratio	2.11
Post-fit Signal Parameter	2.22

TABLE 9.3. The value of the post-fit signal parameter (2.22) agrees with the ratio (2.11) between prod6B and prod6T Monte Carlo simulation predicted CC-COH number of events. The fitter is able to recover the difference in the signal events between the two Monte Carlo simulations.

Figure 9.8 shows the pre-fit, fake data (prod6B NEUT), and post-fit reconstructed event distributions. For the SIG bin, the fake data is higher than the nominal Monte Carlo simulation due to the overprediction of CC-COH in the fake data (as mentioned, the RS model prediction is about a factor of two higher than the BS model prediction). For the SB1 and SB2 bins, the number of events is lower in the fake data than in the nominal Monte Carlo simulation due to the differences in the background event predictions. The χ^2_{postfit} is 1.75, with a p-value of 0.42. The p-value is above 0.32 (1σ), which means the post-fit distribution is consistent (within the statistical uncertainties) with the fake data set.

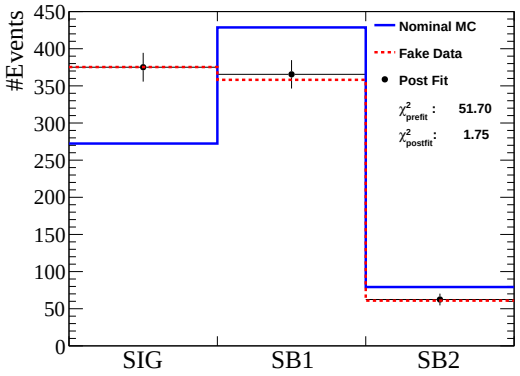

Figure 9.8. Nominal Monte Carlo simulation, fake data, and post-fit (with stat. uncertainty) reconstructed event distributions of the three samples for the ν_μ fake data fit with production 6B NEUT Monte Carlo simulation as fake data. χ^2_{prefit} and χ^2_{postfit} are also shown. The small χ^2_{postfit} indicates the goodness of the fit.

Figure 9.9 shows the nominal Monte Carlo simulation (pre-fit), fake data, and extracted cross sections. The χ^2_σ (equation 8.2) is less than 0.01, with a p-value of 0.97. This study indicates that the fitter framework has enough degrees of freedom (fit parameters) to adjust to the different signal and background models; the extracted cross-section result is compatible with the fake data set cross section.

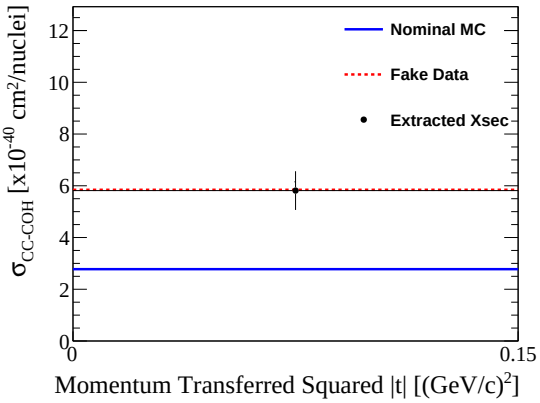

Figure 9.9. Nominal Monte Carlo simulation, fake data, and extracted cross sections for the ν_μ fake data fit with production 6B NEUT Monte Carlo simulation as fake data. The error bar represents the combined (stat. + syst.) uncertainty for the extracted cross section. The extracted cross section is compatible with the fake data set cross section.

9.4.2 Modified Vertex Activity

As described in 4.4.1, the vertex activity (VA) variable used for the analysis is the sum of the detected energy deposition from the particles produced from neutrino interactions. However, the neutrino interaction generators can mismodel the final state proton multiplicity for the background events such as RES and DIS, resulting in an inaccurate estimation of VA.

The MINERvA experiment[3] CC-COH analysis has studied this issue with missing proton energy deposition [33]. The T2K INGRID CC-COH analysis has also performed a similar study [90]. The latter study concludes that an additional 0-100 MeV (uniformly distributed) VA needs to be randomly added to 25% of background events (RES and DIS, see section 1.4) in which the target nucleon is a neutron. The MINERvA and INGRID studies suggest that a neutrino interacts with a neutron-proton correlated pair and produces two protons in some cases. The signal events (COH) are unaffected since the COH process happens at the nucleus level, but the background events are nucleon level interactions. This change in VA is used to construct a fake data set input to test the effect of potential mismodel of VA on this analysis.

Figure 9.10 shows the pre-fit and post-fit parameters. Since no VA-related dial is implemented, the fitter moves the cross-section parameters instead to adjust to the change applied in this fake data set. The post-fit template parameter is only slightly away from 1, indicating that the fitter has enough degrees of freedom (fit parameters) to adjust the nominal Monte Carlo simulation to the fake data set.

[3]The MINERvA (Main Injector Neutrino ExpeRiment to study ν-A interactions) experiment studies neutrino interactions with different nuclei with a high-intensity beam. The various high-precision MINERvA ν-A measurements are used as inputs to experiments such as T2K.

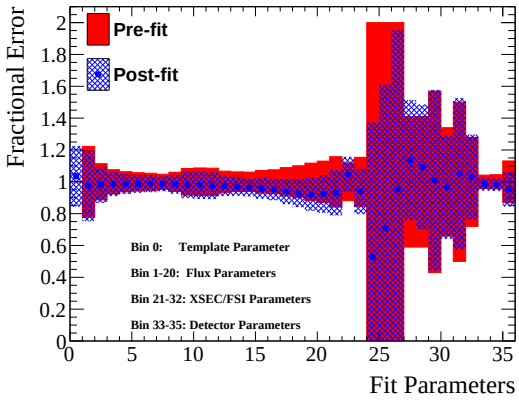

Figure 9.10. Overlayed pre-fit and post-fit parameters with their fractional error for the ν_μ fake data fit with additional 0-100 MeV of VA added to 25% of background events in which the target nucleon is a neutron.

Figure 9.11 shows the pre-fit, fake data, and post-fit reconstructed event distributions. From the fake data distributions, we can see that the change in VA results in reducing the number of events in all three samples, which means the migration of background events out of the selected samples. The χ^2_{postfit} is 1.86, with a p-value of 0.39. This p-value again confirms that the fitter has enough degrees of freedom to accommodate changes to the VA variable.

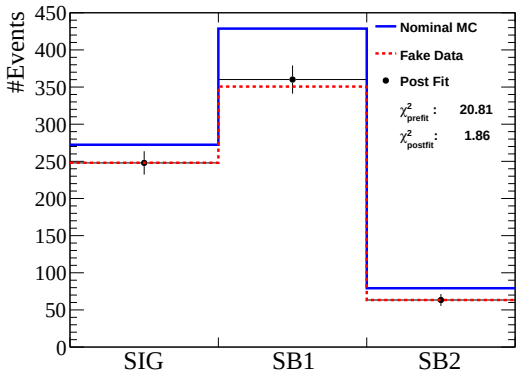

Figure 9.11. Nominal Monte Carlo simulation, fake data, and post-fit (with stat. uncertainty) reconstructed event distributions of the three samples for the ν_μ fake data fit with additional 0-100 MeV of VA added to 25% of the background events in which the target nucleon is a neutron. χ^2_{prefit} and χ^2_{postfit} are also shown.

Figure 9.12 shows the nominal Monte Carlo simulation (pre-fit), fake data, and extracted cross sections. The χ^2_σ is 0.01, with a p-value of 0.92. The extracted cross section is compatible with the fake data set cross section.

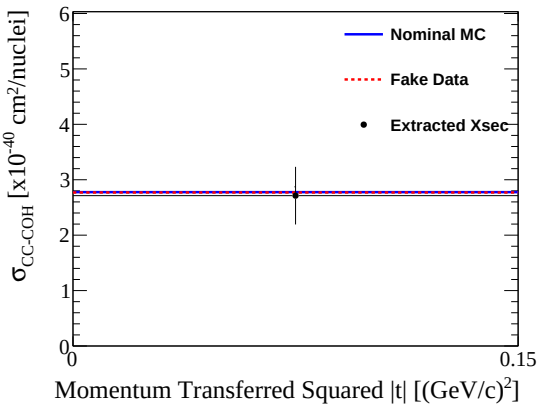

Figure 9.12. Nominal Monte Carlo simulation, fake data, and extracted cross sections for the ν_μ fake data fit with additional 0-100 MeV of VA added to 25% of background events in which the target nucleon is a neutron. The error bar represents the combined (stat. + syst.) uncertainty for the extracted cross section. The extracted cross section is compatible with the fake data set cross section.

9.4.3 Low Q^2 Suppression of Resonant Pion Production

The MINERvA experiment observed tensions between the data and the Monte Carlo simulation in the CC-1π (charged-current interactions with one reconstructed pion) measurements in the Q^2 distribution, where the data are below the Monte Carlo simulation predictions [91]. In order to improve the data and the Monte Carlo simulation agreement, they use a data-driven weight

$$\text{weight} = \frac{A}{1 + \exp\left\{1 - \sqrt{Q^2}/Q_0\right\}}, \tag{9.4}$$

with empirically determined free parameters $A = 0.010, Q_0 = 0.156$ GeV. This suppresses the CC-1π events at low Q^2 region ($Q^2 < 0.7\,\text{GeV}^2$).

For T2K, both the neutrino energy and the Monte Carlo simulation used differ from MINERvA. However, a fake data set constructed with this suppression (to test the fitter framework response) is still valuable. For the MINERvA CC-1π samples, the CC-COH contribution is small (percent level), but for this analysis, the selected sample has high purity of CC-COH. Since COH and RES are modelled differently, they should not be suppressed the same way with one formula. Therefore, one change is needed from the MINERvA low Q^2 suppression. It is only applied to the background RES events instead of the entire CC-1π topology, which includes both RES and COH events.

Figure 9.13 shows the pre-fit and post-fit parameters. The fitter's post-fit template parameter (bin 0) gets a large movement and causes a bias in the number of signal events.

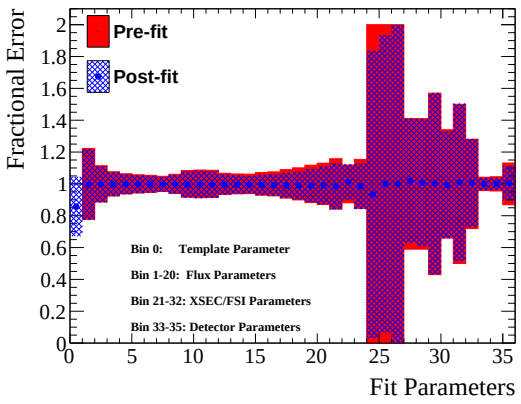

Figure 9.13. Overlayed pre-fit and post-fit parameters with their fractional error for the ν_μ fake data fit with events reweighted according to equation 9.4. The template parameter is moved down significantly compared to the other parameters. This behavior indicates a lack of degree of freedom in Q^2.

Figure 9.14 shows the pre-fit, fake data, and post-fit reconstructed event distributions. The fake data results in a larger decrease in the number of events in the signal region than the sidebands as the events in the signal region are mostly low Q^2 events. The fitter moves the template parameter to compensate for the change and creates a bias in the post-fit number of signal events. The post-fit reconstructed bin χ^2 is 0.08, with a p-value of 0.96. This high p-value indicates a good fit. However, it does not necessarily mean an unbiased fit result.

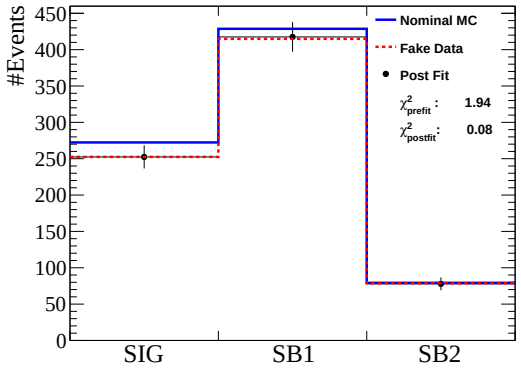

Figure 9.14. Nominal Monte Carlo simulation, fake data, and post-fit (with stat. uncertainty) reconstructed event distributions of the three samples for the ν_μ fake data fit with events reweighted according to equation 9.4. χ^2_{prefit} and χ^2_{postfit} are also shown. The small χ^2_{postfit} suggest a reasonably good fit.

Figure 9.15 shows the nominal Monte Carlo simulation (pre-fit), fake data, and extracted cross sections. The χ^2_σ (equation 8.2) is 0.61, with a p-value of 0.43. As a result of the bias in the post-fit number of signal events, the extracted cross section is also biased. The χ^2_σ is larger than most of the other studies. This study indicates a lack of degrees of freedom in the Q^2 space, which causes a bias in the cross-section result. An additional uncertainty of 16.4% (evaluation described in appendix J) is needed to cover this bias.

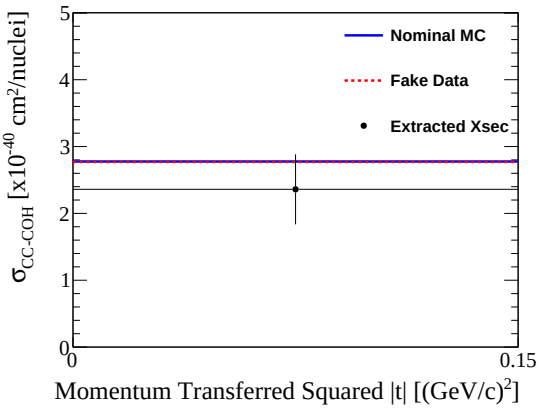

Figure 9.15. Nominal Monte Carlo simulation, fake data, and extracted cross sections for the ν_μ fake data fit with events reweighted according to equation 9.4. The error bar represents the combined (stat. + syst.) uncertainty for the extracted cross section. The bias in the extracted cross section can barely be covered by the uncertainty of the measurement.

9.5 Summary of Results for the ν_μ CC-COH Fitter Studies

Table 9.4 summarizes the results of all the validation studies.[4] The Asimov fit shows the fitter framework is working as expected when all the post-fit parameters remain at the same value. The fits with alternative Monte Carlo simulation indicate the fitter is robust against different signal and background modelling. The studies with varied neutrino flux, vertex activity variable, signal (CC-COH) normalization, and background (CC-RES and CC-DIS) normalization all converge with small χ^2_σ and the corresponding p-values are all above 0.32 (1σ). The p-values are below 0.32 but still larger than 0.05 (2σ) for the fake data sets with $\pm$ 90% RES, which implies larger biases in the cross-section results. For these two studies, small p-values are expected, and the most important message is the convergence of the fits.

[4]The fake data study with prod6B GENIE is in appendix H.1.1 and the study with shifted vertex activity is in appendix H.1.2.

The study with low Q^2 suppression for RES returns small χ^2_{postfit} (meaning it is a good fit), but large χ^2_σ (with p-value of 0.43)[5]. This behaviour suggests that the fitter lacks the degree of freedom in Q^2 and an additional uncertainty (evaluation described in appendix J) is added to cover the bias seen in this study.

[5]This χ^2_σ p-value is still larger than 0.32 due to the large statistical uncertainty in this analysis. Appendix. J table J.1 shows the χ^2_σ p-value of 0.06 without the statistical effect.

Detail	χ^2_{prefit}	χ^2_{postfit}	χ^2_{postfit} **P-value**	**Post-fit** χ^2_σ	χ^2_σ **P-value**
Asimov Data = MC	0	0	1.00	0	1.00
prod6B MC NEUT as fake data	51.70	1.75	0.42	< 0.01	0.97
prod6B MC GENIE as fake data	17.39	4.81	0.09	0.79	0.38
Flux +20% $E_\nu > 2\,\text{GeV}$	20.29	1.34	0.51	< 0.01	0.94
Flux -20% $E_\nu > 2\,\text{GeV}$	22.81	1.90	0.39	< 0.01	0.97
Low Q^2 Suppression for RES	1.94	0.08	0.96	0.61	0.43
Added Vertex Activity	20.81	1.86	0.39	< 0.01	0.92
Shifted Vertex Activity	3.03	0.49	0.78	< 0.01	1.00
ν_μ CC-COH +20%	1.84	0	1.00	0	1.00
ν_μ CC-COH -20%	1.95	0	1.00	0	1.00
ν_μ CC-RES +20%	4.10	0.48	0.79	0.07	0.79
ν_μ CC-RES -20%	4.33	0.56	0.76	0.08	0.78
ν_μ CC-RES +50%	24.71	2.68	0.26	0.37	0.55
ν_μ CC-RES -50%	28.28	4.04	0.13	0.57	0.45
ν_μ CC-RES +90%	76.54	7.58	0.02	1.16	0.28
ν_μ CC-RES -90%	98.01	15.96	< 0.01	2.19	0.14
ν_μ CC-DIS +20%	3.96	0.32	0.85	0.02	0.90
ν_μ CC-DIS -20%	4.22	0.40	0.82	0.01	0.91
ν_μ CC-DIS +50%	23.71	1.76	0.41	0.10	0.75
ν_μ CC-DIS -50%	27.93	3.03	0.22	0.06	0.81
ν_μ CC-DIS +80%	58.37	3.99	0.14	0.26	0.61
ν_μ CC-DIS -80%	76.46	9.69	< 0.01	0.12	0.73

TABLE 9.4. Summary of all the fitter validation studies for the ν_μ CC-COH analysis. The fit details, various χ^2, and the corresponding p-values are shown. All studies have χ^2_σ p-value above 0.05 (2σ).

Chapter 10

The $\bar{\nu_\mu}$ CC-COH Analysis Fitter Studies

10.1 Overview of the Fitter Studies

This chapter mirrors the fitter studies described in chapter 9 for the $\bar{\nu_\mu}$ CC-COH analysis. Table 10.3 shows the location of the studies in this chapter with the purpose of the studies. The deep inelastic scattering (CC-DIS) background studies are not performed since it is not a major source of background in the $\bar{\nu_\mu}$ CC-COH selection. Although the rest of the studies are identical to the ν_μ counterparts, some of the descriptions are duplicated to this chapter to improve the reading experience. The results of all the fitter studies are summarized in section 10.4.

Section	Purpose of the Study
10.2	Fitter framework machinery tests (using the "Asimov fit")
10.3.1	Fitter tests with alternative MC as "data" inputs
10.3.2	Test of the fitter responses with modifications to the VA variable
10.3.3	Test of the fitter responses with CC-RES background events varied in Q^2
10.3.4	Signal definition tests with modified CC-COH normalization
H.2.1	Tests of the fitter responses with modifications to the neutrino flux
H.2.2	Tests with modified normalization of the main background events (CC-RES)

TABLE 10.1. A list of the fitter studies performed for the $\bar{\nu_\mu}$ CC-COH analysis. The section number of each study and the purpose of the studies are listed.

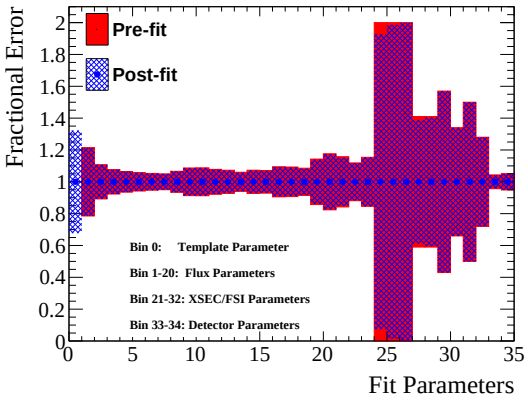

Figure 10.1. Overlayed pre-fit and post-fit parameters with their fractional error for the $\bar{\nu}_\mu$ Asimov fit with the nominal Monte Carlo simulation used as the data input for the fitter. All the post-fit parameters remained the same as the pre-fit values as expected for an Asimov fit. The post-fit uncertainties are mostly the same as the pre-fit uncertainties other than bins 24-26, which are the three DIS dials with 100% prior uncertainties. This behaviour means that the samples have slight constraining power over the DIS background events.

10.2 Asimov Fits: $\bar{\nu}_\mu$ CC-COH

The term "Asimov fit" refers to the study where the fitter's data input is the same as the Monte Carlo simulation input. The purpose of such a fit is to test the machinery of the fitter framework. Since there is no difference between the data and Monte Carlo simulation inputs, all the post-fit parameters are expected to stay the same, which figure 10.1 confirms. The "fit parameters" are the same as the ν_μ parameters shown in table 9.2, except for the detector parameters (2 detector parameters instead of 3).

Figure 10.2 shows the reconstructed event distributions for the 2 samples. The pre-fit and post-fit values are the same by the nature of the Asimov fit; the $\chi^2_{\text{post-fit}}$ is also 0 as expected.

Figure 10.3 shows the nominal Monte Carlo simulation (pre-fit), Asimov data, and extracted cross sections for the Asimov fit - all three cross sections are expected to be the same. The extracted cross-section uncertainty is the combination of the statistical and systematic uncertainties.

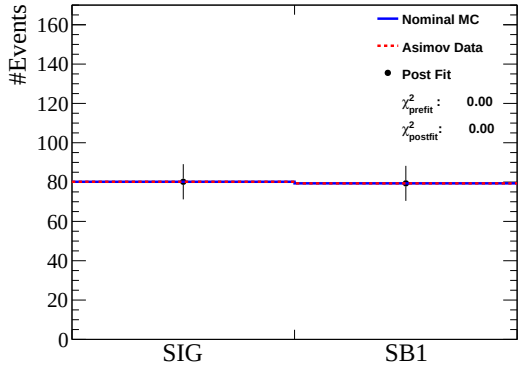

Figure 10.2. Nominal Monte Carlo simulation, Asimov data, and post-fit (with stat. uncertainty) reconstructed event distributions of the 2 samples for the $\bar{\nu_\mu}$ Asimov fit with the nominal Monte Carlo simulation used as the data input for the fitter. No difference is observed between the three distributions as expected for an Asimov fit

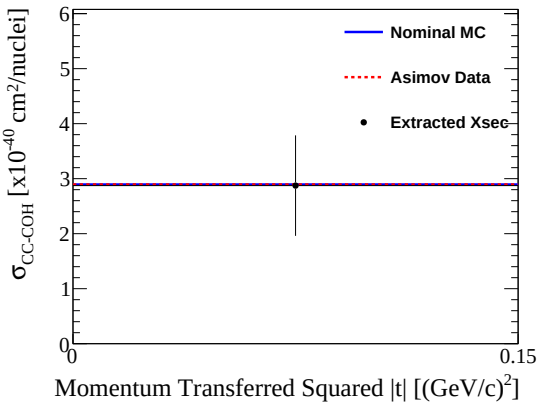

Figure 10.3. Nominal Monte Carlo simulation, Asimov data, and extracted cross sections for the $\bar{\nu_\mu}$ Asimov fit with the nominal Monte Carlo simulation used as the data input for the fitter. The error bar represents the combined (stat. + syst.) uncertainty for the extracted cross section. All three cross sections are exactly the same as expected for an Asimov fit.

10.3 Fake Data Studies: $\bar{\nu}_\mu$ CC-COH

10.3.1 Alternative Monte Carlo simulation Input (prod6B NEUT)

This study uses an alternative ND280 Monte Carlo simulation production (prod6B NEUT) as the fake data. Details regarding the differences between this Monte Carlo simulation and the nominal Monte Carlo simulation (prod6T) are shown in appendix C. The most significant difference is the COH modelling. The fake data set used in this section is the original Rein-Sehgal model (section 2.3.1), and the nominal Monte Carlo simulation uses the Berger-Sehgal model (section 2.3.3). The resulting difference in the signal event prediction is more than a factor of two.

Figure 10.4 shows the pre-fit and post-fit parameters. Table 10.2 shows that the post-fit template (signal) parameter (bin 0 in figure 10.4) is consistent with the difference between the prod6B and prod6T Monte Carlo simulation predicted CC-COH number of events. The rest of the post-fit parameters are changed due to the differences and changes between the two Monte Carlo simulations (various bug fixes in pion kinematics and FSI result in differences in the Monte Carlo simulation prediction of the RES and DIS background events).

prod6B CC-COH	80 events
prod6T CC-COH	34 events
prod6B/prod6T	2.35
Post-fit Signal Parameter	2.19

TABLE 10.2. The value of the post-fit signal parameter (2.19) agrees with the ratio (2.35) between prod6B and prod6T Monte Carlo simulation predicted CC-COH number of events. The fitter is able to recover the difference in the signal events between the two Monte Carlo simulations.

Figure 10.5 shows the pre-fit, fake data (prod6B NEUT), and post-fit reconstructed event distributions. The $\chi^2_{\text{post-fit}}$ is 1.79, with a p-value of 0.18.

Figure 10.6 shows the nominal Monte Carlo simulation (pre-fit), fake data, and extracted cross sections. The χ^2_σ is 0.39, with a p-value of 0.53. This study indicates that the fitter framework has barely enough degrees of freedom (fit parameters) to adjust to the different signal and background models; the extracted cross-section result is still compatible with the fake data fake data set cross section due to the relatively large statistical uncertainty.

10.3.2 Modified Vertex Activity

This study tests the effect of potential mismodel of vertex activity (VA) on this analysis. The motivation of this study has been described in 9.4.2. The fake data set is generated with

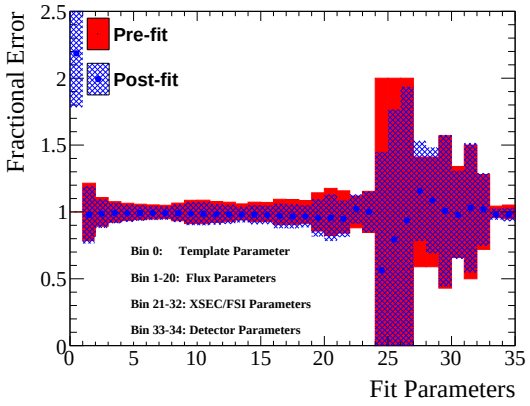

Figure 10.4. Overlayed pre-fit and post-fit parameters with their fractional error for the $\bar{\nu}_\mu$ fake data fit with production 6B NEUT Monte Carlo simulation as fake data. The post-fit template (signal) parameter (bin 0) reflects the difference between the prod6B NEUT and prod6T predictions of CC-COH event rate.

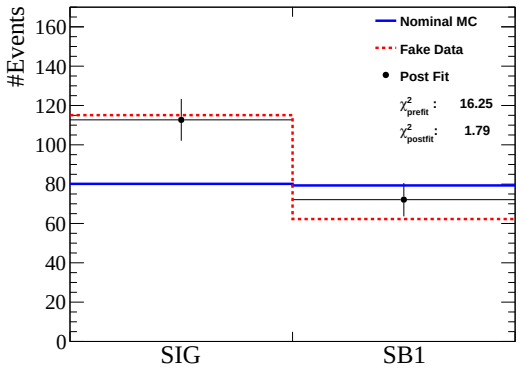

Figure 10.5. Nominal Monte Carlo simulation, fake data, and post-fit (with stat. uncertainty) reconstructed event distributions of the 2 samples for the $\bar{\nu}_\mu$ fake data fit with production 6B NEUT Monte Carlo simulation as fake data. $\chi^2_{\text{pre-fit}}$ and $\chi^2_{\text{post-fit}}$ are also shown. The $\chi^2_{\text{post-fit}}$ is larger compared to the ν_μ study, but the p-value (0.18) is still larger than 0.05 (2 σ).

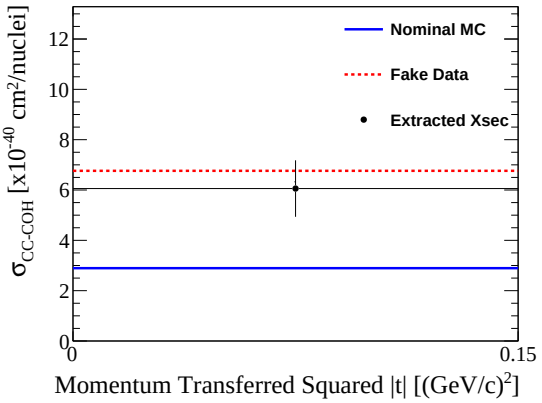

Figure 10.6. Nominal Monte Carlo simulation, fake data, and extracted cross sections for the $\bar{\nu_\mu}$ fake data fit with production 6B NEUT Monte Carlo simulation as fake data. The error bar represents the combined (stat. + syst.) uncertainty for the extracted cross section. The extracted cross section is compatible with the fake data set cross section.

an additional 0-100 MeV (uniformly distributed) VA randomly added to 25% of background events (RES and DIS, see section 1.4) in which the target nucleon is a neutron. The signal events (COH) are unaffected by this change since the COH process happens at the nucleus level.

Figure 10.7 shows the pre-fit and post-fit parameters. Since no VA-related dial is implemented, the fitter moves the cross-section parameters instead to adjust to the change applied in this fake data set. The post-fit template parameter is 0.92, indicating a slight bias (about 8%) in the cross-section result.

Figure 10.8 shows the pre-fit, fake data, and post-fit reconstructed event distributions. From the fake data distributions, we can see that the change in VA results in reducing the number of events in both samples, which means the migration of background events out of the selected samples. The post-fit reconstructed bin χ^2 is 0.19, with a p-value of 0.66. This p-value again confirms that the fitter has enough degrees of freedom to accommodate changes to the VA variable.

Figure 10.9 shows the nominal Monte Carlo simulation (pre-fit), fake data, and extracted cross sections. The χ^2_σ is 0.09, with a p-value of 0.76. The extracted cross section is compatible with the fake data set cross section.

10.3.3 Low Q^2 Suppression of Resonant Pion Production

For the same reasons described in the ν_μ analysis (9.4.3), the effect of low Q^2 suppression of RES needs to be tested for this analysis. The same weight used by the ν_μ analysis is used to

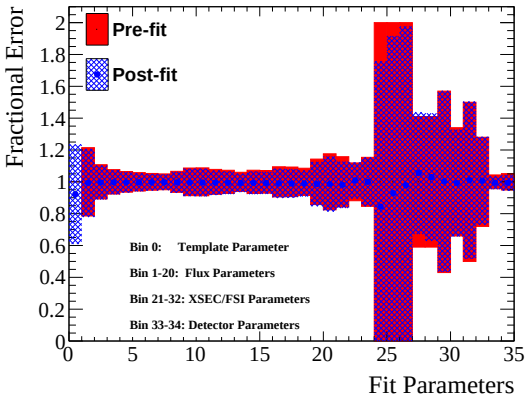

Figure 10.7. Overlayed pre-fit and post-fit parameters with their fractional error for the $\bar{\nu}_\mu$ fake data fit with additional 0-100 MeV of VA added to 25% of background events in which the target nucleon is a neutron.

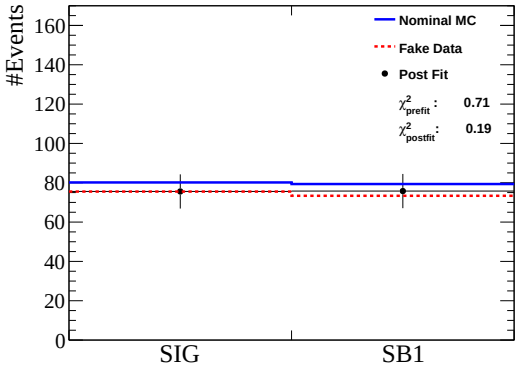

Figure 10.8. Nominal Monte Carlo simulation, fake data, and post-fit (with stat. uncertainty) reconstructed event distributions of the 2 samples for the $\bar{\nu}_\mu$ fake data fit with additional 0-100 MeV of VA added to 25% of the background events in which the target nucleon is a neutron. $\chi^2_{\text{pre-fit}}$ and $\chi^2_{\text{post-fit}}$ are also shown. The small $\chi^2_{\text{post-fit}}$ (0.19) suggest a good fit.

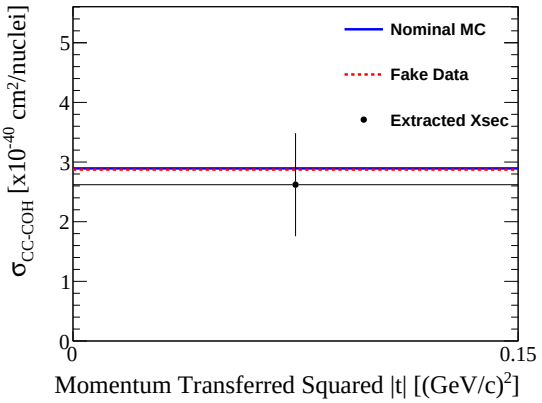

Figure 10.9. Nominal Monte Carlo simulation, fake data, and extracted cross sections for the $\bar{\nu_\mu}$ fake data fit with additional 0-100 MeV of VA added to 25% of background events in which the target nucleon is a neutron. The error bar represents the combined (stat. + syst.) uncertainty for the extracted cross section. The extracted cross section is compatible with the fake data set cross section.

construct the fake data set:

$$\text{weight} = \frac{A}{1 + \exp\left\{1 - \sqrt{Q^2}/Q_0\right\}}, \tag{10.1}$$

with empirically determined free parameters $A = 0.010, Q_0 = 0.156$ GeV [91]. This suppresses the CC-1π events at low Q^2 region ($Q^2 < 0.7\,\text{GeV}^2$).

Figure 10.10 shows the pre-fit and post-fit parameters. The fitter's post-fit template parameter (bin 0) gets a large movement and causes a bias in the number of signal events.

Figure 10.11 shows the pre-fit, fake data, and post-fit reconstructed event distributions. The fake data results in a larger decrease in the number of events in the signal region than the sidebands as the events in the signal region are mostly low Q^2 events. The fitter moves the template parameter to compensate for the change and creates a bias in the post-fit number of signal events. The post-fit reconstructed bin χ^2 is 0.02, with a p-value of 0.89. This high p-value indicates a good fit. However, it does not necessarily mean an unbiased fit result.

Figure 10.12 shows the nominal Monte Carlo simulation (pre-fit), fake data, and extracted cross sections. The χ^2_σ (equation 8.2) is 0.55, with a p-value of 0.46. As a result of the bias in the post-fit number of signal events, the extracted cross section is also biased. The result from this analysis is consistent with the ν_μ analysis - a lack of degrees of freedom in the Q^2 space causes the bias in the cross-section result. An additional uncertainty of 24.5% (evaluation described in appendix J) is needed to cover this bias.

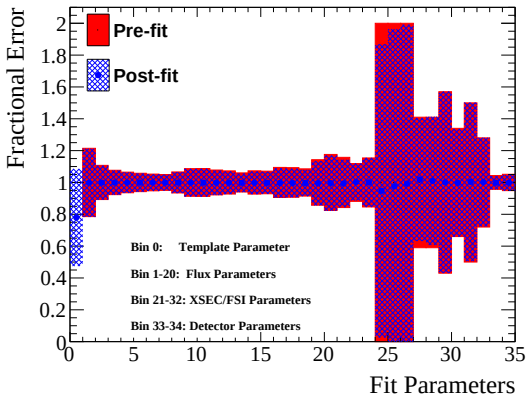

Figure 10.10. Overlayed pre-fit and post-fit parameters with their fractional error for the $\bar{\nu}_\mu$ fake data fit with events reweighted according to equation 10.1. The template parameter is moved down significantly compared to the other parameters. This behavior indicates a lack of degree of freedom in Q^2.

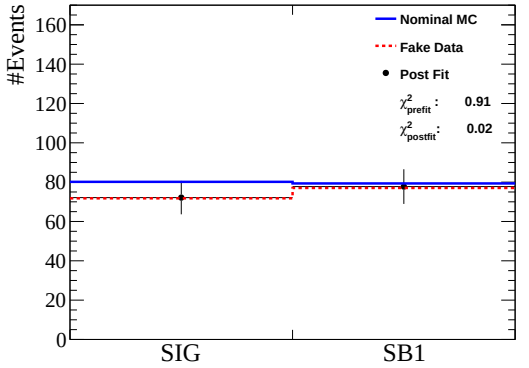

Figure 10.11. Nominal Monte Carlo simulation, fake data, and post-fit (with stat. uncertainty) reconstructed event distributions of the 2 samples for the $\bar{\nu}_\mu$ fake data fit with events reweighted according to equation 10.1. $\chi^2_{\text{pre-fit}}$ and $\chi^2_{\text{post-fit}}$ are also shown. The tiny $\chi^2_{\text{post-fit}}$ (0.02) suggest a very good fit.

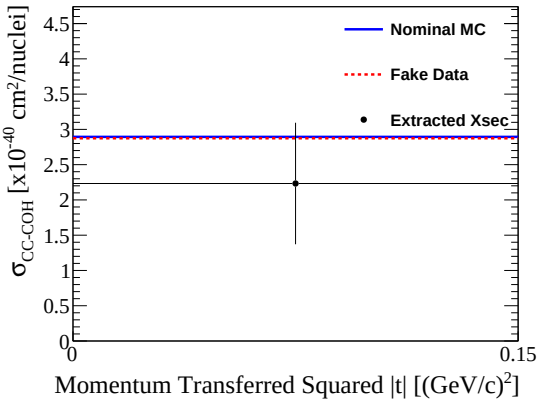

Figure 10.12. Nominal Monte Carlo simulation, fake data, and extracted cross sections for the $\bar{\nu_\mu}$ fake data fit with events reweighted according to equation 10.1. The error bar represents the combined (stat. + syst.) uncertainty for the extracted cross section. The bias in the extracted cross section can barely be covered by the uncertainty of the measurement.

10.3.4 Weighted Signal Events

This study tests the signal definition and the template parameter's response in the fitter. Fake data sets are generated with the true signal events ($\bar{\nu_\mu}$ CC-COH) in the nominal Monte Carlo simulation reweighted by equation 10.2 and equation 10.3. Since only the signal events are reweighted, it is expected that the fitter would adjust only the template parameter.

$$\text{weight(reaction)} = \begin{cases} 1.2, & \nu_\mu \text{ CC-COH} \\ 1, & \text{Everything Else} \end{cases} \tag{10.2}$$

$$\text{weight(reaction)} = \begin{cases} 0.8, & \nu_\mu \text{ CC-COH} \\ 1, & \text{Everything Else} \end{cases} \tag{10.3}$$

Figure 10.13 shows the pre-fit and post-fit parameters. The post-fit template parameter matches exactly with the weight applied to the signal events. All the other parameters remain unchanged as expected.

Figure 10.14 shows the pre-fit, fake data, and post-fit reconstructed event distributions. Again, the post-fit result matches exactly with the fake data distributions with a $\chi^2_{\text{post-fit}}$ of 0, as expected by this study. Figure 10.15 shows the nominal Monte Carlo simulation (pre-fit), fake data, and extracted cross sections. Both of the χ^2_σ are less than 0, with p-values of 1.00. The results from this study suggest that the signal definition in the fitter framework works as designed.

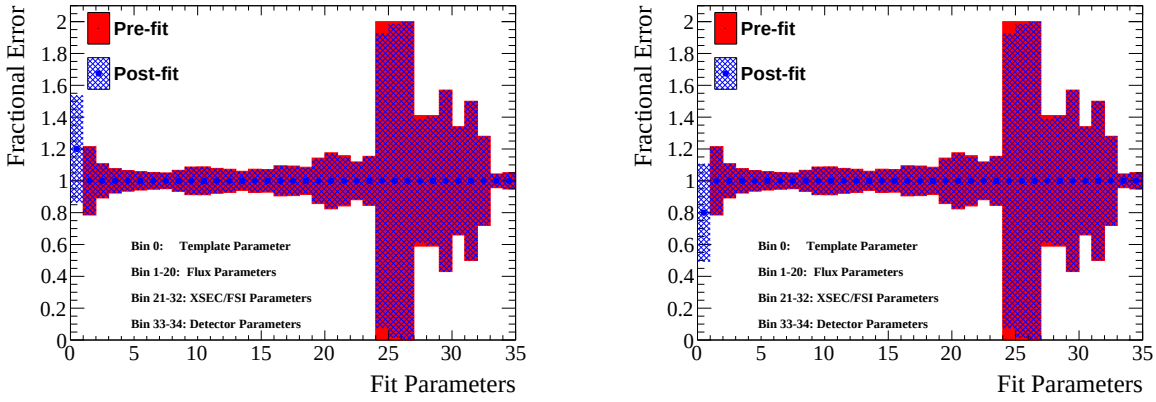

Figure 10.13. Overlayed pre-fit and post-fit parameters with their fractional error for the $\bar{\nu}_\mu$ fake data fit with events reweighted according to equation 10.2 (left) or equation 10.3 (right), where the true signal events ($\bar{\nu}_\mu$ CC-COH) are given a weight of 1.2 (left) or 0.8 (right). The post-fit template parameter (bin 0) returns exactly 1.2 (left) or 0.8 (right).

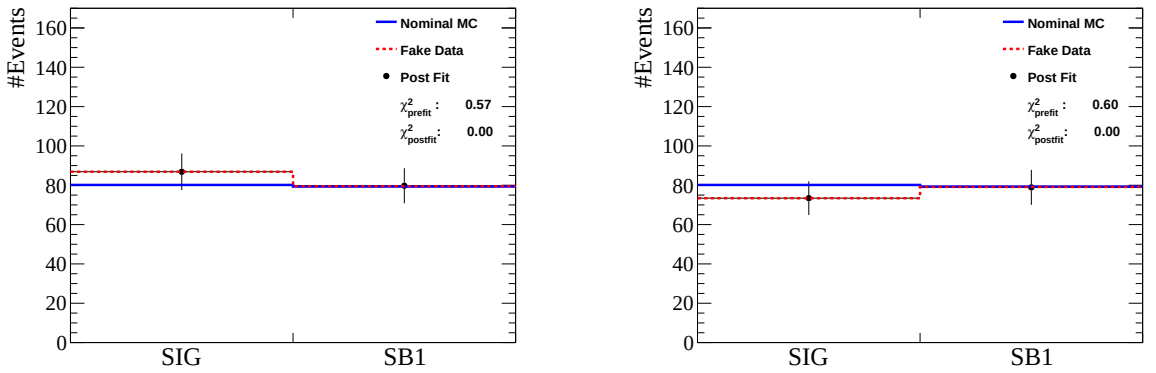

Figure 10.14. Nominal Monte Carlo simulation, fake data, and post-fit (with stat. uncertainty) reconstructed event distributions of the 2 samples for the $\bar{\nu}_\mu$ fake data fit with events reweighted according to equation 10.2 (left) or equation 10.3 (right), where the true signal events ($\bar{\nu}_\mu$ CC-COH) are given a weight of 1.2 (left) or 0.8 (right). The post-fit distributions match exactly with the fake data distributions, with $\chi^2_{\text{post-fit}}$ equal to zero for both studies.

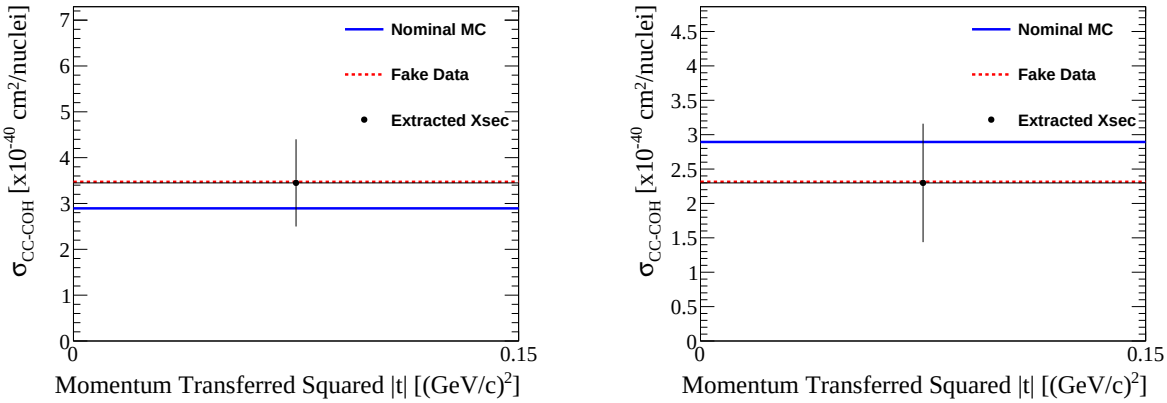

Figure 10.15. Nominal Monte Carlo simulation, fake data, and extracted cross sections for the $\bar{\nu_\mu}$ fake data fit with events reweighted according to equation 10.2 (left) or equation 10.3 (right), where the true signal events ($\bar{\nu_\mu}$ CC-COH) are given a weight of 1.2 (left) or 0.8 (right). The error bar represents the combined (stat. + syst.) uncertainty for the extracted cross section. The extracted cross section (black dot) is exactly the same as the fake data set cross section (dashed red).

10.4 Summary of Results for the $\bar{\nu_\mu}$ CC-COH Fitter Studies

Table 10.3 summarizes the results of all the validation studies. The Asimov fit shows that the fitter framework is working as expected when all the post-fit parameters remain at the same value. The fits with alternative Monte Carlo simulation indicate the fitter is robust against different signal and background modelling. The studies with varied neutrino flux, vertex activity variable, signal (CC-COH) normalization, and background (CC-RES) normalization all converge with small χ^2_σ - the corresponding p-values are all above 0.32 (1σ). The p-values are below 0.32 but still larger than 0.05 (2σ) for the fake data sets with $\pm$ 90% RES, which implies larger biases in the cross-section results. For these two studies, small p-values are expected (due to the extreme changes applied to the RES background events), and the most important message is the convergence of the fits. The study with low Q^2 suppression for RES returns small $\chi^2_{\text{post-fit}}$ (meaning it is a good fit), but large χ^2_σ (with p-value of 0.46)[1]. This behaviour suggests that the fitter lacks the degree of freedom in Q^2 and an additional uncertainty (evaluation described in appendix J) is added to cover the bias seen in this study.

[1]This χ^2_σ p-value is still larger than 0.32 due to the large statistic uncertainty in this analysis. Appendix. J table J.1 shows the χ^2_σ p-value of 0.11 without the statistical effect

Detail	χ^2_{prefit}	χ^2_{postfit}	χ^2_{postfit} **P-value**	**Post-fit** χ^2_σ	χ^2_σ **P-value**
Asimov Data = MC	0	0	1.00	0	1.00
prod6B MC NEUT as fake data	16.3	1.79	0.18	0.39	0.53
Flux +20% $E_\nu > 2\,\text{GeV}$	2.84	0.81	0.37	< 0.01	0.95
Flux -20% $E_\nu > 2\,\text{GeV}$	3.16	1.08	0.30	0.02	0.89
Low Q^2 Suppression for RES	0.91	0.02	0.89	0.55	0.46
Added Vertex Activity	0.71	0.19	0.66	0.09	0.76
$\bar{\nu_\mu}$ CC-COH +20%	0.57	0	1.00	0	1.00
$\bar{\nu_\mu}$ CC-COH -20%	0.60	0	1.00	0	1.00
$\bar{\nu_\mu}$ CC-RES +20%	0.74	0.15	0.69	0.11	0.74
$\bar{\nu_\mu}$ CC-RES -20%	0.77	0.18	0.67	0.13	0.72
$\bar{\nu_\mu}$ CC-RES +50%	4.45	0.89	0.35	0.59	0.44
$\bar{\nu_\mu}$ CC-RES -50%	5.01	1.21	0.27	0.96	0.33
$\bar{\nu_\mu}$ CC-RES +90%	13.8	2.59	0.11	1.56	0.21
$\bar{\nu_\mu}$ CC-RES -90%	17.2	4.52	0.03	3.73	0.05

TABLE 10.3. Summary of all the fitter validation studies for the $\bar{\nu_\mu}$ CC-COH analysis. The fit details, various χ^2, and the corresponding p-values are shown. All studies have χ^2_σ p-value above 0.05 (2σ).

Chapter 11

Results and Cross-Section Measurements

The results of the analyses for this thesis are presented in this chapter. First, the comparisons between the Monte Carlo simulation and the ND280 data are shown in section 11.1. Next, the likelihood fitter results with data are described in section 11.2. Finally, the cross-section measurements are presented in section 11.3.

11.1 Data Unblinding

As mentioned in section 5.2.3, this thesis adopts the "blind analysis" strategy, which means up to this point, the T2K data has not been used (such as for selection development and fitter studies) in order to avoid any unintended biasing to the analysis results. The plots shown in chapter 5 and 6 include the T2K data solely for the purpose of showing the comparisons between the data and the Monte Carlo simulation at each selection step.

This section describes the studies performed after data accessing ("data unblinding"). The data and the Monte Carlo (MC) simulation are compared in these five variables:

- Q^2 - negative four-momentum transferred squared from the neutrino-muon system to the $W^+(W^-)$, the most reliably reconstructed variable in this list as it is only dependent on the muon kinematics in the Monte Carlo simulation.
- p_π and $\cos(\theta_\pi)$ - pion momentum and angle, these are known to have large model dependencies.
- Vertex activity (VA) - one of the selection cut variables (section 4.4.1)

- $|t|$ - momentum transferred squared from the W^+-π^+ (or W^--π^-) system to the target nucleus (the variable used to select SIG (signal region) and SB1 (one of the sidebands). It is expected to have larger modelling uncertainties associated since it is dependent on the pion kinematics.

To further investigate any shape differences of event distributions between the data and the Monte Carlo simulation in the five variables, 2D profile comparisons are also produced. For example, for a 2D distribution of VA vs. Q^2, the profile distributions of VA represent the mean and RMS of VA in each of the Q^2 bin.

11.1.1 ν_μ CC-COH Data and Monte Carlo Simulation Comparisons

Figure 11.1, 11.2 and 11.3 show the data and the Monte Carlo simulation comparisons in VA, $|t|$, Q^2, p_π, and $\cos(\theta_\pi)$ for SIG, SB1, and SB2 respectively. The stacked histograms (from the Monte Carlo simulation) contain Monte Carlo simulation true reaction information. The unstacked histograms (the sum of all the stacked histograms) are plotted with detector systematics. The flux systematics and the cross-section modelling systematics are propagated during the extraction of the cross-section result. They are evaluated together and only in the binning of the analysis (2 bins in $|t|$), which at this point would take a great amount of work to plot them in any other variables. The statistical χ^2 ($\chi^2_{\text{stat.}}$), which is an indicator of the size of the data and Monte Carlo simulation differences, are also computed for each distribution. Overpredictions of events in the Monte Carlo simulation are observed in SB1 and SB2, which suggest overpredictions of the RES and DIS background events. For SIG, SB1 and SB2, the $\chi^2_{\text{stat.}}$ for the VA distributions are higher than the rest of the $\chi^2_{\text{stat.}}$ as a result of the mismodelling of VA, which is one of the analysis variables.

Combinations of 2D distributions and profiles for the five comparison variables (VA, $|t|$, Q^2, p_π, and $\cos(\theta_\pi)$) for SIG, SB1 and SB2 are summarized in figure 11.4, 11.5, and 11.6. The 2D profiles against Q^2 provide the most insight into any shape difference between the data and the Monte Carlo simulation since Q^2 is the most reliably reconstructed variable.

For SIG and SB1, the 2D profile of VA against Q^2 indicates a shape difference between the data and the Monte Carlo simulation; the $\chi^2_{\text{stat.}}$ from VA vs. Q^2 is significantly larger than the $\chi^2_{\text{stat.}}$ of the rest of the variables. This difference motivates the fake data study (appendix H.3) where VA is shifted up by 1 MeV for all the events. In addition, the $\chi^2_{\text{stat.}}$ of the 2D profile of p_π against Q^2 for SIG is much larger than the SB1 $\chi^2_{\text{stat.}}$ (27.88 compared to 3.77); this suggests possible mismodelling of CC-COH pion momentum. However, since the analysis does not directly use the pion momentum variable (it is still used for the reconstruction of

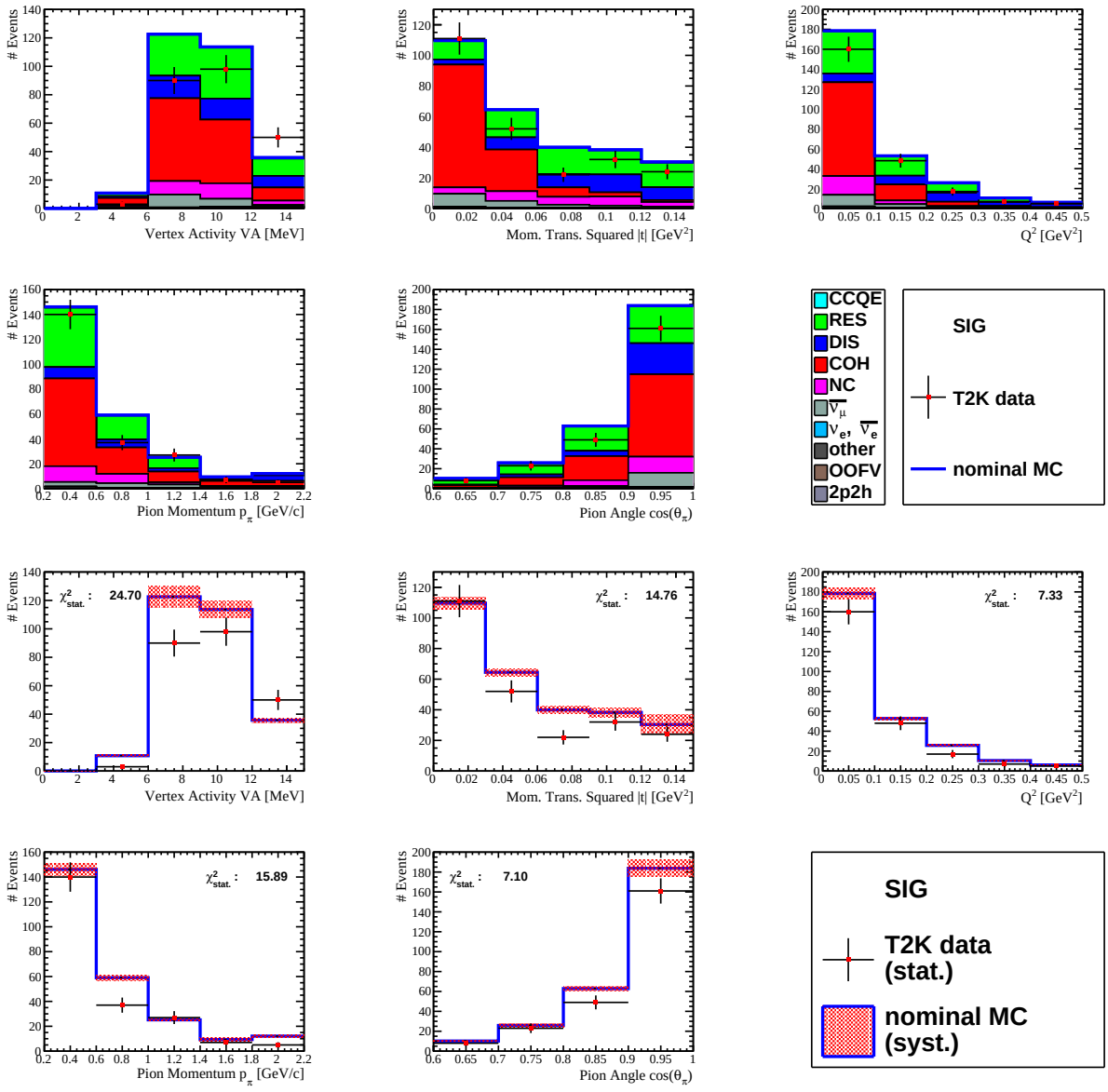

Figure 11.1. ν_μ SIG data and Monte Carlo (MC) simulation comparisons in VA, $|t|$, Q^2, p_π, and $\cos(\theta_\pi)$. The stacked histograms (top two rows) represent the Monte Carlo simulation true reaction types of the events. Shape difference in the VA distribution is observed. The unstacked MC histograms (bottom two rows) are plotted with the detector systematics. The $\chi^2_{\text{stat.}}$ between the data and MC are also computed for each distribution. The VA distribution comparison has the largest $\chi^2_{\text{stat.}}$.

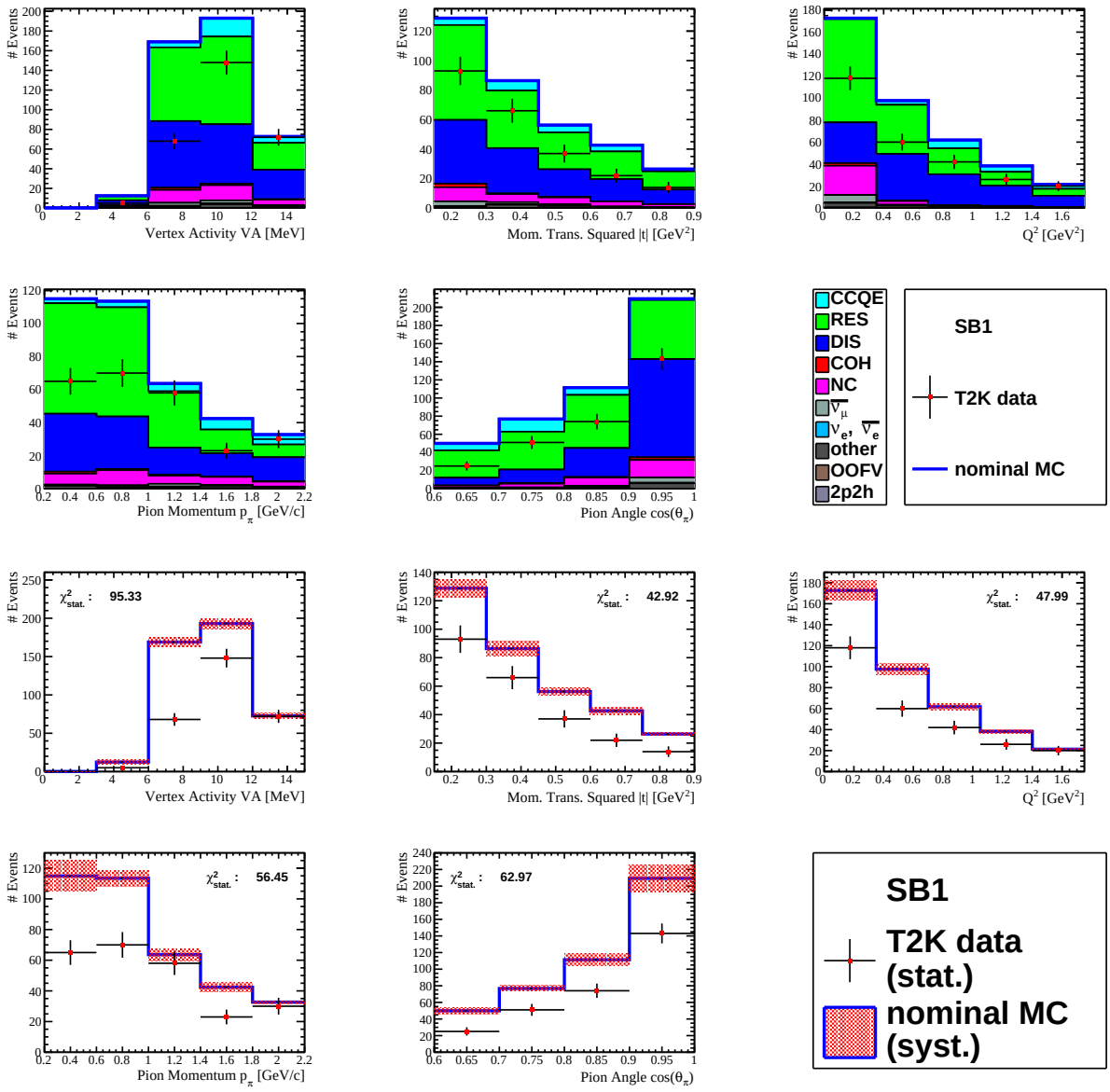

Figure 11.2. ν_μ SB1 data and Monte Carlo (MC) simulation comparisons in VA, $|t|$, Q^2, p_π, and $\cos(\theta_\pi)$. The stacked histograms (top two rows) represent the Monte Carlo simulation true reaction types of the events. Overprediction of events in MC is observed in most bins. Larger discrepancies in the low Q^2, low p_π, and the small θ_π regions are observed. The unstacked MC histograms (bottom two rows) are plotted with the detector systematics. The $\chi^2_{\text{stat.}}$ between the data and MC are also computed for each distribution. The VA distribution comparison has the largest $\chi^2_{\text{stat.}}$, but all the $\chi^2_{\text{stat.}}$ are large due to the normalization difference between data and MC. Mismodelling of the RES and DIS background events in the MC is a likely cause of the large normalization difference.

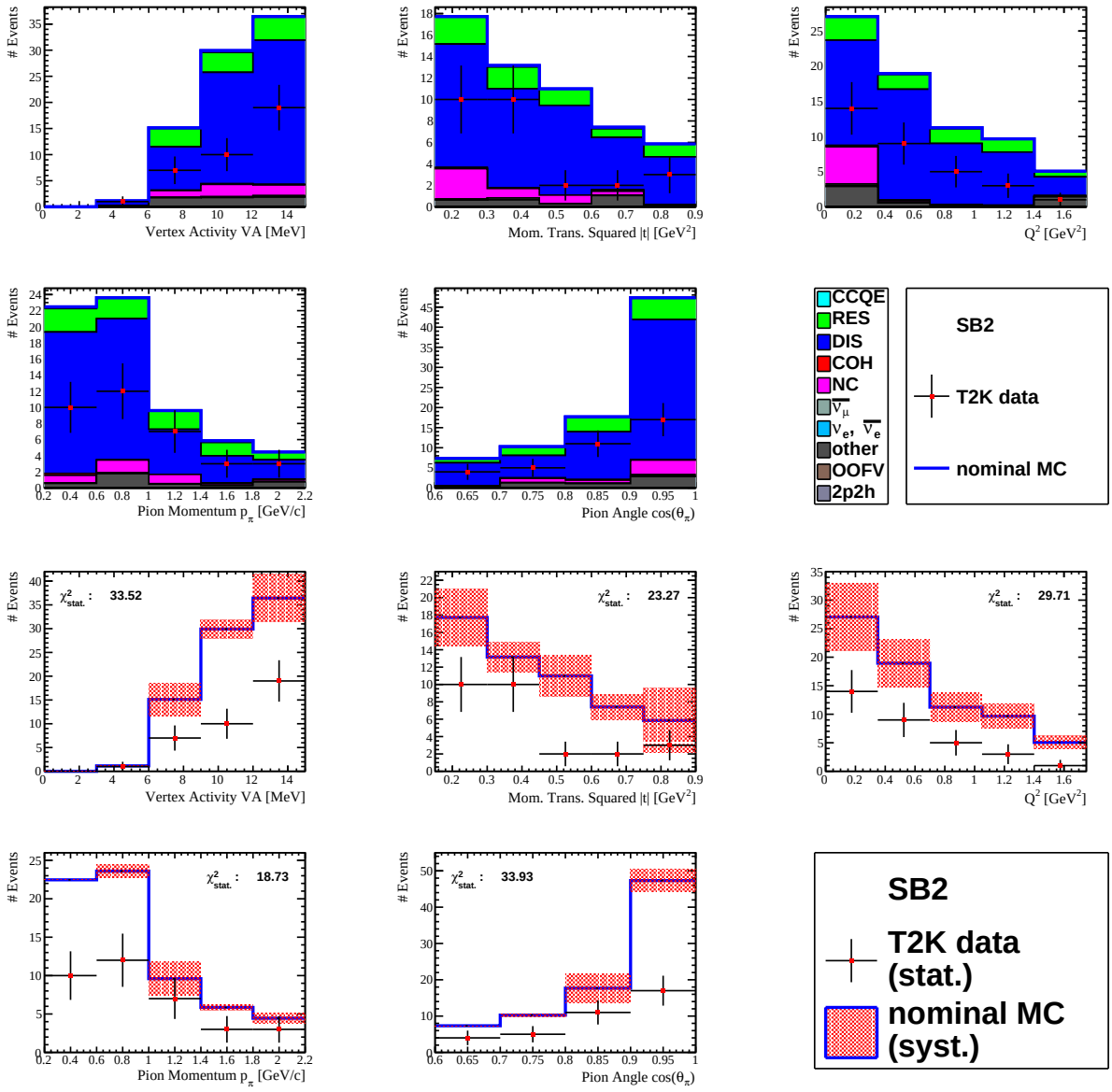

Figure 11.3. ν_μ SB2 data and Monte Carlo (MC) simulation comparisons in VA, $|t|$, Q^2, p_π, and $\cos(\theta_\pi)$. The stacked histograms (top two rows) represent the Monte Carlo simulation true reaction types of the events. Overprediction of events in MC is observed in most bins. Larger discrepancies in the low Q^2, low p_π, and the small θ_π regions are observed. Since SB2 contains 70% DIS, the data and MC difference indicate overprediction of DIS in the MC. The unstacked MC histograms (bottom two rows) are plotted with the detector systematics. The $\chi^2_{\text{stat.}}$ between data and MC are all large due to the normalization difference which is caused by the overprediction of DIS in the MC.

$|t|$), but the impact of the potential mismodelling is minimal.

SB2 has seven times less statistics than SB1, making it difficult to draw any conclusions from the 2D profiles. However, no significant deviation is observed between the data and the Monte Carlo simulation.

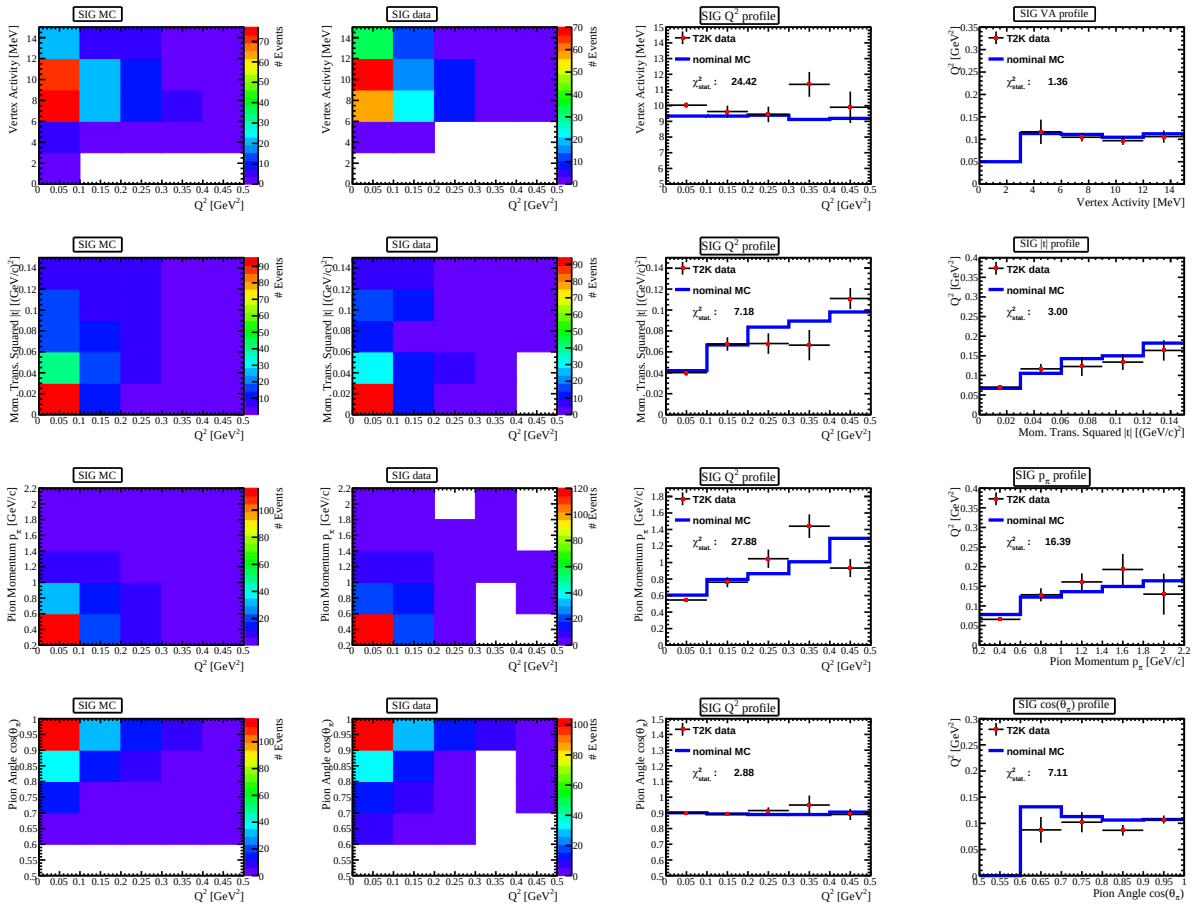

Figure 11.4. ν_μ SIG data and Monte Carlo (MC) simulation comparisons in VA, $|t|$, Q^2, p_π, and $\cos(\theta_\pi)$. The 2D distributions and profiles of the five variables against each other are produced to study shape differences between the data and the MC. There are hints of shape difference coming from the larger $\chi^2_{\text{stat.}}$ in the VA vs. Q^2 (24.42) and p_π vs. Q^2 (27.88) profiles.

11.1.2 $\bar{\nu}_\mu$ CC-COH Data and Monte Carlo simulation Comparisons

Similar comparison plots are produced for the $\bar{\nu}_\mu$ CC-COH SIG and SB1. Figure 11.7 and 11.8 show the data and Monte Carlo simulation comparisons for the five comparison variables (VA, $|t|$, Q^2, p_π, and $\cos(\theta_\pi)$). The stacked histograms contain Monte Carlo simulation true

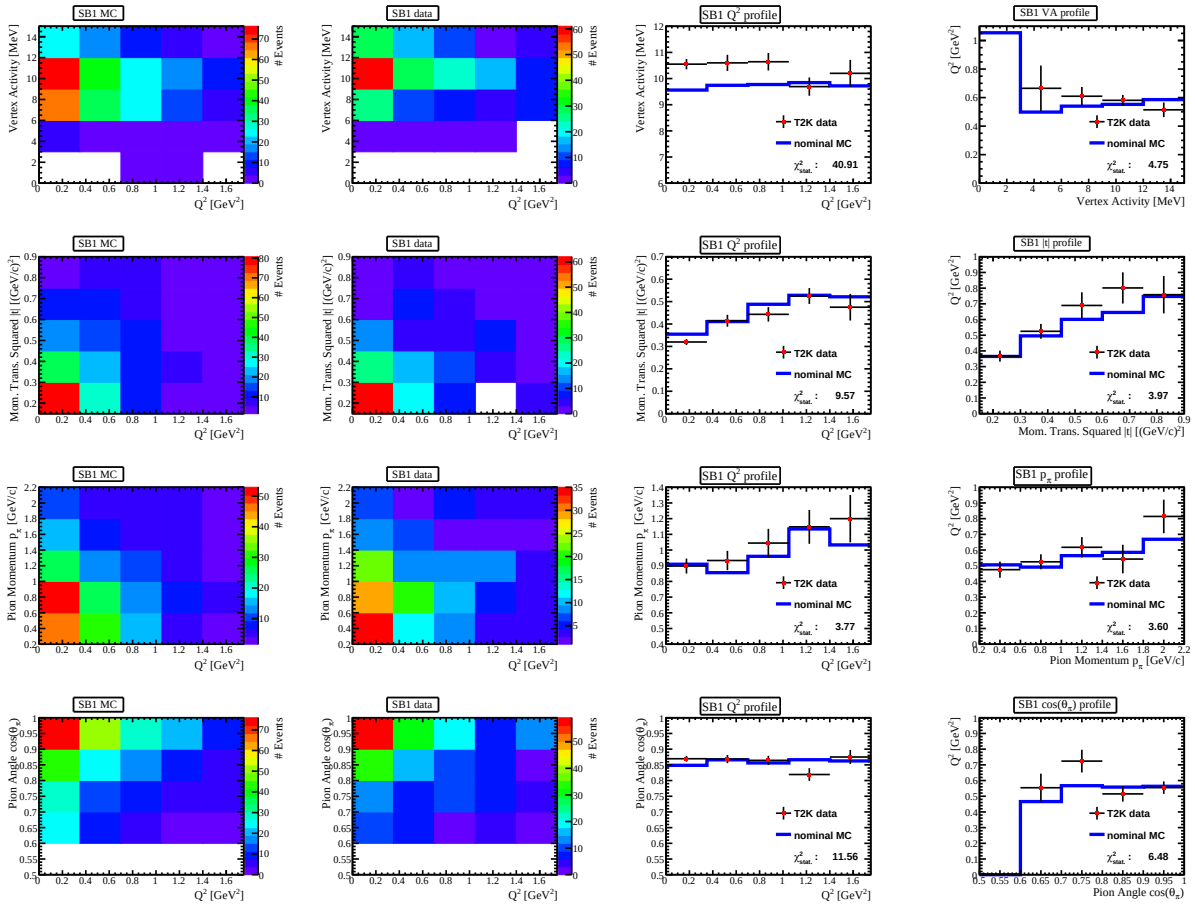

Figure 11.5. ν_μ SB1 data and Monte Carlo (MC) simulation comparisons in VA, $|t|$, Q^2, p_π, and $\cos(\theta_\pi)$. The 2D distributions and profiles of the five variables against each other are produced to study shape differences between the data and the MC. A shape difference is observed in VA; the $\chi^2_{\text{stat.}}$ from the VA vs. Q^2 profile (40.91) is significantly larger than the rest $\chi^2_{\text{stat.}}$.

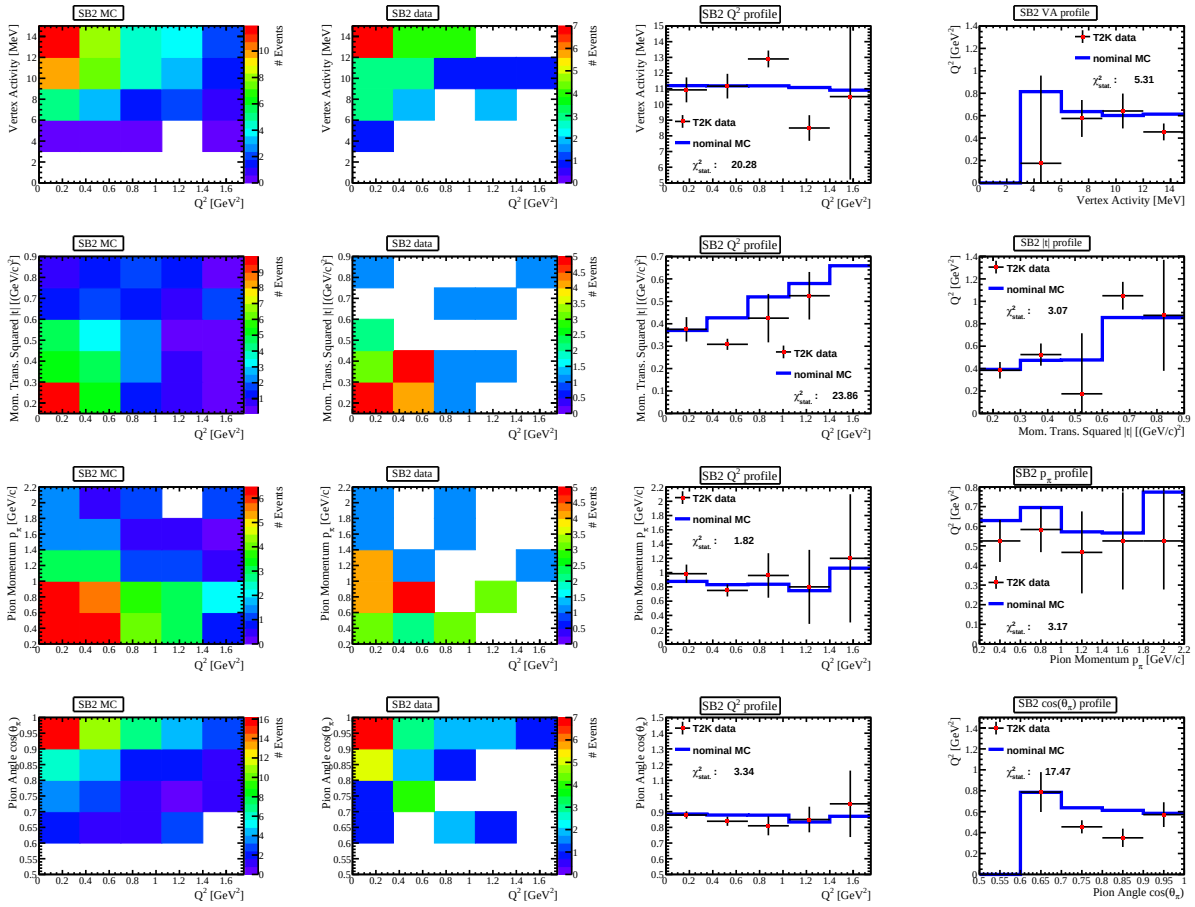

Figure 11.6. ν_μ SB2 data and Monte Carlo (MC) simulation comparisons in VA, $|t|$, Q^2, p_π, and $\cos(\theta_\pi)$. The 2D distributions and profiles of the five variables against each other are produced to study shape differences between the data and the MC. The statistics in SB2 is almost seven times smaller than SB1. It is difficult to draw conclusions from the plots. However, no obvious difference between the data and MC is observed. There are hints of shape difference coming from the larger $\chi^2_{\text{stat.}}$ in the VA vs. Q^2 and $|t|$ vs. Q^2 profiles.

reaction information. The unstacked Monte Carlo simulation histograms are plotted with the detector systematics. The $\chi^2_{\text{stat.}}$, which describes the size of the data and Monte Carlo simulation differences, are also computed for each distribution. Overpredictions of events in Monte Carlo simulation are observed in SB1 in the majority of the bins, which suggests overpredictions of the RES background events. For SIG and SB1, the $\chi^2_{\text{stat.}}$ for the VA distributions suggest possible shape differences. Recall there is no SB2 for the $\bar{\nu}_\mu$ CC-COH selection because deep inelastic scattering is not a significant background.

To study the shape differences, combinations of 2D distributions and the profiles of the five comparison variables for the $\bar{\nu}_\mu$ SIG and SB1 are summarized in figure 11.9 and figure 11.10. The 2D profiles against Q^2 provide the most insight into any shape difference between the data and the Monte Carlo simulation since Q^2 is the most reliably reconstructed variable. There is a hint[1] that the data and Monte Carlo simulation have different VA distribution shapes. Larger $\chi^2_{\text{stat.}}$ (from VA vs. Q^2) are observed in both SIG and SB1. Similar to the ν_μ SIG, the $\chi^2_{\text{stat.}}$ of the 2D profile of p_π against Q^2 for SIG is much larger than the SB1 $\chi^2_{\text{stat.}}$ (24.17 compared to 5.59); this reaffirms the previous suggestion on the possible mismodelling of CC-COH pion momentum. However, since the analysis does not directly use the pion momentum variable, the impact of the potential mismodelling is minimal.

[1] The indication is not as strong as the ν_μ SB1 case.

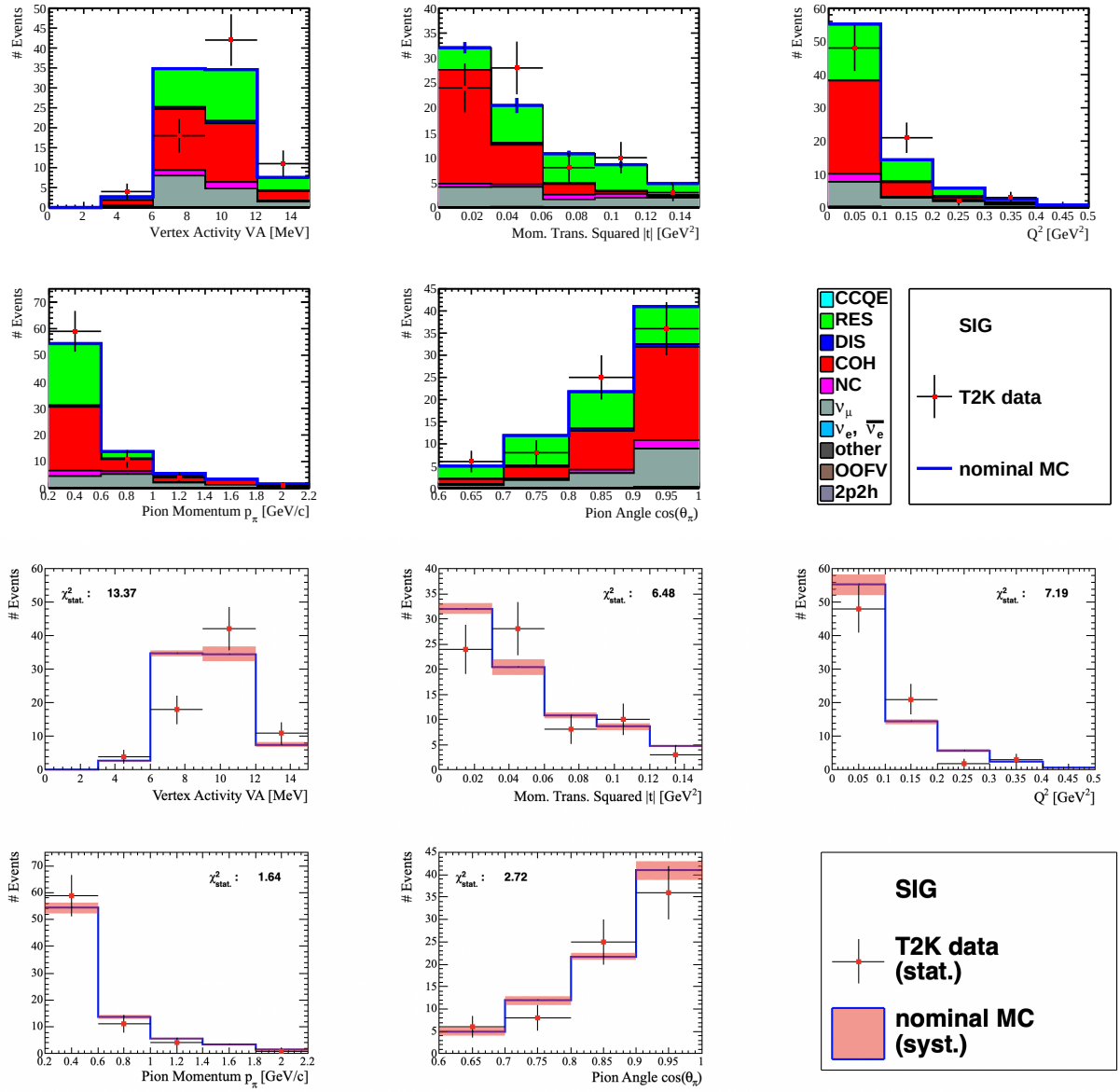

Figure 11.7. $\bar{\nu}_\mu$ SIG data and Monte Carlo (MC) simulation comparisons in VA, $|t|$, Q^2, p_π, and $\cos(\theta_\pi)$. The stacked histograms (top two rows) represent the Monte Carlo simulation true reaction types of the events. The unstacked MC histograms (bottom two rows) are plotted with the detector systematics. The $\chi^2_{\text{stat.}}$ between the data and MC are also computed for each distribution. The VA distribution comparison has a much larger $\chi^2_{\text{stat.}}$, which indicates a possible shape difference.

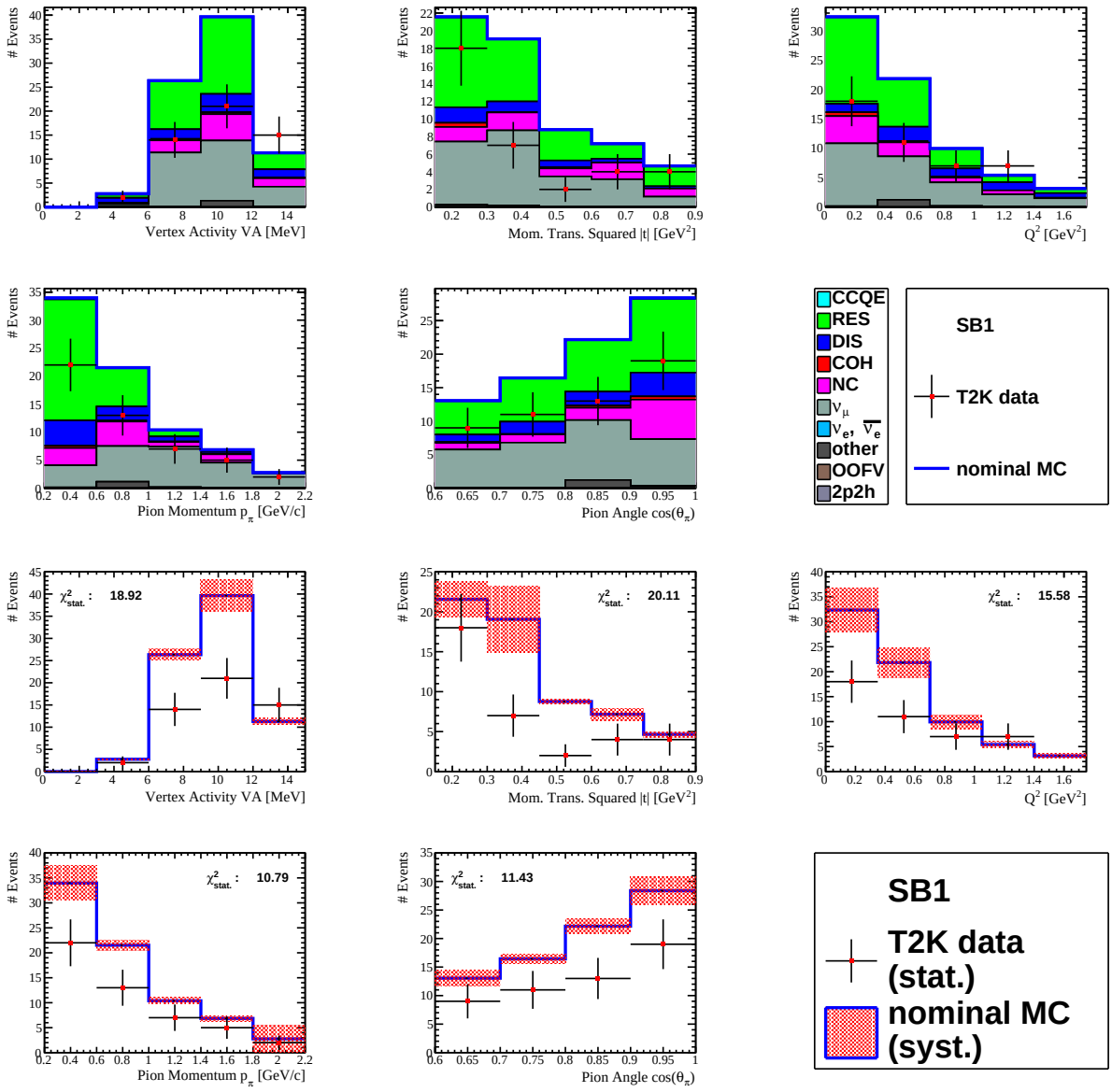

Figure 11.8. $\bar{\nu}_\mu$ SB1 data and Monte Carlo (MC) simulation comparisons in VA, $|t|$, Q^2, p_π, and $\cos(\theta_\pi)$. The stacked histograms (top two rows) represent the Monte Carlo simulation true reaction types of the events. The unstacked MC histograms (bottom two rows) are plotted with the detector systematics. The $\chi^2_{\text{stat.}}$ between the data and MC are also computed for each distribution. The large $\chi^2_{\text{stat.}}$ for all five distributions suggest overprediction of events in the MC. Mismodelling of the RES and ν_μ background events in the MC is a likely cause of the large normalization difference.

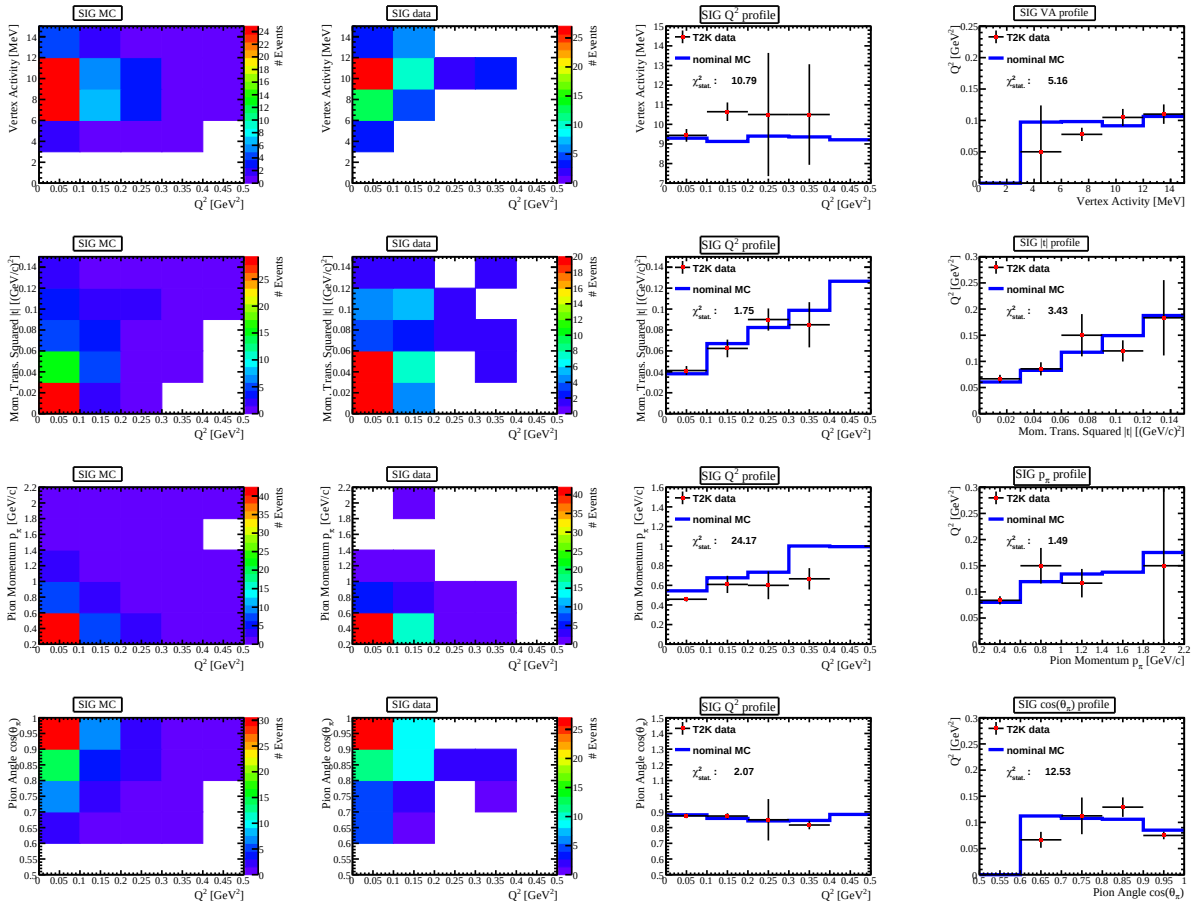

Figure 11.9. $\bar{\nu}_\mu$ SIG data and Monte Carlo (MC) simulation comparisons in VA, $|t|$, Q^2, p_π, and $\cos(\theta_\pi)$. The 2D distributions and profiles of the five variables against each other are produced to study shape differences between the data and the MC. There is a hint of shape difference coming from the larger $\chi^2_{\text{stat.}}$ (10.79) in the VA vs. Q^2 profile. There also seem to be shape difference in p_π, where the $\chi^2_{\text{stat.}}$ in the p_π vs. Q^2 profile (24.17) is large.

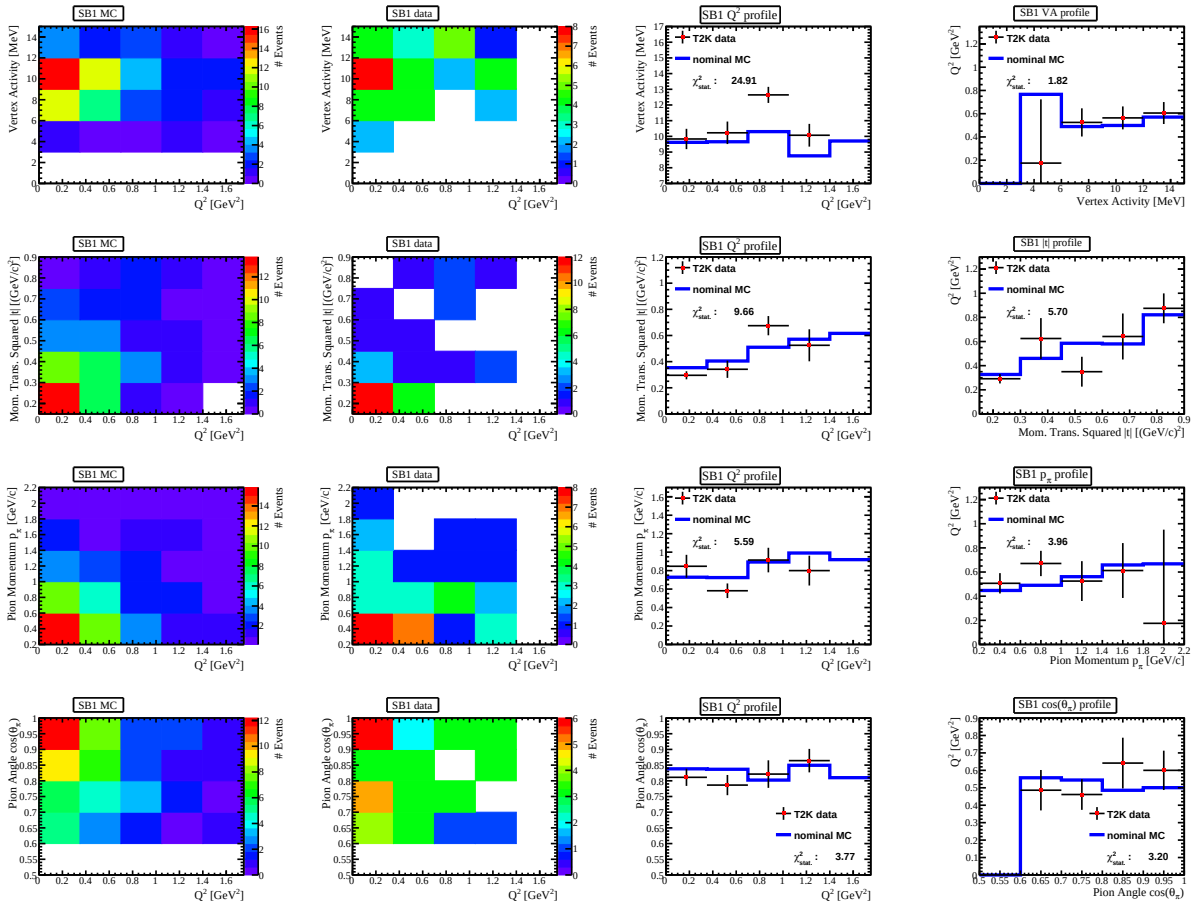

Figure 11.10. $\bar{\nu}_\mu$ SB1 data and Monte Carlo (MC) simulation comparisons in VA, $|t|$, Q^2, p_π, and $\cos(\theta_\pi)$. The 2D distributions and profiles of the five variables against each other are produced to study shape differences between the data and the MC. A shape difference is observed in VA; the $\chi^2_{\text{stat.}}$ from the VA vs. Q^2 profile (24.91) is larger than the rest $\chi^2_{\text{stat.}}$.

11.2 Likelihood Fitter Results

11.2.1 ν_μ CC-COH Likelihood Fitter Results

Figure 11.11 shows the pre-fit and post-fit parameters (the fit parameters are listed in table 9.4). The post-fit DIS dial values (bin 24-26) are shifted significantly from their pre-fit nominal values. This behaviour is expected due to the large data and Monte Carlo simulation difference seen in SB2 (as shown in figure 11.3).

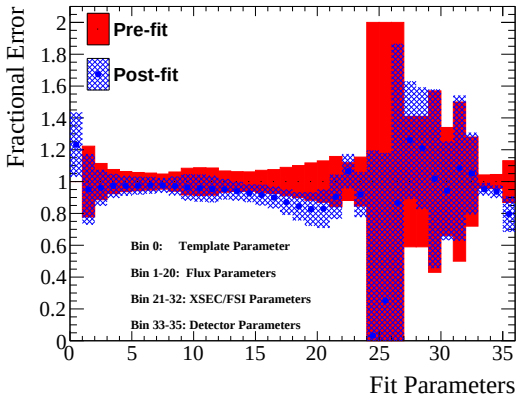

Figure 11.11. Overlayed pre-fit and post-fit parameters with their uncertainties for the ν_μ CC-COH fit with T2K data.

Figure 11.12 shows the reconstructed event distributions of SIG, SB1, and SB2. A reminder that the uncertainties shown here are the statistical uncertainties. Overpredictions of events in the nominal Monte Carlo simulation are observed in all three bins. The χ^2_{postfit} (9.44) improved significantly from the χ^2_{prefit} (82.53), which indicates a much-improved data and Monte Carlo simulation agreement after the fit. The χ^2_{postfit} is not small (9.44) due to the significant difference between data and Monte Carlo simulation in SB2 as a result of overprediction of the DIS background events.

Figure 11.13, 11.14, and 11.15 show the data, nominal Monte Carlo simulation (pre-fit), and post-fit Monte Carlo simulation comparisons in VA, $|t|$, Q^2, p_π, and $\cos(\theta_\pi)$ for SIG, SB1, and SB2. Overall, the $\chi^2_{\text{stat.}}$(post-fit) are reduced from the $\chi^2_{\text{stat.}}$(pre-fit), which suggest improvements to the data and Monte Carlo simulation agreement (especially in the normalization).

The 2D distributions and the profile distribution comparisons are shown in figure 11.16, 11.17, and 11.18. The $\chi^2_{\text{stat.}}$ from the VA vs. Q^2 are all quite large (26.10 for SIG and 39.65 for SB1), which suggest a shape difference between the data and the Monte Carlo simulation after the fit. This is due to the fitter's lack of degree of freedom in the VA space (no dials to

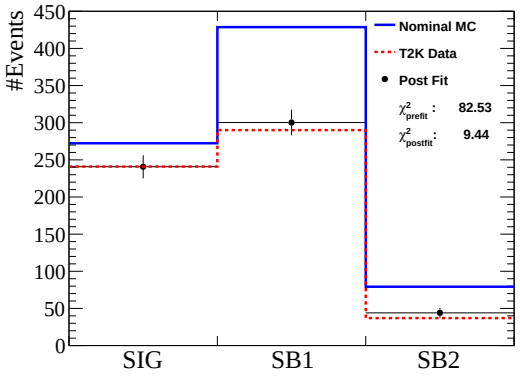

Figure 11.12. Nominal Monte Carlo (MC) simulation (Pre-fit), T2K data, and post-fit (with stat. uncertainty) reconstructed event distributions of the 3 samples for the ν_μ fit for T2K data. The χ^2_{postfit} (9.44) improved significantly from the χ^2_{prefit} (82.53), which indicates a much improved data and Monte Carlo simulation agreement after the fit.

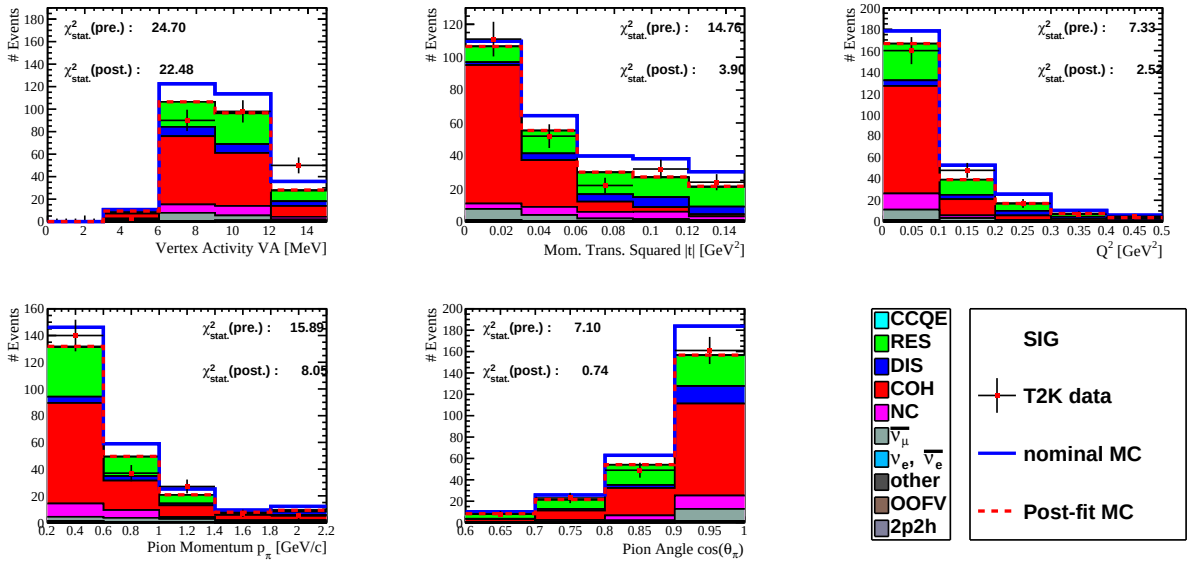

Figure 11.13. ν_μ SIG data, nominal Monte Carlo (MC) simulation (pre-fit), and post-fit Monte Carlo simulation comparisons in VA, $|t|$, Q^2, p_π, and $\cos(\theta_\pi)$. The stacked histograms represent the true reaction types of the events. The smaller post-fit $\chi^2_{\text{stat.}}$ suggest improved data and MC agreement in all five variables after the fit.

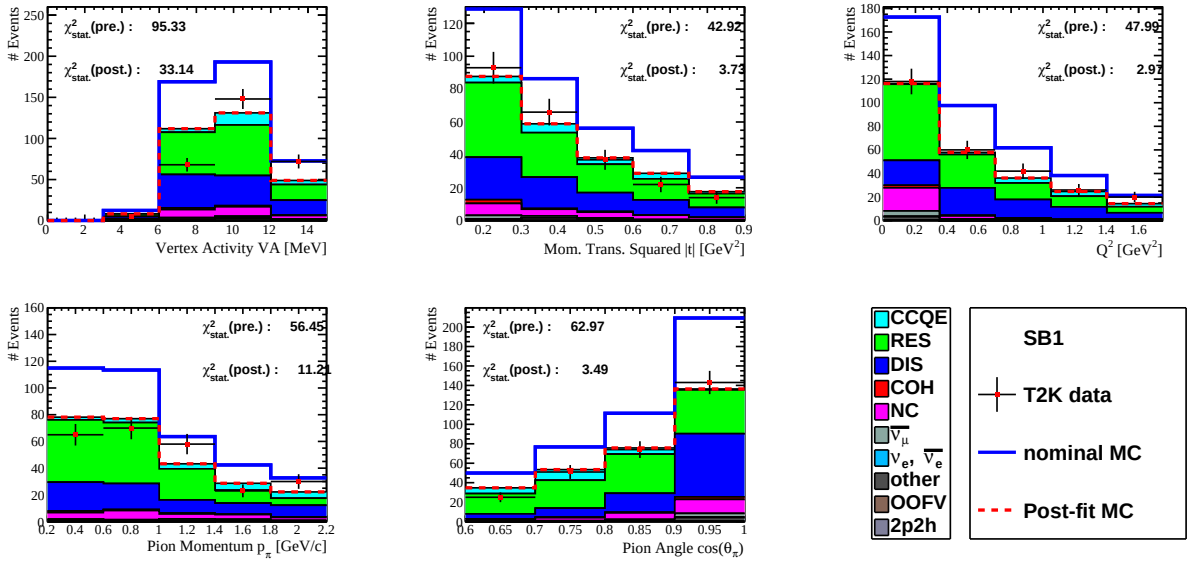

Figure 11.14. ν_μ SB1 data, nominal Monte Carlo (MC) simulation (pre-fit), and post-fit Monte Carlo simulation comparisons in VA, $|t|$, Q^2, p_π, and $\cos(\theta_\pi)$. The stacked histograms represent the true reaction types of the events. The smaller post-fit $\chi^2_{\text{stat.}}$ suggest improved data and MC agreement in all five variables after the fit.

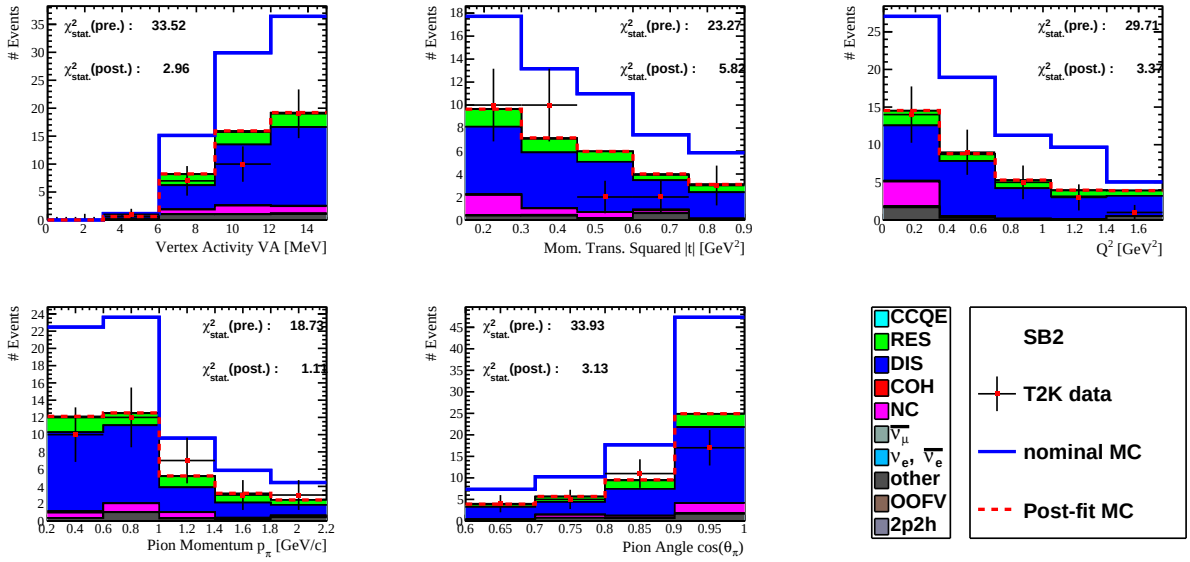

Figure 11.15. ν_μ SB2 data, nominal Monte Carlo (MC) simulation (pre-fit), and post-fit Monte Carlo simulation comparisons in VA, $|t|$, Q^2, p_π, and $\cos(\theta_\pi)$. The stacked histograms represent the true reaction types of the events. The smaller post-fit $\chi^2_{\text{stat.}}$ suggest improved data and MC agreement in all five variables after the fit.

adjust the shape of VA).

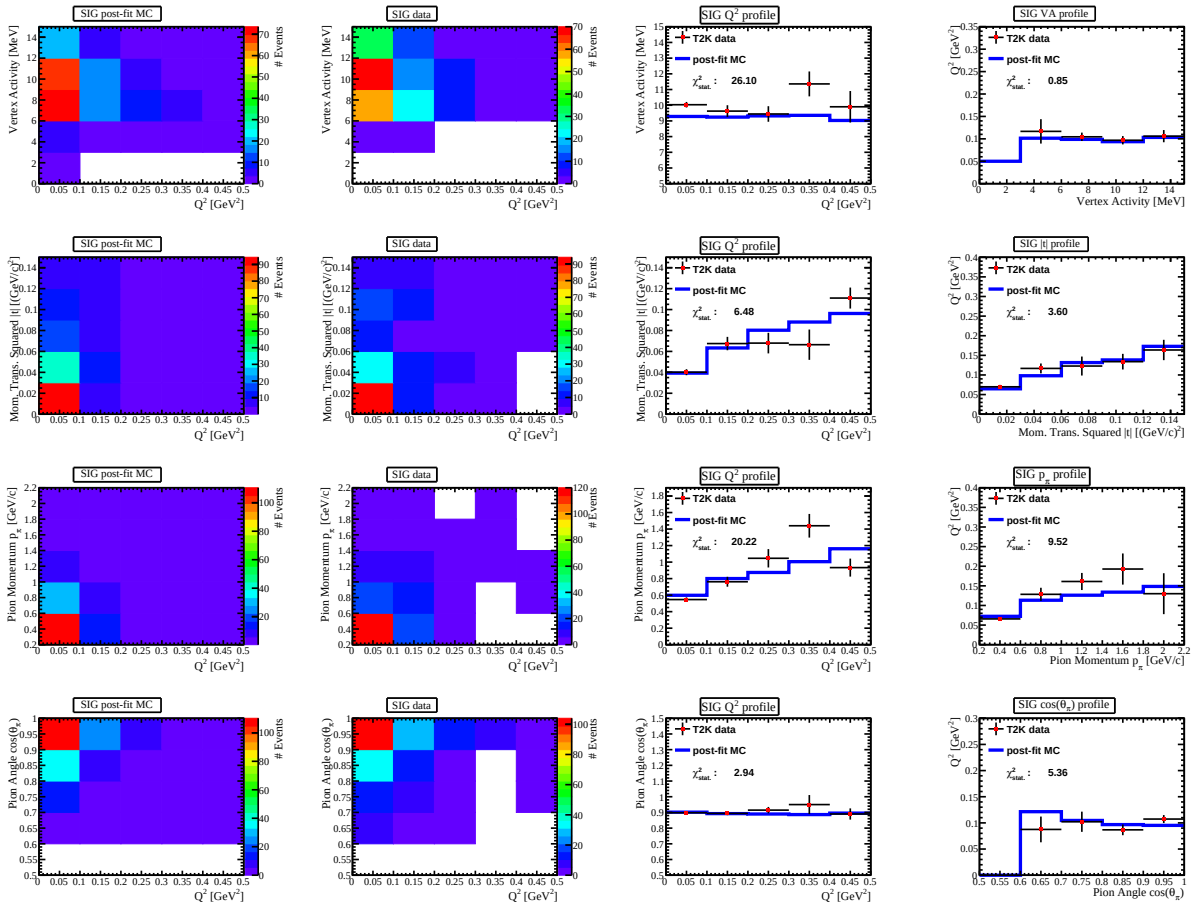

Figure 11.16. ν_μ SIG data and post-fit Monte Carlo (MC) simulation comparisons in VA, $|t|$, Q^2, p_π, and $\cos(\theta_\pi)$. The 2D distributions and profiles of the five variables against each other are produced to study shape differences between the data and the MC. The large post-fit $\chi^2_{\text{stat.}}$ from the VA vs. Q^2 (26.10) and p_π vs. Q^2 (20.22) profiles suggest shape differences in VA and p_π after the fit. This is due to the fitter's lack of degrees of freedom in the VA and p_π space (no dials to adjust the shape of VA and p_π).

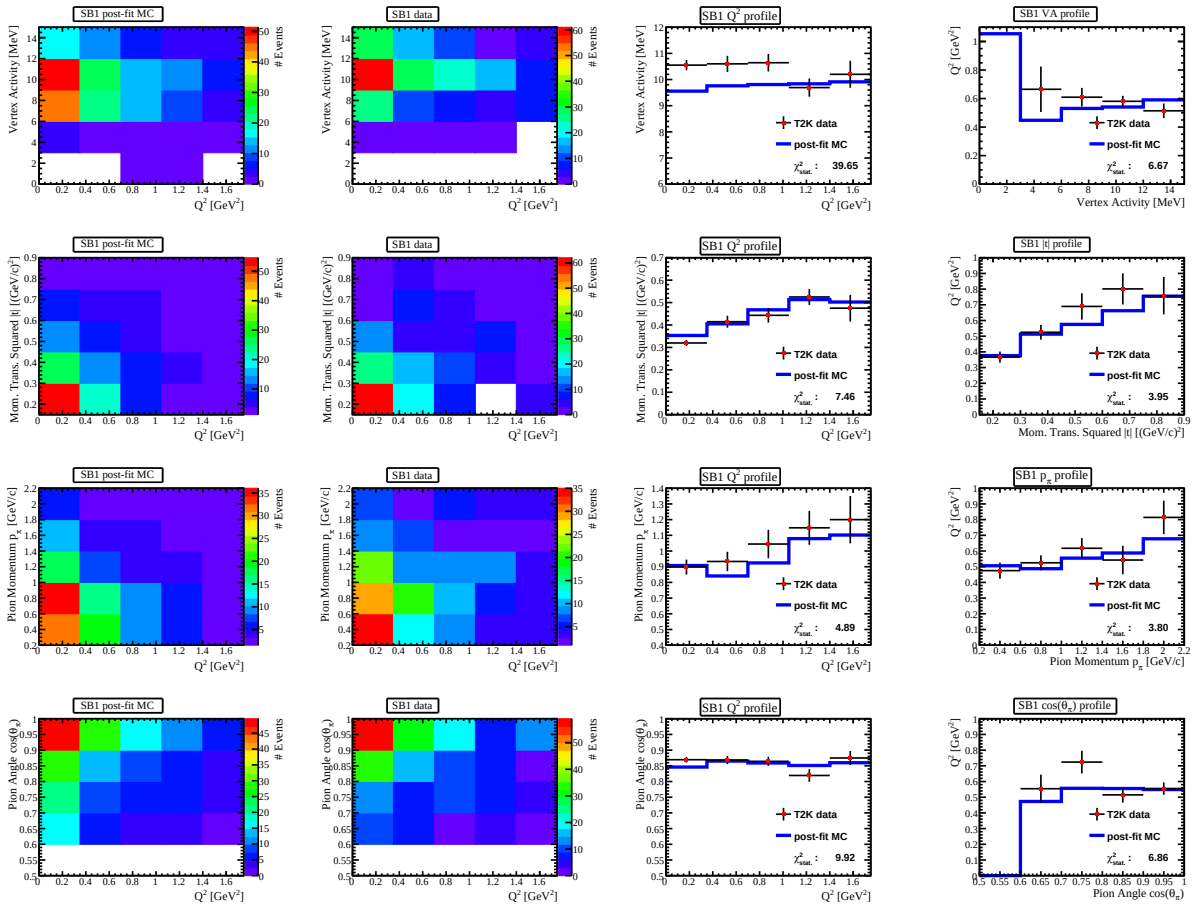

Figure 11.17. ν_μ SB1 data and post-fit Monte Carlo (MC) simulation comparisons in VA, $|t|$, Q^2, p_π, and $\cos(\theta_\pi)$. The 2D distributions and profiles of the five variables against each other are produced to study shape differences between the data and the MC. The $\chi^2_{\text{stat.}}$ of the VA vs. Q^2 profile is 40.91 before the fit (figure 11.5) and 39.65 after the fit (this figure). The shape difference in VA is not improved much after the fit due to the fitter's lack of degree of freedom in the VA space (no dials to adjust the shape of VA).

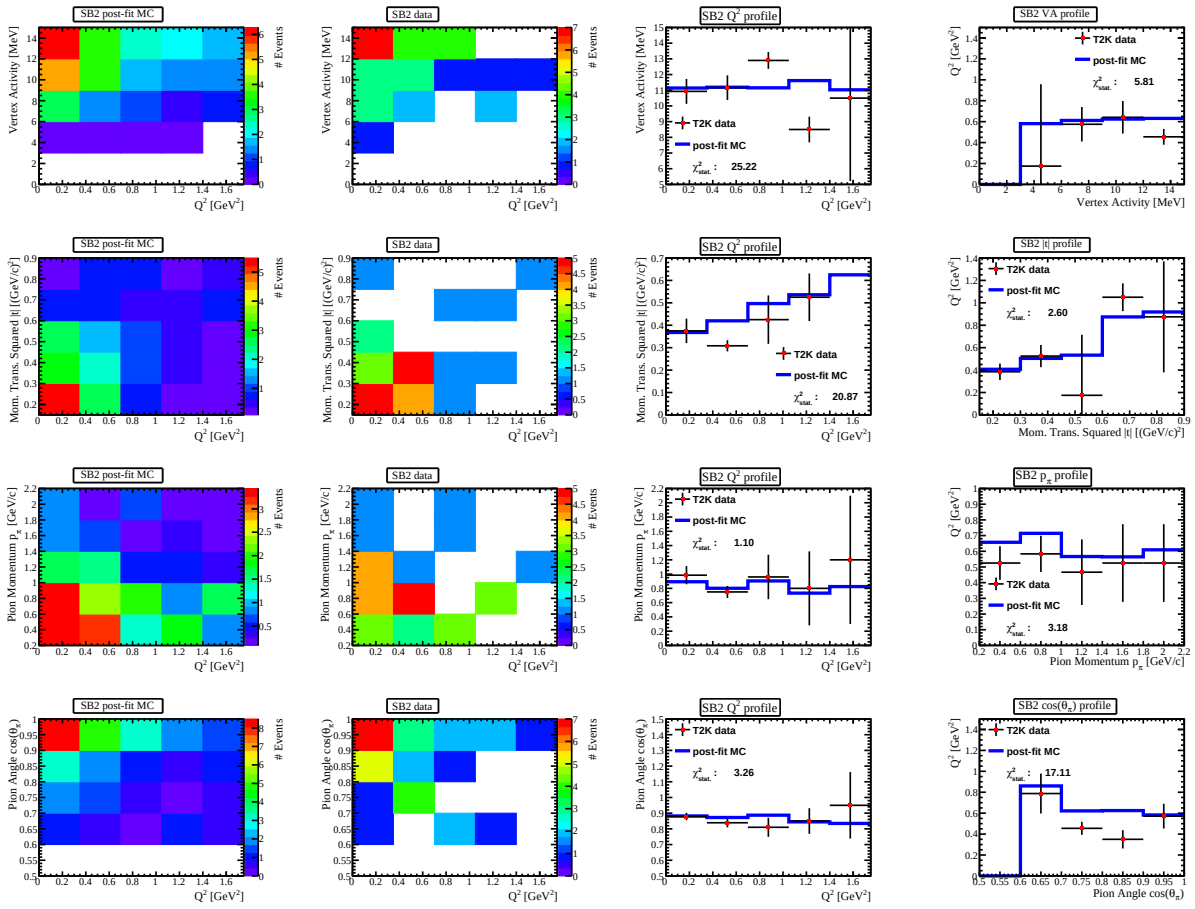

Figure 11.18. ν_μ SB2 data and post-fit Monte Carlo (MC) simulation comparisons in VA, $|t|$, Q^2, p_π, and $\cos(\theta_\pi)$. The 2D distributions and profiles of the five variables against each other are produced to study shape differences between the data and the MC. The statistics in SB2 is almost seven times smaller than SB1. It is difficult to draw conclusions from the plots. However, no obvious difference between the data and MC is observed.

11.2.2 $\bar{\nu}_\mu$ CC-COH Likelihood Fitter Results

Figure 11.19 shows the pre-fit and post-fit parameters (the fit parameters are listed in table 9.4). The DIS dials (bin 24-26) are shifted significantly from their pre-fit nominal values, although the movements are smaller compared to the ν_μ analysis. The reason for the smaller DIS dial movements is because the DIS events are not a major background source for the $\bar{\nu}_\mu$ CC-COH selection.

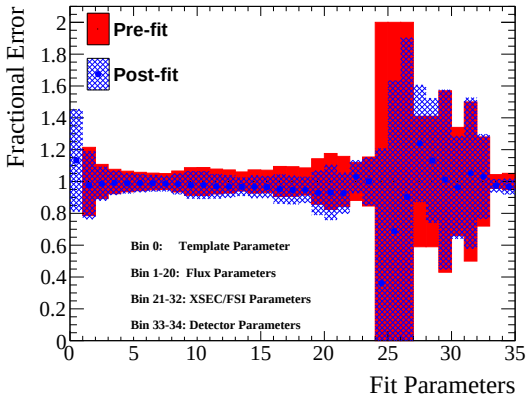

Figure 11.19. Overlayed pre-fit and post-fit parameters with their uncertainties for the $\bar{\nu}_\mu$ CC-COH fit with T2K data.

Figure 11.20 shows the reconstructed event distributions. Large overprediction of events is observed in SB1. The χ^2_{postfit} is 4.62, which suggests that the fitter has difficulties adjusting the background event differences between data and Monte Carlo simulation in SB1.

Figure 11.21 and 11.22 show the data, nominal Monte Carlo simulation (pre-fit), and post-fit Monte Carlo simulation comparisons in VA, $|t|$, Q^2, p_π, and $\cos(\theta_\pi)$ for SIG and SB1. The post-fit $\chi^2_{\text{stat.}}$ are not improved by much since the differences between the data and the MC are already small in all five variables.

The 2D distributions and the profile distribution comparisons are shown in figure 11.23 and 11.24. Overall, the $\chi^2_{\text{stat.}}$(post.) are reduced from the $\chi^2_{\text{stat.}}$(pre.) for both the 1D and the profile comparisons, which suggest improvements in both the normalization and the shape for the five variables after the fit. The signal region $\chi^2_{\text{stat.}}$(post.) are not improved much since the data and the Monte Carlo simulation are already in good agreement.

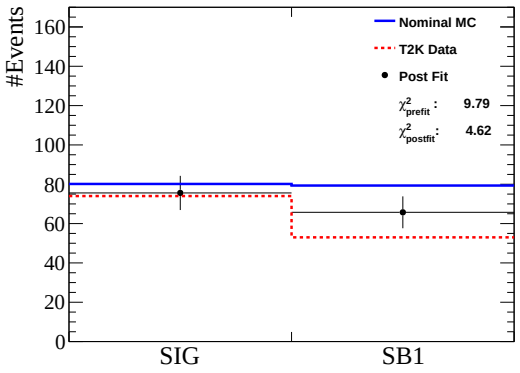

Figure 11.20. Nominal Monte Carlo (MC) simulation (Pre-fit), T2K data, and post-fit (with stat. uncertainty) reconstructed event distributions of the 2 samples for the $\bar{\nu}_\mu$ fit for T2K data. The χ^2_{postfit} (4.62) is improved from the χ^2_{prefit} (9.79), which indicates improved data and Monte Carlo simulation agreement after the fit.

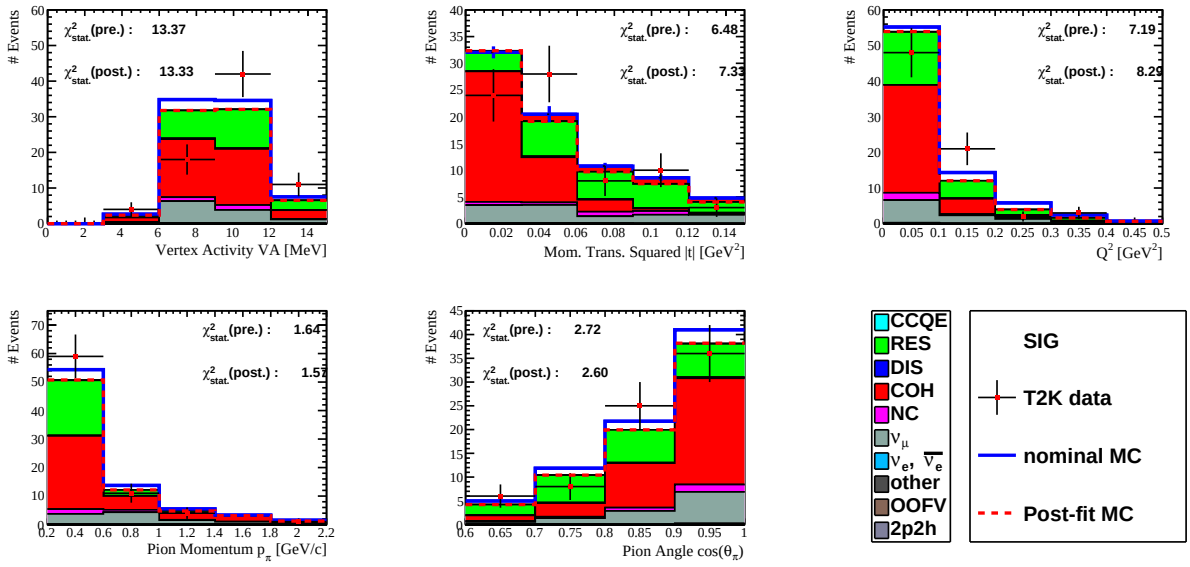

Figure 11.21. $\bar{\nu}_\mu$ SIG data, nominal Monte Carlo (MC) simulation (pre-fit), and post-fit Monte Carlo simulation comparisons in VA, $|t|$, Q^2, p_π, and $\cos(\theta_\pi)$. The stacked histograms represent the true reaction types of the events. The post-fit $\chi^2_{\text{stat.}}$ are not improved by much since the differences between the data and the MC are already small in all five variables.

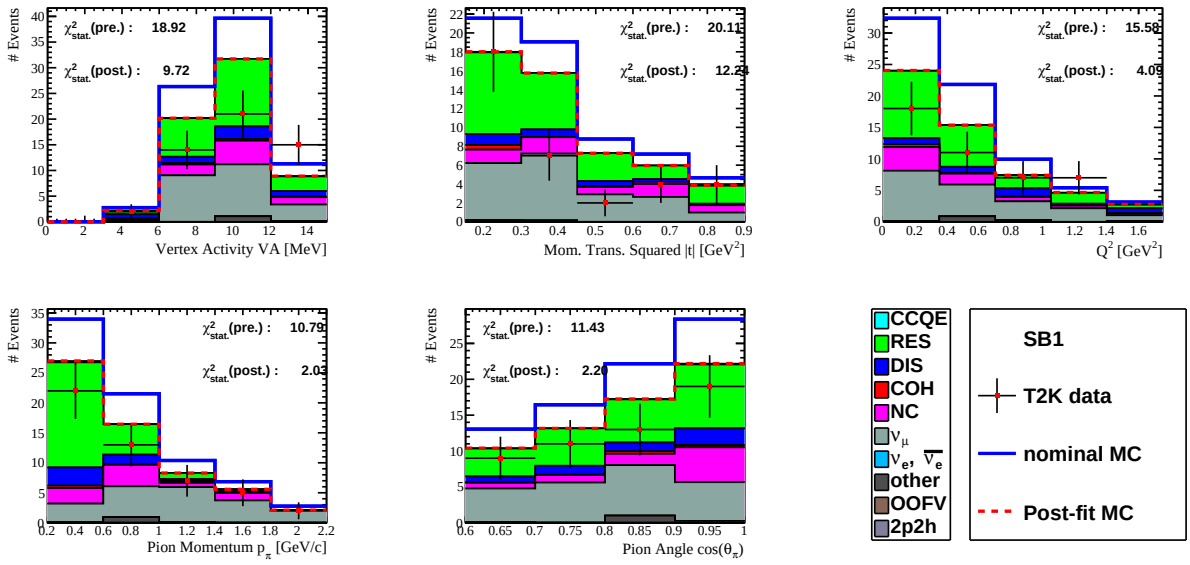

Figure 11.22. $\bar{\nu}_\mu$ SB1 data, nominal Monte Carlo (MC) simulation (pre-fit), and post-fit Monte Carlo simulation comparisons in VA, $|t|$, Q^2, p_π, and $\cos(\theta_\pi)$. The stacked histograms represent the true reaction types of the events. The smaller post-fit $\chi^2_{\text{stat.}}$ suggest improved data and MC agreement in all five variables after the fit.

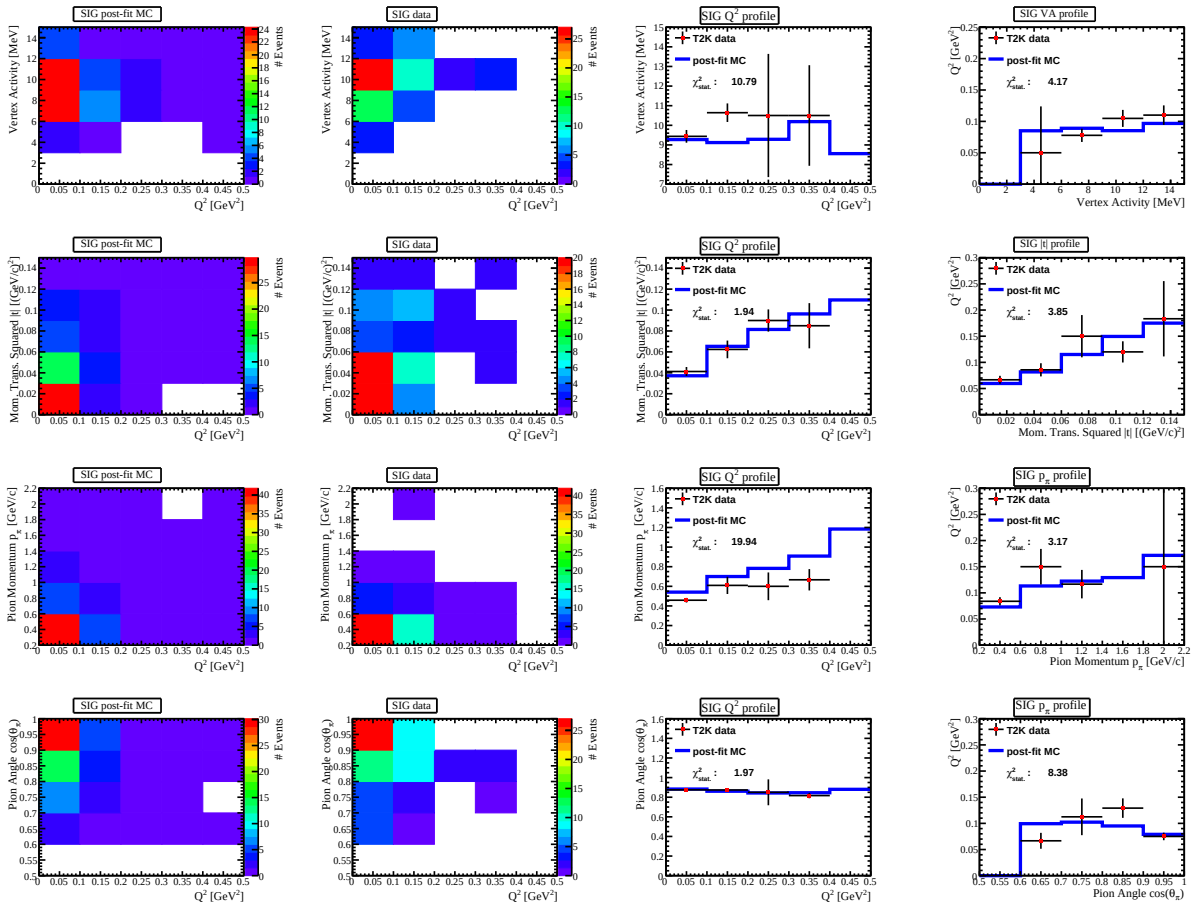

Figure 11.23. $\bar{\nu}_\mu$ SIG data and post-fit Monte Carlo (MC) simulation comparisons in VA, $|t|$, Q^2, p_π, and $\cos(\theta_\pi)$. The 2D distributions and profiles of the five variables against each other are produced to study shape differences between the data and the MC. The $\chi^2_{\text{stat.}}$ of the p_π vs. Q^2 profile is 24.17 before the fit (figure 11.9) and 27.81 after the fit (this figure). The shape difference in p_π is not improved at all (even increased slightly) after the fit due to the fitter's lack of degree of freedom in the p_π space (no dials to adjust the shape of p_π).

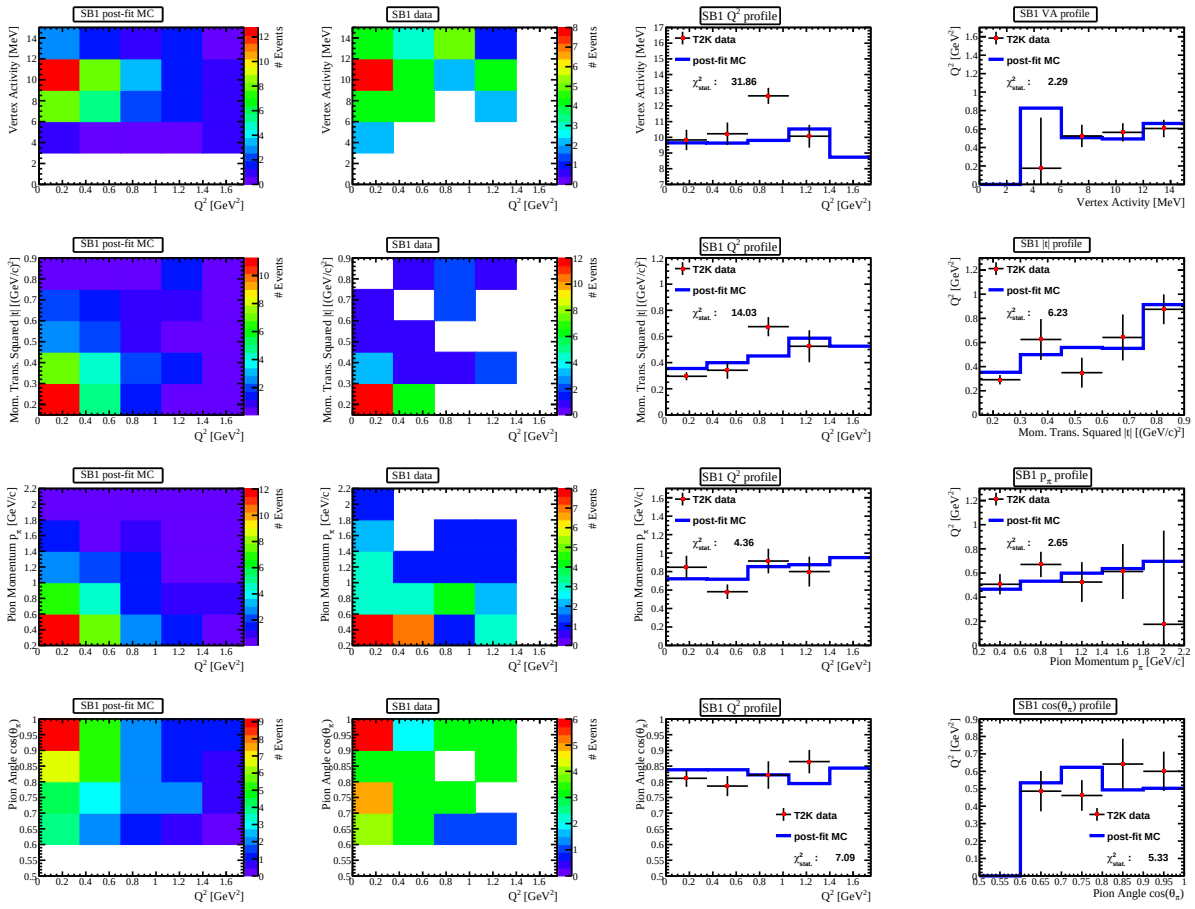

Figure 11.24. $\bar{\nu}_\mu$ SB1 data and post-fit Monte Carlo (MC) simulation comparisons in VA, $|t|$, Q^2, p_π, and $\cos(\theta_\pi)$. The 2D distributions and profiles of the five variables against each other are produced to study shape differences between the data and the MC. The post-fit $\chi^2_{\text{stat.}}$ are not improved by much (compared to figure 11.10) since the differences between the data and the MC are already small in all five variables.

11.3 Cross-section Results

As described in section 4.6, the cross-section results are presented in two formats:

1. $\sigma_{\text{FGD1}}^{\text{CC-COH}}$: the CC-COH cross section on the FGD1 composition of target nucleus shown in table 11.1.

2. $\sigma_{^{12}\text{C}}^{\text{CC-COH}}$: the CC-COH cross section on ^{12}C extrapolated from $\sigma_{\text{FGD1}}^{\text{CC-COH}}$ using equation 11.1 and table 11.1.

The two scaling functions considered for extracted results are: $F(A) = A^{1/3}$, and $F(A) = A^2$.

$$\sigma_{\text{FGD1}}^{\text{CC-COH}} = \sum_i f_i F(A_i) \frac{\sigma_{^{12}\text{C}}^{\text{CC-COH}}}{F(A_C)}, i = C, O, Ti, Si, N \tag{11.1}$$

11.3.1 ν_μ CC-COH Results

The previously published T2K measurement[36] is:

$$\sigma_{^{12}\text{C}}^{\text{CC-COH}} = 3.9 \pm 1.0(\text{stat.})^{+1.5}_{-1.4}(\text{syst.}) \times 10^{-40}\text{cm}^2, \tag{11.2}$$

where the Rein-Sehgal(1983) model was used in the Monte Carlo simulation.

The ν_μ CC-COH cross section on the FGD1 composition of the target nucleus measurement is:

$$\sigma_{\text{FGD1}}^{\text{CC-COH}} = 3.00 \pm 0.70(\text{stat. + syst.}) \times 10^{-40}\text{cm}^2. \tag{11.3}$$

The uncertainty is the combination of statistical and systematic uncertainties. The additional Q^2 uncertainty (described in appendix. J) is also included.

The statistical uncertainty can be estimated based on the statistics of the analysis. The fit shown in section 11.2.1 is performed with only the signal parametered enabled (all the systematic uncertainty parameters are disabled). The uncertainty from this fit gives an estimation of the statistical uncertainty to the cross-section measurement.

Nuclei	C	O	Ti	Si	N
Atomic Mass Number (A)	12	16	48	28	14
Fractional Composition (%)	95.83	3.09	0.46	0.48	0.14

TABLE 11.1. Fractional composition of the FGD1 detector excluding hydrogen. The calculations are shown in appendix D.

Assuming the combined uncertainty is the quadratic sum of the statistical and systematic uncertainties, we can report the cross-section result as:

$$\sigma_{\text{FGD1}}^{\text{CC-COH}} = 3.00 \pm 0.37(\text{stat.}) \pm 0.58(\text{syst.}) \times 10^{-40}\text{cm}^2, \tag{11.4}$$

with a p-value of 0.75 compared to the nominal Monte Carlo simulation cross-section prediction of $2.77 \times 10^{-40}\text{cm}^2$ with the Berger-Sehgal model, as shown in figure 11.25.

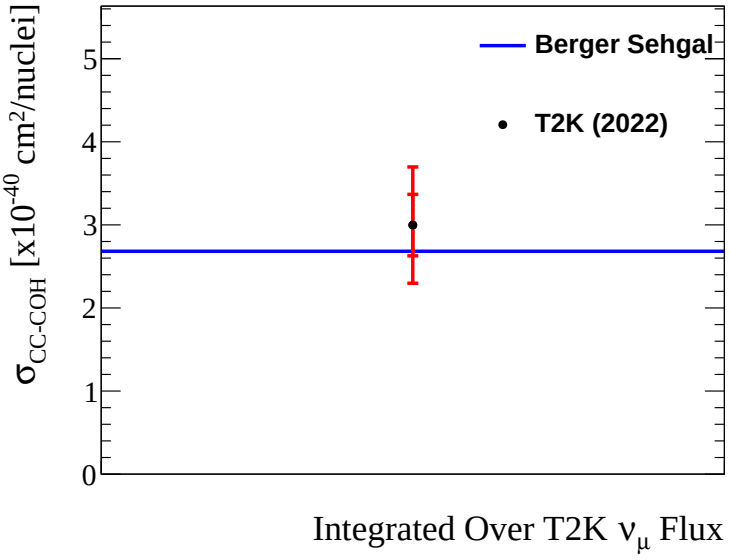

Figure 11.25. Comparison of the MC prediction (Berger Sehgal) and the T2K ν_μ $\sigma_{\text{FGD1}}^{\text{CC-COH}}$ measurement. The inner error bar represents the statistic uncertainty and the outer error bar represents the total measurement uncertainty (the quadradic sum of the statistical and systematic uncertainties). The MC predicted cross section is $2.77 \times 10^{-40}\text{cm}^2$. The T2K measurement is $3.00 \pm 0.37(\text{stat.}) \pm 0.58(\text{syst.}) \times 10^{-40}\text{cm}^2$.

The extracted ν_μ CC-COH cross section on ^{12}C for the various F(A) are:

$$\sigma_{^{12}\text{C}}^{\text{CC-COH}} = \begin{cases} 2.98 \pm 0.37(\text{stat.}) \pm 0.58(\text{syst.}) \times 10^{-40}\text{cm}^2 \ (F(A) = A^{1/3}) \\ 2.69 \pm 0.33(\text{stat.}) \pm 0.52(\text{syst.}) \times 10^{-40}\text{cm}^2 \ (F(A) = A^2). \end{cases} \tag{11.5}$$

The uncertainties for the extracted ^{12}C cross sections are calculated assuming the same fractional uncertainty between the FGD1 and ^{12}C cross sections. The two cross sections cannot be differentiated with the measurement uncertainties. The measurements from this analysis are compatible with this previous result (equation 11.2). In addition, the uncertainties are improved by roughly a factor of two.

The extracted ν_μ CC-COH cross section on ^{12}C for $F(A) = A^{1/3}$ is compared to the

theoretical models in figure 11.26. The T2K result favours the Berger-Sehgal (BS) model over the Rein-Sehgal (RS) model.

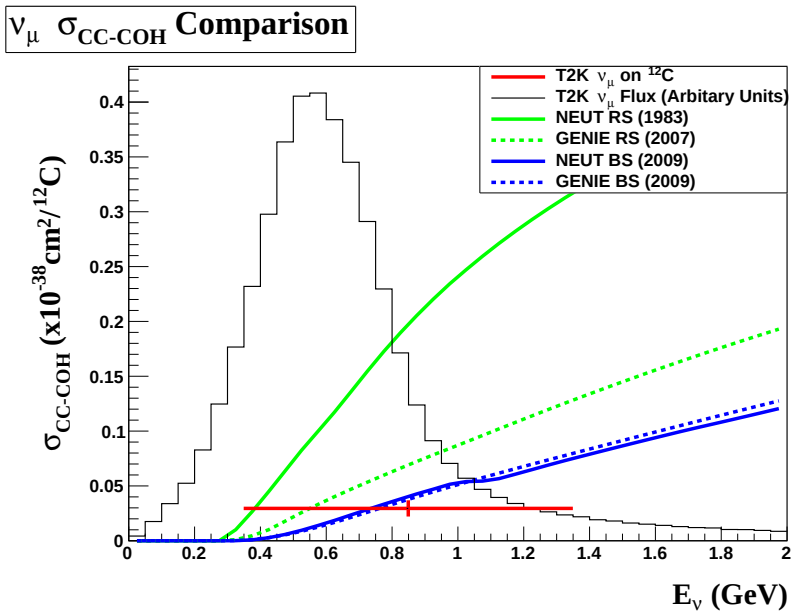

Figure 11.26. The T2K ν_μ CC-COH cross section measurement on C assuming $F(A) = A^{1/3}$. The measurement uncertainty shown is the quadratic sum of the statistical and systematic components. The x-axis error bar covers one standard deviation of the T2K ν_μ flux around the mean neutrino energy of 0.849 GeV. The T2K ν_μ flux is also shown. The Monte Carlo simulation predictions from various theoretical models (described in section 2.3) are shown and the T2K result favours the Berger-Sehgal (BS) model (blue) over the Rein-Sehgal (RS) model (green).

11.3.2 $\bar{\nu}_\mu$ CC-COH Results

The $\bar{\nu}_\mu$ CC-COH cross section on the FGD1 composition of the target nucleus measurement is:

$$\sigma_{\text{FGD1}}^{\text{CC-COH}} = 3.07 \pm 1.11(\text{stat. } + \text{syst.}) \times 10^{-40}\text{cm}^2, \tag{11.6}$$

with a p-value of 0.86 compared to the nominal Monte Carlo simulation cross-section prediction of 2.87×10^{-40}cm^2 with the Berger-Sehgal model, as shown in figure 11.27. The uncertainty is the combination of statistical and systematic uncertainties.

The statistical uncertainty can be estimated based on the statistics of the analysis. Assuming the combined uncertainty is the quadratic sum of the statistical and systematic uncertainties, we can report the cross-section result as:

$$\sigma_{\text{FGD1}}^{\text{CC-COH}} = 3.07 \pm 0.71(\text{stat.}) \pm 0.85(\text{syst.}) \times 10^{-40}\text{cm}^2, \tag{11.7}$$

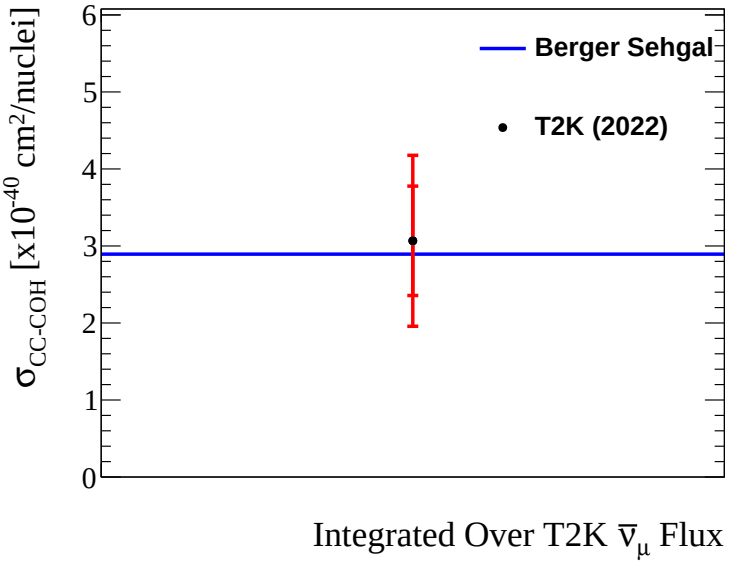

Figure 11.27. Comparison of the MC prediction (Berger Sehgal) and the T2K $\bar{\nu}_\mu$ $\sigma^{\text{CC-COH}}_{\text{FGD1}}$ measurement. The inner error bar represents the statistic uncertainty and the outer error bar represents the total measurement uncertainty (the quadradic sum of the statistical and systematic uncertainties). The MC predicted cross section is $2.87 \times 10^{-40}\text{cm}^2$. The T2K measurement is $3.07 \pm 0.71(\text{stat.}) \pm 0.85(\text{syst.}) \times 10^{-40}\text{cm}^2$.

The extracted $\bar{\nu}_\mu$ CC-COH cross section on ^{12}C for the various F(A) are:

$$\sigma^{\text{CC-COH}}_{^{12}\text{C}} = \begin{cases} 3.05 \pm 0.71(\text{stat.}) \pm 0.84(\text{syst.}) \times 10^{-40}\text{cm}^2 \ (F(A) = A^{1/3}) \\ 2.75 \pm 0.64(\text{stat.}) \pm 0.76(\text{syst.}) \times 10^{-40}\text{cm}^2 \ (F(A) = A^2). \end{cases} \tag{11.8}$$

The two cross sections cannot be differentiated with the measurement uncertainties. The extracted $\bar{\nu}_\mu$ CC-COH cross section on ^{12}C for $F(A) = A^{1/3}$ is compared to the theoretical models in figure 11.28, where the T2K result favours the Berger-Sehgal (BS) model over the Rein-Sehgal (RS) model. This result is the first measurement of $\bar{\nu}_\mu$ CC-COH at the sub-GeV energy region.

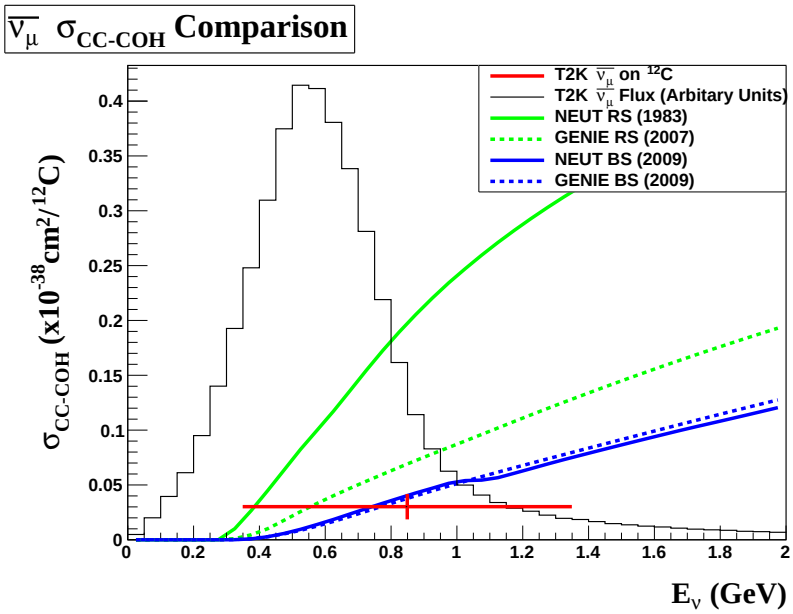

Figure 11.28. The T2K $\bar{\nu}_\mu$ CC-COH cross section measurement on C assuming $F(A) = A^{1/3}$. The measurement uncertainty shown is the quadratic sum of the statistical and systematic components. The x-axis error bar covers one standard deviation of the T2K $\bar{\nu}_\mu$ flux around the mean neutrino energy of 0.849 GeV. The T2K $\bar{\nu}_\mu$ flux is also shown. The Monte Carlo simulation predictions from various theoretical models (described in section 2.3) are shown and the T2K result favours the Berger-Sehgal (BS) model (blue) over the Rein-Sehgal (RS) model (green).

11.4 Conclusion

Neutrino-induced coherent pion production (COH) is a process not well modelled, and only a handful of experimental measurements are available. As a result, the two channels of COH, the charged-current (CC-COH) and neutral-current (NC-COH), have significant modelling uncertainties in the neutrino event generators. In addition, the $\bar{\nu}_\mu$ CC-COH has never been successfully measured at the sub-GeV energy region.

At the near detector ND280 of T2K, neutrino cross-section measurements can be made with the complex of detectors. This thesis presented two CC-COH measurements on carbon targets using the FGD1 detector of ND280 as the target mass.

- The first measurement is the $\bar{\nu}_\mu$ CC-COH cross section on ^{12}C, which is the first measurement of such process at the sub-GeV energy region.
  - $\bar{\nu}_\mu\ \sigma^{\text{CC-COH}}_{^{12}\text{C}} = 3.05 \pm 0.71(\text{stat.}) \pm 0.84(\text{syst.}) \times 10^{-40}\text{cm}^2$
- The second measurement is the ν_μ CC-COH cross section on ^{12}C, which is a statistically updated result from a previous T2K measurement. Systematic uncertainties are also better understood with this new measurement.
  - $\nu_\mu\ \sigma^{\text{CC-COH}}_{^{12}\text{C}} = 2.98 \pm 0.37(\text{stat.}) \pm 0.58(\text{syst.}) \times 10^{-40}\text{cm}^2$

The uncertainties to both measurements are systematically dominated, the leading systematic uncertainty sources include:

- the uncertainties associated with the vertex activity
- the large uncertainties assigned to the deep inelastic scattering (DIS) background events
- the additional uncertainty added to cover the potential bias caused by low Q^2 suppression of the resonant pion production (RES) background events.

These aspects are ongoing topics studied by other analyzers at T2K.

For this thesis, the ν_μ and $\bar{\nu}_\mu$ CC-COH cross sections are measured by separate analyses. However, a joint analysis with both selections can help to constrain some of the background events. For example, the ν_μ interaction backgrounds are treated as irreducible backgrounds in the $\bar{\nu}_\mu$ analysis, but these backgrounds are studied and constrained in the ν_μ analysis. Therefore, a future joint analysis can extrapolate the background constraints from the ν_μ analysis to the $\bar{\nu}_\mu$ analysis.

Appendices

Appendix A

Neutrino Oscillation Derivations

In the theory of "neutrino oscillation", the neutrinos are created in the "flavour" eigenstates,

$$|\nu_\alpha\rangle\,, \qquad (\alpha = \mathrm{e}, \mu, \tau). \tag{A.1}$$

These states are linear combinations (this will be demonstrated in section 1.3.1) of the "mass" eigenstates,

$$|\nu_k\rangle\,, \qquad (k = 1, 2, 3), \tag{A.2}$$

which are the states neutrinos propagate in.

The relations between the flavour and the mass eigenstates are described by the 3×3 Pontecorvo–Maki–Nakagawa–Sakata matrix (PMNS matrix, also referred to as the lepton mixing matrix),

$$\mathbf{U} = \begin{bmatrix} U_{e1} & U_{e2} & U_{e3} \\ U_{\mu 1} & U_{\mu 2} & U_{\mu 3} \\ U_{\tau 1} & U_{\tau 2} & U_{\tau 3} \end{bmatrix}, \tag{A.3}$$

as shown in equation A.4.

$$|\nu_\alpha\rangle = \sum_{k=1,2,3} U^*_{\alpha k}\,|\nu_k\rangle\,. \tag{A.4}$$

The PMNS matrix is a unitary matrix, which means that

$$\mathbf{U}\mathbf{U}^\dagger = \mathbf{U}^\dagger\mathbf{U} = \mathbf{I}, \tag{A.5}$$

where $\mathbf{I}$ is the identity matrix. Using this unitary property, equation A.4 can be inverted and the mass eigenstates can be written as superpositions of the flavour eigenstates:

$$|\nu_k\rangle = \sum_{\alpha=\mathrm{e},\mu,\tau} U_{\alpha k}\,|\nu_\alpha\rangle\,. \tag{A.6}$$

A.1 Derivation of Three-flavour Neutrino Oscillation Probability in the Vacuum

This subsection reviews the derivation of the neutrino oscillation probability by Giunti and Kim [92]. The derivation uses the three flavours of neutrinos in equation A.1 and assumes they propagate in vacuum. The effect of neutrinos travelling through matter is not considered here. Unless otherwise stated, the Planck constant, $\hbar$ and the speed of light, c, are in natural units, which all have numerical values of 1.

The three neutrino mass states in equation A.2 are eigenstates of the Hamiltonian:

$$\mathcal{H}\left|\nu_k\right\rangle = E_k\left|\nu_k\right\rangle, \tag{A.7}$$

where the energy eigenvalues E_k are

$$E_k = \sqrt{p_k^2 + m_k^2}. \tag{A.8}$$

p_k and m_k are the momentum and mass of the neutrino.

Using the Schrödinger equation, we can express the time evolution (t) of the neutrino mass eigenstates as

$$\left|\nu_k(t)\right\rangle = e^{-iE_k t}\left|\nu_k\right\rangle. \tag{A.9}$$

To express the wave function of the neutrino flavour eigenstate evolution over time, let us first assume that the initial flavour state at $t = 0$ is $|\nu_\alpha\rangle$ according to equation A.4. Then, at any time t later, we can write

$$\left|\nu_\alpha(t)\right\rangle = \sum_k U_{\alpha k}^* e^{-iE_k t}\left|\nu_k\right\rangle. \tag{A.10}$$

By substituting equation A.6 into equation A.10, we have:

$$\left|\nu_\alpha(t)\right\rangle = \sum_{\beta=e,\mu,\tau}\left(\sum_k U_{\alpha k}^* e^{-iE_k t} U_{\beta k}\right)\left|\nu_\beta\right\rangle. \tag{A.11}$$

$|\nu_\alpha\rangle$ and $\left|\nu_\beta\right\rangle$ are both flavour states and the unitarity of the PMNS matrix implies orthonormal flavour states ($\left\langle\nu_\alpha|\nu_\beta\right\rangle = \delta_{\alpha\beta}$). At $t = 0$, the neutrino is in any of the three flavour states, and at any later time, the neutrino would be in a superposition of the flavour states. Therefore, the PMNS mixing matrix must be non-diagonal.

To calculate the probability of transition from one flavour state to another, we first find

out the amplitude of $\nu_\alpha \to \nu_\beta$ over time,

$$A_{\nu_\alpha \to \nu_\beta}(t) = \langle \nu_\beta | \nu_\alpha(t) \rangle = \sum_k U^*_{\alpha k} U_{\beta k} e^{-iE_k t}. \tag{A.12}$$

The probability of the flavour transition is

$$P_{\nu_\alpha \to \nu_\beta}(t) = \left| A_{\nu_\alpha \to \nu_\beta}(t) \right|^2 = \sum_{k>j} U^*_{\alpha k} U_{\beta k} U_{\alpha j} U^*_{\beta j} e^{-i(E_k - E_j)t}. \tag{A.13}$$

The indices k and j (k, j = 1, 2, 3) are associated with the orthonormal ($\langle \nu_k | \nu_j \rangle = \delta_{kj}$) mass states. Since neutrinos are ultrarelativistic, meaning they travel almost at the speed of light and have tiny masses,

$$E_k \simeq p + \frac{m_k^2}{2E} \simeq E + \frac{m_k^2}{2E}, \tag{A.14}$$

and t is approximately the distance travelled, L, by the neutrino ($L/\mathrm{c} = L$ since the speed of light is 1 in natural unit). Therefore, the difference in energy can be written as

$$E_k - E_j \simeq \frac{m_k^2 - m_j^2}{2E} = \frac{\Delta m_{kj}^2}{2E}, \tag{A.15}$$

and the probability equation is further simplified into

$$P_{\nu_\alpha \to \nu_\beta}(t) = \sum_{k>j} U^*_{\alpha k} U_{\beta k} U_{\alpha j} U^*_{\beta j} \exp(-i \frac{\Delta m_{kj}^2 L}{2E}), \tag{A.16}$$

where Δm_{kj}^2 is the mass difference squared. This is one of the neutrino oscillation parameters being measured and studied by experiments. The matrix elements can also be expressed as neutrino oscillation parameters. The next subsection describes the parameters and the current understanding of them.

With the use of trigonometric identities and the separation of the real and imaginary parts of the equation, we can also write the neutrino flavour transition probability as:

$$\begin{aligned} P_{\nu_\alpha \to \nu_\beta}(t) = \delta_{\alpha\beta} &- 4 \sum_{k>j} \mathfrak{Re} \left[U^*_{\alpha k} U_{\beta k} U_{\alpha j} U^*_{\beta j} \right] \sin^2 \left(\frac{\Delta m_{kj}^2 L}{4E} \right) \\ &+ 2 \sum_{k>j} \mathfrak{Im} \left[U^*_{\alpha k} U_{\beta k} U_{\alpha j} U^*_{\beta j} \right] \sin \left(\frac{\Delta m_{kj}^2 L}{2E} \right). \end{aligned} \tag{A.17}$$

The derivation of the flavour transition probability for antineutrino follows the same method

described in this subsection and is not repeated. The probability is:

$$P_{\bar{\nu}_\alpha \to \bar{\nu}_\beta}(t) = \delta_{\alpha\beta} - 4\sum_{k>j} \mathfrak{Re}\left[U^*_{\alpha k} U_{\beta k} U_{\alpha j} U^*_{\beta j}\right] \sin^2\left(\frac{\Delta m^2_{kj} L}{4E}\right) - 2\sum_{k>j} \mathfrak{Im}\left[U^*_{\alpha k} U_{\beta k} U_{\alpha j} U^*_{\beta j}\right] \sin\left(\frac{\Delta m^2_{kj} L}{2E}\right). \tag{A.18}$$

Notice that the difference between equation A.17 and equation A.18 is the sign associated with the imaginary part of the equation.

Appendix B

Software Summary

This appendix lists the version number of the software used for the analysis for reference.

B.1 ν_μ CC-COH Analysis

- Data:
  - Production tag: prod6T[1]
  - Data processing: ND280Software v11r31p45
  - Data analyze framework: High-Level-Analysis-at-the-Near-Detector (HIGHLAND) v2r41
  - CC-COH event selection package: numuCCCoherentXSecAnalysis v0r0
- MC:
  - Production tag: prod6T
  - Neutrino flux prediction: Flux Release 13av6
  - Neutrino event generator: NEUT5.4.0.1 Rev.634
  - MC processing: ND280Software v11r31p43
  - MC analyze framework: HIGHLAND v2r41
  - CC-COH event selection and detector error propagation package: numuCCCoherentXSecAnalysis v0r0
  - Cross-section and FSI modelling uncertainty (spline generation): T2KReWeight OA2020

[1]The data (or MC) with different production tags can have different reconstruction packages. Therefore, a tag is needed to differentiate the different productions.

B.2 $\bar{\nu}_\mu$ CC-COH Analysis

- Data:
  - Production tag: prod6T
  - Data processing: ND280Software v11r31p45
  - Data analyze framework: High-Level-Analysis-at-the-Near-Detector (HIGHLAND) v2r41
  - CC-COH event selection package: antiNumuCCCoherentXSecAnalysis v0r0
- MC:
  - Production tag: prod6T
  - Neutrino flux prediction: Flux Release 13av6
  - Neutrino event generator: NEUT5.4.0.1 Rev.634
  - MC processing: ND280Software v11r31p43
  - MC analyze framework: HIGHLAND v2r41
  - CC-COH event selection and detector error propagation package: antiNumuCC-CoherentXSecAnalysis v0r0
  - Cross-section and FSI modelling uncertainty (spline generation): T2KReWeight OA2020

Appendix C

ND280 Monte Carlo Simulation Production 6T

The analysis uses the latest ND280 MC production 6T as the nominal MC. The main difference that affects this analysis is the change of the COH model from RS(1983) to BS(2009). The prediction of the integrated CC-COH event rate is reduced by a factor of two. The modelling of the background events, such as RES and DIS, have also been updated. Table C.1, summarized from TN351[93], shows the main differences in terms of the modelling changes.

MC	Prod6B	Prod6T
NEUT	5.3.2	5.4.0
Nuclear Model	SF (RFG reweighed)	SF
CCQE	SF	SF
2p2h	Nieves et al. (table)	Nieves et al. (table)
RES	Rein-Seghal Graczyk-Sobczyk	Rein-Seghal Graczyk-Sobczyk (bug fix)
COH	Rein-Sehgal (1983)	Berger-Sehgal (2009)
DIS		CKM matrix Bodek-yang correction
p/pion FSI		Improvement & bug fix

TABLE C.1. The differences between prod6B and prod6T in terms of changes in NEUT from version 5.3.2 to 5.4.0. The main difference that affects this analysis is the change of the COH model from RS(1983) to BS(2009).

Appendix D

Number of Carbon Target Nuclei Calculation

The hardware construction of the FGD1 detector and the implementation in the Monte-Carlo simulation are shown in this appendix. The detector dimension and material composition details are used to calculate the number of target nuclei needed to extract the cross-section measurement.

D.1 The FGD1 Detector

The FGD1 detector consists of plastic scintillator bars oriented in the x and y-axis. The scintillator bars are 9.61 mm in thickness, and 196 bars are glued together to form one layer. One X layer and one Y layer (based on the bars' orientation) make up one XY module, and the module is machined to a square with sides of 1864.4mm; this means the outermost layers on both sides are entirely machined away. Another 7 mm are machined away on each side to make room for the bus boards. The entire FGD1 detector contains 15 XY modules. While the plastic scintillator bars are almost entirely made of carbon, the detector contains other elements such as O and Ti, which are included in the materials used to construct the detector, such as coating and glue. Table D.1 shows the fractional composition of the FGD1 along with the areal densities. Uncertainties on the quantities are also shown.

Nuclei	C	O	H	Ti	Si	N
Areal Density (g/cm^2)	1.849	0.0794	0.1579	0.0355	0.0218	0.0031
Uncertainty of Areal Density (%)	0.92	0.58	0.21	0.59	0.43	0.12
Fractional Composition (%)	86	7.0	3.5	1.5	1.0	1.0
Uncertainty of Fractional Composition (%)	0.5	6.0	1.3	16.6	19.7	39

TABLE D.1. The composition of the FGD1 detector. Areal density, the fractional composition of the different element, and the associated uncertainties are shown.

D.2 Number of Carbon Nuclei in FGD1

The cross-section calculation requires the total number of the target nuclei. The total number of Carbon nuclei in FGD1 needs to be calculated since the cross-section measurements are on the Carbon nuclei. Equation D.1 shows the formula to calculate the total number of Carbon nuclei in FGD1 (T_C) presented in this thesis. a_C is the areal density for Carbon shown in table D.1, M_C is the molar mass of Carbon, N_A is the Avogadro's constant. A_{XY} is the area in the XY-plane of the XY module, and N_{XY} is the number of XY modules. A reduced fiducial volume is applied to ensure good vertex activity and good track reconstruction. Each XY module is 1864.4mm by 1864.4mm in size; the side length implemented in MC is 1864.34mm. Since the outermost scintillator bar is mostly machined away to make room for electronics, it will not be used for the analysis. Also, the analysis uses 5x5 scintillator bar layers volume to calculate the vertex activity. As a result, the outermost five scintillator bar layers cannot be used for the analysis. Thus, in the end, six scintillator bar layers have to be excluded on both sides; this translates to 182 scintillator bars per X or Y plane being used for the analysis. Equation D.2 shows the reduced area of the XY modules used for the analysis. The FGD1 detector has 15 XY modules in total, but this analysis excludes the first and last modules to improve track reconstruction - N_{XY} is therefore 13. Finally, putting all the numbers together, equation D.3 shows the calculated total number of Carbon nuclei inside FGD1 for this analysis.

$$T_C = \frac{a_C}{M_C} \cdot N_A \cdot A_{XY} \cdot N_{XY} \tag{D.1}$$

$$A_{XY} = (182 \times 9.61\,\mathrm{mm})^2 = (1749.02\,\mathrm{mm})^2 = 30\,590.7096\,\mathrm{cm}^2 \tag{D.2}$$

$$
\begin{aligned}
T_C &= \frac{a_C}{M_C} \cdot N_A \cdot A_{XY} \cdot N_{XY} \\
&= \frac{1.849\,\mathrm{g\,cm^{-2}}}{12.011\,\mathrm{g\,mol^{-1}}} \cdot 6.02 \times 10^{23}\,\mathrm{mol^{-1}} \cdot 30\,590.7096\,\mathrm{cm^2} \cdot 13 \\
&= 3.69 \times 10^{28}\ \text{Carbon nuclei}
\end{aligned}
\tag{D.3}
$$

D.3 Number of Nuclei in FGD1

Using the same calculation performed to calculate T_C in equation D.3, the number of nuclei for each element in the FGD1 detector can be calculated. The total number of nuclei in FGD1 is:

$$
\begin{aligned}
T_{FGD1} &= \sum_i T_i, i = C, O, Ti, Si, N \\
&= 3.85 \times 10^{28}\ \text{Nuclei}
\end{aligned}
\tag{D.4}
$$

Note that hydrogen is excluded from the calculation since neutrino diffraction (COH on H) is not part of the signal definition. Table D.2 shows the numbers of each target nuclei and the fractional composition.

Nuclei	C	O	Ti	Si	N
Number of Target	3.69×10^{28}	1.19×10^{27}	1.78×10^{26}	1.86×10^{26}	5.30×10^{25}
Fractional Composition (%)	95.83	3.09	0.46	0.48	0.14
Uncertainty of Frac. Comp. (%)	0.5	1.3	16.6	19.7	39

TABLE D.2. The numbers of the various nuclei in FGD1 with the fraction. Carbon is the dominant nuclei.

Appendix E

$|t|$ Derivation

Figure E.1 is a reminder of the Feynman diagram of CC-COH in process E.1. q is the four-momentum transfer from the neutrino-muon system to the $W^+(W^-)$. $|t|$ is the modulus of the four-momentum transferred squared (referred to as "momentum transferred squared" in the appendix) from the W^+-π^+(W^--π^-) system to the target nucleus.

$$\begin{aligned} \nu_\mu + \mathrm{A} &\rightarrow \mu^- + \pi^+ + \mathrm{A} \\ \bar{\nu_\mu} + \mathrm{A} &\rightarrow \mu^+ + \pi^- + \mathrm{A} \end{aligned} \tag{E.1}$$

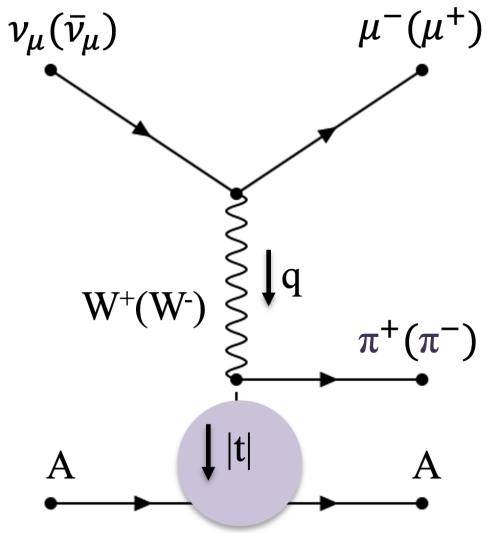

Figure E.1. Feynman diagram of the ν_μ CC-COH process. $|t|$ is the modulus of the four-momentum transferred squared from the W^+-π^+(W^--π^-) system to the target nucleus.

The formula to compute the analysis variable $|t|$ (section 4.4.2) is derived in this appendix. Note that all the vectors used in the derivations in this section are with respect to the neutrino

direction:

$$\overrightarrow{\nu} = (0, 0, z). \tag{E.2}$$

The momentum transferred squared $|t|$ is:

$$|t| = \left|(q - P_\pi)^2\right| = \left|(P_\nu - P_\mu - P_\pi)^2\right|. \tag{E.3}$$

Assuming that no energy is transferred to the target nucleus (infinitely heavy nucleus assumption), the neutrino four-momentum can be expressed solely in muon and pion energy components:

$$P_\nu = (E_\nu, 0, 0, E_\nu) = (E_\mu + E_\pi, 0, 0, E_\mu + E_\pi). \tag{E.4}$$

Using equationE.3 and equationE.4, t can now be expressed with muon and pion kinematics, which are all measurable in detectors:

$$\begin{aligned} t = &(E_\mu + E_\pi - E_\mu - E_\pi)^2 \\ &- (0 - P_\mu^x - P_\pi^x)^2 - (0 - P_\mu^y - P_\pi^y)^2 \\ &- (E_\mu + E_\pi - P_\mu^z - P_\pi^z)^2. \end{aligned} \tag{E.5}$$

Therefore, the modulus of t is:

$$\begin{aligned} |t| = &(E_\mu + E_\pi - P_\mu^z - P_\pi^z)^2 \\ &+ (P_\mu^x + P_\pi^x)^2 + (P_\mu^y + P_\pi^y)^2. \end{aligned} \tag{E.6}$$

With some reorganization, $|t|$ can be written as:

$$|t| = (\sum_{\mu,\pi}^{i}(E_i - P_i^z))^2 + (\sum_{\mu,\pi}^{i}(P_i^x))^2 + (\sum_{\mu,\pi}^{i}(P_i^y))^2. \tag{E.7}$$

The momentums can be separated into the longitudinal:

$$P^L = P^z = P * \cos(\theta) \tag{E.8}$$

and the transverse components:

$$\overrightarrow{P^T} = \left\{P_x, P_y\right\} \tag{E.9}$$

$$\left|\overrightarrow{P^T}\right| = P^T = \sqrt{P_x^2 + P_y^2} = P * sin(\theta). \tag{E.10}$$

$|t|$ can then be expressed in terms of P^L and P^T:

$$|t| = (\sum_{\mu,\pi}^{i}(E_i - P_i^L))^2 + \left|\sum_{\mu,\pi}^{i} \overrightarrow{P_i^T}\right|^2 . \tag{E.11}$$

The next section contains proofs that equation E.7 and equation E.11 are equivalent.

E.1 Derivation of the Transverse Momentum Component of $|t|$

To equate equation E.7 and equation E.11, the following equality needs to be true:

$$(P_\mu^x + P_\pi^x)^2 + (P_\mu^y + P_\pi^y)^2 = \left|\sum_{\mu,\pi}^{i} \overrightarrow{P_i^T}\right|^2 . \tag{E.12}$$

Starting from the left side of the equation:

$$\begin{aligned} LHS &= (P_\mu^x + P_\pi^x)^2 + (P_\mu^y + P_\pi^y)^2 \\ &= (P_\mu^x)^2 + (P_\mu^y)^2 + (P_\pi^x)^2 + (P_\pi^y)^2 \\ &+ 2P_\mu^x P_\pi^x + 2P_\mu^y P_\pi^y \\ &= (P_\mu^T)^2 + (P_\pi^T)^2 \\ &+ 2\overrightarrow{P_\mu^T} \cdot \overrightarrow{P_\pi^T} \\ &= (P_\mu^T)^2 + (P_\pi^T)^2 \\ &+ 2P_\mu^T P_\pi^T \cos(\alpha). \end{aligned} \tag{E.13}$$

Note that in equation E.13:

$$\overrightarrow{P_\mu^T} \cdot \overrightarrow{P_\pi^T} = \left\{P_\mu^x, P_\mu^y\right\} \cdot \left\{P_\mu^x, P_\mu^y\right\} = P_\mu^x P_\pi^x + P_\mu^y P_\pi^y, \tag{E.14}$$

and by the definition of the dot product of two vectors:

$$\overrightarrow{P_\mu^T} \cdot \overrightarrow{P_\pi^T} = \left|\overrightarrow{P_\mu^T}\right| \left|\overrightarrow{P_\pi^T}\right| \cos(\alpha) = P_\mu^T P_\pi^T \cos(\alpha). \tag{E.15}$$

The right-hand side of the equation can be written as:

$$\begin{aligned} RHS &= \left| \sum_{\mu,\pi}^{i} \overrightarrow{P_i^T} \right|^2 \\ &= \left| \overrightarrow{P_\mu^T} + \overrightarrow{P_\pi^T} \right|^2 \\ &= \left| \overrightarrow{P_\mu^T} \right|^2 + \left| \overrightarrow{P_\pi^T} \right|^2 + 2 \left| \overrightarrow{P_\mu^T} \right| \left| \overrightarrow{P_\pi^T} \right| \cos(\alpha) \\ &= (P_\mu^T)^2 + (P_\pi^T)^2 + 2 P_\mu^T P_\pi^T \cos(\alpha) \end{aligned} \tag{E.16}$$

The angle α,

$$\cos(\alpha) = \overrightarrow{e_\mu} \cdot \overrightarrow{e_\pi}, \tag{E.17}$$

is the angle between the outgoing muon and pion.

E.2 Derivation of Formulae Used in This Thesis

This section describes the implementation of the $|t|$ formula equation E.11 in HIGHLAND2, and as used in this analysis.

Equation E.11 has two components, the longitudinal and the transverse components. The longitudinal component can be expressed as:

$$|t|_L = (\sum_{\mu,\pi}^{i} (E_i - P_i^L))^2. \tag{E.18}$$

Using equation E.8, we get:

$$|t|_L = (\sum_{\mu,\pi}^{i} (E_i - \left| \overrightarrow{P_i} \right| \cos\theta_i))^2. \tag{E.19}$$

The transverse component can be expressed as:

$$|t|_T = \left| \sum_{\mu,\pi}^{i} \overrightarrow{P_i^T} \right|^2. \tag{E.20}$$

As discussed in the previous section, the formalism requires all the inputs to be in the neutrino direction coordinate system. Thus, we cannot use eq E.10 to express $\overrightarrow{P_i^T}$. To use inputs in the detector coordinate system, we must do further derivations.

Express $|t|_T$ as the difference between $|t|$ and $|t|_L$:

$$\begin{aligned} |t|_T &= \left| \sum_{\mu,\pi}^{i} \overrightarrow{P_i^T} \right|^2 \\ &= |t - t_L|^2 . \end{aligned} \tag{E.21}$$

With the assumption that ΔE is 0, the difference in four-momentum calculated in equation E.3 will collapse down to three-momentums. We can then write:

$$\begin{aligned} |t|_T &= \left| (\overrightarrow{P_\nu} - \overrightarrow{P_\mu} - \overrightarrow{P_\pi}) - \left[(\overrightarrow{P_\nu} - \overrightarrow{P_\mu} - \overrightarrow{P_\pi}) \cdot \widehat{e_\nu} \right] \widehat{e_\nu} \right|^2 \\ &= \left| \left| \overrightarrow{P_\nu} \right| \widehat{e_\nu} - \left| \overrightarrow{P_\mu} \right| \widehat{e_\mu} - \left| \overrightarrow{P_\pi} \right| \widehat{e_\pi} - \left| \overrightarrow{P_\nu} \right| \widehat{e_\nu} + (\left| \overrightarrow{P_\mu} \right| \widehat{e_\mu} \cdot \widehat{e_\nu}) \widehat{e_\nu} + (\left| \overrightarrow{P_\pi} \right| \widehat{e_\pi} \cdot \widehat{e_\nu}) \widehat{e_\nu} \right|^2 \\ &= \left| \left| \overrightarrow{P_\mu} \right| (\widehat{e_\mu} - (\widehat{e_\mu} \cdot \widehat{e_\nu}) \widehat{e_\nu} + \left| \overrightarrow{P_\pi} \right| (\widehat{e_\pi} - (\widehat{e_\pi} \cdot \widehat{e_\nu}) \widehat{e_\nu} \right|^2 \\ &= \left| \left| \overrightarrow{P_\mu} \right| (\widehat{e_\mu} - \cos\theta_\mu \widehat{e_\nu}) + \left| \overrightarrow{P_\pi} \right| (\widehat{e_\pi} - \cos\theta_\pi \widehat{e_\nu}) \right|^2 \\ &= \left| \sum_{\mu,\pi}^{i} \left[\left| \overrightarrow{P_i} \right| (\widehat{e_i} - \cos\theta_i \widehat{e_\nu}) \right] \right|^2 . \end{aligned} \tag{E.22}$$

Finally, adding equation E.19 and equation E.22, we have:

$$|t| = (\sum_{\mu,\pi}^{i} (E_i - \left| \overrightarrow{P_i} \right| \cos\theta_i))^2 + \left| \sum_{\mu,\pi}^{i} \left[\left| \overrightarrow{P_i} \right| (\widehat{e_i} - \cos\theta_i \widehat{e_\nu}) \right] \right|^2 . \tag{E.23}$$

All the inputs to equation E.23 are now in the detector coordinate system.

Appendix F

Pion Secondary Interaction Systematics

F.1 Introduction to Pion Secondary Interaction

Neutrino interactions in ND280 can produce pions, which can then re-interact with the detector materials - such processes are called pion secondary interactions (pionSI). We can subcategorize the pion secondary interactions into eight different interaction types:

- Elastic Scattering: The pion is scattered elastically; the outgoing pion (the original pion) momentum and angle are changed.
- Quai-Elastic Scattering (QE): The pion is scattered inelastically; there can only be one outgoing pion (of the same charge as the original pion).
- Absorption (ABS): The nucleus absorbs the pion; thus, there should be no outgoing pion.
- Single Charge Exchange (SCX, or CX): Assuming the original pion is charged, exactly one outgoing π^0 is produced from the interaction.
- Double Charge Exchange (DCX): Assuming the original pion is charged, exactly one outgoing pion of the opposite charge is produced from the interaction.
- Multi-Pion Production: Multiple outgoing pions (can be any pions).
- Pion Decay: The pion decays.
- Other: Any other processes (e.g., production of exotic particles).

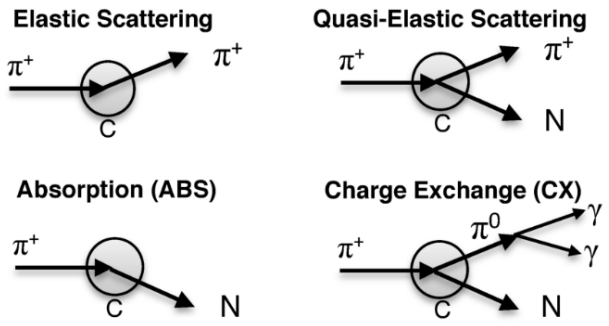

Figure F.1. The most common pion interaction modes on carbon nucleus. N represents the nucleon(s) leaving the carbon nucleus. The plot is taken from [94].

Figure F.1 shows the most common pion interaction modes on carbon nucleus.

For all the T2K analyses that select topologies based on the number of outgoing pions, understanding how pions interact with ND280 detector materials is crucial for two reasons. Firstly, the pion's number (or type) might change and cause the event to fall under the wrong sample topology. For example, a pion absorbed by a nucleus would change the number of detected pions from one to zero, causing a one-pion topology event to be misidentified as a zero-pi topology event. Secondly, even if the interaction does not change the number of detected pions, the momentum or angle could be different, causing the neutrino energy (reconstructed from the kinematic information of the outgoing particles from the neutrino interaction) to be incorrect.

F.2 Pion Secondary Interaction Systematics (2013 Version)

The method of pion secondary interaction (pionSI) systematics evaluation is described in TN-125 [85]. The basic idea of the technique will be briefly explained below.

At the pion energy of the pions produced inside ND280, three interactions are the most relevant (QE, ABS, and CX), and therefore, will be considered for systematics evaluation. Also, only charged pions are considered for the systematics. Neutral pions have a very short lifetime (mean lifetime is 8.5×10^{-17} s), so most of them will decay before interacting with the detector materials. The target materials that were considered can be found in table F.1.

The pion produced from neutrino interactions is propagated with stepping functions inside ND280. After each step, the pion's momentum is evaluated, and the probability of interaction

ND280 Material	Treated As	Code	Added	Comment
Scintillator	Carbon	0	2013	2018: "Scintillator" cover P0D and ECal as well
Air	Oxygen	10	2013	
CO2	Oxygen	10	2013	
Aluminum	Aluminum	20	2013	
AlRoha / AlRoha2	Aluminum	20	2013	
Steel	Iron	30	2013	
Iron	Iron	30	2013	
AlG10	AlG10	40	2013	
WaterSystem	Water	50	2013	2018: Name changed to "Water"
G10FGD1 /G10	G10	60	2013	
FGDGlue	FGDGlue	70	2013	
G10Roha	G10Roha	80	2013	
Polypropylene	Carbon	0	2014	
ActiveWater	Oxygen	10	2014	
GasMixtureTPC	Aluminum	20	2014	
G10FGD2	G10	60	2014	
Epoxy	FGDGlue	70	2014	
Brass	Iron	30	2018	Any heavy materials in P0D or ECal are approximated with Iron
Lead	Lead	90	2018	Only available using NEUT cascade mode
Other	Carbon	0	/	Anything that is missed will be treated as Carbon

TABLE F.1. A list of the target materials in ND280 that are covered by the pion secondary interaction (pionSI) systematics treatment. The name of the material, material code, the years that the materials were supported in the code, are shown.

is calculated. In the 2013 version, GEANT4 is used to model pion interactions. However, it was found that the GEANT4 prediction has significant discrepancies with the external pion scattering data (summarized in TN-033). Therefore, two weights are assigned at each step.

- Correction weight: correct GEANT4 MC to match the external pion scattering data
- Variation weight: use uncertainty in the external data to assign variation to the toy MC for systematics evaluation

F.3 Pion Secondary Interaction Systematics (2018 Version)

F.3.1 Overview of Updates

The pion secondary interaction systematics treatment updates were done following a new pion FSI study described in TN-325 [86]. The main updates to the TN-125 (2013 version) pion secondary interaction systematics treatment are:

- Revised selection of external pion scattering data: only direct measurements are used - data from extrapolation are excluded
- NEUT Monte Carlo is used to describe pion interactions inside ND280: this is achieved with the implementation of the NeutG4CascadeInterface in the ND280 software
- A global fit of NEUT MC prediction to the external data set is performed, resulting in a much better agreement of MC with external data
- Removed the correction weight: since the MC is tuned to the external data, it is not needed to apply the correction weight
- Reduced variation weight: as a result of the fit, the extrapolated data's uncertainty is reduced significantly.
- Supports lead target for the P0D analyses (see table F.1)

Details of some of the updates will be explained in the following sections.

Target				
Al	Ar	Au	B	Bi
C	Ca	Cl	Co	Cu
F	Fe	Ho	N	Na
Nb	Ni	O	Pb	Rh
S	Si	Sn	Ti	Zn
Zr				

TABLE F.2. A list of target materials valid in NeutG4CascadeInterface. Both $\pi^{\pm}$ can be modeled. Pion interactions with materials that are not in this list will be modeled by GEANT4.

F.3.2 NeutG4CascadeInterface

The main update is to use the NEUT Monte Carlo simulation instead of GEANT4 to model pion interactions inside ND280. GEANT4 still models all the other interactions. This is achieved by the NeutG4CascadeInterface, which is now implemented in the ND280Software. The purposes of the interface are:

- Identify if a pion is produced from interactions.
- When the pion incidents on certain target nuclei (shown in table F.2), pass the kinematics of the pion to NEUT and let NEUT decide the interaction probability of the pion.
- Pass the outgoing particles predicted by NEUT to GEANT4 again for particle propagation inside ND280.

F.3.3 NEUT Cascade Model Tuning

The NEUT Cascade model for pion-nucleus scattering is tuned with external data. The work is described in TN-325. The study (post-fit pion interaction cross-sections on various nucleus targets) is used in this iteration of the pion secondary interaction systematics update.

F.3.4 Updated Pion Interaction Cross-sections and Uncertainties

The ND280 Monte Carlo Production 6T has NEUTG4CascadeInterface turned on. Thus, the MC itself already used NEUT to model pion interactions inside ND280. Thus, the pion interaction cross-sections for the systematics evaluation were also updated from GEANT4 to NEUT (results from TN-325). Table F.3 shows the list of cross-sections that are updated. Figure F.2, F.3, F.4, F.5, F.6, F.7, F.8, F.9, F.10, F.11 show the comparison

Pion	Target	Target Code	Updated	Document	Interactions
π^+	Carbon	0	Yes	TN-325	ABS, CX, QE
π^+	Oxygen	10	Yes	TN-325	ABS, CX, QE
π^+	Aluminum	20	Yes	TN-325	ABS, CX, QE
π^+	Iron	30	Yes	TN-325	ABS, CX, QE
π^+	Alg10	40	No	TN-125	ABS, CX, QE
π^+	Water	50	No	TN-125	ABS, CX, QE
π^+	G10	60	No	TN-125	ABS, CX, QE
π^+	FGDGlue	70	No	TN-125	ABS, CX, QE
π^+	G10Roha	80	No	TN-125	ABS, CX, QE
π^+	Lead	90	New	TN-325	ABS, CX, QE
π^-	Carbon	100	Yes	TN-325	ABS, CX, QE
π^-	Oxygen	110	Yes	TN-325	ABS, CX, QE
π^-	Aluminum	120	Yes	TN-325	ABS, CX, QE
π^-	Iron	130	Yes	TN-325	ABS, CX, QE
π^-	Alg10	140	No	TN-125	ABS, CX, QE
π^-	Water	150	No	TN-125	ABS, CX, QE
π^-	G10	160	No	TN-125	ABS, CX, QE
π^-	FGDGlue	170	No	TN-125	ABS, CX, QE
π^-	G10Roha	180	No	TN-125	ABS, CX, QE
π^-	Lead	190	New	TN-325	ABS, CX, QE

TABLE F.3. The cross-sections updated (added) in the 2018 pion secondary interaction (pionSI) treatment. ABS, CX, and QE are all updated respectively for C, O, Al and Fe for incident $\pi^{\pm}$. For the first time Pb is also supported in the pionSI systematics evaluation.

between the GEANT4 prediction and NEUT prediction along with uncertainties. Overall, it is obvious that NEUT describes the data much better than GEANT4 and has much smaller uncertainties. For the pion-nucleus CX interactions, the NEUT and GEANT4 predictions are very different above 600 MeV/c pion momentum; the uncertainty of the NEUT prediction is inflated by 40 mb to cover the difference. The reason for the inflation is that there are no external data points to show which model is correct, and there is no reason to believe any model is incorrect. It is better to cover the difference with an inflated uncertainty band of 40 mb. Since most pions have momentum less than 600 MeV/c, this inflation should have a sub-percent level effect on the pion secondary interaction systematics.

F.3.5 Results of the 2018 Updates

The result of the above updates is more than a factor of two reductions (neutrino tracker NuMu selection, see table F.4, for example) in pion SI, which is one of the leading systematics in many analyses.

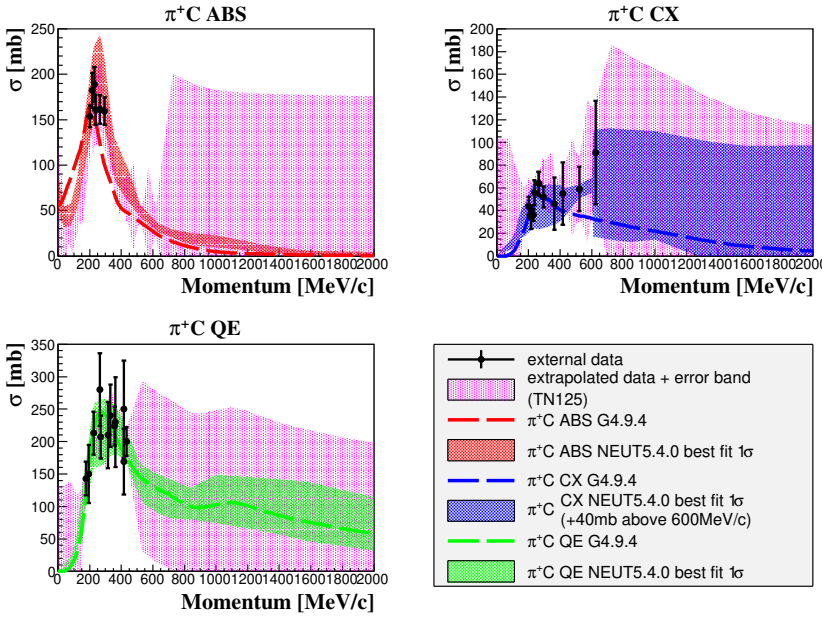

Figure F.2. π^+-C cross-sections for ABS, CX, and QE. The external data are shown as black dots. The TN-125 extrapolated data and error bands are shown in pink. The GEANT4 predictions are shown as dotted lines. The updated NEUT predictions and error bands are shown as solid colour bands. Note that the CX cross-section is inflated by 40 mb above 600 MeV/c. Uncertainties beyond 2 GeV/c are kept constant.

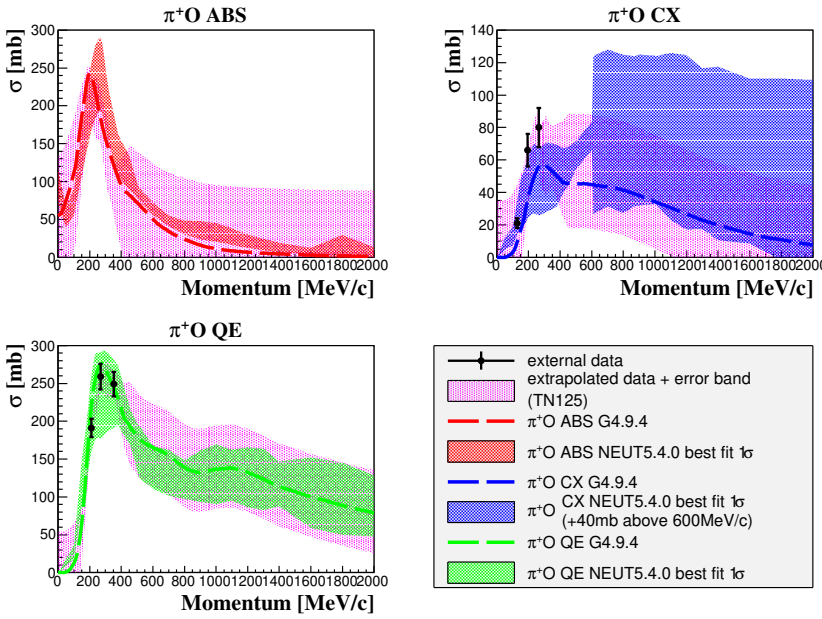

Figure F.3. π^+-O cross-sections for ABS, CX, and QE. The external data are shown as black dots. The TN-125 extrapolated data and error bands are shown in pink. The GEANT4 predictions are shown as dotted lines. The updated NEUT predictions and error bands are shown as solid colour bands. Note that the CX cross-section is inflated by 40 mb above 600 MeV/c. Uncertainties beyond 2 GeV/c are kept constant.

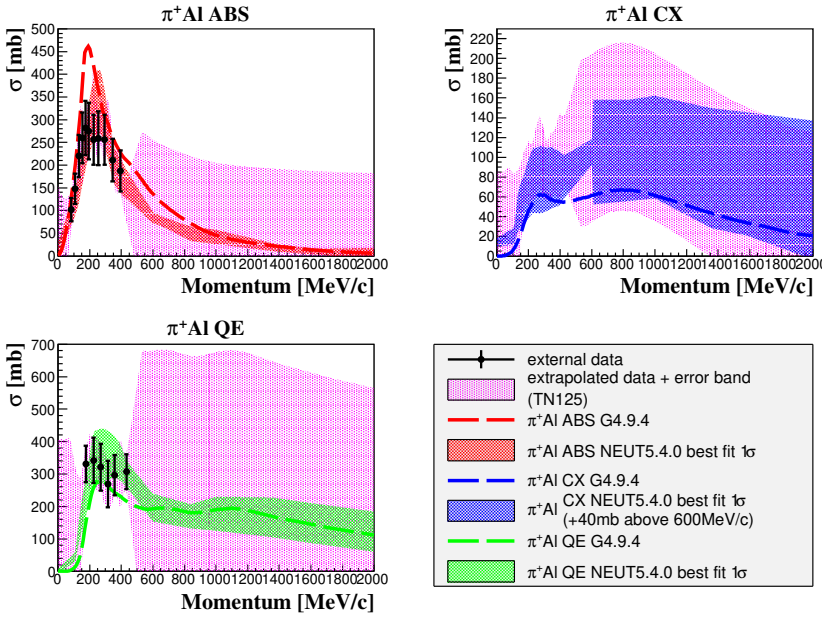

Figure F.4. π^+-Al cross-sections for ABS, CX, and QE. The external data are shown as black dots. The TN-125 extrapolated data and error bands are shown in pink. The GEANT4 predictions are shown as dotted lines. The updated NEUT predictions and error bands are shown as solid colour bands. Note that the CX cross-section is inflated by 40 mb above 600 MeV/c. Uncertainties beyond 2 GeV/c are kept constant.

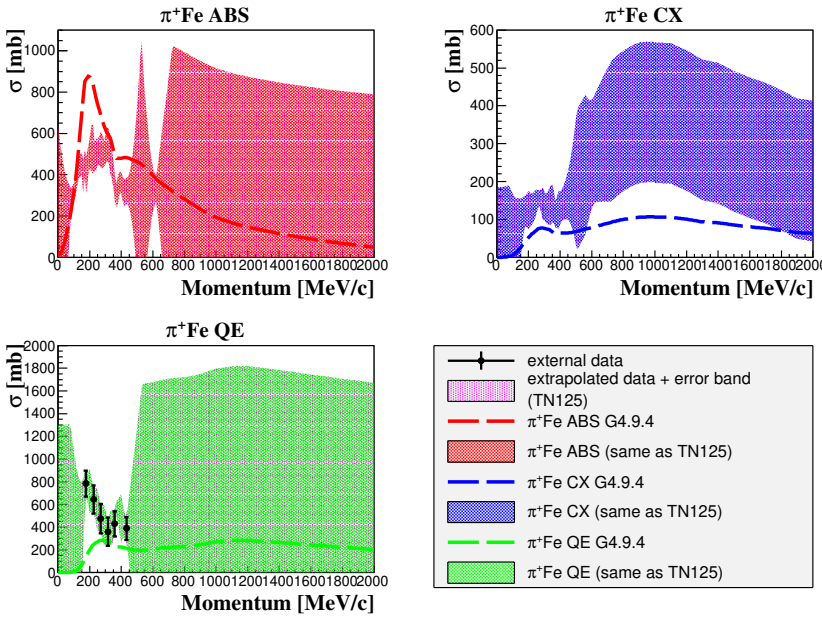

Figure F.5. π^+-Fe cross-sections for ABS, CX, and QE. The external data are shown as black dots. The TN-125 extrapolated data and error bands are shown in pink. The GEANT4 predictions are shown as dotted lines. The updated NEUT predictions and error bands are shown as solid colour bands. Note that the CX cross-section is inflated by 40 mb above 600 MeV/c. Uncertainties beyond 2 GeV/c are kept constant.

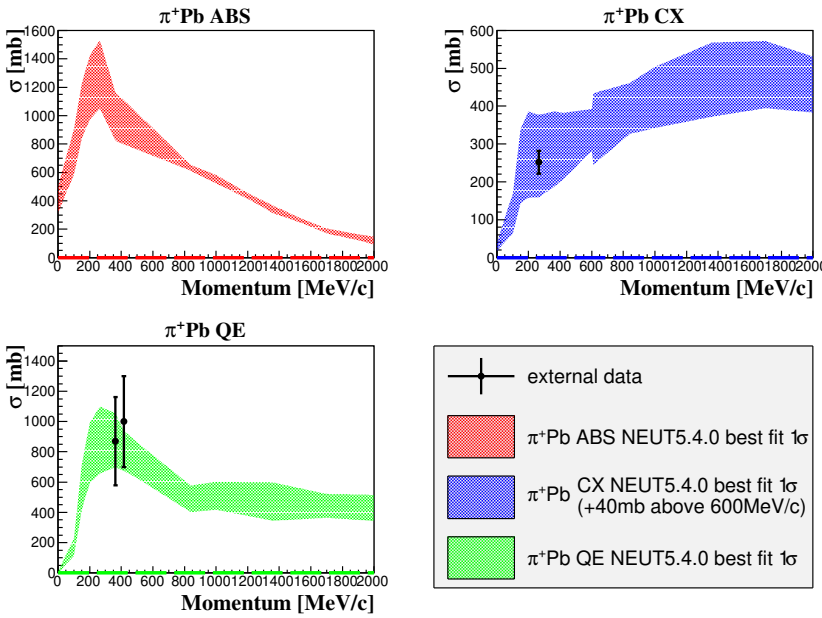

Figure F.6. π^+-Pb cross-sections for ABS, CX, and QE. The external data are shown as black dots. Note that Pb was not supported in the TN-125 version. The updated NEUT predictions and error bands are shown as solid color bands. Note the CX cross-section is inflated by 40 mb above 600 MeV/c. Uncertainties beyond 2 GeV/c are kept constant.

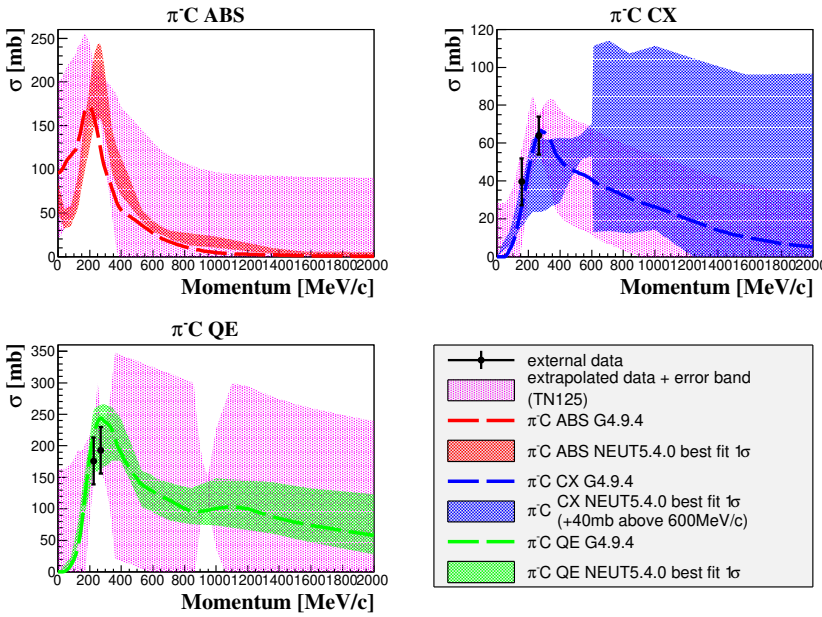

Figure F.7. π^--C cross-sections for ABS, CX, and QE. The external data are shown as black dots. The TN-125 extrapolated data and error bands are shown in pink. The GEANT4 predictions are shown as dotted lines. The updated NEUT predictions and error bands are shown as solid colour bands. Note that the CX cross-section is inflated by 40 mb above 600 MeV/c. Uncertainties beyond 2 GeV/c are kept constant.

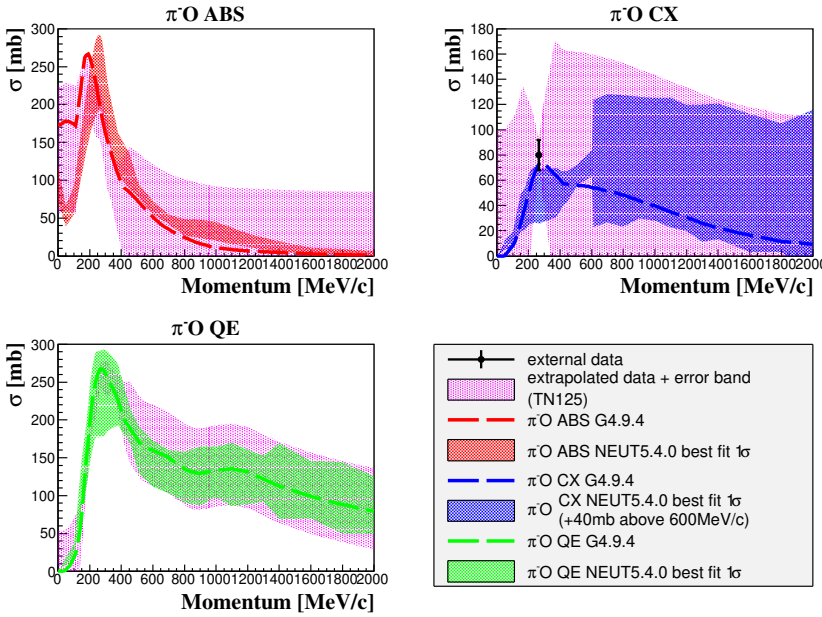

Figure F.8. π^--O cross-sections for ABS, CX, and QE. The external data are shown as black dots. The TN-125 extrapolated data and error bands are shown in pink. The GEANT4 predictions are shown as dotted lines. The updated NEUT predictions and error bands are shown as solid colour bands. Note that the CX cross-section is inflated by 40 mb above 600 MeV/c. Uncertainties beyond 2 GeV/c are kept constant.

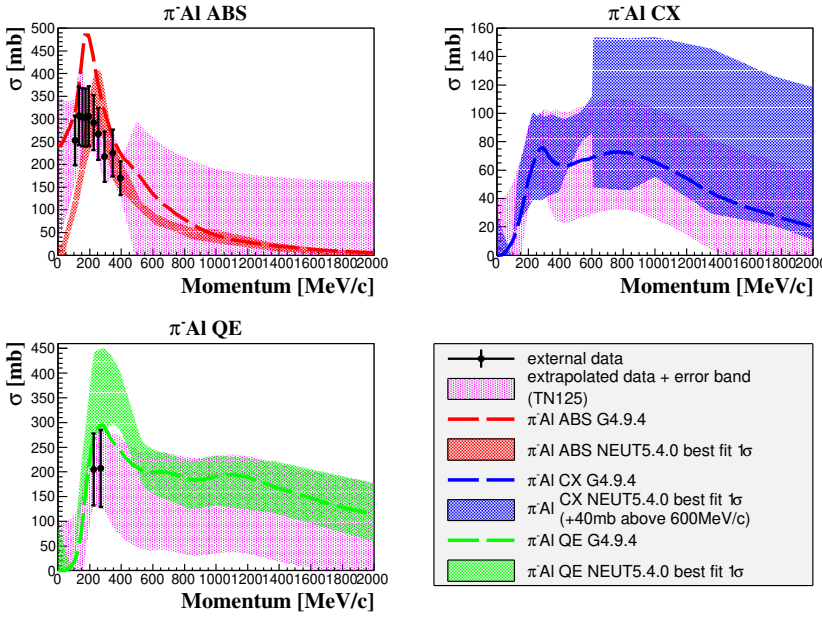

Figure F.9. π^--Al cross-sections for ABS, CX, and QE. The external data are shown as black dots. The TN-125 extrapolated data and error bands are shown in pink. The GEANT4 predictions are shown as dotted lines. The updated NEUT predictions and error bands are shown as solid colour bands. Note that the CX cross-section is inflated by 40 mb above 600 MeV/c. Uncertainties beyond 2 GeV/c are kept constant.

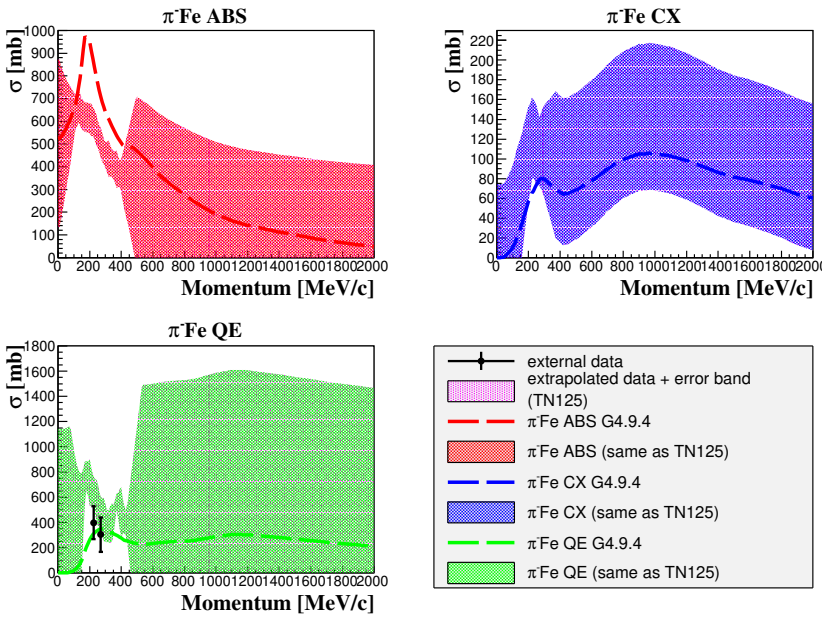

Figure F.10. π^--Fe cross-sections for ABS, CX, and QE. The external data are shown as black dots. The TN-125 extrapolated data and error bands are shown in pink. The GEANT4 predictions are shown as dotted lines. The updated NEUT predictions and error bands are shown as solid colour bands. Note that the CX cross-section is inflated by 40 mb above 600 MeV/c. Uncertainties beyond 2 GeV/c are kept constant.

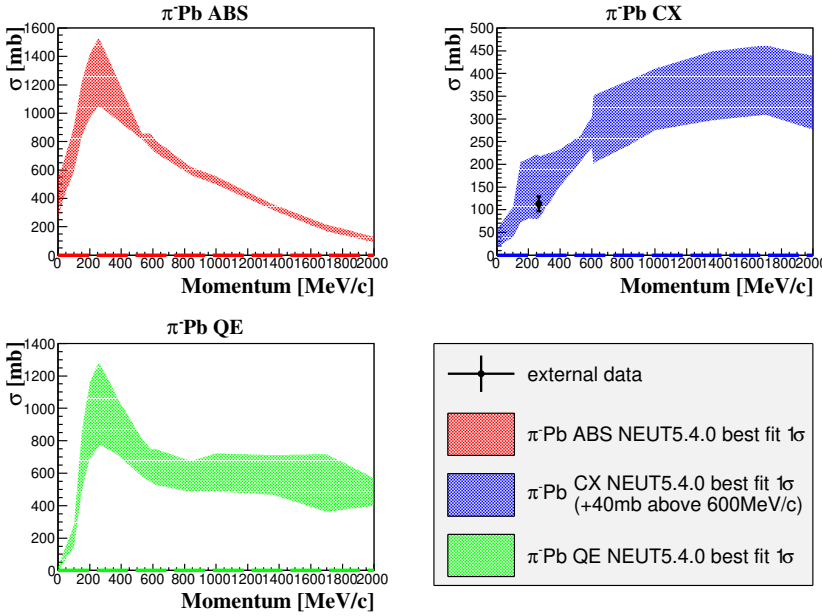

Figure F.11. π^--Pb cross-sections for ABS, CX, and QE. The external data are shown as black dots. Note that Pb was not supported in the TN-125 version. The updated NEUT predictions and error bands are shown as solid color bands. Note the CX cross-section is inflated by 40 mb above 600 MeV/c. Uncertainties beyond 2 GeV/c are kept constant.

Sample	Uncertainty [%]		
	CC-0π	CC-1π	CC-OTH
FGD1 (old)	1.6	3.3	3.9
FGD1 (updated)	0.7	1.3	1.7
FGD2 (old)	1.1	3.2	3.5
FGD2 (updated)	0.6	1.5	1.5

TABLE F.4. Pion secondary interaction (pionSI) systematics comparison between old (2013 version) and new (2018 version) treatments. Neutrino multi-pion selection package is used. It is clear that in all the samples (in both FGDs), pionSI systematics are reduced by at least a factor of two.

Appendix G

Additional Validations

G.1 Spline Validation Procedure

The validations performed on the dials for cross-section and final-state interaction (FSI) uncertainties listed in table 7.2 are shown in this appendix. Three things are being checked:

1. Effect of the dial values on the entire selection.

   Different dial values should result in weights applied to some events in the selection. The size of deviations from the nominal MC would suggest the effect of the changes to the dial value.

2. The accuracy of the splines.

   The splines are parameterized as functions of topologies, reactions, and reconstructed bins in $|t|$. T2KReWeight is used to generate the splines from the event-by-event weights. Therefore, the accuracy of the splines, compared to the actual weights, needs to be checked. Ratio plots between the distributions calculated from the splines weights and the actual weights are produced. An accuracy around 0.5%-1% is considered acceptable.

3. Dials only affecting relevant reactions.

Since a specific dial corresponds to a particular model's parameter inside the neutrino interaction generator, only relevant reactions described by that model should respond to the dial value changes. For example, the M_A^{RES} dial should only affect the RES events. If somehow it affects the DIS events, it would suggest a mistake in producing the splines.

As a reminder of the selection as a function of $|t|$, the first bin corresponds to the signal region, and the second bin corresponds to the sidebands.

G.2 An Example of the Spline Validations

Since the validation procedures are the same for all the dials, an example of the spline validation is shown in this section. The validations for all the rest of the dials are documented in TN-391 [95].

One of the DIS background dials used in this analysis is "CC DIS BY", which is an on-off "switch" dial for the Bodek-Yang (BY) correction. Figure G.1 shows the effect of the dial value changes (in 7 steps) to the selection and the accuracy of the dial (within 0.6%). Figure G.2 demonstrates that only DIS events are affected by the variation of the CC DIS BY dial.

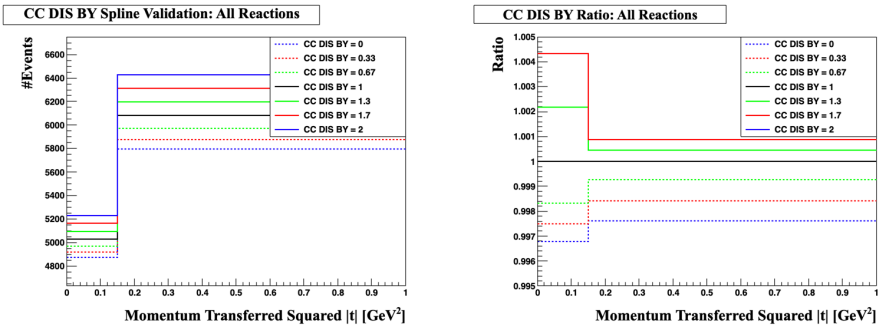

Figure G.1. The effects of the different dial values of the CC DIS Bodek-Yang dial characterized by the splines (left) and the accuracy of the splines (right) for the selection (all reactions) as a function of $|t|$. The accuracy of the dial is within 0.6%.

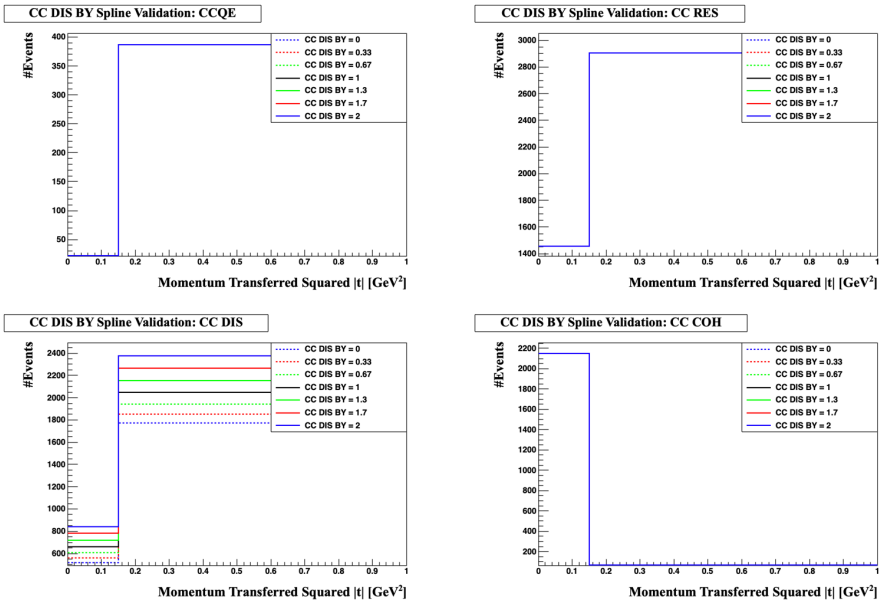

Figure G.2. The effects of the different dial values of the CC DIS Bodek-Yang dial characterized by the splines for the selection (broken down to CCQE, CCRES, CCDIS and CCCOH) as a function of $|t|$. Only the DIS events are affected by this dial as intended.

Appendix H

Additional Fake Data Studies

H.1 Additional Fake Data Studies: ν_μ CC-COH

H.1.1 Alternative MC Input (prod6B GENIE)

This study uses a previous ND280 MC production (prod6B GENIE) as fake data. The neutrino event generator used is GENIE [89]. Both signal and background events modelling differ between this MC and the nominal prod6T MC. The COH model used in prod6B GENIE is RS(2007).

Figure H.1 shows the pre-fit and post-fit parameters. Figure H.2 shows the pre-fit, post-fit, and prod6B GENIE reconstructed event distributions. The $\chi^2_{\text{post-fit}}$ is 4.81, with a p-value of 0.09. Figure 9.9 shows the nominal MC (pre-fit), fake data, and extracted cross sections. The χ^2_σ is 0.79, with a p-value of 0.38.

H.1.2 Shifted VA Distribution

The VA distribution shift, included in the hybrid fake data set in H.3, is tested with a fake data study with this change alone.

Figure H.4 shows the pre-fit and post-fit parameters. The fitter moves the cross-section parameters to adjust to the change in this fake data set. The post-fit template parameter is only slightly away from 1, which indicates the rest of the parameters are enough to adjust the changes made in this fake data set. Note that there is no VA-related dial implemented.

Figure H.5 shows the pre-fit, post-fit, and fake data reconstructed event distributions. The change in VA results in migrating background events out of the selected samples. The $\chi^2_{\text{post-fit}}$ is 0.49, with a p-value of 0.78.

Figure H.6 shows the nominal MC (pre-fit), fake data, and extracted cross sections. The

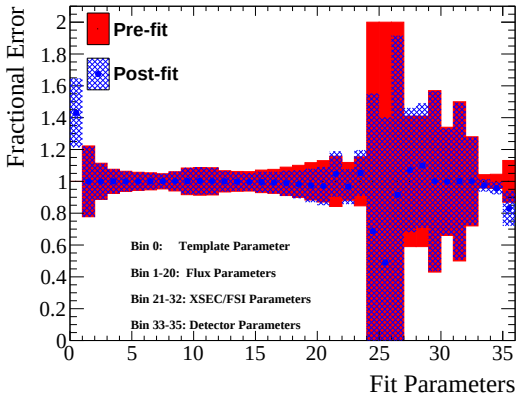

Figure H.1. Overlayed pre-fit and post-fit parameters with their uncertainties for the ν_μ fake data fit with production 6B GENIE MC as fake data.

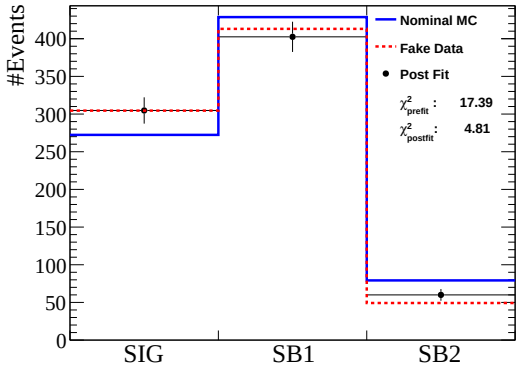

Figure H.2. Nominal MC (pre-fit), fake data, and post-fit (with stat. uncertainty) reconstructed event distributions of the three samples for the ν_μ fake data fit with production 6B GENIE MC as fake data. $\chi^2_{\text{pre-fit}}$ and $\chi^2_{\text{post-fit}}$ are also shown.

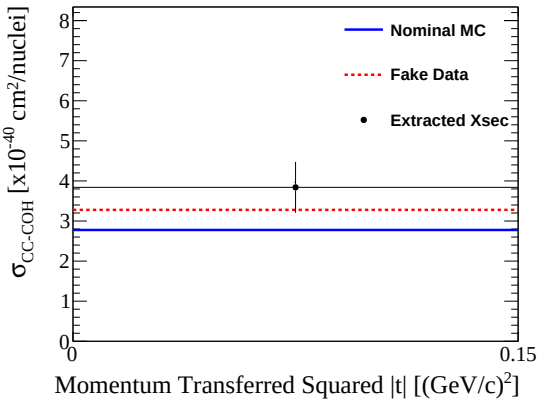

Figure H.3. Nominal MC (pre-fit), fake data, and extracted cross sections for the ν_μ fake data fit with production 6B GENIE MC as fake data. The error bar represents the combined (stat. + syst.) uncertainty for the extracted cross section.

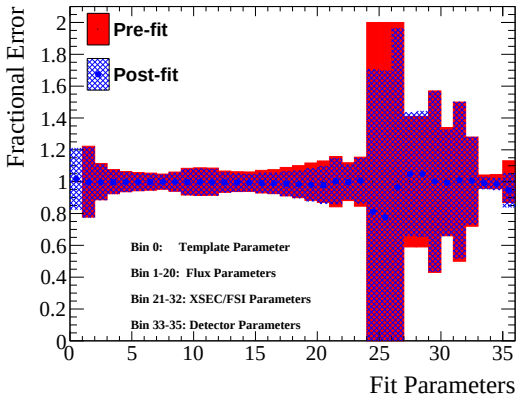

Figure H.4. Overlayed pre-fit and post-fit parameters with their uncertainties for the ν_μ fake data fit with the VA distribution shifted up by 1 MeV.

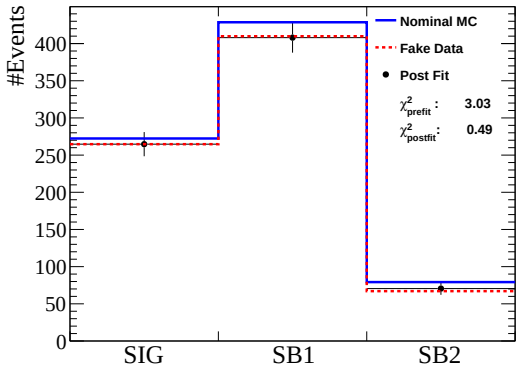

Figure H.5. Nominal MC (pre-fit), fake data, and post-fit (with stat. uncertainty) reconstructed event distributions of the three samples for the ν_μ fake data fit with the VA distribution shifted up by 1 MeV. $\chi^2_{\text{pre-fit}}$ and $\chi^2_{\text{post-fit}}$ are also shown.

cross-section χ^2_σ is 0.02, with a p-value of 0.89. The extracted cross section is compatible with the fake data truth.

H.1.3 Neutrino Energy Reweights

The effect of the uncertainties in the prediction of the neutrino flux on the analysis needs to be studied. Fake data sets reweighted from the nominal Monte Carlo simulation, where the events are weighted based on the neutrino energy, are used to perform the study. The flux uncertainty is around 5% at the neutrino flux peak (0.6 GeV), and around 10-20% after 2 GeV. Two tests are performed with the weights shown in equation H.1 and equation H.2 assuming a reasonable variation to be ± 20%, which is applied to the events with neutrino energy greater than 2 GeV.

$$\text{weight}(E_\nu) = \begin{cases} 1, & E_\nu \leq 2\,\text{GeV} \\ 1.2, & E_\nu > 2\,\text{GeV} \end{cases} \tag{H.1}$$

$$\text{weight}(E_\nu) = \begin{cases} 1, & E_\nu \leq 2\,\text{GeV} \\ 0.8, & E_\nu > 2\,\text{GeV} \end{cases} \tag{H.2}$$

Figure H.7 shows the pre-fit and post-fit parameters. The flux parameters' behaviour matches the weights applied to the events. The changes to the flux parameters occur from bins 13-20, which corresponds to true neutrino energy of 2 GeV and above. Parameters other than the flux parameters, such as the DIS and FSI parameters (bin 24-32), also change since most DIS backgrounds are reweighted in the fake data sets.

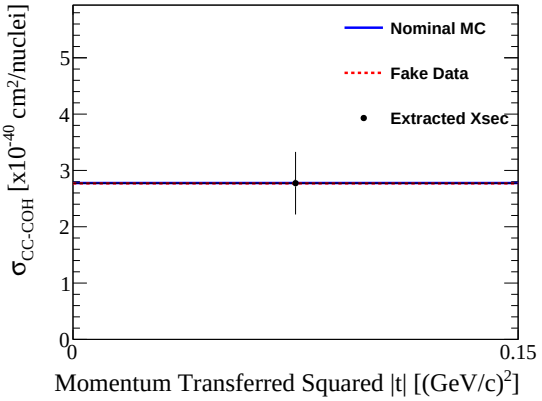

Figure H.6. Nominal MC (pre-fit), fake data, and extracted cross sections for the ν_μ fake data fit with the VA distribution shifted up by 1 MeV. The error bar represents the combined (stat. + syst.) uncertainty for the extracted cross section. The extracted cross section is compatible with the fake data truth.

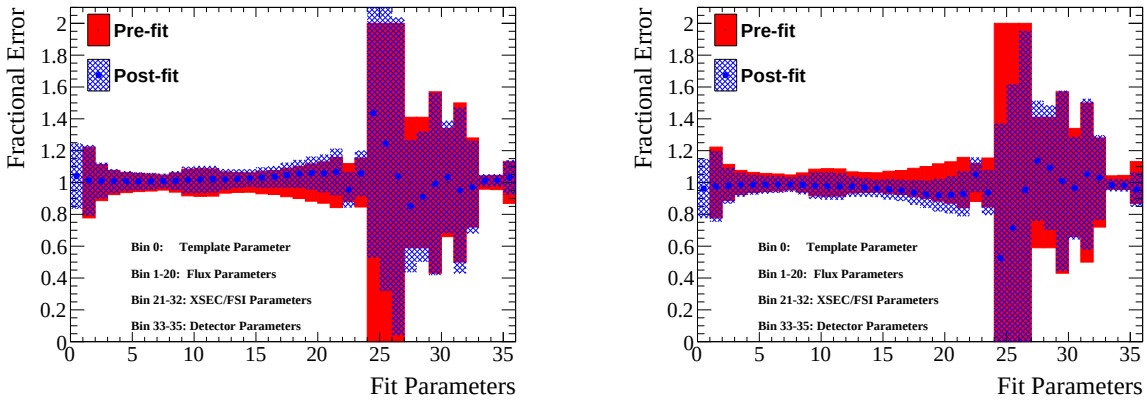

Figure H.7. Overlayed pre-fit and post-fit parameters with their fractional error for the ν_μ fake data fits with events reweighted according to equation H.1 (left) or equation H.2 (right), where the events with true neutrino energy above 2 GeV are given a weight of 1.2 (left) or 0.8 (right).

Figure H.8 shows the pre-fit, fake data, and post-fit reconstructed event distributions. χ^2_{postfit} for the two tests are 1.34 and 1.90, which correspond to p-values of 0.51 and 0.39. These p-values mean that the post-fit distributions are consistent (within the statistical uncertainties) with the fake data sets.

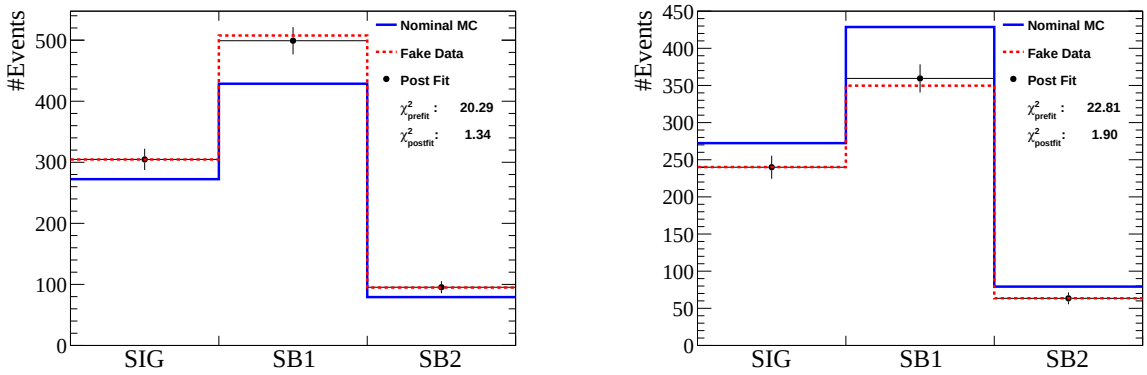

Figure H.8. Nominal Monte Carlo simulation, fake data, and post-fit (with stat. uncertainty) reconstructed event distributions of the three samples for the ν_μ fake data fits with events reweighted according to equation H.1 (left) or equation H.2 (right), where the events with true neutrino energy above 2 GeV are given a weight of 1.2 (left) or 0.8 (right). χ^2_{prefit} and χ^2_{postfit} are also shown.

Figure H.9 shows the nominal Monte Carlo simulation (pre-fit), fake data, and extracted cross sections. Both of the χ^2_σ are less than 0.01, with p-values of 0.94 and 0.97. The tests suggest that the variations in the neutrino flux (motivated by the T2K neutrino flux uncertainties) have little effect on the analysis result.

H.1.4 Weighted Background (Resonant Pion Production)

This study tests the fitter's response to different levels of variations to one of the major background sources (RES). Fake data sets are generated with the true ν_μ CC-RES events in the nominal Monte Carlo simulation reweighted according to either equation H.3, H.4, or H.5. Since each sample only contains one analysis bin, the analysis is sensitive only to the overall normalization but not so much to the shapes of distributions (e.g., pion momentum) in each sample. Hence the fake data sets only adjust the overall normalization.

$$\text{weight}(\text{reaction}) = \begin{cases} 1.2, & \text{reaction} = \nu_\mu \text{ CC-RES} \\ 1, & \text{Everything Else} \end{cases} \tag{H.3}$$

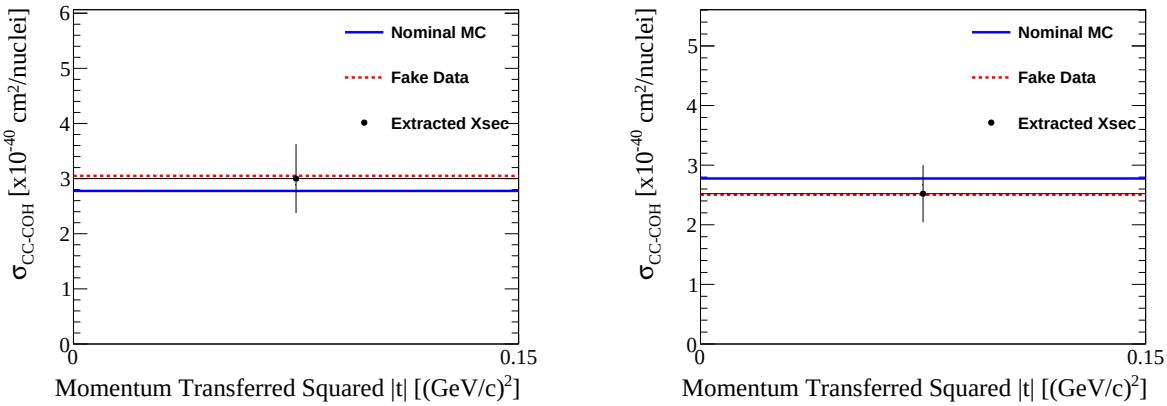

Figure H.9. Nominal Monte Carlo simulation, fake data, and extracted cross sections for the ν_μ fake data fits with events reweighted according to equation H.1 (left) or equation H.2 (right), where the events with true neutrino energy above 2 GeV are given a weight of 1.2 (left) or 0.8 (right). The error bars represent the combined (stat. + syst.) uncertainties for the extracted cross sections.

$$\text{weight(reaction)} = \begin{cases} 1.5, & \text{reaction} = \nu_\mu \text{ CC-RES} \\ 1, & \text{Everything Else} \end{cases} \tag{H.4}$$

$$\text{weight(reaction)} = \begin{cases} 1.9, & \text{reaction} = \nu_\mu \text{ CC-RES} \\ 1, & \text{Everything Else} \end{cases} \tag{H.5}$$

Due to the limited statistics of this analysis, it is also important to test the effect of reduced RES backgrounds to check for any bias toward a low number of events in samples. Thus, fake data sets with equal amount of deflation of RES are generated with weights according to either equation H.6, H.7, or H.8.

$$\text{weight(reaction)} = \begin{cases} 0.8, & \text{reaction} = \nu_\mu \text{ CC-RES} \\ 1, & \text{Everything Else} \end{cases} \tag{H.6}$$

$$\text{weight(reaction)} = \begin{cases} 0.5, & \text{reaction} = \nu_\mu \text{ CC-RES} \\ 1, & \text{Everything Else} \end{cases} \tag{H.7}$$

$$\text{weight(reaction)} = \begin{cases} 0.1, & \text{reaction} = \nu_\mu \text{ CC-RES} \\ 1, & \text{Everything Else} \end{cases} \tag{H.8}$$

The reason for choosing ±90% is to avoid the unphysical scenario of obliterating the RES backgrounds (-100%) and being symmetric with the test.

Figure H.10 shows the pre-fit and post-fit parameters. Bins 21-23 correspond to the RES

background-related cross-section dials and the post-fit values match the changes to RES in each fake data set. However, the DIS background dials (bins 24-26) also move since the two types of background events co-exist in the two background sidebands. The signal is not modified in any of the fake data sets. The post-fit template parameters drift away from 1, which means the cross-section results will be biased with changes to RES. The level of deviation is correlated with the amount of change applied to the RES backgrounds.

Figure H.11 shows the pre-fit, post-fit and fake data reconstructed event distributions. The χ^2_{postfit} increases as the weight increases. However, all fits converged, which indicates the robustness of the framework in case of extreme data and Monte Carlo simulation disagreement due to the mismodeling of the RES background events.

Figure H.12 shows the nominal Monte Carlo simulation (pre-fit), fake data, and extracted cross sections. The bias to the extracted cross section increases as the weight for the RES background events increases. The results indicate that the measurement uncertainty would still cover the bias in the cross-section result if the overall normalization of RES from the Monte Carlo simulation prediction is accurate with $\pm$ 50%. There is no indication of such a large mismodel of RES from past T2K analyses.

H.1.5 Weighted Background (Deep Inelastic Scattering)

This study tests the fitter's response to different levels of variations of another major background source (DIS). Fake data sets are generated with the true ν_μ CC-DIS events in the nominal Monte Carlo simulation reweighted according to either equation H.9, H.10, or H.11. Since each sample only contains one analysis bin, the analysis is sensitive only to the overall normalization but not so much to shapes of the distributions (e.g., pion momentum) in each sample. Hence the fake data sets only adjust the overall normalization.

$$\text{weight(reaction)} = \begin{cases} 1.2, & \text{reaction} = \nu_\mu \text{ CC-DIS} \\ 1, & \text{Everything Else} \end{cases} \tag{H.9}$$

$$\text{weight(reaction)} = \begin{cases} 1.5, & \text{reaction} = \nu_\mu \text{ CC-DIS} \\ 1, & \text{Everything Else} \end{cases} \tag{H.10}$$

$$\text{weight(reaction)} = \begin{cases} 1.8, & \text{reaction} = \nu_\mu \text{ CC-DIS} \\ 1, & \text{Everything Else} \end{cases} \tag{H.11}$$

Similar to the RES case, equal amount of deflation of DIS are tested with fake data sets with a weight according to either equation H.12, H.13, or H.14. Also, since the DIS sideband contains mostly DIS background events, it is essential to test how the fitter would behave

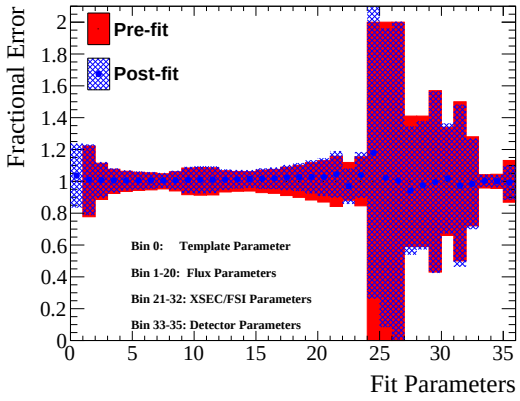

(a) weight(CC-RES)=1.2

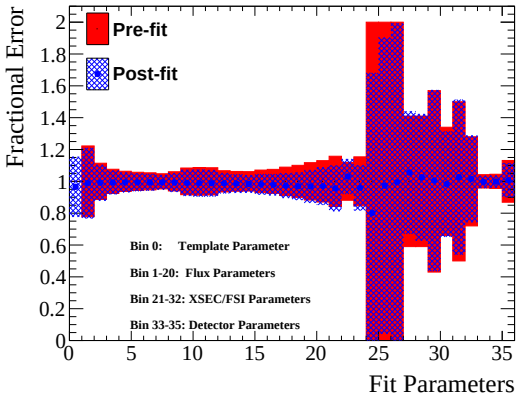

(b) weight(CC-RES)=0.8

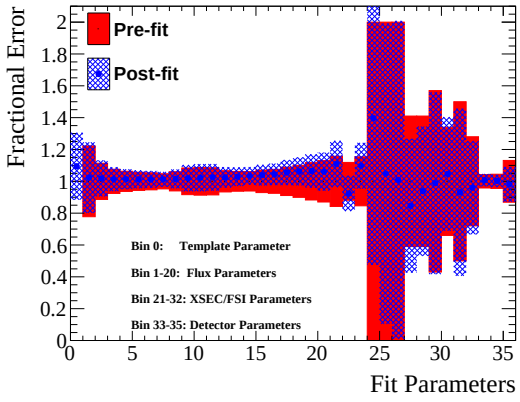

(c) weight(CC-RES)=1.5

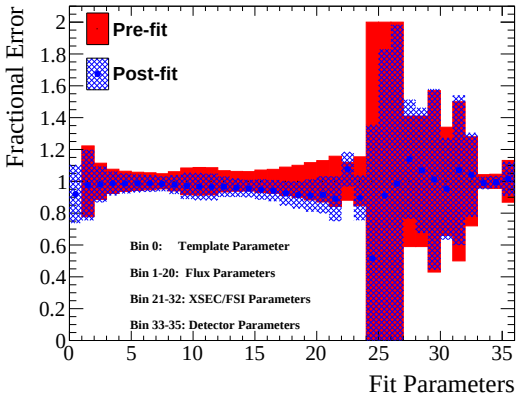

(d) weight(CC-RES)=0.5

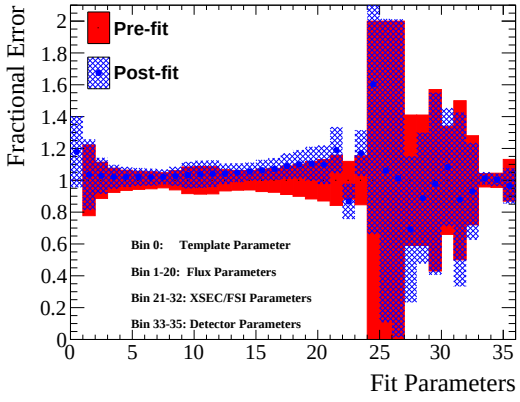

(e) weight(CC-RES)=1.9

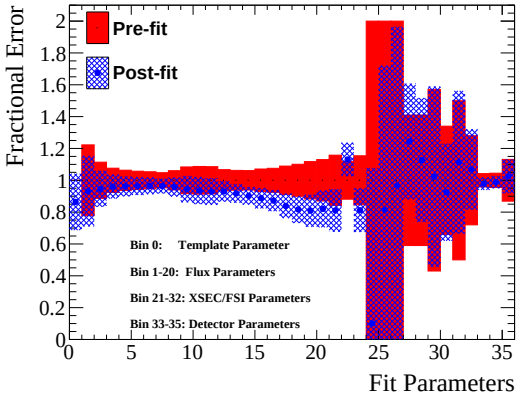

(f) weight(CC-RES)=0.1

Figure H.10. Overlayed pre-fit and post-fit parameters with their fractional error for the ν_μ fake data fit with events reweighted according to equation H.3-H.8, where the ν_μ CC-RES background events are given weights. The template parameter is expected to stay at 1, the deviated post-fit template parameters indicate biases in the cross-section.

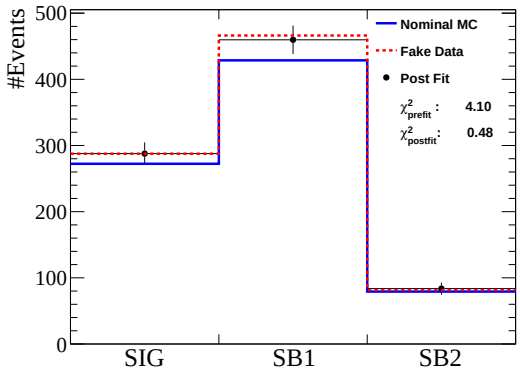

(a) weight(CC-RES)=1.2

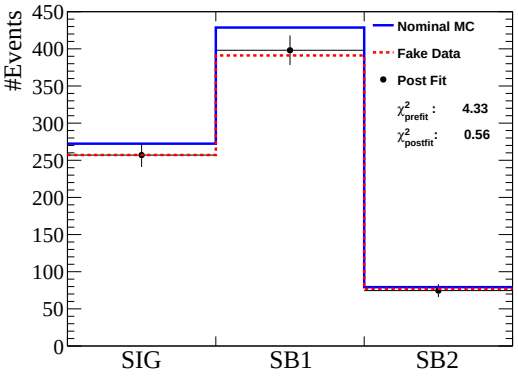

(b) weight(CC-RES)=0.8

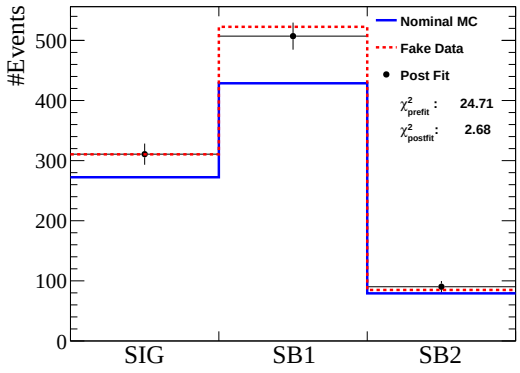

(c) weight(CC-RES)=1.5

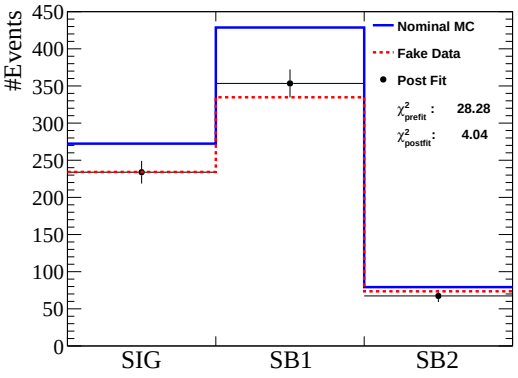

(d) weight(CC-RES)=0.5

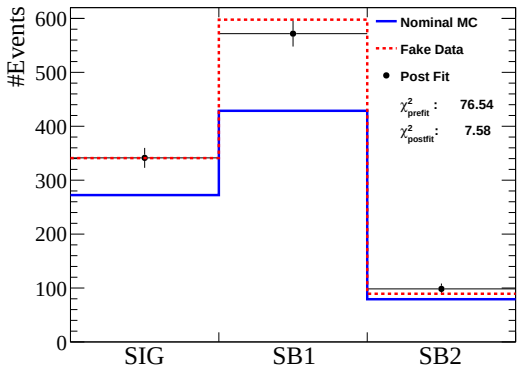

(e) weight(CC-RES)=1.9

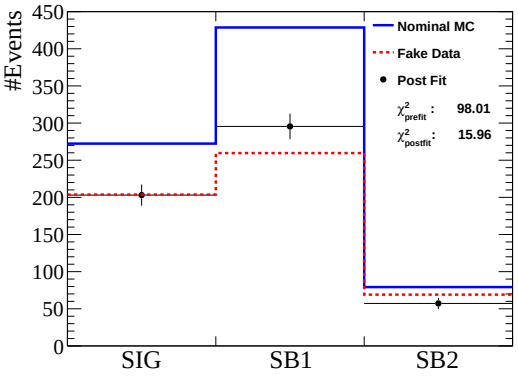

(f) weight(CC-RES)=0.1

Figure H.11. Nominal Monte Carlo simulation, fake data, and post-fit (with stat. uncertainty) reconstructed event distributions of the three samples for the ν_μ fake data fit with events reweighted according to equation H.3-H.8, where the ν_μ CC-RES background events are given weights. χ^2_{prefit} and χ^2_{postfit} are also shown. The decreased χ^2_{postfit} in all cases indicate improvements in the agreement between the post-fit results and the fake data.

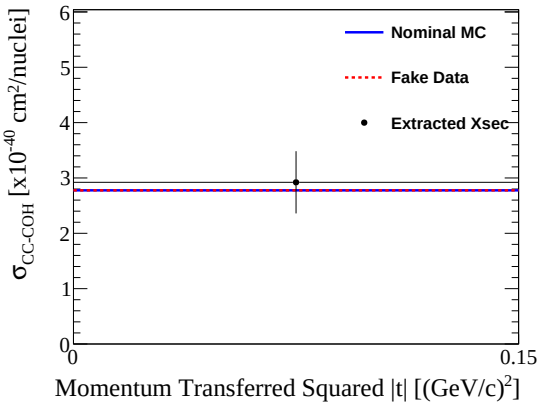

(a) weight(CC-RES)=1.2

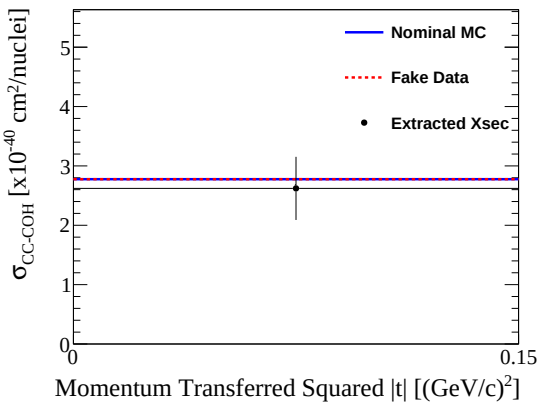

(b) weight(CC-RES)=0.8

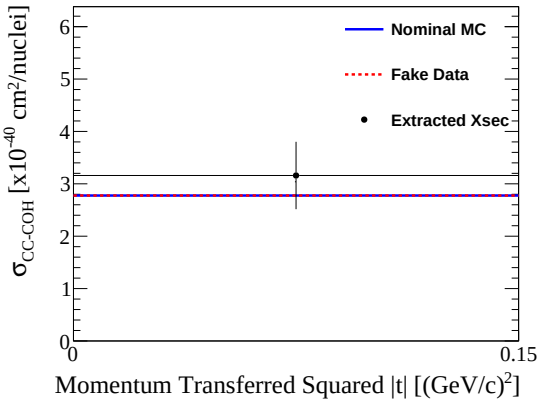

(c) weight(CC-RES)=1.5

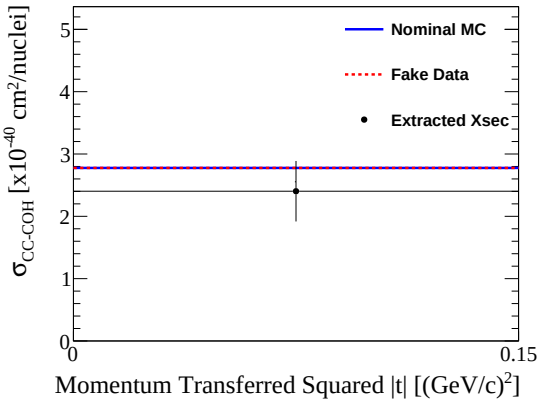

(d) weight(CC-RES)=0.5

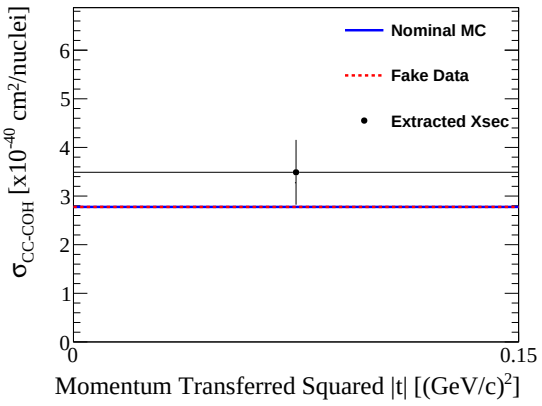

(e) weight(CC-RES)=1.9

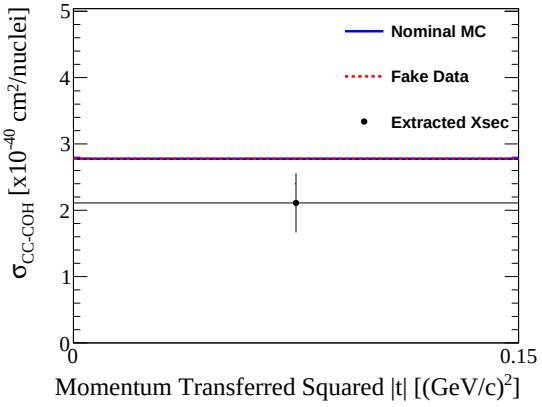

(f) weight(CC-RES)=0.1

Figure H.12. Nominal Monte Carlo simulation, fake data, and extracted cross sections for the ν_μ fake data fit with events reweighted according to equation H.3-H.8, where the ν_μ CC-RES background events are given weights. The error bar represents the combined (stat. + syst.) uncertainty for the extracted cross section. The measurement uncertainties cover the bias in the extracted cross sections until the weight applied to CC-RES exceeds 50%.

when one of the samples contains only a few events.

$$\text{weight(reaction)} = \begin{cases} 0.8, & \text{reaction} = \nu_\mu \text{ CC-DIS} \\ 1, & \text{Everything Else} \end{cases} \tag{H.12}$$

$$\text{weight(reaction)} = \begin{cases} 0.5, & \text{reaction} = \nu_\mu \text{ CC-DIS} \\ 1, & \text{Everything Else} \end{cases} \tag{H.13}$$

$$\text{weight(reaction)} = \begin{cases} 0.2, & \text{reaction} = \nu_\mu \text{ CC-DIS} \\ 1, & \text{Everything Else} \end{cases} \tag{H.14}$$

The reason for choosing ±80% is to avoid the unphysical scenario of obliterating the DIS backgrounds (-100%) and being symmetric with the test. The fit with -90% DIS did not converge, possibly due to the fitter having an issue with the DIS sideband having too few events. Details of this failure mode are included in H.

Figure H.13 shows the pre-fit and post-fit parameters. The post-fit values of the DIS dials (bins 24-26) match the changes applied to DIS in each fake data set.

Figure H.14 shows the pre-fit, fake data, and post-fit reconstructed event distributions. The χ^2_{postfit} increases as the weight increases. The non-convergence of the CC-DIS -90% fit and the convergence of the CC-DIS -80% fit suggest the fitter framework's limitation regarding deflating the DIS background. Note that such a large deviation from the nominal Monte Carlo simulation is not expected.

Figure H.15 shows the nominal Monte Carlo simulation (pre-fit), fake data, and extracted cross sections. The extracted cross sections are not as biased as the RES-modified fake data studies due to the additional DIS sideband constraint.

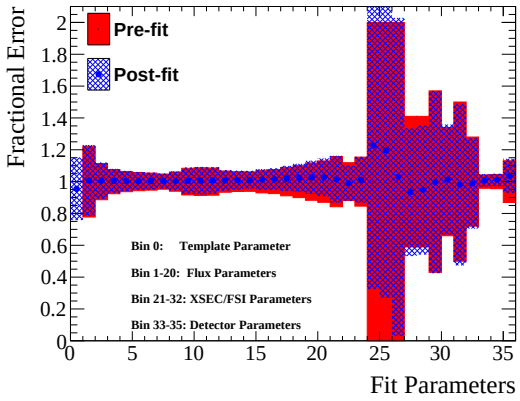

(a) weight(CC-DIS)=1.2

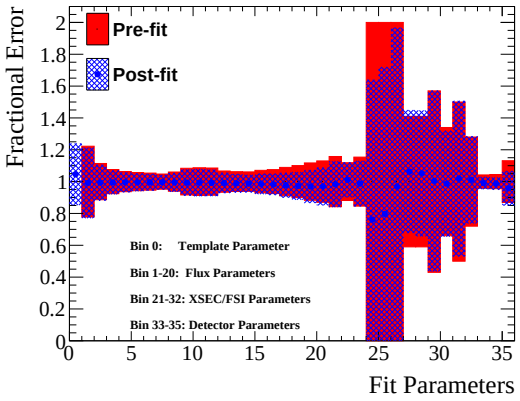

(b) weight(CC-DIS)=0.8

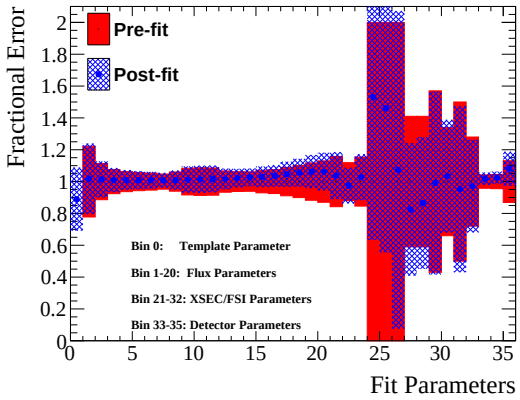

(c) weight(CC-DIS)=1.5

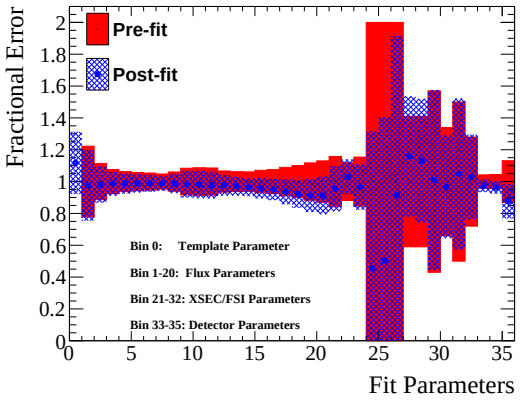

(d) weight(CC-DIS)=0.5

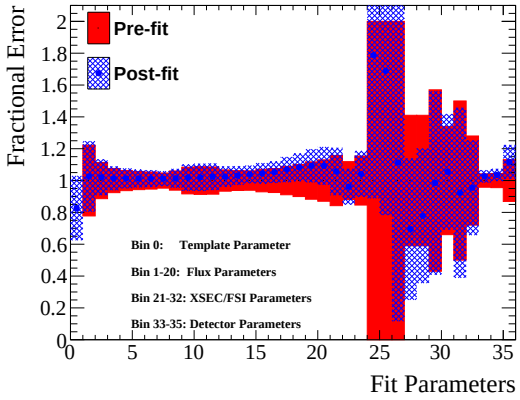

(e) weight(CC-DIS)=1.8

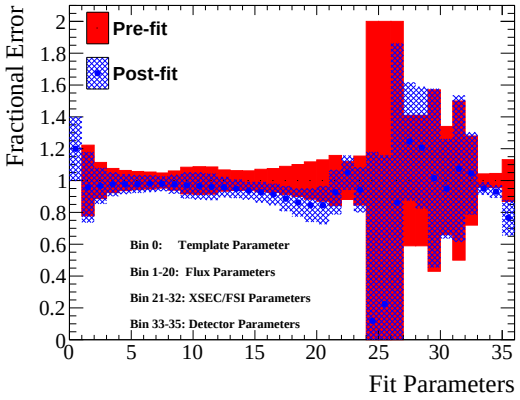

(f) weight(CC-DIS)=0.2

Figure H.13. Overlayed pre-fit and post-fit parameters with their fractional error for the ν_μ fake data fit with events reweighted according to equation H.9-H.14, where the ν_μ CC-DIS background events are given weights.

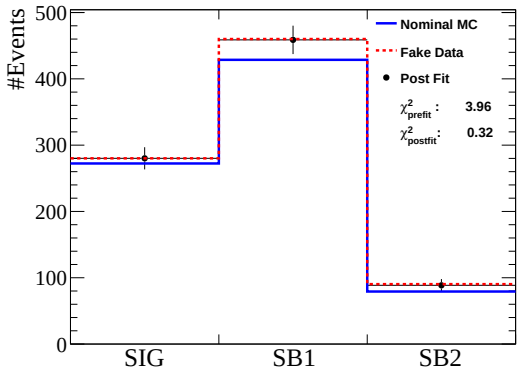

(a) weight(CC-DIS)=1.2

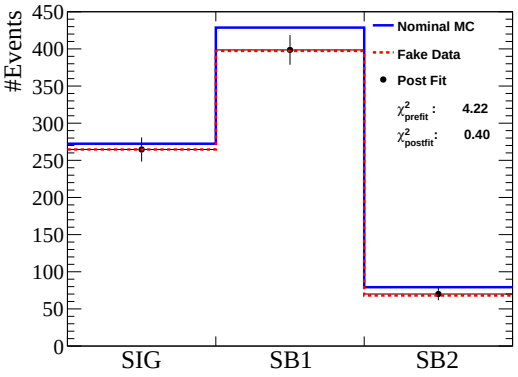

(b) weight(CC-DIS)=0.8

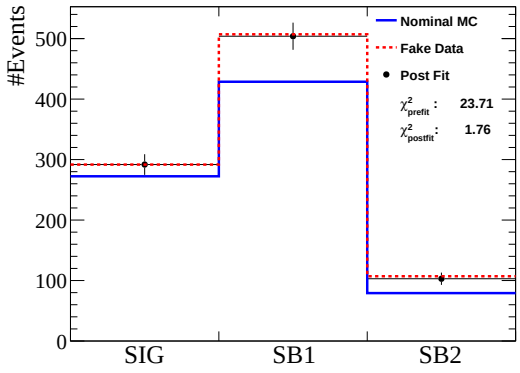

(c) weight(CC-DIS)=1.5

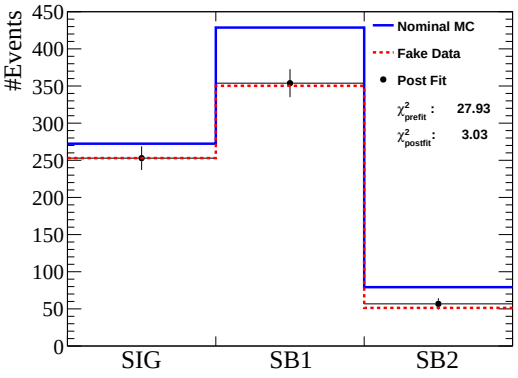

(d) weight(CC-DIS)=0.5

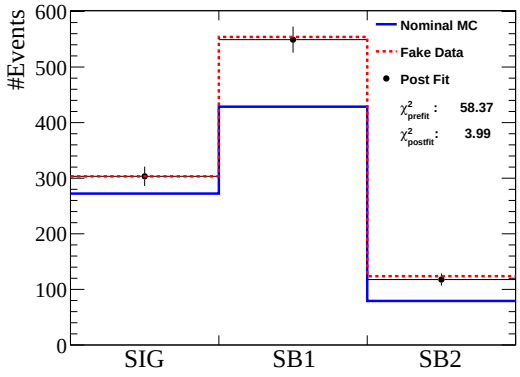

(e) weight(CC-DIS)=1.9

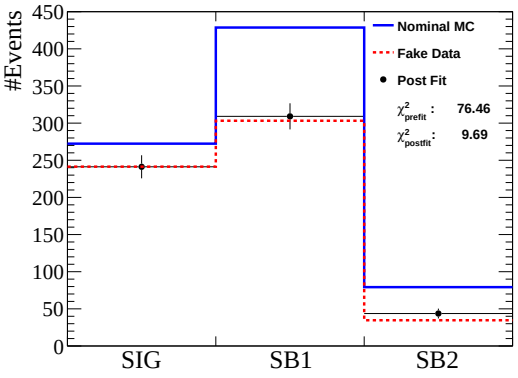

(f) weight(CC-DIS)=0.1

Figure H.14. Nominal Monte Carlo simulation, fake data, and post-fit (with stat. uncertainty) reconstructed event distributions of the three samples for the ν_μ fake data fit with events reweighted according to equation H.9-H.14, where the ν_μ CC-DIS background events are given weights. χ^2_{prefit} and χ^2_{postfit} are also shown.

H.2 Additional Fake Data Studies: $\bar{\nu}_\mu$ CC-COH

H.2.1 Neutrino Energy Reweights

The effect of the uncertainties in the prediction of the neutrino flux on the analysis needs to be studied. Fake data sets reweighted from the nominal Monte Carlo simulation, where the events are weighted based on the true neutrino energy, are used to perform the study. Two tests are performed with the weights shown in equation H.15 and equation H.16 - these are the same formula used for the ν_μ studies.

$$\text{weight}(E_\nu) = \begin{cases} 1, & E_\nu < 2\,\text{GeV} \\ 1.2, & E_\nu > 2\,\text{GeV} \end{cases} \tag{H.15}$$

$$\text{weight}(E_\nu) = \begin{cases} 1, & E_\nu < 2\,\text{GeV} \\ 0.8, & E_\nu > 2\,\text{GeV} \end{cases} \tag{H.16}$$

Figure H.16 shows the pre-fit and post-fit parameters. The flux parameters' behaviour matches with the weights applied to the events. The changes to the flux parameters occur from bins 13-20, which corresponds to true neutrino energy of 2 GeV and above. Parameters other than the flux parameters, such as the DIS and FSI parameters (bin 24-32), also change since most DIS backgrounds are reweighted in the fake data sets.

Figure H.17 shows the pre-fit, fake data, and post-fit reconstructed event distributions. The $\chi^2_{\text{post-fit}}$ are 0.81 and 1.08, respectively, which correspond to p-values of 0.37 and 0.30. These p-values mean that the post-fit distributions are (barely for the second study) consistent (within the statistical uncertainties) with the fake data sets.

Figure H.18 shows the nominal Monte Carlo simulation (pre-fit), fake data, and extracted cross sections. Both of the χ^2_σ are less than 0.02, with p-values of 0.95 and 0.89. The tests suggest that the T2K beam variation in the neutrino flux has little effect on the analysis result.

H.2.2 Modified Background (Resonant Pion Production)

This study tests the fitter's response to different levels of variations to one of the major background sources (RES). Fake data sets are generated with the true $\bar{\nu}_\mu$ CC-RES events in the nominal Monte Carlo simulation reweighted according to either equation H.17, H.18, or H.19. Since each sample only contains one analysis bin, the analysis is sensitive only to the overall normalization but not so much to the shapes of the distributions (e.g., pion

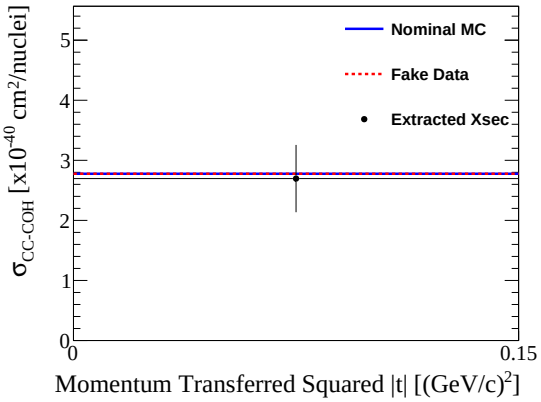

(a) weight(CC-DIS)=1.2

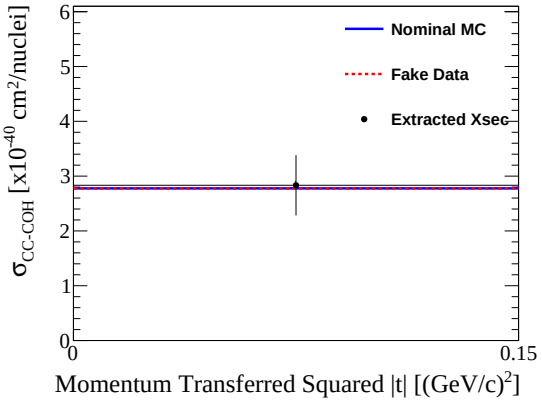

(b) weight(CC-DIS)=0.8

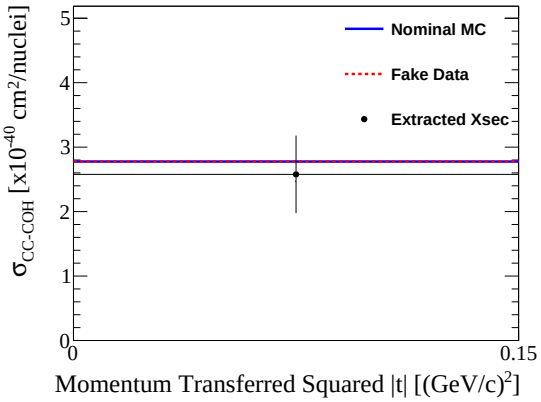

(c) weight(CC-DIS)=1.5

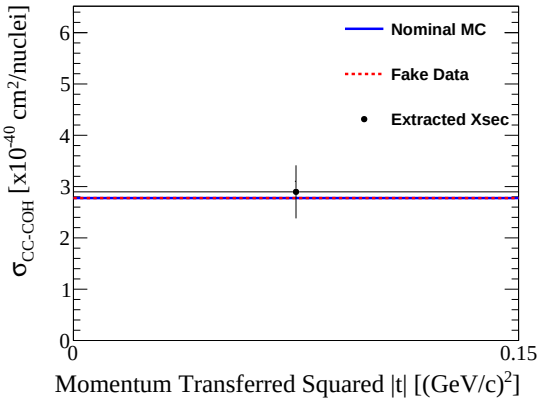

(d) weight(CC-DIS)=0.5

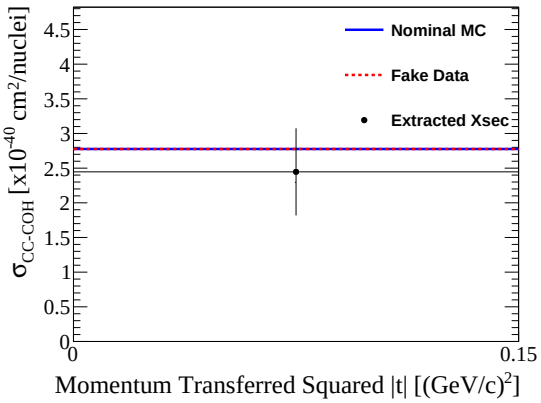

(e) weight(CC-DIS)=1.9

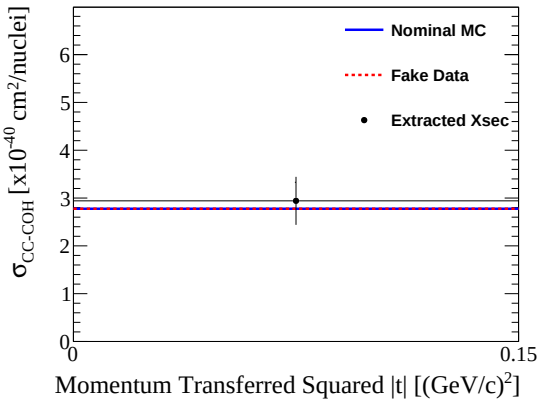

(f) weight(CC-DIS)=0.1

Figure H.15. Nominal Monte Carlo simulation, fake data, and extracted cross sections for the ν_μ fake data fit with events reweighted according to equation H.9-H.14, where the ν_μ CC-DIS background events are given weights. The error bar represents the combined (stat. + syst.) uncertainty for the extracted cross section.

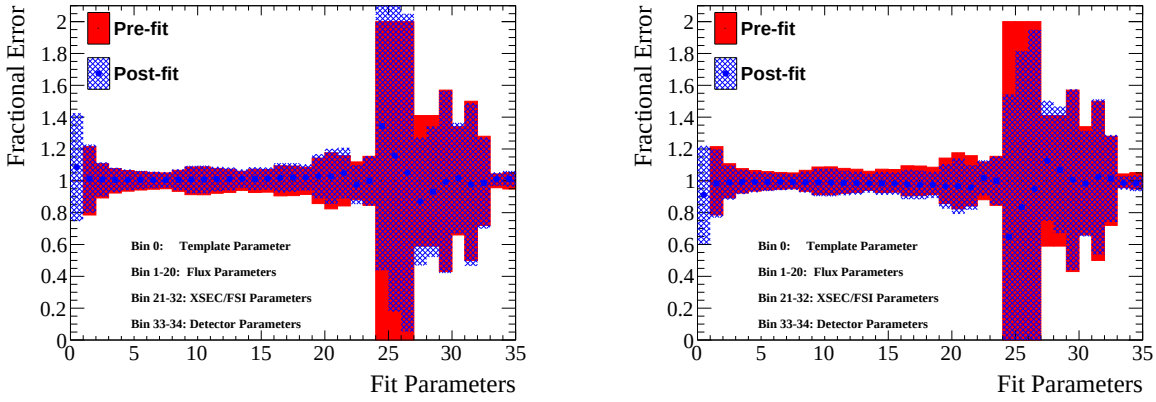

Figure H.16. Overlayed pre-fit and post-fit parameters with their fractional error for the $\bar{\nu_\mu}$ fake data fit with events reweighted according to equation H.15 (left) or equation H.16 (right), where the events with true neutrino energy above 2 GeV are given a weight of 1.2 (left) or 0.8 (right).

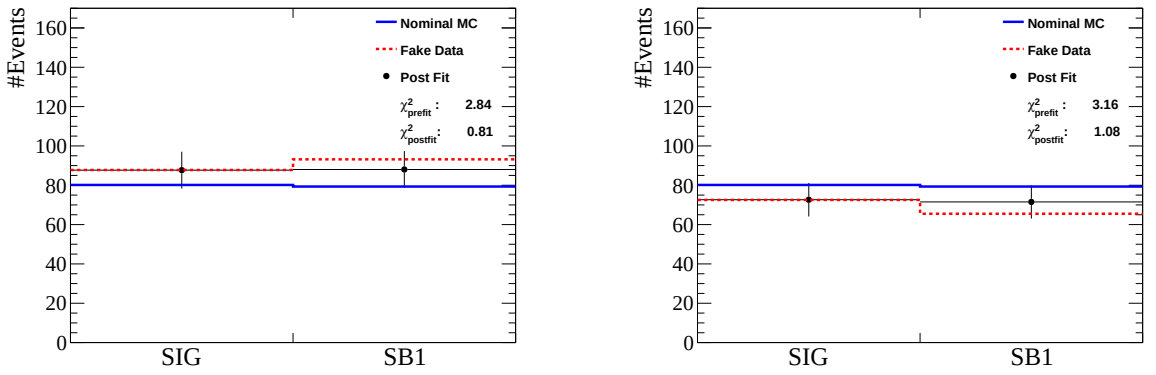

Figure H.17. Nominal Monte Carlo simulation, fake data, and post-fit (with stat. uncertainty) reconstructed event distributions of the 2 samples for the $\bar{\nu_\mu}$ fake data fit with events reweighted according to equation H.15 (left) or equation H.16 (right), where the events with true neutrino energy above 2 GeV are given a weight of 1.2 (left) or 0.8 (right). $\chi^2_{\text{pre-fit}}$ and $\chi^2_{\text{post-fit}}$ are also shown.

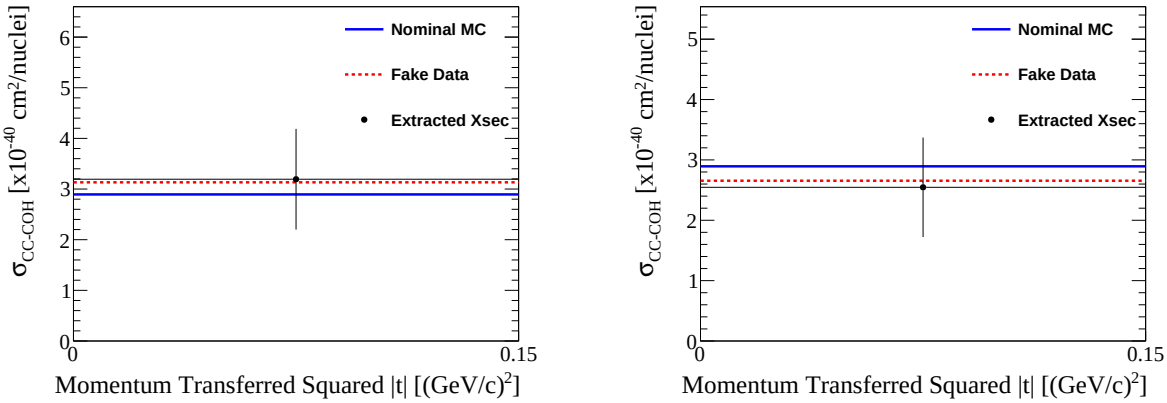

Figure H.18. Nominal Monte Carlo simulation, fake data, and extracted cross sections for the $\bar{\nu}_\mu$ fake data fit with events reweighted according to equation H.15 (left) or equation H.16 (right), where the events with true neutrino energy above 2 GeV are given a weight of 1.2 (left) or 0.8 (right). The error bar represents the combined (stat. + syst.) uncertainty for the extracted cross section.

momentum) in each sample. Hence the fake data sets only adjust the overall normalization.

$$\text{weight(reaction)} = \begin{cases} 1.2, & \bar{\nu}_\mu \text{ CC-RES} \\ 1, & \text{Everything Else} \end{cases} \tag{H.17}$$

$$\text{weight(reaction)} = \begin{cases} 1.5, & \bar{\nu}_\mu \text{ CC-RES} \\ 1, & \text{Everything Else} \end{cases} \tag{H.18}$$

$$\text{weight(reaction)} = \begin{cases} 1.9, & \bar{\nu}_\mu \text{ CC-RES} \\ 1, & \text{Everything Else} \end{cases} \tag{H.19}$$

Due to the limited statistics of this analysis, it is also important to test the effect of reduced RES backgrounds to check for any bias toward a low number of events in samples. Thus, fake data sets with equal amount of deflation of RES are generated with weights according to either equation H.20, H.21, or H.22.

$$\text{weight(reaction)} = \begin{cases} 0.8, & \bar{\nu}_\mu \text{ CC-RES} \\ 1, & \text{Everything Else} \end{cases} \tag{H.20}$$

$$\text{weight(reaction)} = \begin{cases} 0.5, & \bar{\nu}_\mu \text{ CC-RES} \\ 1, & \text{Everything Else} \end{cases} \tag{H.21}$$

$$\text{weight(reaction)} = \begin{cases} 0.1, & \bar{\nu_\mu} \text{ CC-RES} \\ 1, & \text{Everything Else} \end{cases} \tag{H.22}$$

The reason for choosing ±90% is to avoid the unphysical scenario of obliterating the RES backgrounds (-100%) and being symmetric with the test.

Figure H.19 shows the pre-fit and post-fit parameters. Bins 21-23 correspond to the RES background-related cross-section dials, and the post-fit values match the changes to RES in each fake data set. However, the DIS background dials (bins 24-26) also move since the two types of background events co-exist in the two background sidebands. The post-fit template parameters drift away from 1, which means the cross-section results will be biased with changes to RES. The level of deviation is correlated with the amount of change applied to the RES backgrounds.

Figure H.20 shows the pre-fit, post-fit and fake data reconstructed event distributions. The $\chi^2_{\text{post-fit}}$ increases as the weight increases. However, all fits converged, which indicates the robustness of the framework in case of extreme data and Monte Carlo simulation disagreement due to the mismodeling of the RES background events.

Figure H.21 shows the nominal Monte Carlo simulation (pre-fit), fake data, and extracted cross sections. The bias to the extracted cross section increases as the weight for the RES background events increases. The results indicate that the measurement uncertainty would still cover the bias in the cross-section result if the overall normalization of RES from the Monte Carlo simulation prediction is accurate with ± 50%.

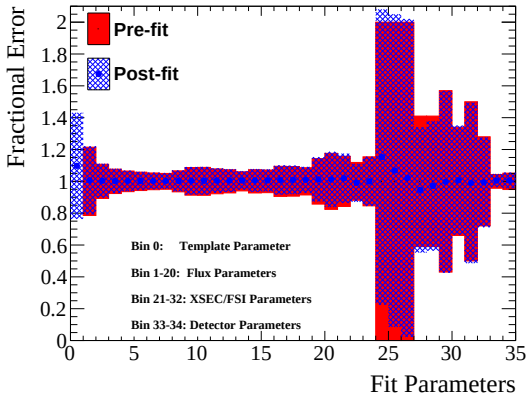

(a) weight(CC-RES)=1.2

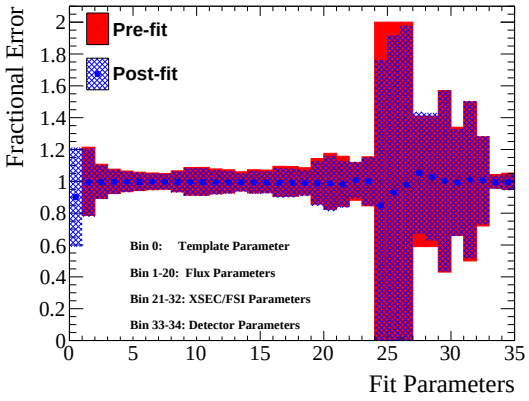

(b) weight(CC-RES)=0.8

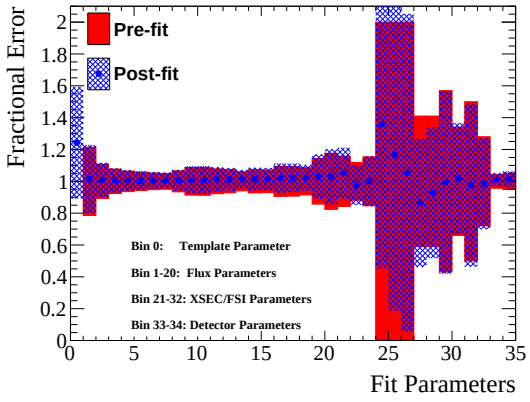

(c) weight(CC-RES)=1.5

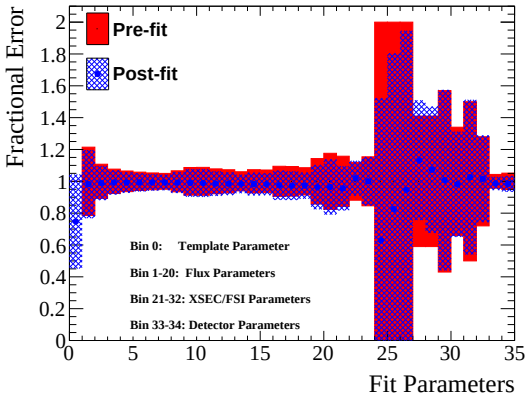

(d) weight(CC-RES)=0.5

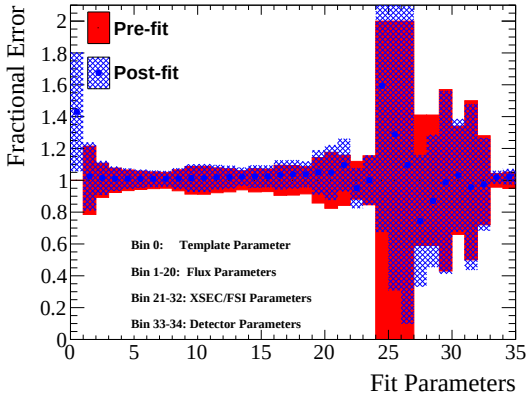

(e) weight(CC-RES)=1.9

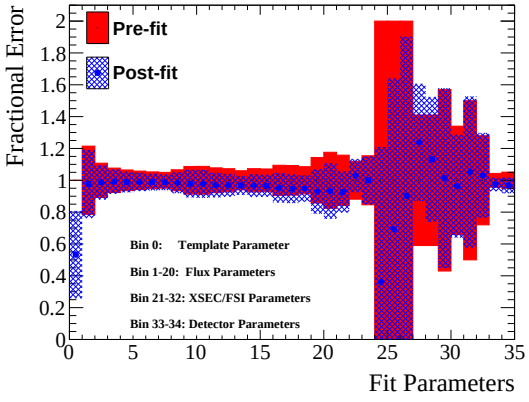

(f) weight(CC-RES)=0.1

Figure H.19. Overlayed pre-fit and post-fit parameters with their fractional error for the $\bar{\nu}_\mu$ fake data fit with events reweighted according to equation H.17-H.22, where the $\bar{\nu}_\mu$ CC-RES background events are given weights. The post-fit template parameter indicates the cross-section results will be biased.

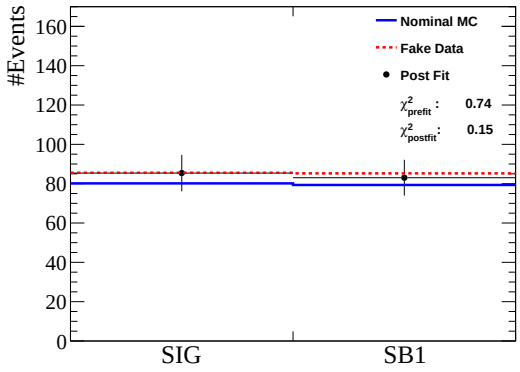

(a) weight(CC-RES)=1.2

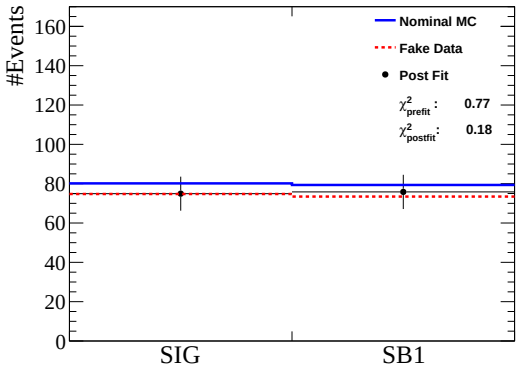

(b) weight(CC-RES)=0.8

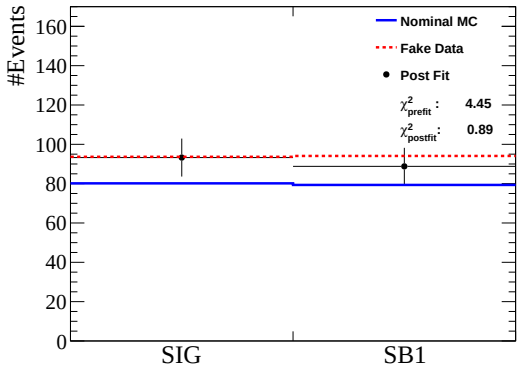

(c) weight(CC-RES)=1.5

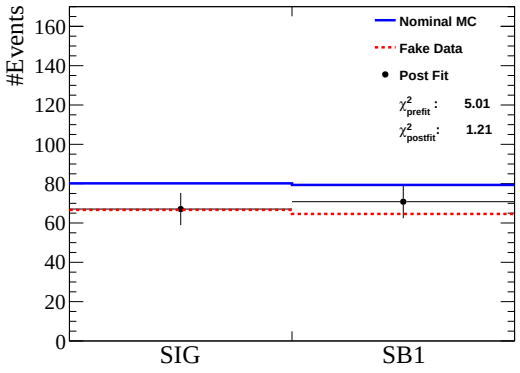

(d) weight(CC-RES)=0.5

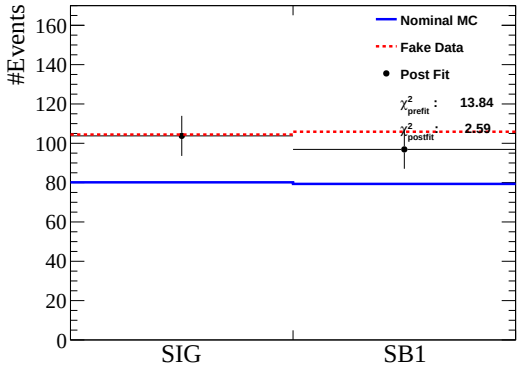

(e) weight(CC-RES)=1.9

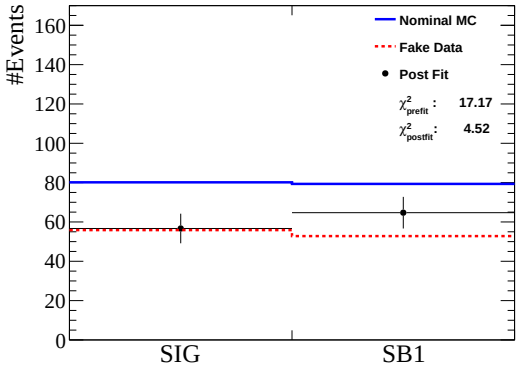

(f) weight(CC-RES)=0.1

Figure H.20. Nominal Monte Carlo simulation, fake data, and post-fit (with stat. uncertainty) reconstructed event distributions of the 2 samples for the $\bar{\nu_\mu}$ fake data fit with events reweighted according to equation H.17-H.22, where the $\bar{\nu_\mu}$ CC-RES background events are given weights. $\chi^2_{\text{pre-fit}}$ and $\chi^2_{\text{post-fit}}$ are also shown. The decreased χ^2_{postfit} in all cases indicate improvements in the agreement between the post-fit results and the fake data.

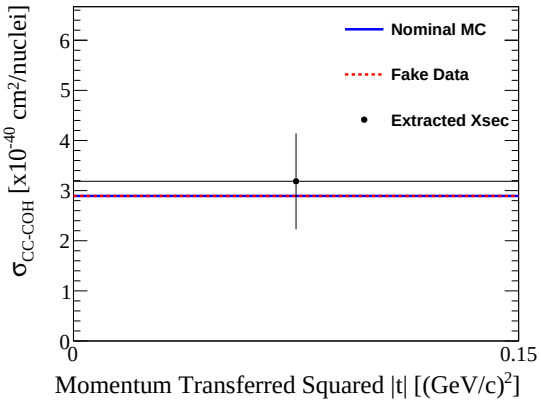

(a) weight(CC-RES)=1.2

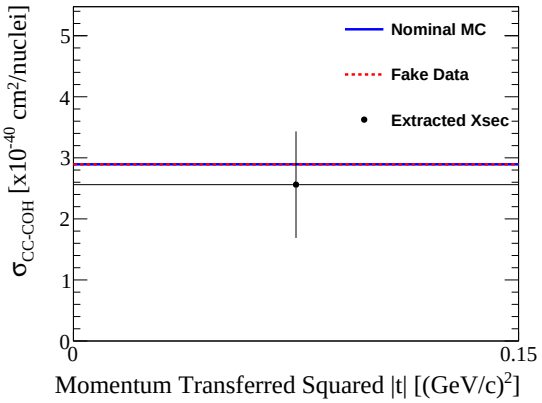

(b) weight(CC-RES)=0.8

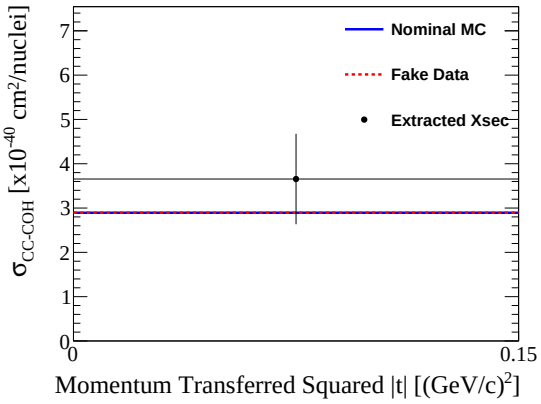

(c) weight(CC-RES)=1.5

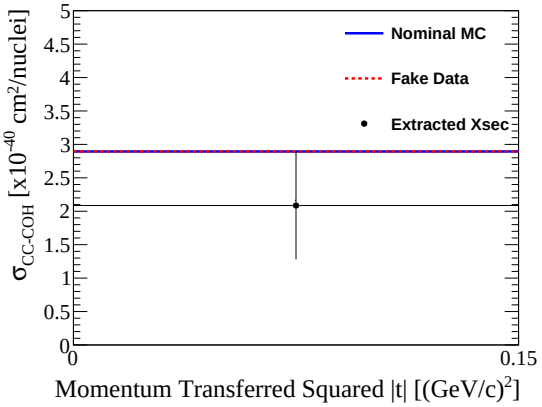

(d) weight(CC-RES)=0.5

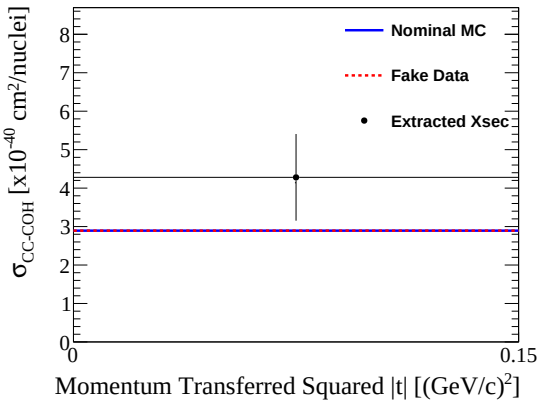

(e) weight(CC-RES)=1.9

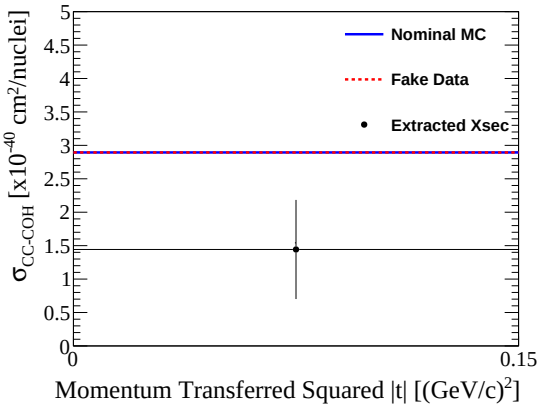

(f) weight(CC-RES)=0.1

Figure H.21. Nominal Monte Carlo simulation, fake data, and extracted cross sections for the $\bar{\nu_\mu}$ fake data fit with events reweighted according to equation H.17-H.22, where the $\bar{\nu_\mu}$ CC-RES background events are given weights. The error bar represents the combined (stat. + syst.) uncertainty for the extracted cross section. The bias to the extracted cross section is covered by the uncertainty of the measurement.

H.3 Data Motivated Fake Data Studies

Motivated by the fake data studies performed before data unblinding (section 9.4 and 10.3) and the data and MC differences in all samples (section 11.1), additional fake data studies have been performed with hybrid (combination of the changes applied to the fake data studies) fake data inputs. Two of the studies (one for ν_μ and one for $\bar{\nu}_\mu$) are shown here, which feature the following changes:

- +1MeV of VA to all the background events.
    - This is motivated by the data and MC comparisons in 11.1 (figure 11.5). The fake data study is performed in H.1.2
- Additional VA applied to 25% of the background events which the target nucleon is a neutron.
    - Fake data studies with this change are performed in 9.4.2 and 10.3.2.
- Low Q^2 suppression to the RES background events.
    - Fake data studies with this change are performed in 9.4.3 and 10.3.3.
- +19% (ν_μ fit) or +18 % ($\bar{\nu}_\mu$ fit) CC-COH events.
    - These values are taken from the post-fit results with data from 11.2.1 and 11.2.2.
    - Fake data studies where the CC-COH events are reweighted are performed in 9.2 and 10.3.4.
- -50% CC-DIS events.
    - The CC-DIS and CC-RES events are reweighted after applying all the changes described above to account for the remaining difference between the data and the fake data. Fig H.22 shows the agreement between the two.
    - Fake data studies with these background events reweighted are performed in H.1.5.
- +10% CC-RES events.
    - Fake data studies with these background events reweighted are performed in H.1.4 and H.2.2.

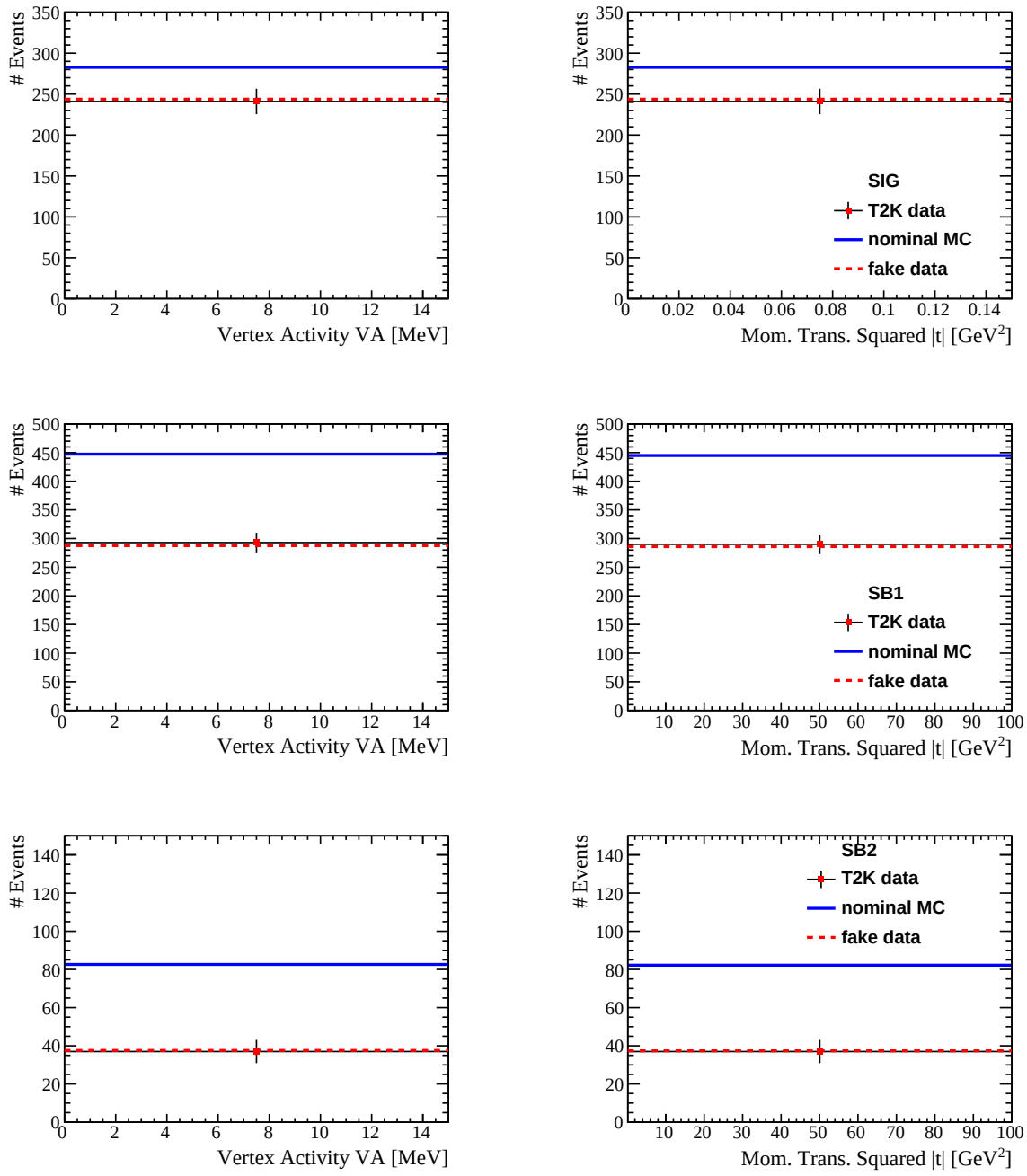

Figure H.22. ν_μ SIG, SB1 and SB2 data, MC, and data-motivated fake data 1-bin comparisons in VA and $|t|$. For the fake data shown here, 1 MeV of VA is added to all background events, an additional of 25% VA is added to the background events in which the target nucleon is a neutron, and low Q^2 suppression is applied to the RES background events. The post-fit result with data from 11.2.1 is also applied to the CC-COH events. Then, to achieve agreement between the fake data and the data, the RES and DIS background events are normalized (+10% for RES and -50% for DIS).

Figure H.23,figure H.24 and figure H.25 show the ν_μ data and MC comparisons (for the signal region, SB1, and SB2) in VA, $|t|$, Q^2, p_π, and $\cos(\theta_\pi)$ where the stacked histograms contain true reaction information. The improved agreement between the fake data and data can be observed in all distributions. The 2D distributions and the profiles of the four comparison variables (for the signal region, SB1, and SB2) are shown in figure H.26,figure H.27 and figure H.28. The differences between the fake data and data in the VA vs. Q^2 profile are improved in all three samples.

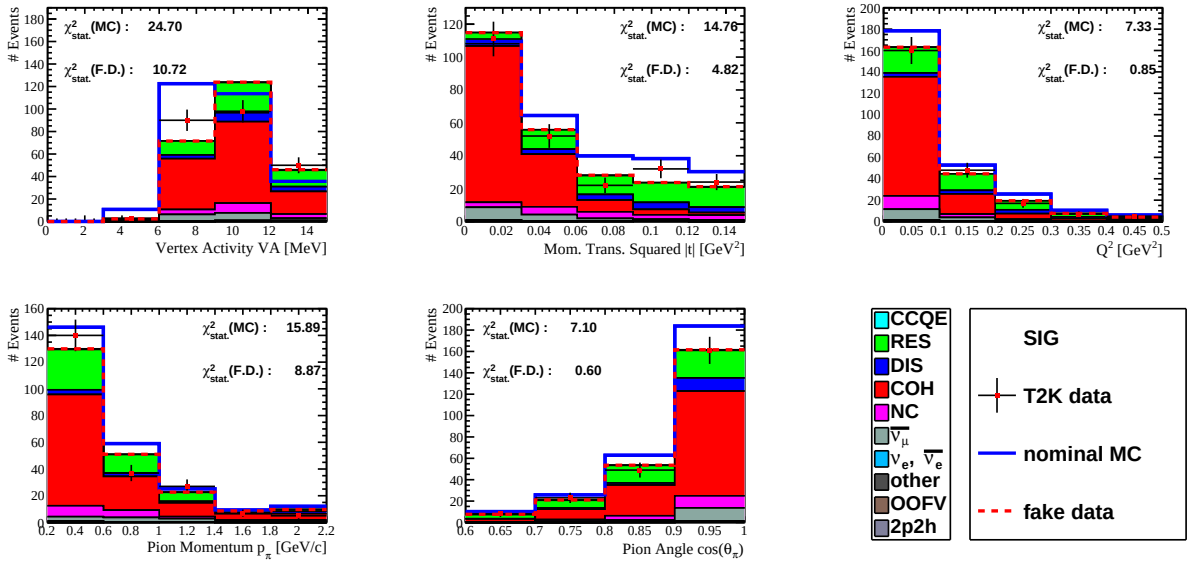

Figure H.23. ν_μ signal region data, MC, and data-motivated fake data comparisons in VA, $|t|$, Q^2, p_π, and $\cos(\theta_\pi)$. The stacked histograms represent the true reaction types of the events. Agreement to data is improved for the fake data in all variables.

The same changes applied to the hybrid ν_μ fake data set are applied to the $\bar{\nu}_\mu$ nominal MC. Figure H.29 shows the data, MC, and data-motivated fake data comparisons in VA and $|t|$. The fake data agrees with data within the statistical uncertainties. This agreement suggests the similarity of the background events between the ν_μ and $\bar{\nu}_\mu$ analysis.

Figure H.30 and figure H.31 show the $\bar{\nu}_\mu$ data and MC comparisons (for the signal region and SB1) in VA, $|t|$, Q^2, p_π, and $\cos(\theta_\pi)$ where the stacked histograms contain true reaction information. The improved agreement between the fake data and data can be observed in all distributions. The 2D distributions and the profiles of the four comparison variables (for the signal region and SB1) are shown in figure H.32 and figure H.33. The differences between the fake data and data in the VA vs. Q^2 profile are improved in both samples.

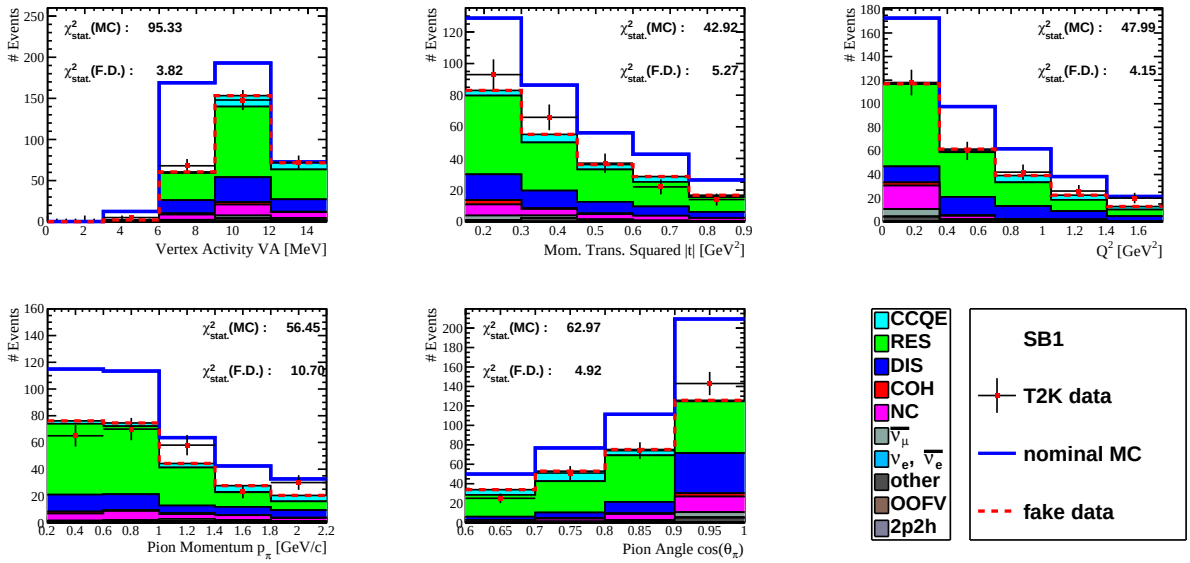

Figure H.24. ν_μ SB1 data, MC, and data-motivated fake data comparisons in VA, $|t|$, Q^2, p_π, and $\cos(\theta_\pi)$. The stacked histograms represent the true reaction types of the events. Agreement to data is improved for the fake data in all variables.

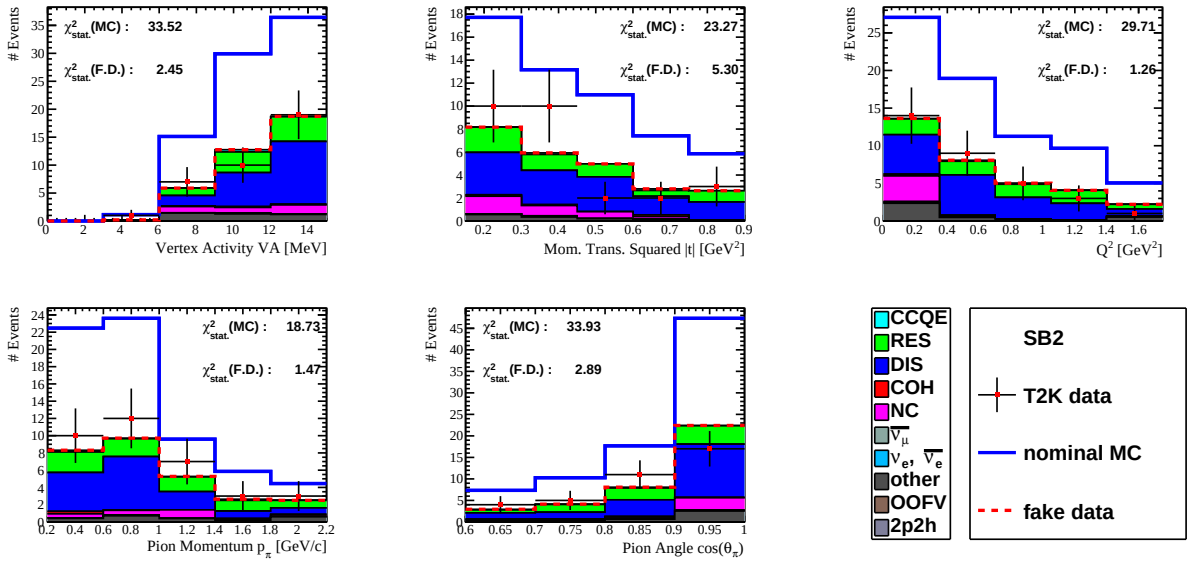

Figure H.25. ν_μ SB2 data, MC, and data-motivated fake data comparisons in VA, $|t|$, Q^2, p_π, and $\cos(\theta_\pi)$. The stacked histograms represent the true reaction types of the events. Agreement to data is improved for the fake data in all variables.

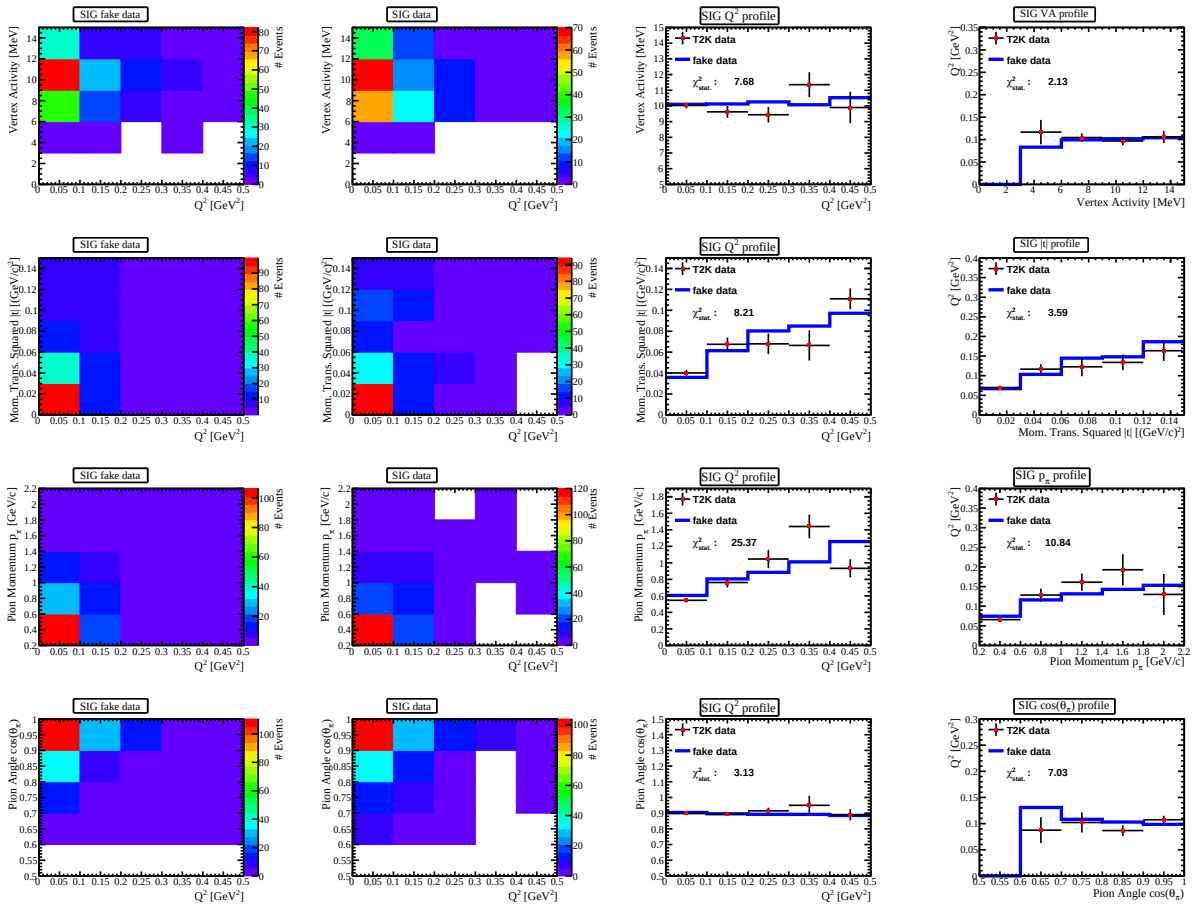

Figure H.26. ν_μ signal region data, MC, and data-motivated fake data comparisons in VA, $|t|$, p_π, and Q^2. The 2D distributions and profiles of the four variables against each other are produced to study shape differences between the data and the MC. For the profile distribution of VA vs. Q^2, with the +1MeV shift of the VA distribution, the fake data agreement to data is better than the nominal MC.

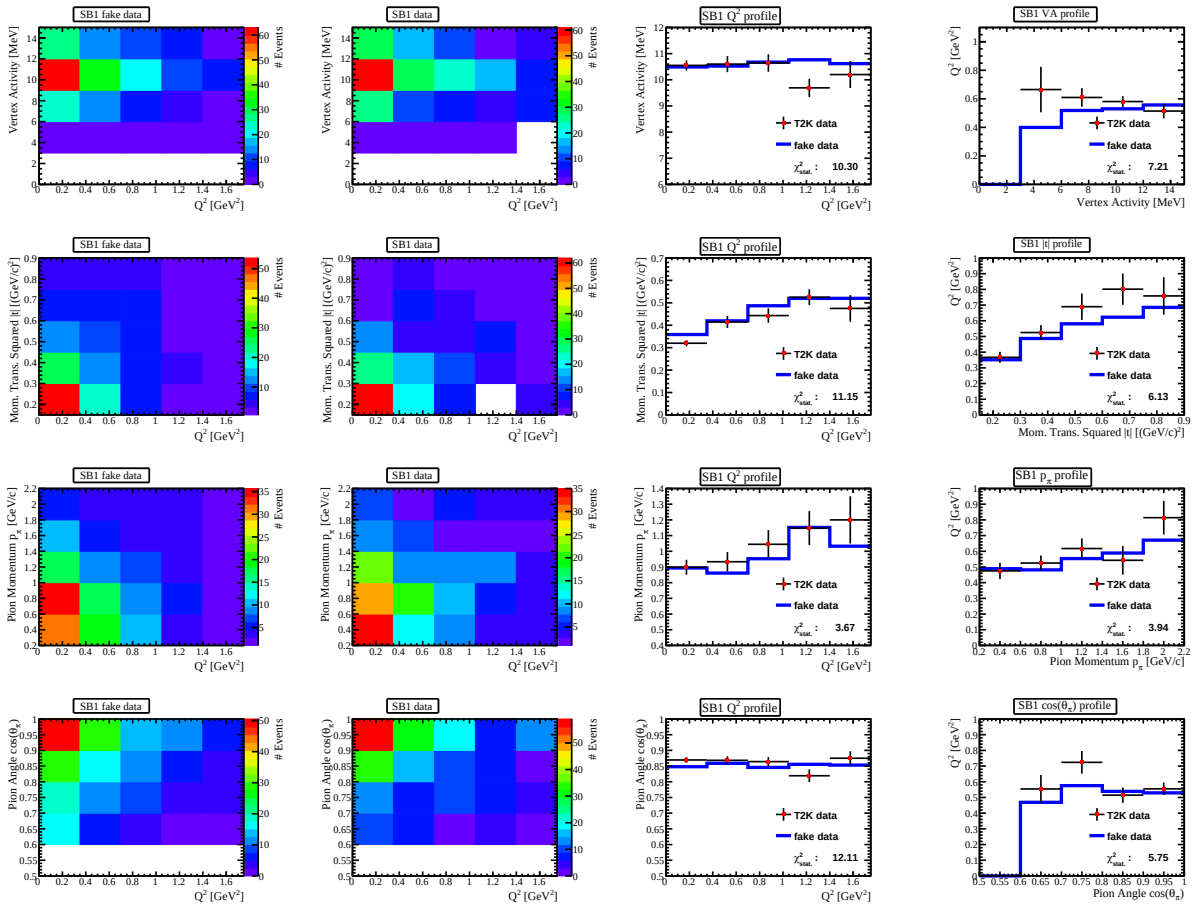

Figure H.27. ν_μ SB1 data, MC, and data-motivated fake data comparisons in VA, $|t|$, p_π, and Q^2. The 2D distributions and profiles of the four variables against each other are produced to study shape differences between the data and the MC. For the profile distribution of VA vs. Q^2, with the +1MeV shift of the VA distribution, the fake data agreement to data is better than the nominal MC.

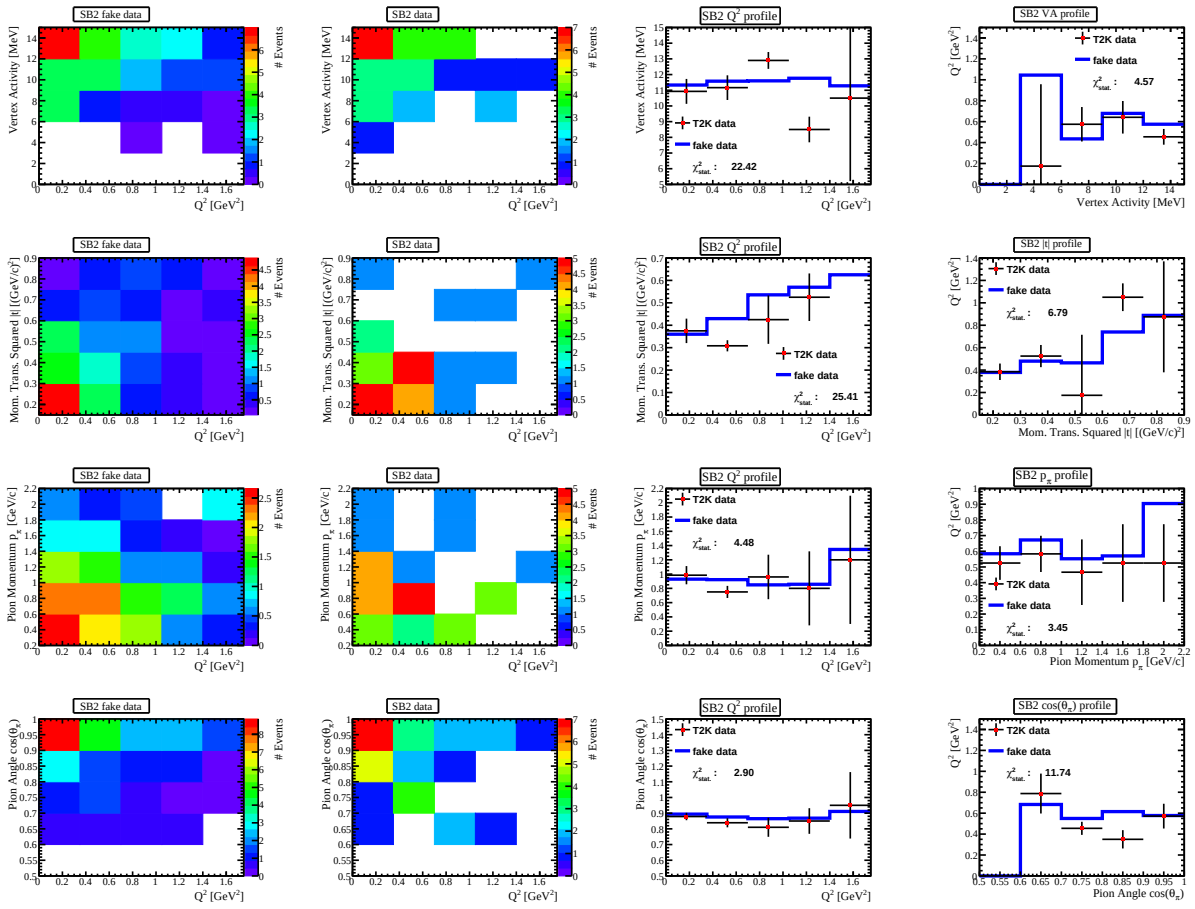

Figure H.28. ν_μ SB2 data, MC, and data-motivated fake data comparisons in VA, $|t|$, p_π, and Q^2. The 2D distributions and profiles of the four variables against each other are produced to study shape differences between the data and the MC. For the profile distribution of VA vs. Q^2, with the +1MeV shift of the VA distribution, the fake data agreement to data is better than the nominal MC.

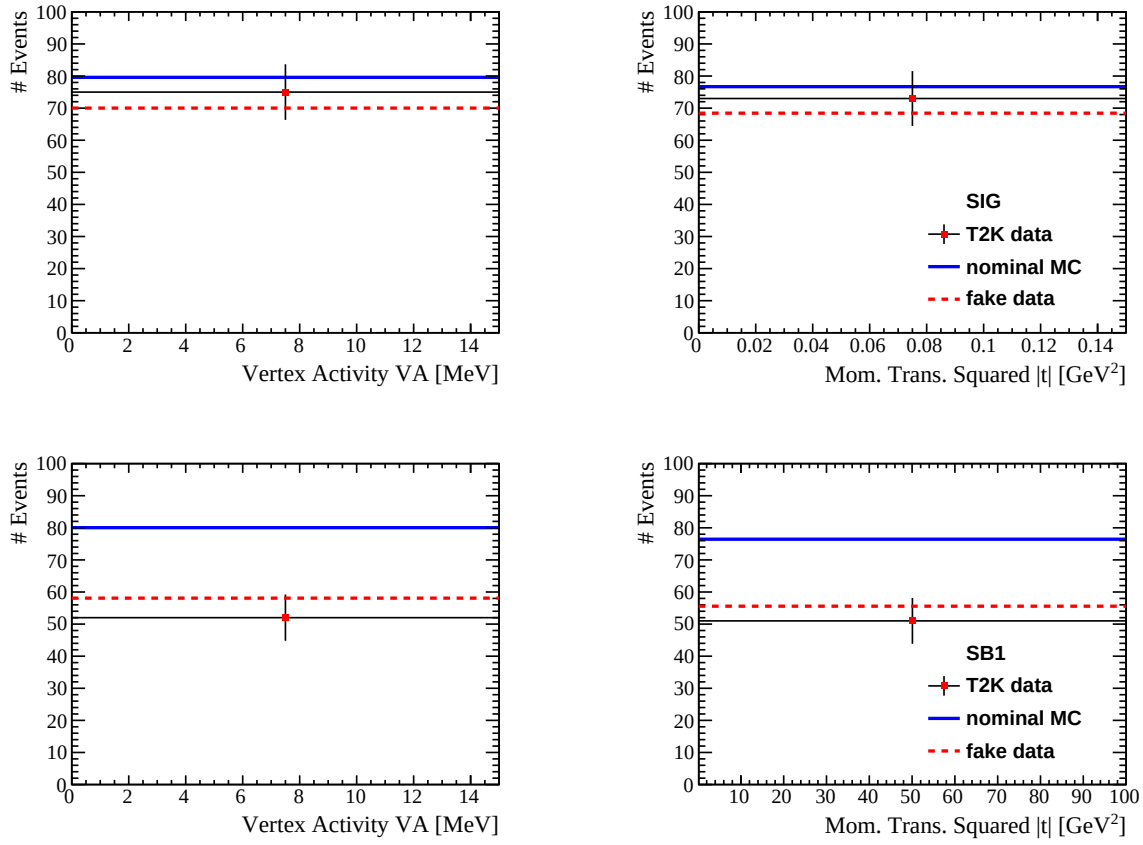

Figure H.29. $\bar{\nu}_\mu$ SIG and SB1 data, MC, and data-motivated fake data 1-bin comparisons in VA and $|t|$. The changes applied to the fake data sets are the same as the ν_μ case. Without any additional tuning of the background events, the fake data agrees with data within the statistical uncertainties.

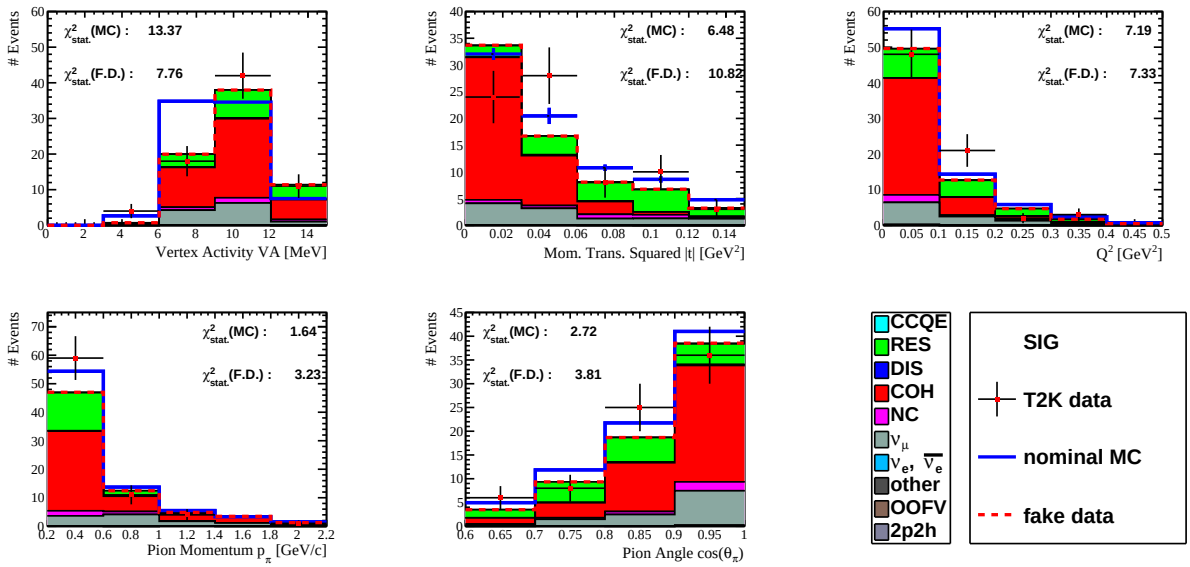

Figure H.30. $\bar{\nu}_\mu$ signal region data, MC, and data-motivated fake data comparisons in VA, $|t|$, Q^2, p_π, and $\cos(\theta_\pi)$. The stacked histograms represent the true reaction types of the events. Agreement to data is improved for the fake data in all variables.

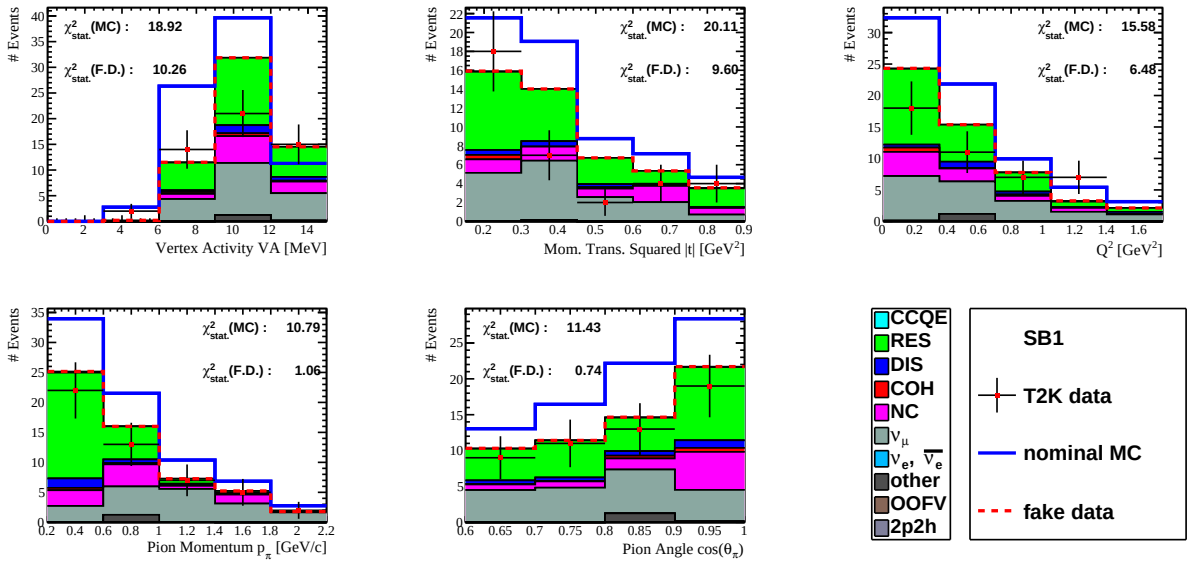

Figure H.31. $\bar{\nu}_\mu$ SB1 data, MC, and data-motivated fake data comparisons in VA, $|t|$, Q^2, p_π, and $\cos(\theta_\pi)$. The stacked histograms represent the true reaction types of the events. Agreement to data is improved for the fake data in all variables.

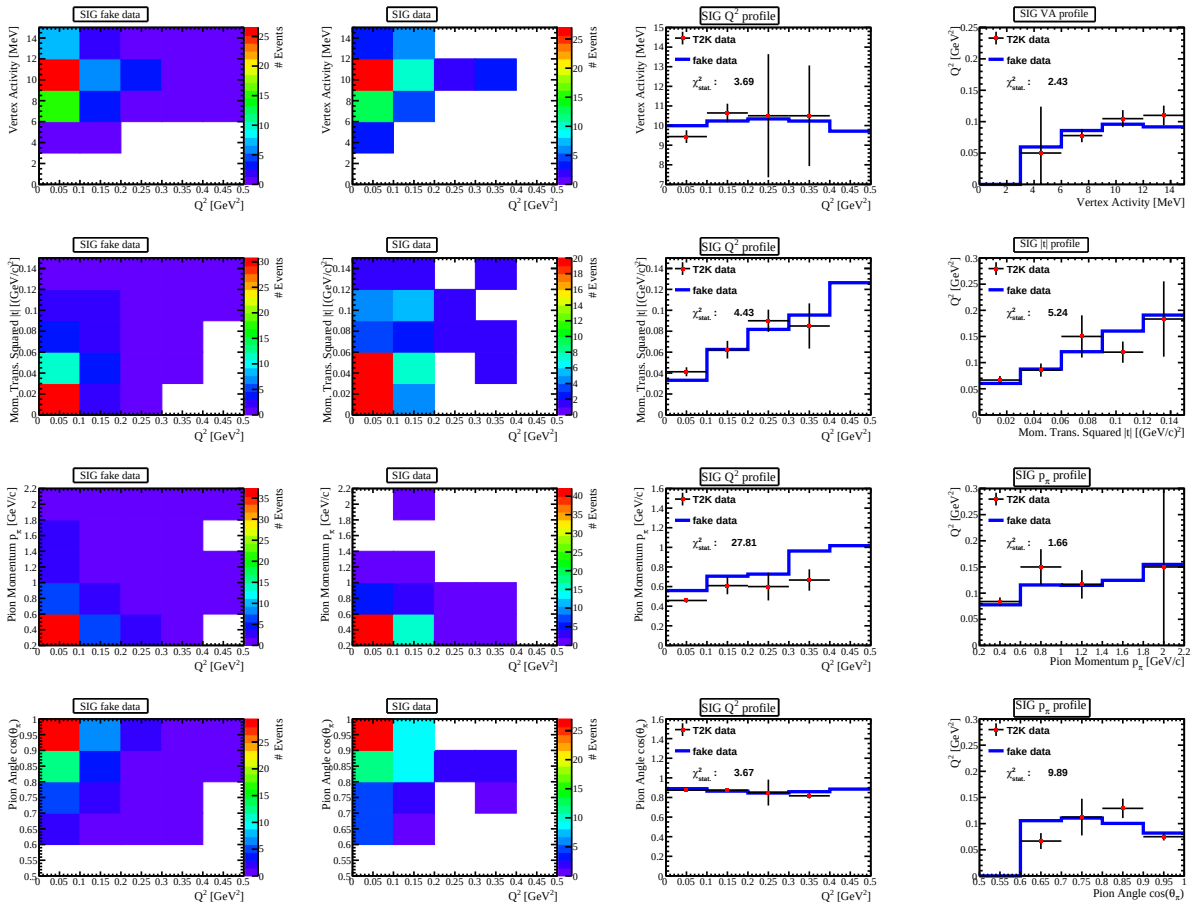

Figure H.32. $\bar{\nu}_\mu$ signal region data, MC, and data-motivated fake data comparisons in VA, $|t|$, p_π, and Q^2. The 2D distributions and profiles of the four variables against each other are produced to study shape differences between the data and the MC. For the profile distribution of VA vs. Q^2, with the +1MeV shift of the VA distribution, the fake data agreement to data is better than the nominal MC.

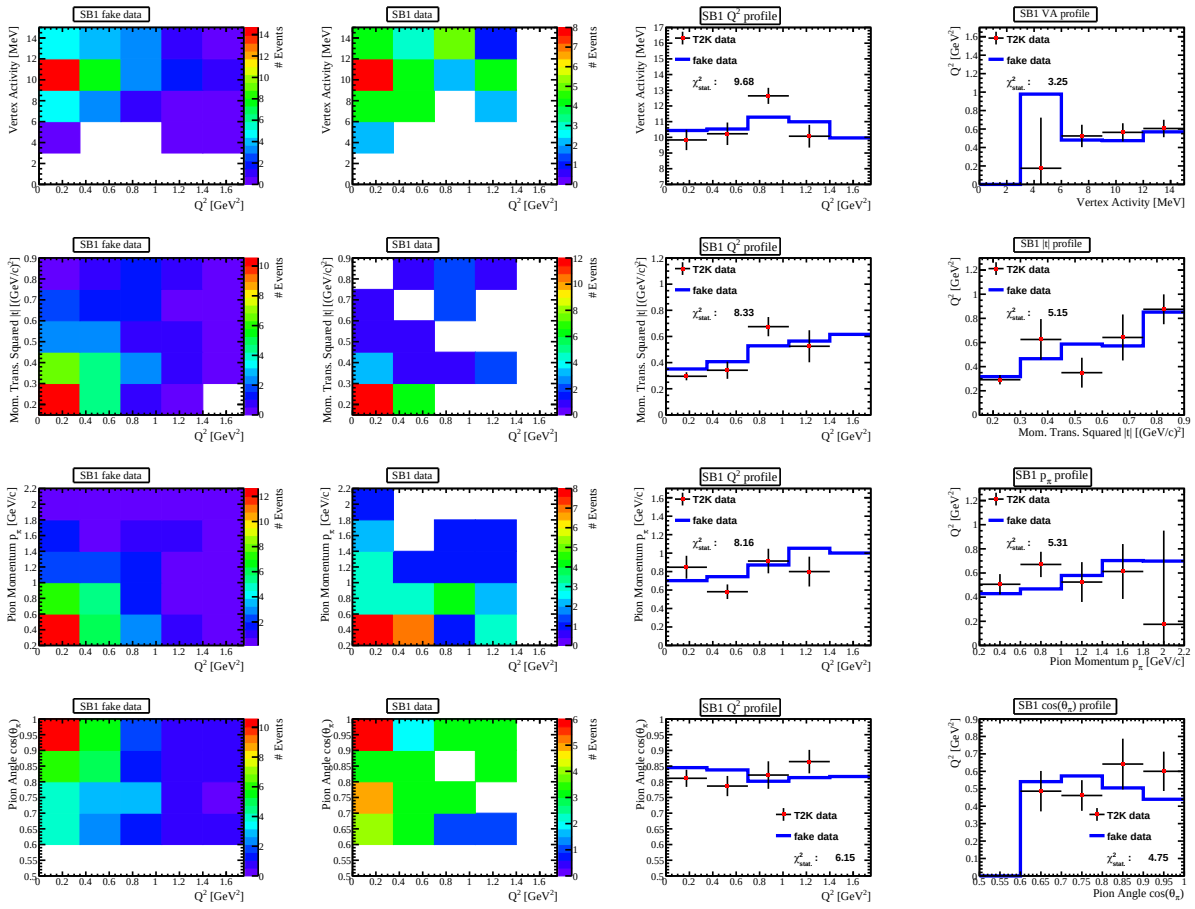

Figure H.33. $\bar{\nu}_\mu$ SB1 data, MC, and data-motivated fake data comparisons in VA, $|t|$, p_π, and Q^2. The 2D distributions and profiles of the four variables against each other are produced to study shape differences between the data and the MC. For the profile distribution of VA vs. Q^2, with the +1MeV shift of the VA distribution, the fake data agreement to data is better than the nominal MC.

H.4 Additional Fake Data Sets Considered

H.4.1 Modified Background (CC-1π)

In 5.6.1, a difference in pion momentum and angle of the RES background events is observed between SIG and SB1. To investigate the $|t|$ dependency on the differences observed, SIG and SB1 are divided into five regions in $|t|$:

1. $0\,\mathrm{GeV}^2 < |t| \leq 0.05\,\mathrm{GeV}^2$ (SIG)
2. $0.05\,\mathrm{GeV}^2 < |t| \leq 0.1\,\mathrm{GeV}^2$ (SIG)
3. $0.1\,\mathrm{GeV}^2 < |t| \leq 0.15\,\mathrm{GeV}^2$ (SIG)
4. $0.15\,\mathrm{GeV}^2 < |t| \leq 0.3\,\mathrm{GeV}^2$ (SB1)
5. $|t| > 0.3\,\mathrm{GeV}^2$ (SB1),

and figure H.34 shows the pion kinematic distributions comparisons of the five regions.

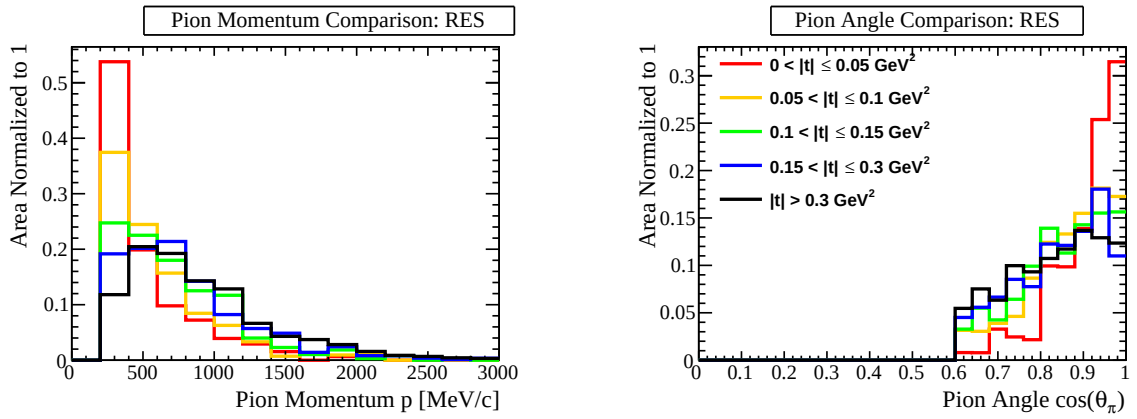

Figure H.34. Pion kinematics comparisons of the RES events between different regions in $|t|$ of the ν_μ CC-COH selection SIG and SB1. Difference in pion momentum and angle is seen between the first two $|t|$ regions with the rest of the events.

To study the effect of possible pion momentum mis-modelling to the analysis, the CC-1π topology events (events with one reconstructed pion) are reweighted as a function of pion momentum p_π:

- $\mathrm{W} = 1.25,\ 200\,\mathrm{MeV}\,c^{-1} < \mathrm{p}_\pi \leq 300\,\mathrm{MeV}\,c^{-1}$
- $\mathrm{W} = 0.90,\ 300\,\mathrm{MeV}\,c^{-1} < \mathrm{p}_\pi \leq 400\,\mathrm{MeV}\,c^{-1}$
- $\mathrm{W} = 0.80,\ 400\,\mathrm{MeV}\,c^{-1} < \mathrm{p}_\pi \leq 800\,\mathrm{MeV}\,c^{-1}$

- W = 1.00, else.

This reweighting function is adapted from the T2K ND280 FGD1 CC-1π sample (used by the near detector fit BANFF) data and MC comparison in p_π shown in figure H.35. Fig H.36 shows the number of reconstructed events in the three samples (SIG, SB1, and SB2). SB2 is not affected by the reweighting as expected since it does not contain CC-1π events. The effect on SIG and SB1 is also insignificant, so no fitter study is performed.

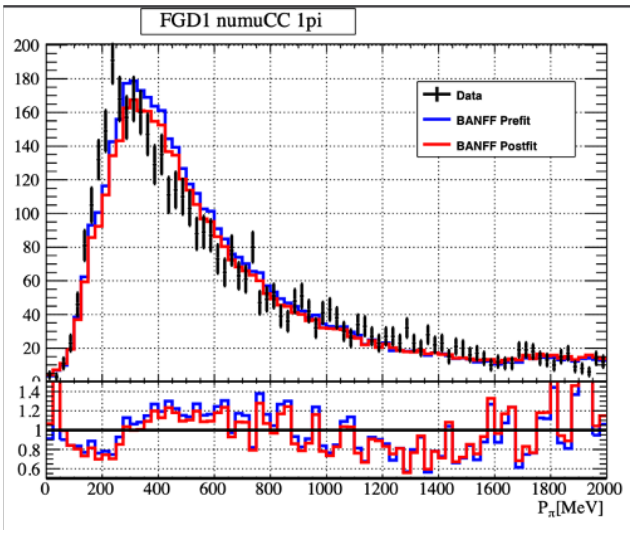

Figure H.35. The T2K ND280 FGD1 CC-1π sample data and MC comparison in p_π. The data suggest underestimation of the CC-1π events at low pion momentum, and overestimation of the CC-1π events at higher pion momentum.

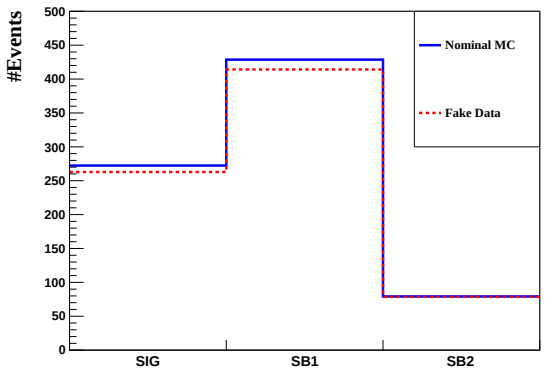

Figure H.36. Nominal MC and fake data reconstructed event distributions of the 3 samples. The CC-1π events are reweighted (in p_π) according to the data and MC difference seen in the FGD1 CC-1π sample.

H.5 Failure Modes

H.5.1 ν_μ CC-DIS -90%

The fake data studies performed for the reweighting of the DIS events in the ν_μ analysis are shown in H.1.5. The fit with -90% of DIS failed to converge. A possible reason for the non-convergence is the statistics in SB2 (it consists of 79 reconstructed events with 70% of DIS). The number of events in SB2 dropped to 29 due to this extreme change in DIS, making the fitter struggle to converge.

Appendix I

Additional Data and Monte Carlo Simulation Comparisons

This appendix examines the data and MC agreement with a sample not used by the analysis, namely the events with exactly 3 FGD1 tracks. In 5.2.3, figure 5.3 shows the event distribution in terms of number of FGD1 tracks. SIG and SB1 events have exactly two FGD1 tracks, and SB2 events have more than 3 FGD1 tracks. For SB2, the reason to exclude the events with exactly 3 FGD1 tracks is to boost the purity in DIS backgrounds - SB2 contains 70% of these backgrounds.

The events with exactly 3 FGD1 tracks are selected as an additional region (AR1). Figure I.1 shows the data and MC comparisons in VA, $|t|$, Q^2, p_π, and $\cos(\theta_\pi)$. MC has some overprediction, but the uncertainties mostly cover the differences. Fig I.2 shows the 2D comparisons and the profile distribution comparisons. There is some shape difference seen from the $|t|$ vs. Q^2 profile distribution, but overall, there are no obvious shape differences.

While SB2 indicates a significant normalization difference in DIS, AR1, with more than 50% DIS events, indicates roughly 20% MC overprediction of events. One difference between SB2 and AR1 is the amount of RES events. In SB1, the data and MC normalization difference are also small (the large $\chi^2_{\text{stat.}}$ for data and MC comparisons are primarily due to the mismodelling of VA). In addition, as shown in figure I.3 and I.4, the NEUT interaction breakdown is slightly different between SB2 and AR1 - AR1 contains more NEUT multi-π production events, which is more similar to SB1.

Overall, the data and MC comparisons in AR1 show no surprises but provide some interesting insights for future analyses in modelling RES and DIS events.

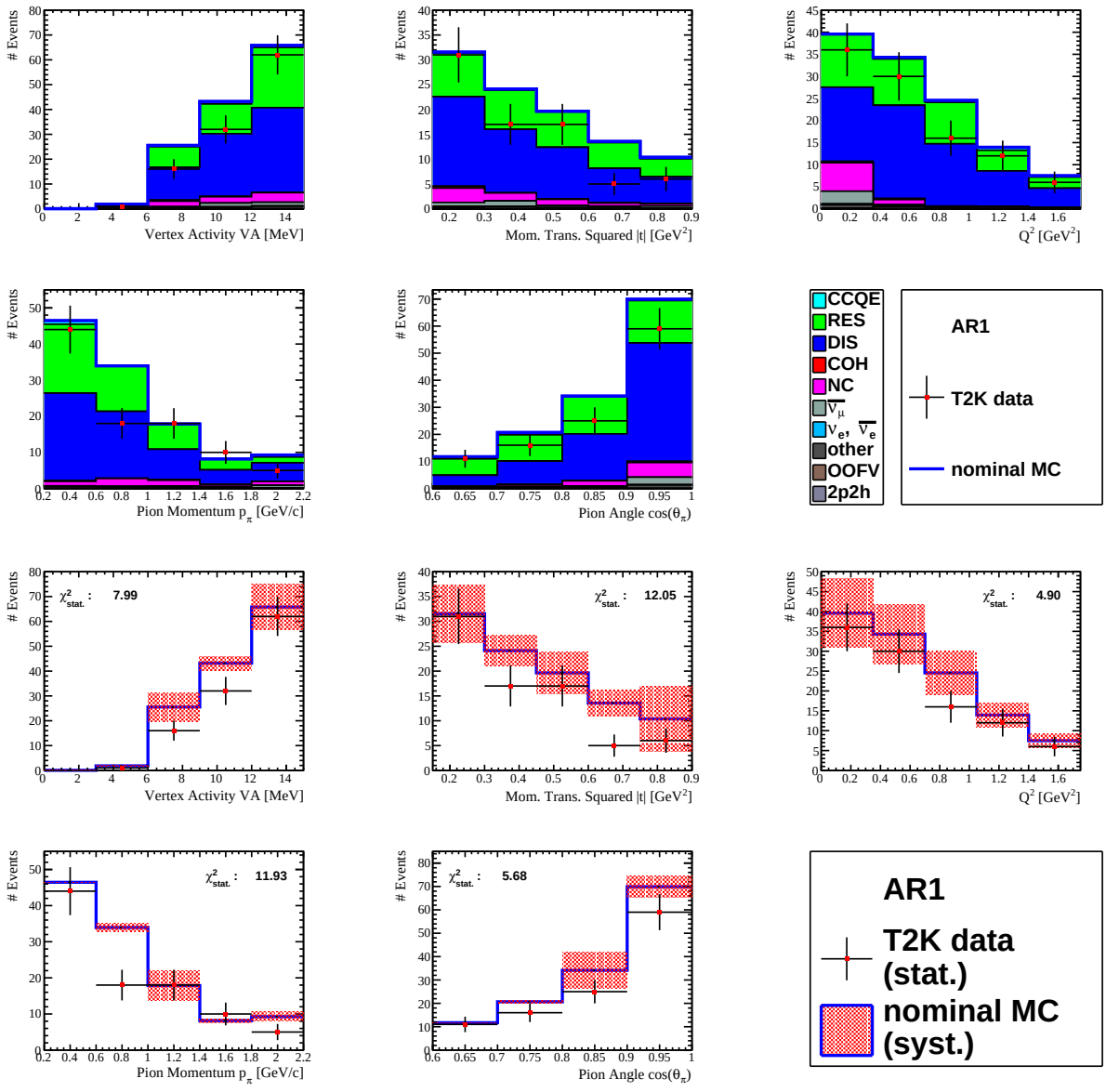

Figure I.1. ν_μ AR1 data and MC comparisons in VA, $|t|$, Q^2, p_π, and $\cos(\theta_\pi)$. The stacked histograms (top two rows) represent the true reaction types of the events. Overall, the data and MC are in good agreement with no obvious normalization difference.

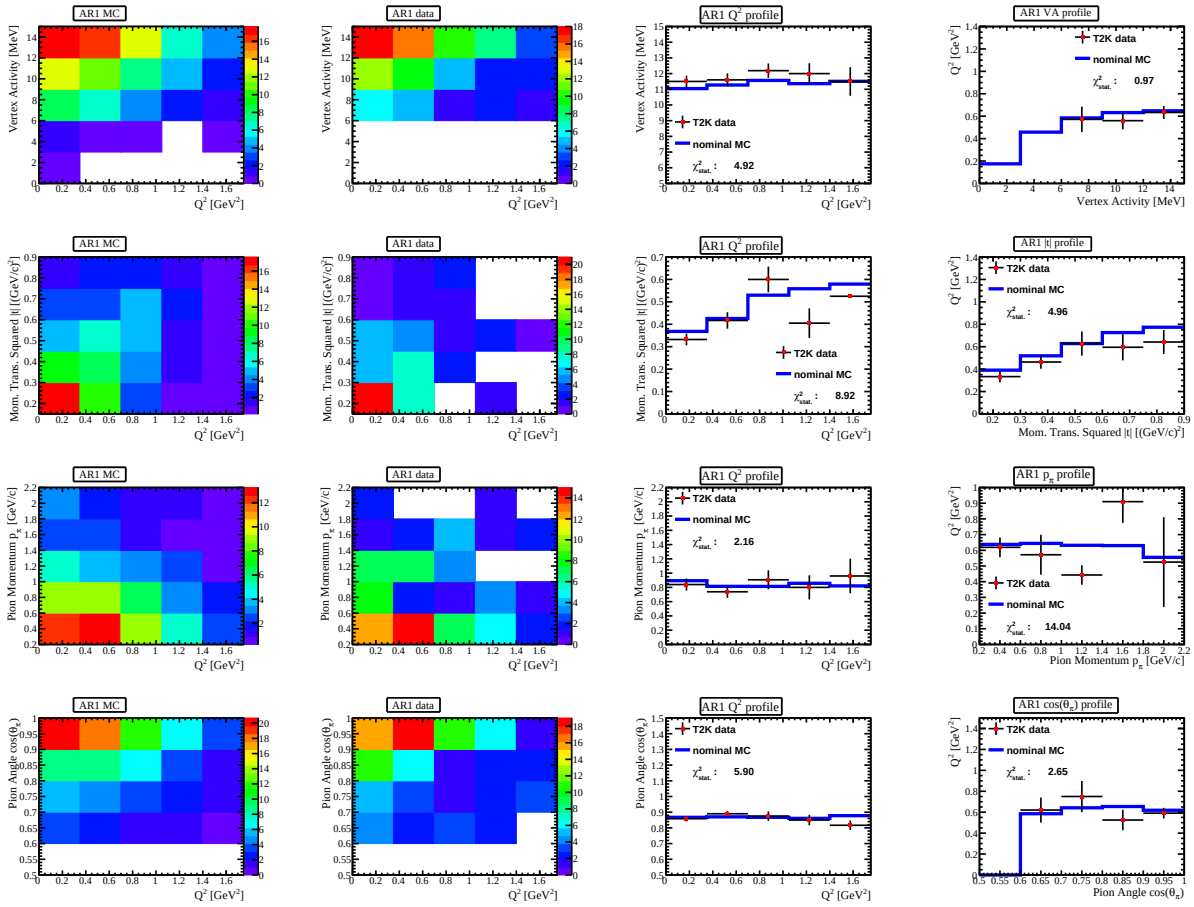

Figure I.2. ν_μ AR1 data and MC comparisons in VA, $|t|$, Q^2, p_π, and $\cos(\theta_\pi)$. The 2D distributions and profiles of the five variables against each other are produced to study shape differences between the data and the MC. There are hints of shape difference coming from the slightly larger $\chi^2_{\text{stat.}}$ in the $|t|$ vs. Q^2 profile distribution, hinting a possible shape difference.

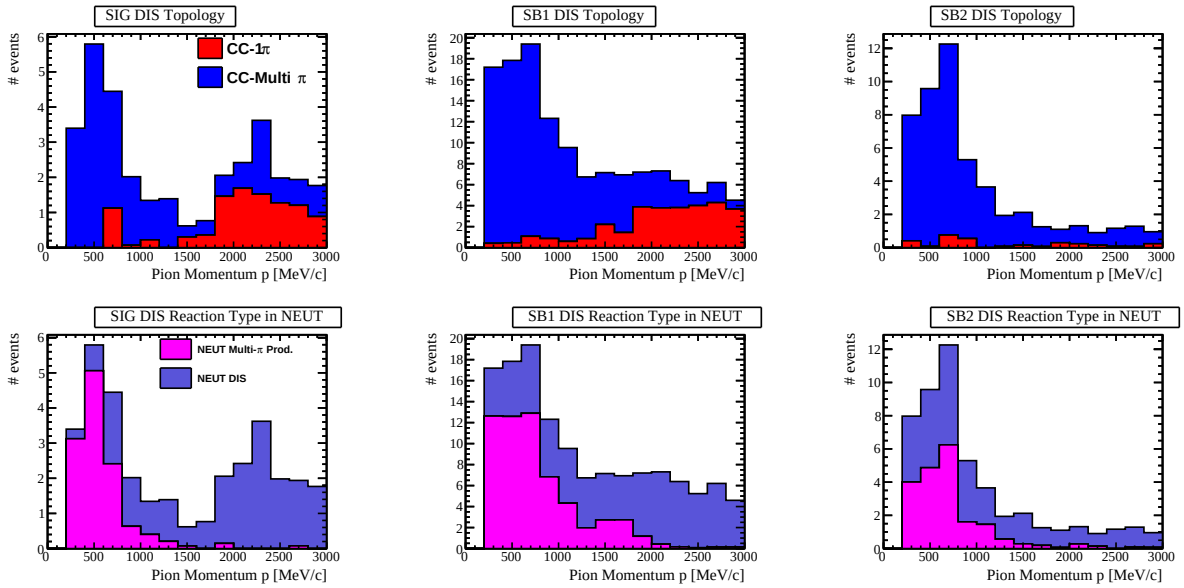

Figure I.3. The topology and NEUT reaction breakdown of the DIS events in SIG, SB1, and SB2. The double-peaked structure of pion momentum in SIG is caused by different topology and NEUT reaction contributions.

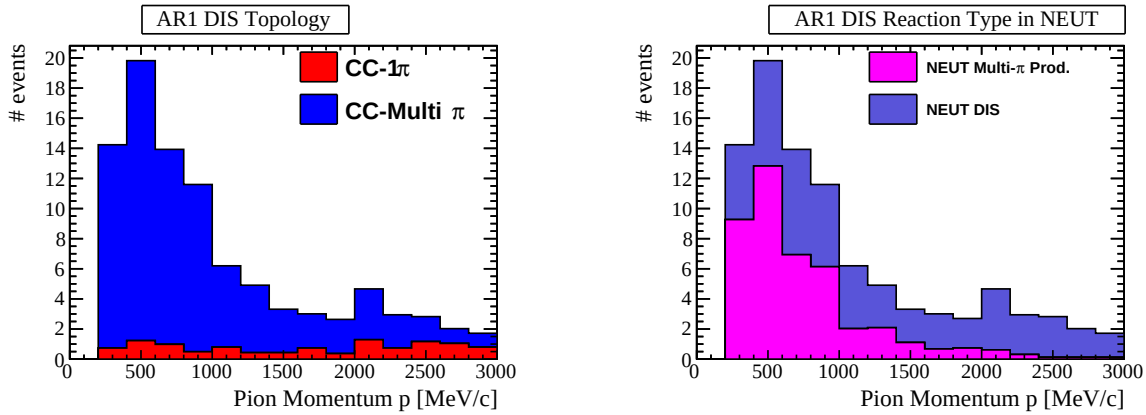

Figure I.4. The topology and NEUT reaction breakdown of the DIS events in AR1. AR1 contains more NEUT multi-π production events compared to SB2 (figure I.3).

Appendix J

Additional Q^2 Uncertainty Study

In this appendix, the motivation for an additional Q^2 uncertainty is reviewed. In addition, the evaluation of the uncertainty is also explained.

In the fake data studies where RES events are suppressed in the low Q^2 region (9.4.3 and 10.3.3), the fitter results have low p-values compared to the other studies. Additionally, there are no cross-section modelling dials that deal with such a shape change in the Q^2 distribution.

The p-values for the extracted cross-section are 0.43 for the ν_μ CC-COH measurement and 0.47 for the $\bar{\nu_\mu}$ CC-COH measurement. These values suggest that given the statistical and systematic uncertainties, the extracted cross-section is less than 1-σ away from the true cross-section. However, this p-value takes the relatively large statistical uncertainty, the flux and detector systematics, into account.

Although the fitter framework cannot evaluate the cross-section modelling uncertainty alone, it can still be approximated. First, the statistical uncertainty can be approximated by running the Asimov fit with only the template (signal) parameter. Then the combined statistical and cross-section modelling uncertainty can be approximated by rerunning the Asimov fit with the template parameter and the cross-section and FSI parameters enabled, and the other parameters disabled. Finally, assuming the two sources of uncertainties are added in quadrature, the cross-section modelling systematic uncertainty using this method can be extracted. The cross-section modelling systematic uncertainty is 10.8% for the ν_μ CC-COH analysis and 19.8% for the $\bar{\nu_\mu}$ CC-COH analysis.

For the fake data studies where RES events are suppressed in the low Q^2 region (9.4.3 and 10.3.3), the χ^2_σ and corresponding p-values can be evaluated with the cross-section modelling systematic uncertainty alone. Table J.1 shows the χ^2_σ and p-values for the fake data studies. The χ^2_σ and p-values are evaluated with the full measurement uncertainties and the cross-section modelling systematic uncertainties alone. For the latter, the uncertainties do not cover the bias in the cross-section results, resulting in the low p-value of 0.06 and 0.11.

	ν_μ	$\bar{\nu_\mu}$
Measurement Uncertainty (%)	25.3	44.2
χ^2_σ	0.62	0.52
P-value	0.43	0.47
Cross-section Modelling Systematic Uncertainty (%)	10.8	19.8
χ^2_σ	3.41	2.56
P-value	0.06	0.11

TABLE J.1. The χ^2_σ and p-values for the ν_μ and $\bar{\nu_\mu}$ fake data studies where RES events are suppressed in the low Q^2 region. The χ^2_σ and p-values are evaluated with the full measurement uncertainties and the cross-section modelling systematic uncertainties alone. For the latter, the uncertainties do not cover the bias in the cross-section results, resulting in the low p-value of 0.06 and 0.11.

The idea is to have the cross-section modelling systematic uncertainties to cover the bias in the cross-section results for these two fake data studies. Therefore, an additional uncertainty of 16.4% (ν_μ) and 24.6% ($\bar{\nu_\mu}$) is added in quadrature to the cross-section modelling systematic uncertainties to achieve χ^2_σ of 1. Table J.2 shows the χ^2_σ and p-values computed with the cross-section modelling systematic uncertainties before and after the inflation.

	ν_μ	$\bar{\nu_\mu}$
Cross-section Modelling Systematic Uncertainty (%)	10.8	19.8
χ^2_σ	3.41	2.56
P-value	0.06	0.11
Inflated Cross-section Modelling Systematic Uncertainty (%)	20.0	31.6
χ^2_σ	1.0	1.0
P-value	0.32	0.32

TABLE J.2. The χ^2_σ and p-values for the ν_μ and $\bar{\nu_\mu}$ fake data studies where RES events are suppressed in the low Q^2 region. The χ^2_σ and p-values are evaluated with the cross-section modelling systematic uncertainties before and after the inflation. For the latter, the χ^2_σ are 1.0 as intended since the inflated systematic uncertainties cover the bias in the cross sections.

To see the effect of the additional Q^2 uncertainties to the cross-section results, cross-section uncertainties from the data motivated hybrid fake data studies, shown in H.3, are inflated (added 16.4% (ν_μ) and 24.6% ($\bar{\nu_\mu}$) in quadrature to the cross-section uncertainties). Table J.3 shows the change in the cross-section uncertainties, the χ^2_σ and the p-values.

The additional Q^2 uncertainties result in a 6% increase (29% inflation) for the ν_μ fake data study and an 8% increase (21% inflation) for the $\bar{\nu_\mu}$ fake data study. This approach is

	ν_μ	$\bar{\nu_\mu}$
Cross-section Modelling Systematic Uncertainty (%)	21	39
χ^2_σ	0.841	0.273
P-value	0.36	0.60
Inflated Cross-section Modelling Systematic Uncertainty (%)	27	47
χ^2_σ	0.521	0.216
P-value	0.47	0.64

TABLE J.3. The χ^2_σ and p-values for the ν_μ and $\bar{\nu_\mu}$ fake data studies where RES events are suppressed in the low Q^2 region. The χ^2_σ and p-values are evaluated with the cross-section modelling systematic uncertainties before and after the inflation. For the latter, the χ^2_σ are both reduced due to the inflated systematic uncertainties.

certainly not ideal but is the best option available at the moment. Future analysis will benefit from cross-section modelling dials that deal with shape changes in the Q^2 distribution.

Bibliography

[1] F. Reines. The Early Days of Experimental Neutrino Physics. *Science*, 203(4375):11–16, 1979.

[2] et al. C. Cowan, F. Reines. Detection of the Free Neutrino: a Confirmation. *Science*, 124(3212):103–104, 1956.

[3] D.H. Perkins. *Introduction to High Energy Physics*. Cambridge University Press, 2000.

[4] C. Cowan and F. Reines. The Neutrino. *Nature*, 178:446–449, 1956.

[5] J. Formaggio and G. Zeller. From eV to EeV: Neutrino cross sections across energy scales. *Reviews of Modern Physics*, 84(3):1307–1341, Sep 2012.

[6] J. Bahcall. Solar Models: An Historical Overview. *Nuclear Physics B - Proceedings Supplements*, 118:77–86, Apr 2003.

[7] N. G. Cooper. Celebrating the neutrino. *Los Alamos Science*, (25), 12 1997.

[8] A.D. Sakharov. Violation of CP invariance, C asymmetry, and baryon asymmetry of the Universe. *Sov.Phys.Usp.*, 34(5):392, 1991.

[9] M. Fukugita and T. Yanagida. Baryogenesis without grand unification. *Phys.Lett.B*, 174:45–47, 1986.

[10] K. Abe et al. The T2K Experiment. *Nucl.Instrum.Meth.A*, 659:106–135, 2011.

[11] K. Abe et al. Indication of Electron Neutrino Appearance from an Accelerator-produced Off-axis Muon Neutrino Beam. *Phys.Rev.Lett.*, 107:041801, 2011.

[12] R.N. Cahn et al. White Paper: Measuring the Neutrino Mass Hierarchy, 2013.

[13] I. Esteban et al. The fate of hints: updated global analysis of three-flavor neutrino oscillations. *Journal of High Energy Physics*, 2020(9), Sep 2020.

[14] NuFIT 5.0 (2020). http://www.nu-fit.org.

[15] D. Griffiths. *Introduction to Elementary Particles*. WILEY-VCH, 2004.

[16] T. Koga et al. ND280 global charge identification systematic error. www.t2k.org/docs/technotes/353, 2019.

[17] K. Abe et al. Measurement of neutrino and antineutrino oscillations by the T2K experiment including a new additional sample of ν_e interactions at the far detector. *Phys.Rev.D*, D96:092006, 2017.

[18] S. Adler. Tests of the Conserved Vector Current and Partially Conserved Axial-Vector Current Hypotheses in High-Energy Neutrino Reactions. *Phys. Rev.*, 135:B963–B966, 1964.

[19] D. Rein and M Sehal. Coherent π^0 Production in Neutrino Reactions. *Nucl.Phys.B*, B223:29–44, 1983.

[20] C. Piketty and L. Stodolsky. Diffraction Model of High-Energy Leptonic Interactions. *Nucl.Phys.B*, B15:571–600, 1970.

[21] J.D. Bjorken. Asymptotic Sum Rules at Infinite Momentum. *Phys.Rev.*, 179:1547, 1969.

[22] K.S. Kuzmin el al. Quasielastic axial-vector mass from experiments on neutrino-nucleus scattering. *Eur.Phys.J.*, C54:517–538, 2008.

[23] M.H. Ahn et al. Measurement of Neutrino Oscillation by the K2K Experiment. *Phys.Rev.D*, D74:072003, 2006.

[24] H. Tanaka. K2K coherent pion production in SciBar. *Nucl.Phys.B (Proc. Suppl.)*, 159:38–43, 2006. Proceedings of the 4th International Workshop on Neutrino-Nucleus Interactions in the Few-GeV Region.

[25] D. Rein and M Sehal. PCAC and the Deficit of Forward Muons in π^+ Production by Neutrinos. *Nucl.Phys.B*, B657:207–209, 2007.

[26] Ch. Berger and M Sehal. Partially conserved axial vector current and coherent pion production by low energy neutrinos. *Phys.Rev.D*, D79:053003, 2009.

[27] H. Faissner et al. Observation of neutrino and antineutrino induced coherent neutral pion production off Al^{27}. *Phys.Lett.B*, 125:230–236, 1983.

[28] P. Marage et al. Observation of coherent diffractive charged current interactions of antineutrinos on neon nuclei. *Phys.Lett.B*, 140:137–141, 1984.

[29] H.-J. Grabosch et al. Coherent Pion Production in Neutrino and Antineutrino Interactions on Nuclei of Heavy Freon Molecules. *Z.Phys.C*, 31:203–211, 1986.

[30] S. Willocq et al. Coherent production of single pions and p mesons in charged-current interactions of neutrinos and antineutrinos on neon nuclei at the Fermilab Tevatron. *Phys.Rev.D*, 47(7):2661–2674, 1993.

[31] S. Willocq et al. Coherent singlechargedpion production by neutrinos. *Phys.Lett.B*, 313:267–275, 1993.

[32] B. Acciarri et al. First Measurement of Neutrino and Antineutrino Coherent Charged Pion Production on Argon. *Phys.Rev.Lett*, 113:261801, 2014.

[33] A. Higuera et al. Measurement of Coherent Production of $\pi^{\pm}$ in Neutrino and Anti-Neutrino Beams on Carbon from E_{ν} of 1.5 to 20 GeV. *Phys.Rev.*, 113:261802, 2014.

[34] M. A. Acero et al. Measurement of Neutrino-Induced Neutral-Current Coherent π^0 Production in the NOvA Near Detector. *Phys.Rev.D*, D102:012004, 2020.

[35] K. Hiraide et al. Search for charged current coherent pion production on carbon in a few-GeV neutrino beam. *Phys.Rev.D*, D78:112004, 2008.

[36] K. Abe et al. Measurement of coherent pi + production in low energy neutrino-carbon scattering. *Phys.Rev.*, 117:192501, 2016.

[37] T. Katoh et al. Present status of the J-PARC control system. pages 302 – 304, 06 2005.

[38] S. Bhadra et al. Optical transition radiation monitor for the T2K experiment. *Nucl.Instrum.Meth.A*, 703:45–58, 2013.

[39] K.T. McDonald. An Off-Axis Neutrino Beam, 2001.

[40] B. Kirby. *Measurement of an Off-Axis Neutrino Beam Energy Spectrum.* PhD thesis, University of British Columbia, 2012.

[41] K. Abe et al. The T2K ND280 off-axis pi–zero detector. *Phys.Rev.D*, D87:012001, 2013.

[42] T.T. Böhlen et al. The FLUKA Code: Developments and Challenges for High Energy and Medical Applications. *Nuclear Data Sheets*, 120:211–214, 2014.

[43] A. Ferrari et al. FLUKA: a multi-particle transport code. 2005.

[44] R. Brun et al. GEANT3. 1987.

[45] M. Apollonio et al. Forward production of charged pions with incident protons on nuclear targets measured at CERN Proton Synchroton. *Phys.Rev.C.*, C80:035208, 2009.

[46] A. Acharya et al. Measurement of the production cross section of 31 GeV/c protons on carbon via beam attenuation in a 90-cm-long target. *Phys. Rev. D*, 103:012006, Jan 2021.

[47] A. Fiorentini et al. Flux Prediction and Uncertainty Updates with NA61 2009 Thin Target Data and Negative Focussing Mode Predictions . www.t2k.org/docs/technotes/217, 2018.

[48] K. Abe et al. Measurements of the T2K neutrino beam properties using the INGRID on-axis near detector. *Nucl.Instrum.Meth.A*, 694:211–223, 2012.

[49] S. Assylbekov et al. The T2K ND280 off-axis pi–zero detector. *Nucl.Instrum.Meth.A*, 686:48–63, 2012.

[50] P.-A. Amaudruz et al. The T2K fine-grained detectors. *Nucl.Instrum.Meth.A*, 696:1–31, 2012.

[51] N. Abgrall et al. Time projection chambers for the T2K near detectors. *Nucl.Instrum.Meth.A*, 637:25–46, 2011.

[52] D. Allan et al. The electromagnetic calorimeter for the T2K near detector ND280. *JINST*, 8:P10019, 2013.

[53] S. Aoki et al. The T2K Side Muon Range Detector (SMRD). *Nucl.Instrum.Meth.A*, 698:135–146, 2013.

[54] J. Imber et al. Super-Kamiokande event displays for T2K Run5-6 analysis candidates. www.t2k.org/docs/technotes/219, 2015.

[55] K. Abe et al. Measurement of the neutrino-oxygen neutral-current quasielastic cross section using atmospheric neutrinos at Super-Kamiokande. *Physical Review D*, 99(3), Feb 2019.

[56] Y. Hayato. A neutrino interaction simulation program library NEUT. *Acta Phys.Polon.B*, 40:2477–2489, 2009.

[57] K. Abe et al. Proposal for an Extended Run of T2K to 20×10^{21} POT. 2016.

[58] C.Licciardi and M. Barbi. Particle identification wiht the Fine Grained Detectors. www.t2k.org/docs/technotes/103, 2012.

[59] D.I. Scully et al. Measurement of Charged Current Coherent Production in FGD1. www.t2k.org/docs/technotes/191, 2015.

[60] S.S. Wilks. The Large-Sample Distribution of the Likelihood Ratio for Testing Composite Hypotheses. *Ann.Math.Statist.*, 9(1):60–62, 1938.

[61] A.B. Cudd et al. Measurement of flux-integrated joint on/off-axis numu CC0pi cross-section using FGD1 and the Proton Module. www.t2k.org/docs/technotes/384, 2019.

[62] S. Bolognesi et al. Model independent numu CC0pi cross-section in ND280. www.t2k.org/docs/technotes/214, 2014.

[63] D. Coplowe et al. Probing nuclear effects with a CC0Pi+Np differential cross-section measurement. www.t2k.org/docs/technotes/287, 2017.

[64] A. Ajm et al. Measurement of NuMu and AntiNuMu CC-0pi cross-section on carbon. www.t2k.org/docs/technotes/337, 2019.

[65] M.B. Avanzini et al. Measurement of flux-integrated cross-section on Oxygen and Oxygen/Carbon ratio of CC0pi events in FGD1+FGD2. www.t2k.org/docs/technotes/338, 2019.

[66] P. Bartet et al. ν_μ CC event selections in the ND280 tracker using Run 2+3+4 data. www.t2k.org/docs/technotes/212, 2015.

[67] A. Roodman. Blind Analysis in Particle Physics, 2003. PhyStat2003.

[68] K. Fusshoeller et al. Muon antineutrino and neutrino Charged-Current multiple pion selections in antineutrino mode. www.t2k.org/docs/technotes/273, 2020.

[69] E.T. Atkin et al. NIWG model and uncertainties for 2019-2020 oscillation analysis. www.t2k.org/docs/technotes/344, 2019.

[70] K.M. Graczyk el al. Electroweak form factors of the $\Delta(1232)$ resonance. *Phys.Rev.D*, D90:093001, 2014.

[71] A. Bodek and U.K. Yang. Modeling Neutrino and Electron Scattering Cross Sections in the Few GeV Region with Effective LO PDFs. *AIP Conference Proceedings*, 670:110–117, 2003.

[72] T. Yang et al. A Hadronization Model for Few-GeV Neutrino Interactions. *Eur.Phys.J*, C63:1–10, 2009.

[73] E.S. Pinzon. π-Nucleus Scattering Cross Sections. International Workshop on Frontiers in Electroweak Interactions of Leptons and Hadrons, 2016.

[74] C. Bojechko et al. Measurement and Correction of Magnetic Field Distortions in the Time Projection Chambers. www.t2k.org/docs/technotes/061, 2013.

[75] E. Frank et al. B-field calibration and systematic errors. www.t2k.org/docs/technotes/081, 2011.

[76] A. Cervera et al. Study of momentum resolution and scale using tracks that cross multiple TPCs. www.t2k.org/docs/technotes/222, 2014.

[77] C. Giganti et al. Particle Identification with the T2K TPC. www.t2k.org/docs/technotes/001, 2009.

[78] A. Fiorentini. ND280 TPC cluster efficiency. www.t2k.org/docs/technotes/234, 2015.

[79] Y. Petrov et al. ND280 TPC Track Reconstruction Efficiency. www.t2k.org/docs/technotes/163, 2016.

[80] F. Sanchez et al. ND280 global charge identification systematic error. www.t2k.org/docs/technotes/226, 2016.

[81] W. Oryszczak et al. FGD systematics: PID and IsoRecon hybrid efficiency. www.t2k.org/docs/technotes/223, 2015.

[82] J. Kim et al. Michel Electron Tagging in the FGDs. www.t2k.org/docs/technotes/104, 2015.

[83] F. Dufour et al. Systematics on Out-of-Fiducial-Volume Backgrounds in the ND280 Tracker. www.t2k.org/docs/technotes/098, 2015.

[84] C. Bojechko et al. CC-multiple-pion numu event selections in the ND280 tracker using Run 1+2+3+4 data. www.t2k.org/docs/technotes/152, 2013.

[85] J. Myslik. Pion Systematics. www.t2k.org/docs/technotes/125, 2013.

[86] E. Pinzon. Tuning of the NEUT Cascade Model using $\pi^{\pm}$-A Scattering External Data to Improve Final State Interaction and Secondary Interaction Systematic Uncertainties. www.t2k.org/docs/technotes/325, 2017.

[87] K. Mahn et al. FGD mass checks. www.t2k.org/docs/technotes/122, 2012.

[88] P. Martins et al. Measurement of Charged Current Coherent Production in FGD2. www.t2k.org/docs/technotes/290, 2017.

[89] C. Andrepoulos et al. The GENIE neutrino Monte Carlo generator. *Nuclear Instruments and Methods in Physics Research Section A: Accelerators, Spectrometers, Detectors and Associated Equipment*, 614(1):87–104, 2010.

[90] S. Cao et al. A Search for the $\nu\mu$ Charged-Current Coherent Pion Production with the Proton Module. www.t2k.org/docs/technotes/261, 2018.

[91] P. Stowell et al. Tuning the GENIE Pion Production Model with MINERvA Data. *Phys.Rev.D*, D100:072005, 2019.

[92] C. Giunti and C. Kim. *Fundamentals of Neutrino Physics and Astrophysics*. Oxform University Press, 2007.

[93] Y. Hayato et al. The NEUT Neutrino Monte-Carlo Generator: Physics and User Manual. www.t2k.org/docs/technotes/351, 2018.

[94] E.S. Pinzon. *Measurement of Pion-Carbon Cross Sections at DUET and Measurement of Neutrino Oscillation Parameters at the T2K Experiment*. PhD thesis, York University, 2017.

[95] M. Yu. Measuring the ν_μ and $\bar{\nu_\mu}$-induced Charged-Current Coherent Pion Production Cross Section On Carbon Using the T2K Near Detector ND280. www.t2k.org/docs/technotes/391, 2022.